DALHOUSIE UNIVERSITY

To comply with the Canadian Privacy Act the National Library of Canada has requested that the following pages be removed from this copy of the thesis:

Preliminary Pages
- Examiners Signature Page
- Dalhousie Library Copyright Agreement

Appendices
- Copyright Releases (if applicable)

A COMPREHENSIVE APPROACH TO MODELING AND ELIMINATING SANDING PROBLEMS DURING OIL PRODUCTION

by

Alireza Nouri

Submitted
in partial fulfillment of the requirements
for the degree of

DOCTOR OF PHILOSOPHY

Major Subject: Civil Engineering
at

DALHOUSIE UNIVERSITY

Halifax, Nova Scotia August, 2004

Your file Votre référence
ISBN: 0-494-02120-9
Our file Notre référence
ISBN: 0-494-02120-9

DEDICATION

To My Parents

TABLE OF CONTENTS

LIST OF TABLES

Page

LIST OF FIGURES

Page

LIST OF SYMBOLS AND ABBREVIATIONS

C_p	plastic projected cohesion (kPa)
C_r	plastic real cohesion (kPa)
CTC	conventional triaxial compression
DD	drawdown (kPa)
E	Young's modulus (MPa)
F_c	cohesion force (kN)
g_i	gravitational acceleration (m/Sec^2)
g^s	shear potential function
h	height of the pay zone (m)
H( )	the constitutive model
HCS	hollow cylinder sample
K_{ij}	the mobility tensor (m^{3}Sec/kg)
K_f	the bulk modulus of the fluid (kPa)
K_w	bulk modulus of water (kPa)
M	inertial mass of a node (kg)
P	pore pressure (kPa)
q_i	the mass discharge ((kg/Sec)/m^2)
q_v	the input fluid mass per unit volume ((kg/m^3)/Sec)
Q	fluid flow rate (m^3/sec)
r	the radius of investigation (m)
r_e	external radius (m)
r_w	cavity radius (m)
R	average grain diameter (m)
T	time (sec)
$\dot{u}_i$	velocity in i direction (m/sec)
UCS	unconfined compressive strength (MPa)
α	damping factor
β	water volume angle (rad)
χ	ratio of the total opening area to the total area of the wellbore
Δe_j^{ps}	the principal plastic shear strain increments
Δe_i	principal strain increments
$\Delta P_{capillary}$	capillary pressure (kPa)

ε_{ij}	the strain tensor
ε^{c}	effective strain at which cohesion is lost
$\bar{\varepsilon}^{p}$	effective strain (hardening parameter)
e_3^{pt}	The tensile hardening parameter
ε^{f}	effective strain associated with the limit friction angle
ε_v	volumetric strain
ξ	the variation of volume of fluid in unit volume of porous material
φ	bilinear friction angle at high confining pressure (degree)
φ_{cv}	the friction angle of constant volume (degree)
ϕ	porosity of the geomaterial (%)
ϕ_r	friction angle associated with the low stress portion of the bilinear envelope (degree)
ψ	dilation angle
γ	surface tension between two fluids (N/m)
k	intrinsic permeability (m^2)
λ	a factor accounting for the effect of the non-uniform grain distribution on the rock strength
ν	Poison's ratio
μ	viscosity of the fluid (kN/(m.sec))
η_v	the input fluid mass of per unit volume ($kg/(m^3.sec)$)
ρ_f	density of the fluid (k/m^3)
ρ_s	density of the geomaterial (kPa)
σ	normal stresses (kPa)
σ_{ij}	stress tensor (kPa)
σ_r	radial total stresses (kPa)
σ_θ	tangential total stresses (kPa)
σ_{UCS}	Unconfined Compressive Strength (kPa)
σ'_{ij}	effective stress tensor (kPa)
σ'_r	radial effective stress (kPa)
σ'_θ	tangential effective stress (kPa)
σ'_y	vertical effective stress (kPa)
σ'_v	volumetric effective stress (kPa)
$\sum F_i$	the net force on a node
τ	shear stresses (kPa)

ACKNOWLEDGEMENTS

I am thankful to God, the creator of the Universe, for his innumerable blessings.

I sincerely thank my parents for their love, devotion, and continued encouragement to gain further education.

I am very much thankful to Dr. Hans Vaziri, the initiator of this project, for putting faith on me and giving me opportunity to work on this project, for all his encouragements and supports and for granting me a free will to explore the validity of my ideas.

I would also like to express my deep appreciation to my co-supervisor, Dr. Rafiq Islam, for his guidance, encouragements, and extraordinary patience throughout this research. This is not only his support but also unique lessons of life, and creative thinking which I will carry for the rest of my life.

I also thank all of my committee members, Dr. Steven Butt for his valuable suggestions throughout the conduct of the experiments, Dr. Matiur Rahman, Dr. Lei Liu, and Dr. Ian Moore for reading and evaluating the thesis.

I am thankful to Dr. Farid Taheri for collaborating in developments of interesting ideas to me.

Nader Cheraghi and Noushin Mohammadi are especially thanked for their continuous support and encouragements.

I thank Ray Dube and Brian Lickense for their technical support in setting-up the experiments. Instant helps of Carolyn for administration part are gratefully acknowledged.

I also like to acknowledge those EEC group members who were involved in this project at some time and gave their contributions. Especially, I am thankful to Mr. Hadi Belhaj, Gary Zadsman, Naji Shomakhi, and Adam Donald for their help in conducting some of the experiments, and reading some of the papers.

My special thanks also go to Sarah Pace for her efforts in polishing this thesis.

Killam trustees for their financial support are gratefully acknowledged. This study was also partly supported by NSERC and AIF which are thankfully acknowledged.

Finally, I like to thank to all those who gave me all co-operation.

ABSTRACT

Sand production in the petroleum industry is a phenomenon of solid particles being produced together with reservoir fluid. This is a major problem that operating oil companies have faced for many years. To date, despite several research studies, sand production remains a nightmare for petroleum engineers.

Sanding-related problems are known to have increased production costs considerably: corrosion of the pipelines and other instruments, sand-oil separation cost, possible wellbore choke and repeated shut-in and clean-up of the wellbore are examples. On the other hand, a controlled sanding or even sand production invocation has proven very effective for increasing production rates, especially in heavy oil recovery, asphalt wells, and low PI wells. This thesis adopts a comprehensive approach to understand, model and, where necessary, prevent sand production. A new completion technique is presented for eliminating sand production altogether.

Even though many researchers have tried to predict sand production in the past, none suggested a comprehensive model that would take care of a range of failure and sand production mechanisms. Moreover, rare models predict sanding rate and volume along with the onset of sanding. This thesis presents a comprehensive numerical modeling of sand production whose criteria derive from the physics of sanding, taking the sequential nature of sand production into consideration.

The numerical model simulated two series of experiments on large-scale samples, one with vertical, and another horizontal well. The behaviour of the sample under loading, as well as the rate and volume of sanding, agreed reasonably well with the experimental results. This confirms that the criteria used for the model captured the essence of sanding.

An expandable completion technique is proposed which uses composite material. Two different techniques are proposed for implementation in horizontal and vertical/slanted wellbores. Even though the technique that is suggested for horizontal wellbore is deployable in all other wellbores, in order to reduce the cost and ease the installation process, another technique is suggested for vertical and slanted wellbores.

To alleviate some of the concerns and uncertainties on the interactions between an expandable liner and the medium around it, a series of experiments were conducted using hollow cylinder synthetic sandstone samples involving both fine and coarse grained sands at varying degrees of consolidation, including totally non-cemented samples. A stiffener, which was a representative of the proposed expandable completion technique, supported the central hole of a series of samples, while another series used open hole completion.

The actual influence of pore collapse on the severity of the damage to the rock could not be established, although the failure was readily noted. The experiments showed that a sample in the state of pore collapse retains its structure. In addition, the interlock between the grains is enhanced as the material compacts. The experiments showed that the material in the state of pore collapse produced little sand. The stiffener was also successful in eliminating general shear and tensile failure of the medium around the well. The experiments showed that a stiffener highly alleviated the amount of the produced sand and the magnitude of sanding, if any at all, depended on the aperture size. If the aperture size is too large, local shear failure may occur in the material at the opening location. Therefore, limited amount of sanding may be produced before stable arches develop.

Experiments on non-cemented highly porous sand-pack samples equipped with the stiffener indicated spontaneous sand production under single-phase flow. However, the situation was highly alleviated under a two-phase flow condition. As a result, capillarity played a determining role in holding the grains together and forming stable arches.

Finally, a straightforward analytical methodology is introduced which can predict the critical drawdown associated with the onset of sanding under either of single- or two-phase fluid flow. This formulation was applied to the experimental data of both weakly consolidated and unconsolidated sandstones. A remarkable agreement between the experimental observations and analytical predictions was concluded.

The proposed completion technique proved its efficacy for alleviating sand production. Additionally, the numerical and analytical modeling schemes demonstrated their capability to capture the essence of sanding. Therefore, the use of the tools presented in this thesis seems very promising for the future of sanding prediction and control.

Chapter 1: Introduction

Introduction

Improved methods of constructing and producing wells can increase field profitability. In any field development, a significant percentage of capital (typically 60%) is consumed by the material and construction costs of wells. Once on-stream, particularly in the later stages of field life, individual well productivity becomes vitally important for the project's continuing economic health.

In well construction and productivity optimization, many problems arise in connection with the geomechanics of the reservoir and the overlying layers, including wellbore stability, sand production, and hydraulic fracturing. Wellbore stability and sand production are the focus of the research proposal and experimental results presented in the following thesis. These problems cost the industry hundreds of millions of dollars per year. Sand production related costs do not appear to be properly managed due to the following:

(1) in many wells expensive sand control measures are employed that may induce a significant production impairment (for instance, gravel packing a horizontal well can add several hundreds of thousands of dollars to the completion cost and significantly reduce the production potential (typically 40 to 50%) due to plugging);

(2) Some completion techniques do not prevent sanding (for instance, all the open hole completions such as slotted liners or liners with external casing packer. Some others not only do not prevent sand production, but encourage it (for instance: cemented, cased and perforated completion techniques); and

(3) if sand production is induced under properly designed and controlled conditions, a manifold improvement in oil and gas production can be achieved.

The objective of the proposed research is to provide a practical and fundamentally sound method for predicting and controlling sand production. A numerical model is presented for a real time modeling of sanding. Further, an analytical tool is suggested that can provide a quick estimation of the safe operation conditions in both single- and two-phase

flow conditions. According to the interpretation of the numerical modeling and experimental observations, a novel completion technique is suggested which can eliminate the sanding issue entirely with little impairment in wellbore productivity. The interaction of this completion with the wellbore is studied in a series of experiments on synthetic samples with various degrees of consolidation and fluid flow conditions.

Background

Sand production takes place if the material around the cavity is disaggregated and, additionally, operational conditions cause powerful enough seepage forces to produce the grain particles. Disaggregation of the material initiates from cavity faces and propagates inside the medium. Material disaggregation can take place if the material fails under excessive drawdown or depletion, or any combination of the two. Depletion and drawdown may fail the medium under shear, tensile, or pore collapse mechanisms or a combination of these. After failure of the rock disaggregates the material, the resulted grains may be produced by the existence of enough pressure gradients in tension. Friction between the grains and capillary tension are the resisting forces against the grain's movements.

Numerical Modeling of Sand Production

Several analytical and numerical models are available for predicting the onset of sand production. On the basis of the strength properties, effective stress state, and flow regime in the formation, the circumstances resulting in sand production can be captured. These models, however, imply that once sand production is initiated, the entire formation becomes unstable. As such, they cannot be used effectively to examine scenarios involving limited sand production and the ability to optimize production.

The numerical model proposed in this thesis is intended to predict not only the onset of sand production but also the episodic nature of sanding and its influence on productivity. The proposed model can be used to design operational practices for controlling sanding to optimize production. For instance, a scheme for well pressure drawdown can be adopted to minimize or maximize sanding.

A Proposed Completion Technique for Eliminating Sand Production

The issue of completion technique arises where the numerical modeling indicates that sand production is a threat to wellbore stability and/or production costs. In these circumstances, sanding must be obstructed. Current completion techniques remain expensive and technically problematic, particularly where some eliminate sanding but dramatically impair wellbore productivity, e.g. gravel packing. The rest, including the most used, the cemented-cased-perforated technique, cannot solve the associated wellbore instability. It may even deteriorate the sanding.

In this thesis, a composite based completion technique is proposed for high alleviation or even elimination of sand production problems with little impairment of wellbore productivity. This completion technique attacks sanding by preventing shear disaggregation of the medium, which is a necessary condition for any sanding to occur.

The objective is to develop a screen that is easy and fast to install and expand, highly compliant to wellface shape, and possesses adequate strength and stiffness for the intended application. Moreover, it must also possess adequate corrosion resistance properties. There should be no restriction on mesh size opening (solid to highly porous). This technique eliminates the difficulties that have been implicit in current expandable techniques, the greatest being the elastic deformation that returns upon relaxing the loading for expansion of a hard shell metal liner.

The composite screen, in its flexible state, is lowered to the target zone. It is expanded against the wellbore wall by inflation/heat. The originally flexible system becomes stiff and strong via a curing process induced by the elevated temperature. The expanded screen will form to yield the designed mesh opening.

In the presence of an expandable completion, no disaggregation related to shear failure occurs, since the presence of the stiffener entirely eliminates any such possibility. Within material that has been consolidated to any degree, the only possible failure mechanism around the stiffener is pore collapse. When this occurs, the grain cement bonds break and sand grains contact each other, shrinking the volume. The sand production experiments verify if any failed material in volumetric mode may be produced.

Proposed Tasks

This research is comprised of the following three main tasks.

First Task: Material Characterization

A full investigation is carried out to characterize the yield envelopes of the material. Conventional Triaxial Compression (CTC) experiments were used to characterize the shear envelope. The cap was characterized by conducting Uniaxial Strain Triaxial (UST) experiments. A number of UCS experiments on samples with coarse and fine grain distribution of various ages were conducted.

Moreover, the physical properties of the material including porosity, permeability, density, and specific gravity were determined.

Second Task: Numerical Modeling

The second task was to develop a numerical modeling scheme for analyzing sand production. The proposed numerical modeling is capable of evaluating the onset of sanding, as well as a live prediction of the sanding rate under various operational schemes.

Why numerical modeling?

Despite great efforts undertaken to improve techniques for predicting sand production, practice in the field proves that a quantitatively accurate prediction of volumetric solid production is still to be developed, especially for poorly-cemented sandstones. Existing models may predict the onset of sand production and analyze cavity stability and rock failure. However, they cannot predict the volumetric production of sand over time as a function of applied stresses, fluid flow rates, and changes in water saturation.

Third Task: Sand Production Experiments

The third task was large-scale sand production experimental modeling. The experiments were conducted on both hollow cylinder samples with an open hole completion, as well as on samples completed with the proposed completion strategy.

Two different set-ups were used in the experimental program. The first set-up was used to conduct experiments in order to validate the numerical modeling scheme. These experiments are discussed in Chapter 2. The other set-up was used in all the rest of the experimental modeling. Results of these experiments appear in Chapters 4 through 6.

The main difference of the two set-ups lies in the way the radial stresses are generated. In the first set-up, radial stresses can be applied independently of the axial stress. This is done by increasing the pressure of the hydraulic oil surrounding the sample by a controller. In the second set-up, the sample is laterally restrained. Therefore, radial stresses are generated automatically as axial stresses are varied.

The reason behind replacing the first set-up by the second set-up was to enhance the controllability of the experiments, which improved their repeatability and, therefore, reproducibility of the results. It was extremely difficult to conduct repeatable experiments using the first set-up due to the possible penetration of the membrane which wrapped the samples into the permeable zone surrounding each sample.

A perfect match to the operational conditions as practiced in the field would have been to set the in situ conditions in terms of axial and pore pressure. This would be followed by a gradual decline in wellbore pressure (drawdown). However, this practice is extremely difficult to be duplicated in a laboratory setting. This is because it needs two pumps which can provide high pressure and at the same time high flow rate, one to be used in the exterior and another in the interior boundary. To circumvent this difficulty, another procedure was used in the tests that provided equivalent conditions in terms of flow rate and effective stress conditions. The procedure is explained in the body of the thesis, and the effects of drawdown and depletion on effective stresses in the medium around the wellbore are elaborated in Chapter 3.

Experiments on Weakly Consolidated Samples with Open hole Completion

The importance of weakly-consolidated sandstone is indicated by the fact that an estimated seventy per cent (70%) of the world's total oil and gas reserves are found in poorly-consolidated reservoirs. Meanwhile, poorly-consolidated sandstones, marked with weak existing cohesion among grains, are the most common solid producers.

Sand production experiments were performed on hollow cylinder samples simulating an open hole completion, with a central hole representing a wellbore and the sample representing the reservoir. Experiments were run with single- and two-phase pore fluid involving both fine and coarse grained sandstone. Open hole experiments were intended to be the standard experiments of those completed.

Experiments on Completed Weakly Consolidated Sandstone

The objective of this study is to conduct fundamental research into various aspects of the interaction between expandable and weakly-consolidated mediums. Among the main effects to take into account was the possible pore collapse of the medium during production. There remained a level of uncertainty regarding the possible effects of pore collapse on the severity of the damage to the rock. Moreover, it was not clear if the pore collapse could degrade the material to the level of the constituent grains supplying a source for sand production. Another objective was to investigate the level of the possible effect of the expansion on productivity of the wellbore.

Experiments on Completed Unconsolidated (Sand-Pack) Samples

General non-cementation provides the worst-case scenario when it comes to sand production in any reservoir. There may be two different sources of non-cementation. First, it is found in unconsolidated sandstones (the level of consolidation is defined based on the degree of cementation). Secondly, material failure under excessive loading conditions may degrade the initial rock type material to soil type.

Anticipated Significance of the Work

Although a completion technique capable of eliminating sand production is clearly of paramount importance to the oil industry, no comprehensive investigation into the behaviour of a medium reinforced by an expandable completion technique had yet been undertaken in the laboratory. Furthermore, there had been no model developed or available that would be of use in predicting and controlling sand production under realistic conditions, even though better understanding of the mechanisms resulting in initiation and progression of sand production and its concomitant impact on productivity is vital in generating tremendous savings in capital and operating costs throughout the oil and gas industry, and the concepts themselves can be applied to both new fields and mature reservoirs.

The anticipated results of the proposed study provide solutions that conform to the industry's current philosophy of emphasizing production improvement, the maintenance of existing facilities, and the extension of their useful life by a few more years. On the one hand, the majority of the largest existing fields have reached, or have gone beyond,

plateau production and few major new fields have been discovered, while most newer fields are smaller or present substantial development difficulties.

Such are the main outlines of the bigger picture that has rendered implementation of new and cost-effective technologies to increase production so essential. It marks the path to remaining profitable. Without such propping-up, the fossil fuel supply picture becomes cloudier. The prospect of ongoing and increasing fuel-price volatility looms more threateningly. The concomitant uncertainty must eventually strip power in the capital and consumer markets out of the hands of those interested in maintaining and improving production and place it in the lap of the speculators. These forces then ride the sudden increases in fossil fuel prices induced artificially by their financial manipulations to the point that bull market becomes bear-ish and some "readjustment" (or similar euphemism for a crash) takes more and more units out of production regardless of the potential that may yet remain to be produced from any given reservoir.

Scope of the Thesis

This thesis contains eight chapters and five appendices.

Chapters 2 and 3 are devoted to numerical modeling of sand production experiments. Chapter 2 contains a paper which numerically models an experiment on an open hole hollow cylinder sample representing a vertical hole. The experiment of the paper comprising the second chapter used a trixial setup, referred to only in this chapter. For the remaining experiments, another setup was designed and used that was consolidation-based. The reason for the switch was to ease some of the difficulties encountered in running the experiments and strengthen the degree and likelihood of reproducibility of the results that should be expected from sticking to the desired test plan. Prior to the design of the experimental set-up, a study was conducted into the intended equipment design, as well as sample sizing, and elaborated in Appendix A. Chapter 3 comprises a paper which numerically models an experiment on a sample with an open-hole horizontal well in a large block test. The mathematical formulation of the numerical model is reflected in Appendix B.

Chapter 4 deals with experimental studies on samples with an open-hole completion. The paper of this chapter elaborates the quality of sample preparations and material

characterization. This paper presents the results of sand production experiments on samples with single- and two-phase pore fluid. The experiments of this chapter are used as standard tests which are repeated for samples with supported boreholes. Moreover, some observations on sand production in single- and two-phase flow are elaborated.

Chapters 5 and 6 are two papers which focus on sanding issue in a wellbore completed by a stiffener. A stiffener is a representative of the proposed expandable technique. This thesis presents a novel expandable completion technique which is intended for elimination of sand production. Appendix E is devoted to elaborating this completion idea. Chapter 5 is a paper which experiments the stiffener effect in the behaviour of weakly-consolidated samples, as was used in the experiments on samples with an open-hole completion. The experiments of this paper are all under single-phase flow. Chapter 6 discusses experiments on non-cemented samples with a completed central. Both single- and two-phase fluid flow were considered in the experiments. Finally, Chapter 7 summarizes the findings of this research and draws some conclusions. Chapter 8 discusses recommendations for advancement of this research. First, further experimental and mathematical analyses, which should be conducted before the proposed completion technique can be implemented in practice, are reviewed. Then, the opportunities for further enhancements of the numerical modeling are discussed.

In all of the papers which build Chapters 2 through 6, the first author has played the main role in conducting the experiments, numerical modeling, and writing. The contribution of the co-authors has been in the level of either supervision, or assisting in conducting the experiments or taking part in discussions and sharing ideas.

Chapter 2: Sand Production Prediction: A New Set of Criteria for Modeling Based on Large-Scale Transient Experiments and Numerical Investigation

Publication Status: Accepted (Acceptance Date: March 23, 2004), SPE 90273, SPE Annual Conference and Exhibition, Houston, TX, Sep. 2004.

Abstract

Using novel physical model experiments and numerical analyses, a set of criteria are proposed that can be used to determine the onset of sanding and its severity in terms of rate and duration.

Experiments on large-scale hollow cylinder specimens were conducted involving real time sand production measurement under various conditions. Synthetic sandstone was used in the experiments whose strength properties were comprehensively determined. A numerical approach was used for simulating the proposed experiments. The material behaviour was simulated using an elasto-plastic stress-strain relationship. The model simulated interaction between fluid flow and mechanical deformation of the medium in predicting sand production. The criteria considered for sanding were more comprehensive than those conventionally used, and included modeling strain softening of the material accompanied by shear band formation, as well as tensile failure. In the post disaggregation phase, additional features were considered including allowing for the removal of the disaggregated material and making the necessary adjustments to the size and properties of the domain under consideration. Hence, the model is considered to be suitable for time-dependent analysis of the rock as it undergoes disaggregation and production induced by depletion, drawdown, and water-cut. By relating the sand rate to production over the life of a field, the tool can be used in assisting with the completion and operation design of the wells.

The model shows good agreement with experimental results in terms of rock deformation and sand rate. It predicted the onset of shear failure and the subsequent strain softening initiated from the cavity face and propagated inside the medium. Strain softening proved to be the main mechanism for material disaggregation. The agreement between the

numerical and experimental results under comprehensive and complex conditions bodes well for its field applications.

Introduction

Despite the incredible effort to improve the prediction of sand production, field practices demonstrate that quantitatively accurate prediction of volumetric solid production has yet to be developed, especially for poorly cemented sandstones. Existing models can predict the onset of sand production and analyze cavity stability and rock failure; however, they cannot predict the volumetric production of sand over time as a function of applied stresses, fluid flow rate, and changes in water saturation.

A brief description of the existing models is introduced in the following paragraphs.

Modeling Strategies

Several analytical and numerical models are available for predicting sand production (e.g, Perkins & Wintergarden, 1988; Vaziri et al., 1997b; Vaziri and Palmer, 1998; Sanffilipo et al., 1995; Morita et al., 1998; Risnes et al., 1982). Some of these models assume sanding is due to seepage (tensile failure), while others base it on the level of strain (compression). Most of the models predict sanding initiation (Weingarten and Perkins, 1992; Morita et al., 1989a&b; Kessler et al., 1993; Sanfilippo et al., 1995; Veeken et al., 1991; Tronvoll & Halleck, 1994; Wang & Dusseault, 1996). Some other models view sand production as a mixed hydro-mechanical process (Tronvoll et al., 1992; Tronvoll et al., 1997a; Tronvoll et al., 1997b, Charlez, 1997; Papamichos and Malmanger, 1999).

Shear or Tensile Failure

Numerous types of shear failure models have been published. An elastic brittle failure model is easy to implement (Edwards et al., 1983; Coates and Denoo, 1981; Nordgren, 1977; Stein, 1988; Edwards et al., 1988), but the disadvantage is that it does not offer a very realistic description of friable and loose materials. An elastic-plastic material model involves more computational effort and, in return, enables a more realistic description of the material behaviour (Morita et al., 1989a; Stein, 1988).

Stability criterion based on tensile failure has been expressed in terms of the drawdown pressure gradient at the cavity wall (Morita et al., 1989a; Morita et al., 1989b). A critical

value of the pressure gradient was first derived by Bratli et al. (1981). The fact that the disintegration phase is overlooked in the stage of modeling is the major weakness of this model.

Weingarten and Perkins (1992) proposed an analytical model using the Mohr-Coulomb criterion, and assumed sphere geometry for perforation cavity. Tensile failure was used as a criterion for the initiation of sanding. Moreover, they suggested that shear failure took place in the reservoir of an offshore field and took the shear failure of the reservoir as a criterion for depletion induced sanding. This assumption is incorrect considering the uniaxial strain condition of the reservoir, which may lead to pore collapse rather than shear failure. Morita and Fuh (1998) used a finite element numerical modeling to predict the onset of sanding. They used the Mohr-Coulomb and Drucker-Prager models with a critical plastic strain as a criterion for sanding. This criterion does not have any theoretical nor physical meaning, and overlooks the process which leads to sanding. They also realized the importance of the discharge of failed material on the possible progression of failure into the competent material and, consequently, the release of more material for production. Moreover, they analysed a cased and perforated vertical wellbore and compared the conditions leading to sanding with those of an open hole completion of a horizontal well. They concluded that if sand problems are observed from existing perforated vertical wells, a sand control device must be prepared when a horizontal well is planned.

A well-accepted conceptual model for sand production has been produced by Morita et al. (1989a &b). Within this model, sand production can either be triggered by compressive (shear) failure, induced by a combination of in-situ stress and drawdown; or by tensile failure, induced by the near-cavity pore pressure gradient. Compressive failure around the borehole leads to the formation of breakouts adjacent to the cavity. Whether compressive failure or tensile failure prevails will depend on the values of in situ stresses, drawdown, and flow rate in relation to the rock strength. The extreme condition of compressive failure at zero flow rate is analogous to hollow cylinder collapse (Antheunis et al., 1976a; Antheunis et al., 1976b; Veeken et al., 1991). The other extreme, tensile failure at near zero near-cavity effective stress, would be similar to the unconsolidated sand failure experiments as performed by Hall and Harrisburger (1970), or Bratli and

Risnes (1981). Van den Hoek et al. (1996) presented the results of the theoretical and experimental studies into the prediction of the sand trigger around cylindrical and hemi-spherical cavities in weak sandstones under a variety of in situ stress and flow rate conditions. The theoretical analysis was based on the bifurcation theory. It showed that the preference of compressive or tensile failure around a cavity only depends on the cavity size. Large cavities (e.g. boreholes) are consistently prone to compression failure, whereas small cavities (e.g. perforations) are equally subject to compressive or tensile failure, depending on material properties

Erosion Based Models

Some of the proposed models work based on an erosion mechanism. According to Durett et al. (1977), erosion takes place if the drag force exerted on a surface particle exceeds the apparent cohesion between surface particles. Hence, fluid velocity becomes an important factor. This is confirmed by field experience; in loosely consolidated formations sand production from open holes tend to be less than those from perforated completions (Philips and Whitt, 1983; Barril and Gay, 1983). Papamichos and Malmanger (1999) proposed a model based on an erosion mechanism. Their model solves the equilibrium equation with a continuity equation of fluid flow, solid, and fluidized solid. The deficiency of their model is mainly related to the number of parameters that cannot be readily evaluated. In their proposed model, cohesion, elastic modulus, permeability, and sand production coefficients are all related to porosity and are all calibration parameters. Stavropoulou et al. (1998) proposed a model that is similar to what Papamichos and Malmanger (1999) proposed. They used an elastic-perfect-plastic model with the Mohr-Coulomb envelope as a failure criterion. Therefore, their model is subject to the same deficiencies as the other model, combined with to the fact that elasticity is not a sufficient constitutive model for geomaterials. In addition, Geilikman et al. (1997) and Vardoulakis et al. (1996) proposed an erosion based model which suppresses all rock deformation and strength characteristics, and in which mass transport is emphasised. The rock is treated as a loose cohesionless material.

In all of these models, erosion is mainly governed by the ability of grains to pass through interconnected void spaces and matrix defects are considered as erosion starter points.

Application of the Bifurcation Theory into Modeling Sand Production

In the context of the bifurcation theory, the cavity stability problem has been numerically studied by Papanastasiou and Vardoulakis (1992), who performed large-scale finite element computations and followed the evolution of localization into the post-bifurcation regime. Tronvoll et al. (1993) developed a finite element code which incrementally solves the axisymmetric problem for the trivial solution and checks in every increment the condition for non-axisymmetric bifurcation modes.

On the subject of the concurrency of shear band formation and bifurcation points, Tronvoll et al. (1993) suggested that for an associated material, surface instability occurs at the peak of the material response. However, for a non-associated material, surface instabilities are not possible as they are preceded by shear band formation. On the other hand, for a material that obeys a non-coaxial flow rule, surface instabilities (bifurcation) occur in the hardening regime and therefore may precede shear-band formation.

Although such analyses are important in studying the progressive localization, they become prohibitively expensive for the examination of the influence of various constitutive models, parametric studies, and generally routine applications in practice. Additionally, all of the presented models based on the bifurcation theory predict the onset of sanding, and stand short in modeling the transient nature of the problem.

Assumption of Wormhole Development

Wang et al. (2001) incorporated a three-phase three-dimensional geomechanical model. They assumed wormholes develop from perforations when the pressure gradient exceeds the UCS of the disaggregated material. In their model, deformation is not coupled with multiphase flow in the porous medium. In addition, input data to characterize the wormhole propagation are massive and usually not available. The assumption of sanding in the form of wormhole propagation is questionable in the first place.

Role of Water-Breakthrough on Sanding

Typically it is reported that the onset of sand production is observed at water breakthrough (Tronvol et al., 2001; Vaziri el. al, 2002). Han and Dusseault (2002) and Vaziri et al. (2002) proposed the various possible mechanisms that may hasten the instability depending on the degree of water saturation and the cement mineralogy. For

instance, water changes the multi-phase flow behaviour by changing the relative permeability. Water can also weaken the sandstone whose constituents react to water, e.g. shale, some clay minerals, and carbonate cementation. While the aforementioned effects have some influence, in many situations it is difficult to make any link between such mechanisms and an immediate sanding following water-cut. Numerous studies have linked the immediate instability of the grains upon water breakthrough to the destruction of capillary induced cohesion between the grains.

Bianco and Halleck (2001) performed some experiments on poorly consolidated sandstones subjected to water influx. In their experiments, confining pressure was kept constant during the test, while single-phase and two-phase experiments were carried out. Two-phase experiments were performed at two different levels of flow rate. According to the results, single-phase saturated sand did not develop enough cohesive strength to support a stable arch and sand was produced massively. However, a small increase in the wetting-phase saturation developed enough cohesive strength to stabilize an arch, reducing sand production. Lower connate water content increased the level of flow rate to induce sanding.

Han and Dusseault (2002) presented a model to evaluate the magnitude of capillary cohesion, as well as the behaviour of the medium with an increasing level of water saturation. They concluded that the order of magnitude of capillary cohesion is the same as seepage forces. Therefore, this effect should not be neglected. Moreover, capillary cohesion degrades very quickly with the increase of water saturation. The most degradation of the capillary cohesion occurs within a small percentage of water saturation, approximately the first 5%. The possibility of the chemical reactions with water is also discussed, but it noted out that in water breakthrough, capillary changes play a dominant role whereas chemical reactions may only become an issue in the long term.

Vaziri et al. (2002) proposed a FEM fully-coupled fluid flow and deformation. The result was that even a small amount of residual cohesion is sufficient to hold back a large mass of failed sand. The conclusion was that common criteria based on critical drawdown, minimum bottom hole pressure, depletion or fluid flow velocity failed to predict the

outcome by a relatively large margin. All these cases were subjected to high drawdown and depletion and did not produce any sanding until water production was encountered.

Experimental Studies

Experimental studies focused on both determination of material properties and sand production. For determining material properties, solid samples of small sizes were used. For sand production experiments, Hollow Cylinder Samples (HCS) of large sizes were deployed.

Getting sandstone samples from the field is usually expensive and difficult. Weakly-consolidated sandstones are especially difficult to core in the oil-wells and recover to the surface undisturbed. Moreover, in the experimental studies, the use of consistent samples is preferable, increasing the likelihood that the results obtained would be reproducible in future or ongoing research. For samples extracted from the quarries, a quick spatial change of physical and mechanical properties are common. This inconsistency usually introduces difficulties in the interpretation of the results. Therefore, it was decided to depend on synthetic sandstone samples that can closely represent sandstone formations therefore facilitating the control of important parameters.

Manufacturing the Synthetic Samples

Both small size samples for material characterization and HCS used the same recipe for the sample mix and preparation procedure.

Material Composition

The synthetic sandstone consists of sand, Portland cement, and water. The material composition contained a weight ratio of 0.11 for cement/sand, and 1.25 for water/cement.

Grain Size Distribution of the Sand Used in Sample Making

Grain size distributions of the Silica sand grains ranged between 100 to 1000 μm as shown in Figure 2.1.

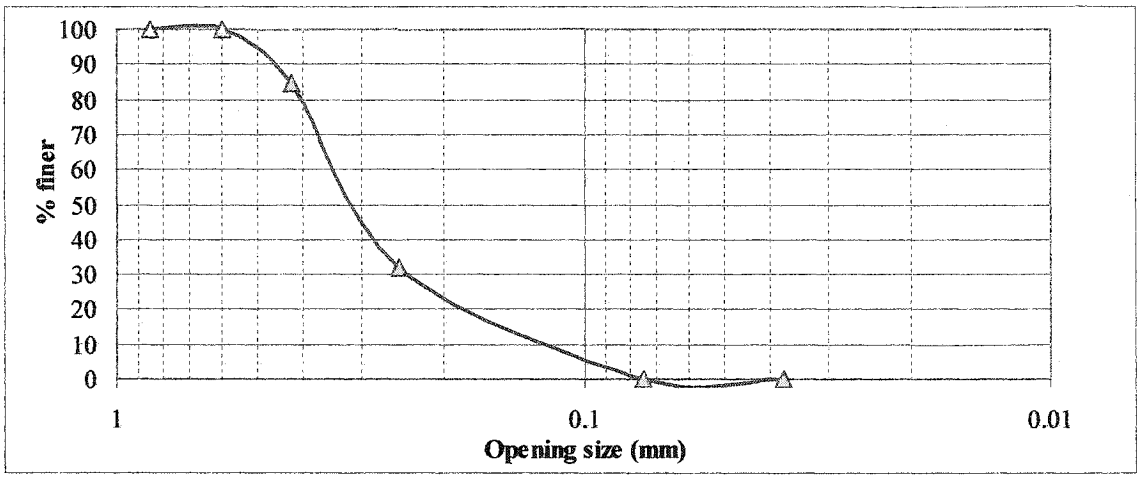

Figure 2.1. Grain size distributions of the sand used in synthetic samples

Manufacturing Process

Sand, cement, and water are mixed into slurry, and then slightly pre-compacted when packed by a spatula into a mould and vibrated by gentle hits. To prevent the formation of distinct layers, the top of each layer was ploughed.

Casting of small solid samples was carried out in a cylindrical mould made of Playtex material. The internal diameter of the mould was 54 mm and the height was approximately 110 mm. Casting of HCS was performed in an aluminium mould with an 125 mm inside diameter, and a central rod which created the hole in the centre.

After each casting (both small and large samples), the sample remained in the mould for 3 days. It was then taken out of the mould and put in water for 18 days at ambient temperature. After this, the sample was put in an oven set to 50°C.

All of the samples were ground at both ends. For the HCS, epoxy was applied in order to make a stiff smooth cap at each end. The samples were kept dry in the oven and saturated before the start of each experiment.

Stringent quality control was implemented during the casting to obtain uniform material properties in each sample, as well as from one sample to another. The process of sample making was consistent for all samples in order to make sure that they would provide reproducible results.

Material Properties

The synthetic sandstone was described for both physical and mechanical properties. For the mechanical description, Unconfined Compressive Strength (UCS), and Conventional Triaxial Compression tests (CTC) were considered. UCS is a conventional strength indicator and CTC tests described the shear envelope of the Mohr-Coulomb model.

These parameters were fed into the numerical analyses which used a Mohr-Coulomb based model.

Determination of the Mohr-Coulomb Envelope

In order to capture the physics of the failure and to consider the possible contribution of all the aforementioned failure mechanisms, a bilinear Mohr-Coulomb mixed hardening/softening model was used in the simulations. A schematic of the model is depicted in Figure 2.2.

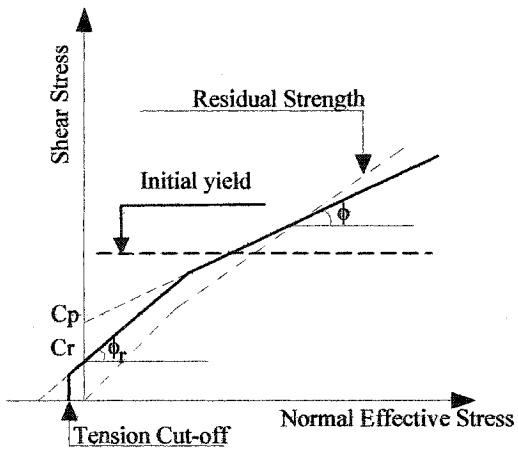

Figure 2.2. Bilinear strain hardening/softening Mohr-Coulomb model

According to the model, tensile failure takes place when the stress tensor meets the tension cut-off. Shear failure occurs when the stress tensor touches the shear envelope. Theoretically, shear failure may only take place adjacent to the cavity faces where there is a possibility of differential deformation to take place.

Table 2.1 summarizes the mechanical properties of the synthetic sandstones. Shear envelope is also depicted in Figure 2.3. The shear envelope of Figure 2.3 is based on the CTC experiments, and the peak axial effective stress was used for obtaining the envelope. It is crucial, however, to realize that at low lateral stresses, the material may undergo a

massive strain softening which cause disaggregation. Therefore, the ultimate axial stresses instead of peak axial stress must be used to conclude the real cohesion of the disaggregated material at low confining pressure. If such a methodology is used, a real cohesion of close to zero will be determined at such conditions.

Table 2.1. Mechanical properties of the synthetic sandstone

UCS (MPa)	Young's modulus E (MPa)	ν	C_p (kPa)	C_r (kPa)	φ (degrees)	φ_r (degrees)
2.1	400	0.05	870	300	34	46

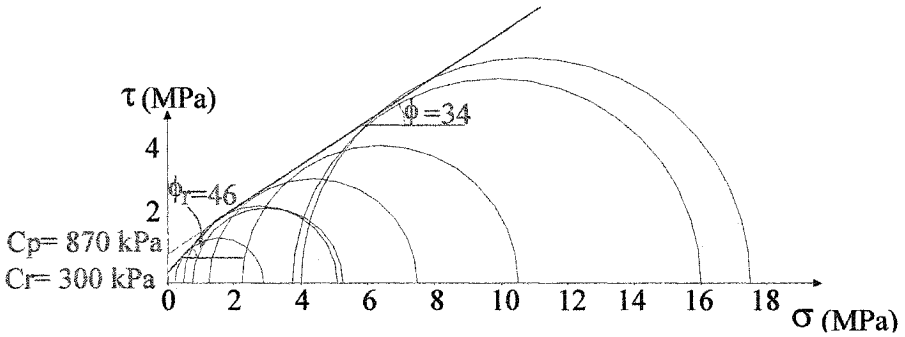

Figure 2.3. Mohr-Coulomb envelope of the synthetic sandstone

Physical Properties of Sandstone Samples

The physical properties of the synthetic samples are listed in Table 2.2.

Table 2.2. Physical properties of the synthetic sandstone

D10/D50/D90 (Micron)	Dry density (kg/m^3)	Saturated density (kg/m^3)	Porosity	Initial permeability (md)	Specific gravity
120/300/500	1610	1980	36-40	3600	2.67

A thin section was manufactured from a coarse-grained synthetic sandstone sample. The photomicrograph of this thin section is shown in Figure 2.4 under cross-polarized light. The grain shape is angular to sub-angular, and the grain size distribution is confirmed to be well sorted.

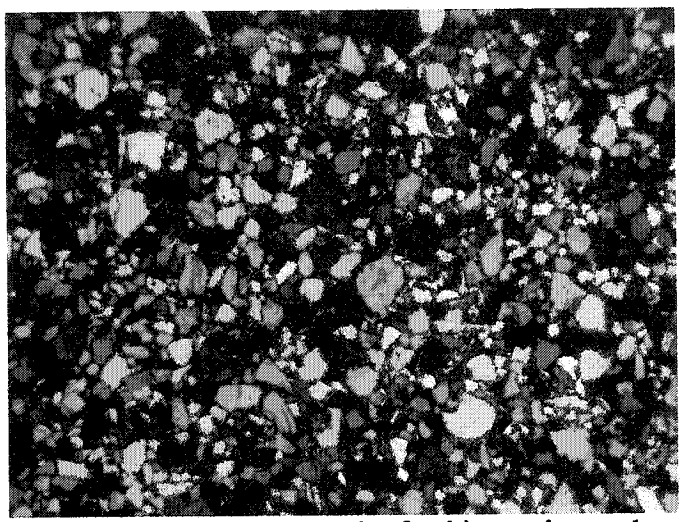

Figure 2.4. Microphotograph of a thin section under cross-polarized light; field of view is 11 mm

Sand Production Test Equipment

Simulated production was undertaken by using a 150 mm triaxial cell, which could accommodate samples of 125 mm in diameter. The testing equipment is shown in Figure 2.5. It includes a loading unit, flow set-up, sanding measurements unit, and instrumentation.

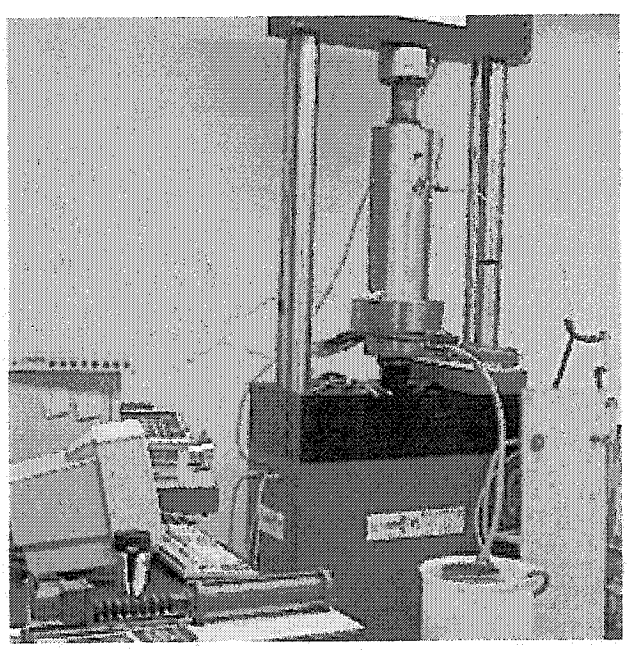

Figure 2.5. Photograph of the set-up used in sand production experiments

The individual units are elaborated as follows.

Axial Loading Unit

The axial loading unit can apply up to 250 kN of force to the top platen which sits on the top of the sample. It is designed with feedback control and continuous displays of axial load and platen displacement, and an IEEE computer interface with a built-in stepping motor.

To increase the axial loading capacity of the equipment, a top chamber is designed which is connected to the bottom chamber as shown in the schematic of Figure 2.6. Therefore the hydraulic oil of the top chamber is pressurized as much as the confining pressure. This pressure is transferred to the piston and adds to the axial loading capacity.

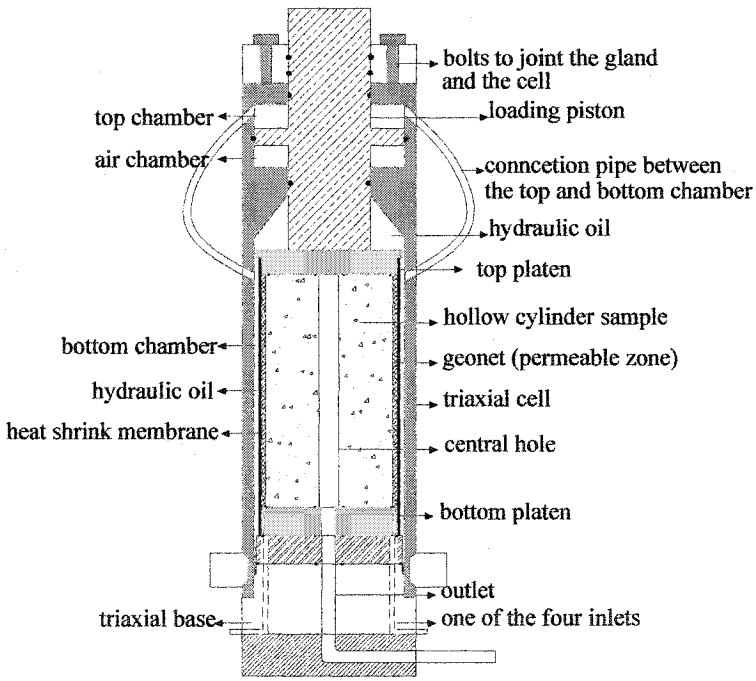

Figure 2.6. A schematic configuration of a synthetic hollow cylinder sandstone positioned between the top and bottom plates

Radial Loading Unit

A high pressure triaxial cell which allows confining pressure up to 64 MPa (10000 psi) is used in the experiments. The cell is initially filled with hydraulic oil. A controller with a

maximum capacity of 64 MPa is used for supplying the confining pressure. This controller is equipped with a digital pressure/volume controller.

Fluid Flow Unit

Figure 2.7 shows a schematic of the fluid flow unit. The flow system was set up to supply a radial inward flow. A high flow rate positive displacement pump with a maximum pressure capacity of 700 kPa was used for supplying fluid flow during the test. The fluid was supplied to the pump from a tank with nearly 200 liter volume capacity. A manifold was used to divide the flow from the pump to four vessels in the base of the cell. Fluid was injected through four tubes to small holes in the circumference of the bottom platen as illustrated in Figure 2.7. The small holes were connected to a high permeable zone of geonet, which was deployed around the sample.

The fluid and any produced sand were collected in the wellbore at the centre of the sample. The wellbore was connected to the outlet and was kept at atmospheric pressure during the testing.

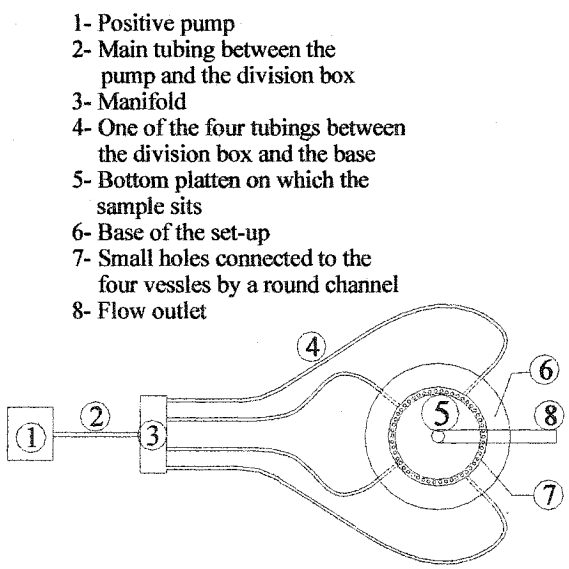

Figure 2.7. A schematic of configuration of the fluid flow vessels

High Permeable Zone around the Sample

A highly porous mesh, geonet, is used to provide a permeable zone around the sample as shown in Figure 2.8. Geonets are bi-planar drainage products, consisting of parallel sets of extruded ribs overlying a similar set at various angles.

The bottom of the permeable zone sits on the small holes of the bottom platen. These small holes are the supply lines of the fluid and are connected to the four main vessels in the base as shown in Figure 2.6.

The permeability of the geonet measured approximately 100 times greater than that of the samples. This system diverted the axial flow in the permeable zone to radial in the sample toward the central hole.

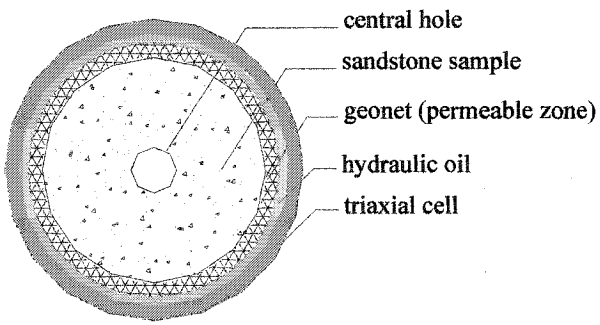

Figure 2.8. A cross section of the triaxial cell containing the sample and the geonet

Sand Measurement Units

From the sieve analysis results, grains are distributed in the range of 0.10-0.85 mm as shown in Figure 2.1. Therefore, a sieve #400 (aperture size 0.0375 mm) would suffice to entrap practically 100% of the produced material. The sieve sits on a tripod inside the tank. A pair of sieves was used and a digital balance weighed the produced sand.

By interchanging the sieve as necessary, the amount of the produced sand during consecutive time intervals could be measured. The produced sand was weighed in regular time intervals.

Instrumentation

Both axial load and displacements were measured by built-in transducers on the loading frame. The confining pressure was measured and displayed by a built-in pressure transducer of the 64 MPa digital pressure/volume controller. A dial gauge pressure measurement unit with a maximum pressure capacity of 690 kPa (100 psi), as well as a digital pressure transducer, were connected to the manifold to precisely measure the fluid pressure in the manifold box.

Two flow-meters were connected to the tubing of fluid supply. The minimum and maximum capacities of the flow meters were 3 and 250 cm^3/sec respectively.

Conducting the Sand Production Experiment

The synthetic sandstone sample was first saturated with water in a container under about vacuum pressure. It was subsequently wrapped by a layer of highly permeable geonet as illustrated in the schematic of Figure 2.6. The combination of the samples and the layer of geonet were wrapped in a heat shrink membrane shrunk against the sample by applying heat. The sample was then laid on the bottom platen and was covered by a triaxial chamber. Subsequently, the whole set-up was placed in the axial loading frame and a slight axial loading was applied to sit the axial loading piston on the top platen. The chamber was filled with hydraulic oil; and the tubing and controllers were all connected.

During simulated production, axial and radial stresses of the exterior boundary were increased independently. A pressure drawdown was applied between the sample and the central hole by using a high flow rate pump. The produced sand was collected on sieve #400 and periodically weighed. Thus, the sand volume and rate could be measured during the course of the experiment.

Observations of the Sand Production Experiment

Figure 2.9 shows the loading process and the associated sand production as a function of axial deformation. Throughout the experiment, radial stress was increased to as much as nearly 40% of the axial stress. Fluid flow was established at an axial stress of nearly 6000 kPa, as shown in Figure 2.10.

According to Figure 2.9, the curve of axial stress-deformation started with an elastic segment. As loading continued, more and more plasticity developed due to the formation of micro cracking in the sample.

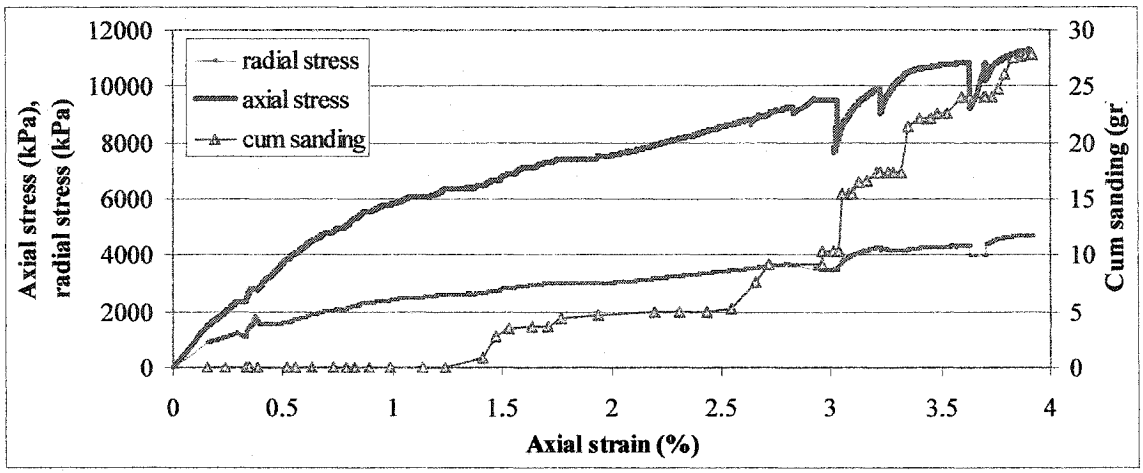

Figure 2.9. Cumulative Sanding and effective stresses as a function of axial strain

As Figure 2.10 indicates, both flow rate and drawdown increased in the beginning of the experiment. A gradual decrease of drawdown occurred as membrane started to penetrate into the mesh of the geonet which was a flaw in the experiment conduct. This incidence gradually decreased the permeability of the geonet, and reduced the net level of drawdown. It heated up the pump, which was working at its maximum working pressure and induced a few shut-ins. The first shut-in took place at an axial strain of 2.7% where confining pressure was nearly 3.5 MPa. Two more shut-ins occurred in the loading path.

As shown in Figure 2.10, although a continuous sanding was detected even under low flow rates, it was believed from the analysis that a flow rate below 50 cc/sec could not thoroughly produce all of the disintegrated material.

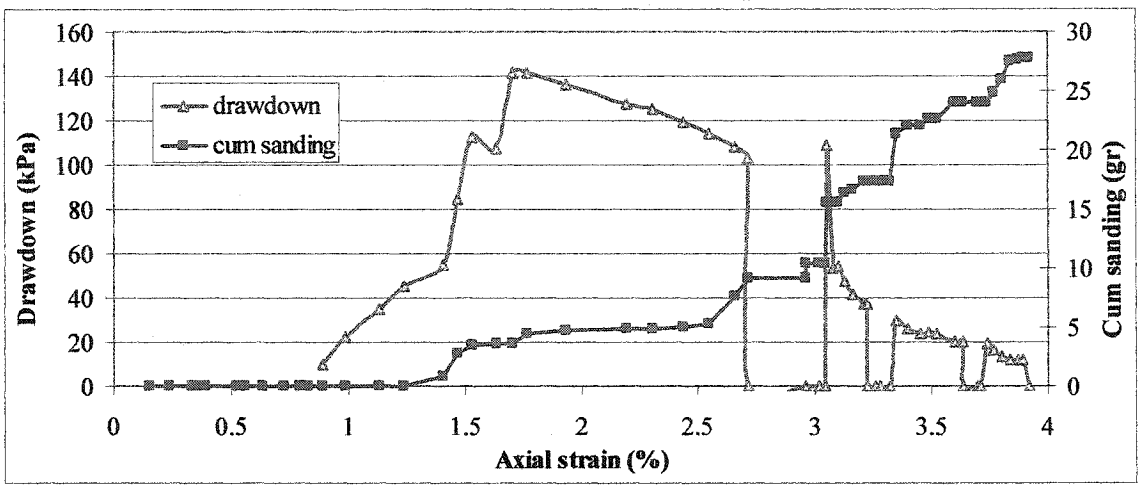

Figure 2.10. Drawdown and cumulative sanding vs. axial strain

Figure 2.11 illustrates grain size distribution of the original constituent grains and the produced sand. The analysis shows that the produced material is coarser than the original material. The maximum grain size increased from 1 mm to 5 mm.

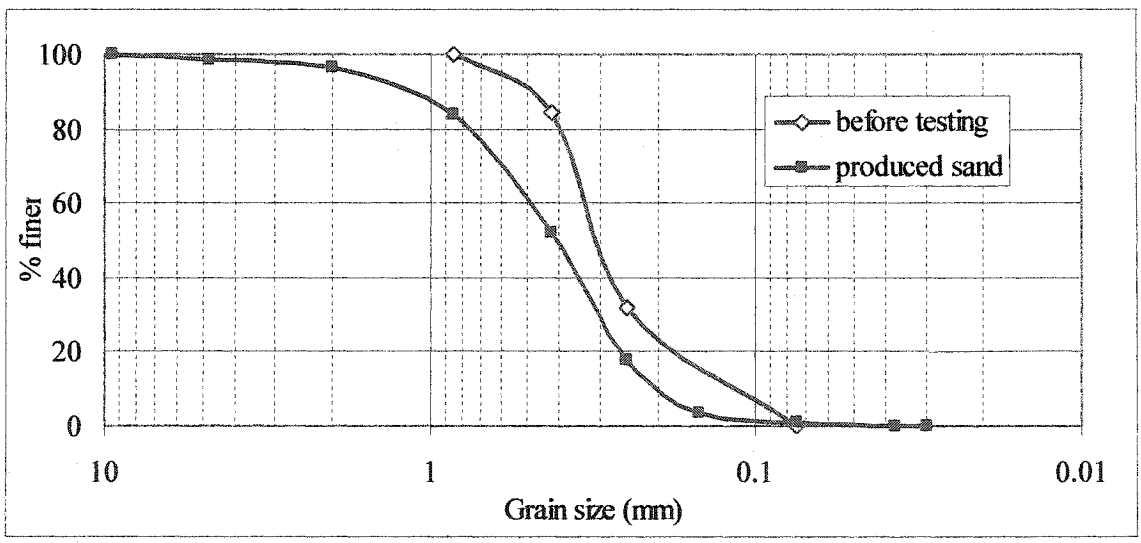

Figure 2.11. Grain size distribution of the constituent grains of the synthetic sandstone and the produced sand

Figures 2.12 and 2.13 are photographs of the two ends of the sample after the completion of the test. Failure and removal of surface material of the well face are observed at both ends.

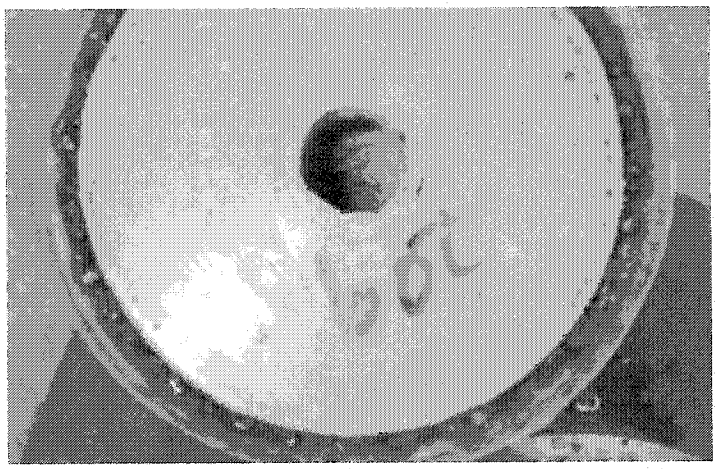

Figure 2.12. Bottom end of the sample indicating failure occurred at the well face

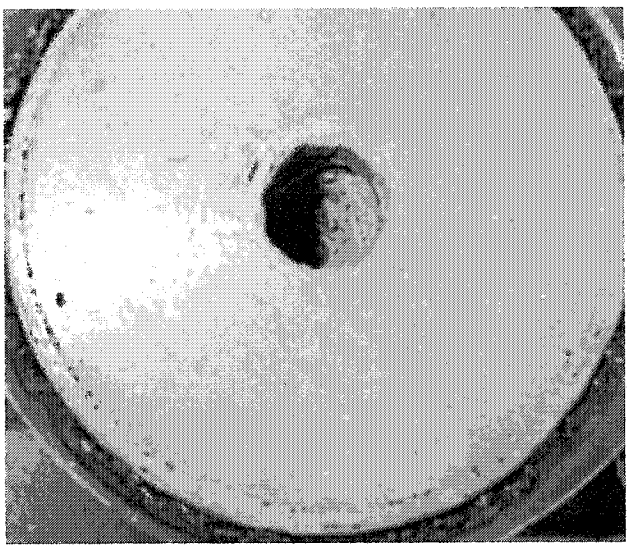

Figure 2.13. Photograph of failure at the well face of the top portion of the sample

Numerical Modeling of Sand Production

The governing equations of equilibrium and fluid flow in the reservoir have been employed in an incremental form in a finite difference program, FLAC. This program uses an explicit, time-marching Lagrangian analysis in contrast to an Eulerian formulation: the right hand side of all equations consist of known values, because the time step is chosen to be small. Therefore, information cannot physically transmit from one element to the other within that small time step (Cundal and Board, 1988).

In the simulations, the Mohr-Coulomb model, one of the most recognized models for engineers, was used. One of the major advantages of this model is that it is

uncomplicated and, moreover, its parameters are physically meaningful. By combining this model with a strain hardening/softening scheme, a powerful tool was provided which could simulate the complex behaviour of the medium and its disaggregation process.

Axial symmetry was assumed in the simulations. The primary unknown parameters are the pore fluid pressure and the solid velocities in two perpendicular directions in a plane along the axis of the wellbore.

Sanding Criteria

The assumptions and procedure as used in the proposed modeling scheme have the significant advantage of agreeing with the physics of the problem: sanding takes place if the rock adjacent to the cavity is directly failed due to tension, or if the failed rock under shear falls into tension. For this procedure to work an elastic-perfect plastic model is not sufficient and a hardening/softening model should be deployed. For the material to be disaggregated, it must fall into the strain softening regime. Strain softening has an additional consequence: it induces effective stresses relaxation which makes it possible for the drag forces of seepage to develop tensile stresses and produce the disaggregated material in tension.

In the loading process of the sample in the experimental program, the material behaves in an entirely elastic manner at the onset of loading. Because of stress concentration, plastic zones start developing from the edge of the central hole under the continued loading. The onset of plasticity is accompanied by a strain hardening regime. Despite the plasticity in the strain hardening process, the mechanical integrity of the rock is not destroyed, as large plastic strains are associated with increasing shear stress. In the hardening course, the deformation becomes more and more inelastic due to a continued micro-cracking and particle sliding. It is hypothetical that at the stage of strain hardening, no sand can be produced. Near the end of the hardening regime, axial stress scarcely increases and this means that the elastic strain rate is almost zero. As a result, all further strain increments are of a fully plastic nature.

In the absence of the effective normal stress at the cavity face, the softening regime dominates around the cavity subsequent to the hardening phase, which consequently, leads to the creation of shear bands in the affected region. This state causes the effective

stresses around the cavity to reduce to near zero. As little normal stress exists between the grains, there will be little frictional resistance to hold the grains together. Moreover, drag forces caused by seepage cannot transfer to the material in shear and/or compressional forms since material at this state cannot take any effective stresses. Therefore, seepage induced drag forces induce tensile stresses in the disaggregated material and may be able to produce the material in tension.

More sanding will develop the size of the cavity, which in return may expand the zone of strain softening. Therefore, it is critical to capture the process of material removal in any modeling of continued sanding. In the proposed numerical model, as soon as an element satisfies the sanding criteria, it is entirely removed from the mesh, and subsequently new boundaries are defined. Therefore, the pattern of cavity development is visible at different stages of the loading.

Analysis Process

In the analysis, the initial pore pressure and stresses are set to zero. Boundary axial and radial stresses, as well as boundary pressure, are given step-like increases according to the experimental practice. At each step, an undrained response is allowed to develop before allowing flow to take place. Subsequently, a coupled fluid-mechanical analysis is performed.

After each step is complete, a check is conducted to identify the elements that satisfy the sanding criteria. All of the eligible elements which are in the immediate neighbourhood of the cavity face are eliminated from the mesh, and their volume is added to the produced sand. Subsequently, the boundary conditions are applied to the newly defined boundaries.

Mobilized Mechanical Input Data

Table 2.3 shows the mobilized mechanical data that were used in the analysis. In this table, cohesion, friction angle, and dilation are presented as a function of the shear hardening parameter. The shear hardening parameter is elaborated in equations 13-A through 15-A. Also, guiding functions for mobilized friction angles, cohesion, and dilation angles are presented in equations 16-A through 18-A. Tensile strength is continuously updated using up to date real cohesion by using the following formula:

$$\sigma^t = \frac{C_r}{\tan\varphi} \qquad [2.1]$$

Furthermore, it is assumed that tensile failure completely disaggregates the material. Therefore, the tensile strength of the elements that fail in tension is reduced to zero. As the rock material is disaggregated and its real cohesion is reduced to zero, its tensile strength is also presumably reduced to zero (unless capillarity exists which provides a marginal real cohesion and tensile strength). It is this tensile strength of the disaggregated material which is the most important in the modeling of sand production rather than the tensile strength of the intact rock.

Table 2.3. Mobilized shear envelope parameters

Shear hardening parameter (%)	0	0.5	1.2	2.2	3.0	6.0	10.0
C_p (kPa)	2600	2559	2496	2410	2258	1480	955
C_r (kPa)	2600	2512	2100	800	130	80	10
φ (degree)	0	13.8	20.5	25.4	28.1	32.8	35.3
φ_r (degree)	0	17.4	25.6	33.9	37.01	42.8	46.5
ψ (degree)	0	0	0	3.2	6.3	13.8	13.8

The Finite Difference Mesh

The problem considered consists of a cylindrical sample with an inner diameter of 25.4 mm and an outer diameter of 125 mm. A half section along the axis of the sample was discretized by axisymmetric elements as shown in Figure 2.14. The finite difference mesh includes 1200 elements with solid velocities in radial and axial directions, and pore pressure as unknown parameters. A finite difference mesh was set with finely spaced elements near the wellbore. These elements were designed coarser away from the wellbore so as to reduce their total number, while at the same time not compromising the accuracy of the computations. Several mesh configurations were tested to ensure that the results were independent of grid spacing.

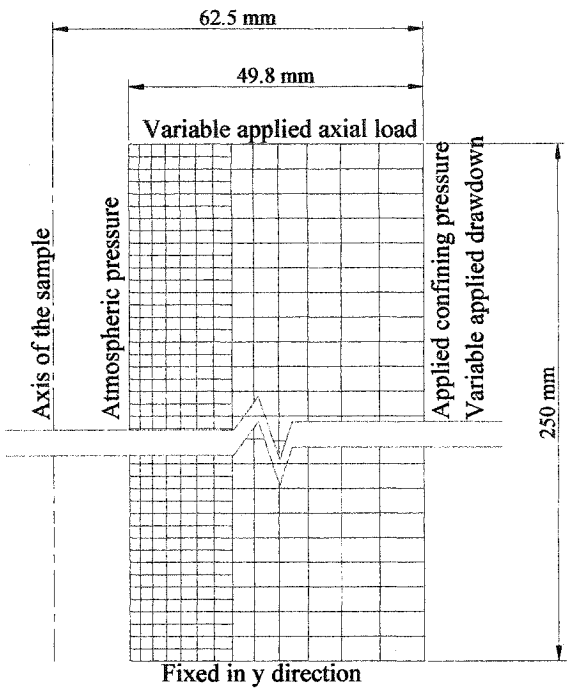

Figure 2.14. Finite difference mesh and boundary conditions

Boundary Conditions

Boundary conditions of both mass balance and momentum equations were defined to reflect the real testing conditions as shown in the schematic of Figure 2.6, and the loading conditions as shown in Figures 2.9 and 2.10.

For the loading boundary conditions, vertical displacements were fixed at the bottom boundary, while the variable axial loading was applied from the top boundary. A variable horizontal stress was applied at the outer round boundary to model the varying confining pressure. Zero loading was defined at the central hole boundary to model the atmospheric pressure condition in the central open hole.

For the flow boundaries, the central hole was kept at atmospheric pressure throughout the experiment. The external round boundary was also set to comply with a varying drawdown as indicated in Figure 2.10. The top and bottom boundaries were also set to zero normal flow velocity.

Results and Discussions

Figure 2.15 compares the cumulative sand production resulting from experimental and numerical modeling. The agreement between the experimental and numerical values is remarkable. It is emphasized that from any numerical analysis of sand production, the prediction of the severity of sanding should be the main focus of the modeling. As such, the order of magnitude of the sanding rate and volume should normally be an issue of concern. The predicted results not only qualitatively agreed with the experimental results, but were also reasonably well matched with the experimental values in terms of cumulative sanding.

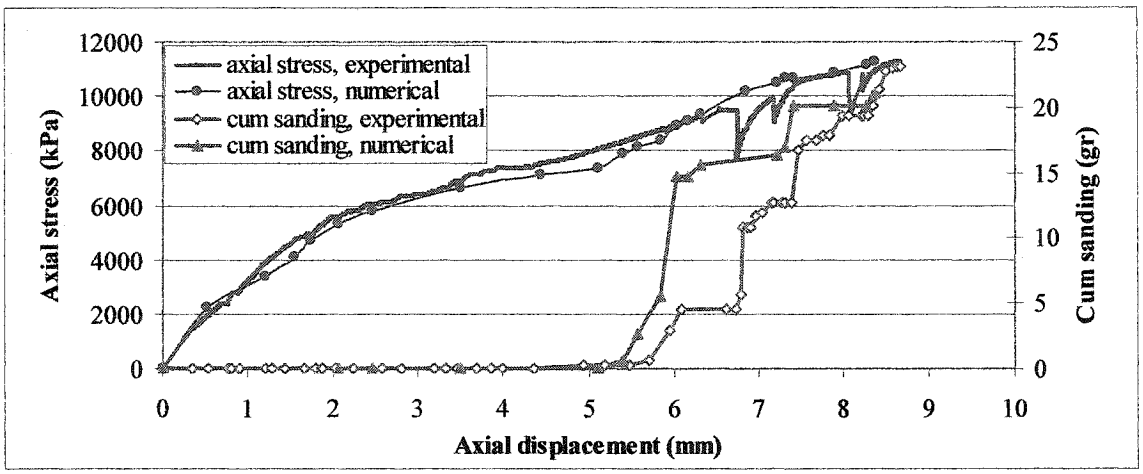

Figure 2.15. A comparison of the experimental and numerical cum sand production and axial stress-deformation curves

Drag Forces Induced by Seepage

A separate numerical analysis was conducted to estimate the magnitude of the seepage forces and induced effective stresses. The same geometry and discretization as used in the main analysis were considered in this simulation. The central hole was kept at atmospheric pressure and the pressure at the external round boundary was set at 141 kPa, which was the maximum pressure that was applied in the experiment. No axial loading and confining pressures were applied to the sample in this independent analysis. Similar to the bottom boundary, the top boundary was restrained in vertical direction.

Figures 2.16 through 2.18 show the results of such analysis. The sign convention in all of these is that pore pressure at compression is positive while effective stresses at

compression are negative. Figure 2.16 shows that radial stress starts from zero at the well face and increases to its maximum at the outer boundary. Pore pressure exhibits a similar trend, however, it builds up more slowly than the radial stresses. Therefore, the profile of effective radial stress peaks somewhere in the middle, but is zero at both boundaries.

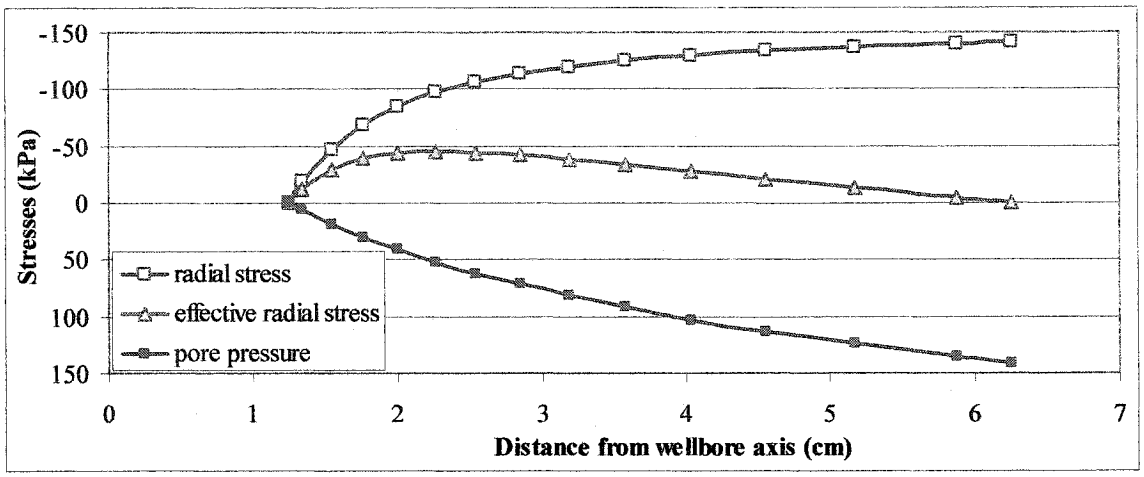

Figure 2.16. Profiles of radial total and effective stresses and pore pressure

Tangential stresses show a different trend from the radial stresses. Figure 2.17 shows the profiles of tangential total and effective stresses, as well as the pore pressure. The graphs indicate that tangential stresses peak at the well face and show a gradual decline toward the outer boundary.

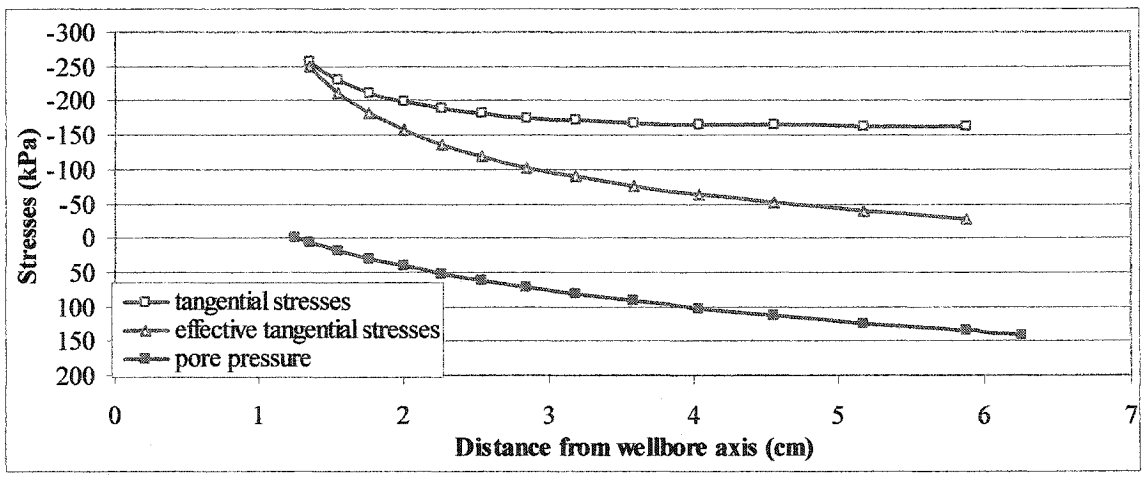

Figure 2.17. Profiles of tangential total and effective stresses and pore pressure

Figure 2.18 shows the profiles of effective radial and tangential stresses. The graph shows that the maximum difference between the two occurs at the well face, which induces the maximum shear stresses at this location.

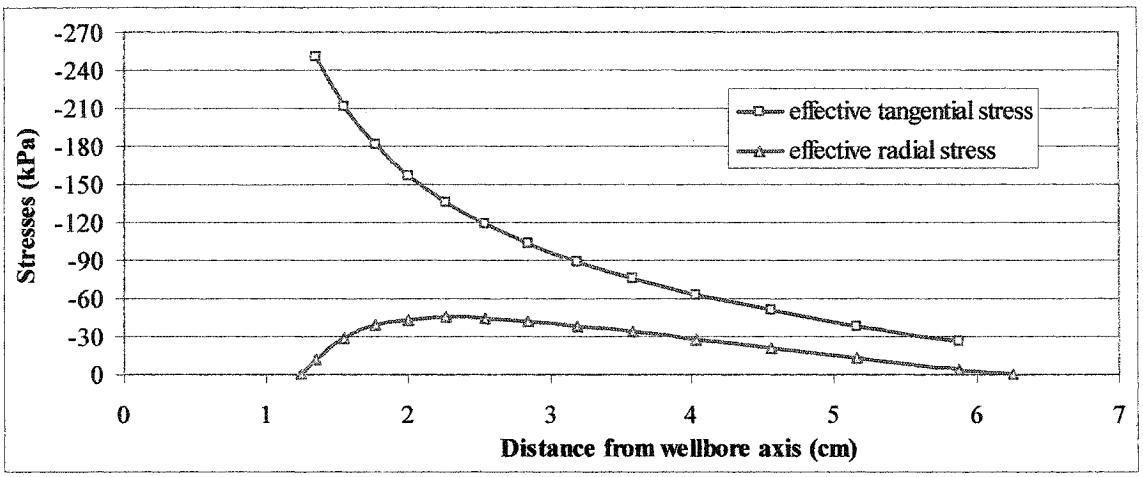

Figure 2.18. Profiles of effective radial and tangential stresses

The above analysis assumed elasticity in the material in this virtual case. However, in case of disaggregated material around a cavity, it is expected that no shear stresses can be developed in the disaggregated material at the cavity face. Therefore, those seepage forces that cannot transfer to grains in the form of shear stresses are expected to induce tensile stresses, which may be able to produce the material once the tensile strength of the disaggregated material is exceeded.

The Sample Response at Different Levels of Drawdown

To examine the extent of the effect of the interaction between fluid flow and mechanical loading in the experiment, two additional analyses were conducted. The main analysis (standard case) complied with the experimental loading condition. In the first additional analysis (first case), drawdown associated with the standard analysis was eliminated, and in the next (second case), drawdown was tripled. In the first and second cases, everything including the mechanical loading, mechanical boundary conditions, geometry, and discretization, were the same as the standard case.

Figure 2.19 compares the response of the standard case with the results of the analyses with increased and decreased drawdown. For zero drawdown, sanding was reduced to

nil, as expected. At the same time, the deformation of the sample was only negligibly reduced. This is because the magnitude of the pore pressures in the sample under the applied drawdown was not large enough to change the effective stresses significantly. Moreover, the amount of the produced sand in the standard case was not large enough to considerably reduce the cross section of the sample.

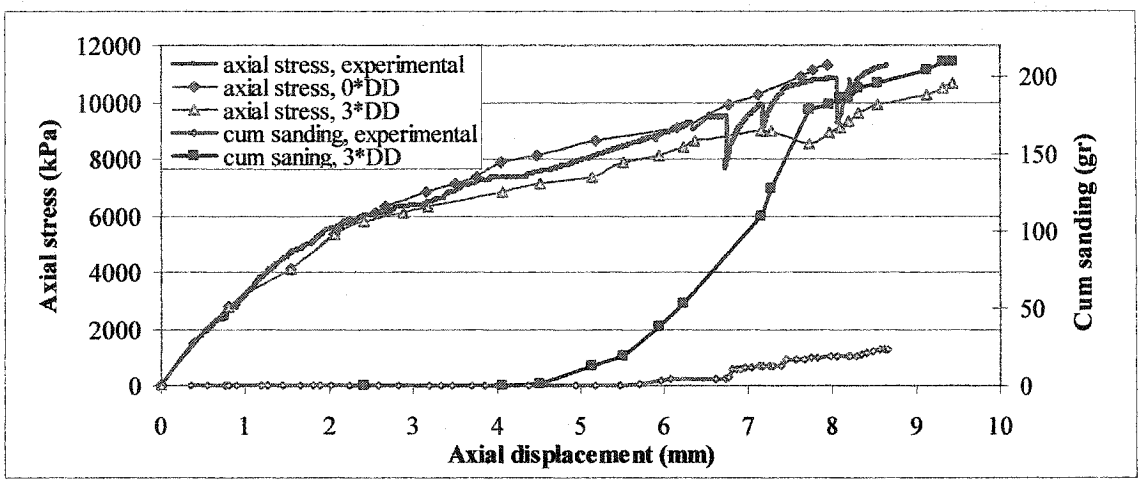

Figure 2.19. Profiles of axial stresses and cumulative sanding at different levels of drawdown

Figure 2.19 compares the axial loading-deformation and sand production of the standard and the second case. The results show a dramatic increase in the scale of sand production. This increase is due to enlarged drag forces of seepage which provoke more tensile stresses in the disaggregated material around the central hole. In addition, deformation of the sample shows an increase. The increased level of pore pressure as a result of higher drawdown is expected to reduce the effective stresses at a constant axial and lateral loading. Therefore, the increased level of deformation of the sample must be caused by another factor. It is believed that the material removal and, therefore, a smaller cross section as a result of sanding, is the main culprit.

These observations suggest that the seepage induced forces, although small, have a tremendous impact on the magnitude of sanding. The amount of tensile stresses in the disaggregated material is a direct function of the magnitude of drawdown. Small tensile strength of the disaggregated material can be overcome by small tensile stresses that are developed by drag forces of seepage.

Conclusion

A sand production experiment was conducted on a hollow cylinder sample. In this experiment, axial and radial loadings were gradually increased, and a single-phase flow was established. Axial loading and deformation, fluid flow rate, drawdown pressure, and sand production were recorded during the experiment. The experimental program was to verify a numerical scheme, and study the numerous parameters that play important roles in sanding issues.

The assumptions and tools used in the proposed numerical modeling were consistent with the physics of sand production. One of the major components was the bilinear strain hardening/softening Mohr-Coulomb model. This model more than adequately captured the responses of the medium to the applied loading and seepage conditions. The criteria that were used in the modeling scheme also showed that they could easily capture the sanding rate and volume. Strain softening of the material and effective stress relaxation on the cavity face appeared to be essential to any sand production, and therefore should be captured in the simulations. Drag forces of seepage appear to generate tensile stresses in the disaggregated material. The criterion of sand production is met once the tensile strength of the disaggregated material is overcome by the tensile stresses.

For a live modeling of sanding, the removal of the elements that fulfill the sanding criteria was crucial. The removal of this material redistributes the effective stresses around the cavity and propagates the shear failure front.

The proposed numerical modeling scheme predicted the rate and volume of sanding. The predictions appeared to agree reasonably well with the experimental results.

Another numerical investigation was conducted on seepage induced effective stresses in a medium around an open hole. The results indicated that assuming elasticity, seepage forces induce maximum shear stresses and compressional tangential stress at the cavity face. If the material in this area underwent strain softening and disaggregation, it might not be able to stand the shear stresses developed by seepage forces. Therefore, seepage forces may develop tensile stresses that once overcoming the tensile strength, would produce the material. Here the role of capillarity is highlighted, which generates a small cohesion adding to the tensile strength of the disaggregated material. Albeit minor, it

may be sufficient to resist the usually small tensile stresses that are generated by seepage forces.

The sand production analysis was repeated for two virtual cases, in one of which drawdown was tripled relative to the main experimental practice. This analysis shows a radical increase in sand production as well as in deformations of the sample. This shows that drawdown and seepage forces, although small relative to the in situ effective stresses, have a significant impact in the severity of sand production.

The excellent predictions of the numerical model and their conformity with the experimental observations suggest that the criteria used in the modeling captured the essence of sanding. Therefore, the use of this numerical tool in sanding prediction seems very promising.

Acknowledgements

The authors would like to thank NSERC, and the Killam trustees for their financial support.

Nomenclature

C_p = plastic projected cohesion (kPa)

C_r = plastic real cohesion (kPa)

CTC= conventional triaxial compression

DD= drawdown (kPa)

E= Young's modulus (MPa)

g_i = gravitational acceleration (m/Sec^2)

g^s = shear potential function

H( )= the constitutive model

HCS= hollow cylinder sample

K_{ij} = the mobility tensor (m^{3}Sec/kg)

K_f = the bulk modulus of the fluid (kPa)

m= inertial mass of a node (kg)

q_i = the mass discharge ((kg/Sec)/m^2)

q_v = the input fluid mass per unit volume ((kg/m^3)/Sec)

UCS= unconfined compressive strength (MPa)

α = damping factor

Δe_j^{ps} = the principal plastic shear strain increments

Δe_i = principal strain increments

ε_{ij} = the strain tensor

ε_v = the volumetric strain of solid

e_3^{pt} = the tensile hardening parameter

ε^f = effective strain associated with the limit friction angle

ε^c = a constant similar to ε^f in the hardening relation for the mobilised friction angle

ξ = the variation of volume of fluid in unit volume of porous material

φ = bilinear friction angle at high confining pressure

φ_r = bilinear friction angle at low confining pressure

ψ = dilation angle

κ = the hardening parameter

ν =Poison's ratio

ρ = density of the geomaterial (kg/m^3)

σ = normal stresses (kPa)

σ^t = tensile strength (kPa)

$\sum F_i$ = the net force on a node

τ = shear stresses (kPa)

References

Antheunis, D., J. Geertsma, and P.B. Vriezen, "Mechanical Stability of Perforation Tunnels In Friable Sandstones", *Proc. 31th Annual Petr. Mech. Engr. Conf. of the ASME*, Mexico City, 1976a.

Antheunis, D., P.B. Vriezen, B.A. Schipper, and A.C. van der Vlis, "Perforation Collapse: Failure of Perforated Friable Sandstones", *SPE 5750, European Spring Meeting*, Amsterdam, 1976b.

Barril, R.J., and L.G. Gay, "Controlling Sand Production in High Rate Gas Wells", *World oil*, pp. 52-56, 1983.

Bianco, L.C.B., and P.M. Halleck, "Mechanisms of Arch Instability and Sand Production in Two-Phase Saturated Poorly Consolidated Sandstones", *SPE 68932, SPE European Formation Damage Conference*, the Netherlands, 2001.

Bratly, R.K., and R. Risnes, "Stability and Failure of Sand Arches", *SPEJ*, pp. 236-248, 1981.

Charlez, P.A., *Rock Mechanics-Vol 2: Petroleum Applications*, Editions Technip, 1st Edition, 1997.

Coates, D.R., and S.A. Denoo, "Mechanical Properties Program Using Borehole Analysis, and Mohr's Circle", *Proceedings SPW/La 22nd Annual Logging Symposium*, pp. 23-26, 1981.

Cundall P.A., and M. Board, "A Microcomputer Program for Modelling Large-Strain Plasticity Problems", *Numerical Methods in Geomechanics. Proc. 6th Int. Conf. on Numerical Methods in Geomechanics*, Innsbruck, Austria, April 11-15, Swododa C.(ed), Rotterdam, Balkema, pp. 2101-2108, 1988.

Durrett, J.L., W.T. Golbin, J.W. Murray, and R.E. Tighe, "Seeking a Solution to Sand Control", *JPT*, pp. 1664-1672, 1977.

Edwards, D., H. Joranson, and J. Spurlin, "Field Normalization of Formation Mechanical Properties", *SPWLA, 29th Annual Logging Symposium*, 1988.

Edwards, D.P., Y. Sharma, and A. Charron, "Zones of Sand Production Identified by Log-Derived Mechanical Properties: A Case Study", *Proceeding SPWLA 8th European Formation Evaluation Symposium*, London, 1983.

Geilikman, M.B., F.A.L. Dullien, and M.B. Dusseault, "Erosional Creep of Fluid-Saturated Granular Medium", *J. of Eng. Mechanics of ASCE*, no. 123, pp. 653-659, 1997.

Hall, C.D., and W.H. Harrisburger, "Stability of Sand Arches: A Key to Sand Control", *J. Pet Technology*, pp. 821-829, 1970.

Han, G., M.B. Dusseault, "Quantitative Analysis of Mechanisms for Water-Related Sand Production", *SPE 73737, SPE Symposium and Exhibition on Formation Damge*, Lafayette, Louisiana, 2002.

Kessler, N., Y. Wang, and F.J. Santarelli, "A Simplified Pseudo-3D Model to Evaluate Sand Production Risk in Deviated Cased Holes", *SPE 26541, Proc. 68th SPE Annual Tech. Mtg.*, **2**, 1993.

Morita, N., D.L. Whitfill, I. Massie, and T.W. Knudsen, "Realistic Sand Production Prediction: Numerical Approach", *SPE 16989, SPE Prod. Eng.*, 15-24, 1989a.

Morita, N., D.L. Whitfill, O.P. Fedde, and T.H. Lovik, "Parametric Study of Sand Production Prediction: Analytical Approach", *SPE 16990, SPE Prod. Eng.*, pp. 25-33, 1989b.

Morita, N., and G.F. Fuh, "Prediction of Sand Problems of a Horizontal Well From Sand Production Histories of Perforated Cased Wells", *SPE 48975, SPE Annual Technical Conference and Exhibition*, New Orleans, Louisiana, 1998.

Nordgren, R.P., "Strength of Well Completions", *Proceeding 18th US Symposium on Rock Mechanics*, Keystones, Co, 4A3-1, 4A3-9, 1977.

Papamichos, E., and E.M. Malmanger, "A Sand Erosion Model for Volumetric Sand Productions in a North Sea Reservoir", *SPE 54007, SPE Latin American and Caribbean Petroleum Engineering Conference*, Caracas, Venezuela, 1999.

Papanastasiou, P., and I. Vardoulakis, "Numerical Treatment of Progressive Localisation in Relation to Borehole Stability", *Int. Journal Numer. Anal. Meth. Geomech.*, no.16, pp. 389-424, 1992.

Perkins, T.K., and J.S. Weingarten, "Stability and Failure of Spherical Cavities in Unconsolidated Sand and Weakly Consolidated Rock", *SPE 18244, 63rd Annual Technical Conference*, Houston, Texas, 1988.

Philips, F.L., and S.R. Whitt, "Success of Openhole Completions in the Northeast Butterfly Field, Southern Oklahoma", *SPE 11555, Production Operation Symposium*, Oklahoma City, 1983.

Risnes, R., R.K. Bratli, and P. Harsrud, "Sand Stresses around a Wellbore", *SPEJ*, pp. 883-898, 1982.

Sanfilippo F., G. Ripa, M. Brignoli, and F.J. Santarelli, "Economical Management of Sand Production by a Methodology Validated on an Extensive Database of Field Data", *SPE 30472, Annual Technical Conference*, Dallas, 1995.

Stavropoulou, M., P. Papanastasiou, and I. Vardoulakis, "Coupled Wellbore Erosion and Stability Analysis", *Int. J. Num. Anal. Methods Geomech.*, no. 22, pp. 749-769, 1998.

Stein, N., "Calculate Drawdown That Will Cause Sand Production", *World Oil*, pp. 48-49, 1988.

Tonvol, J., A. Skjarstein, and E. Papamichos, "Sand Production: Mechanical Failure or Hydromechanic Erosion?", *Int. J. Rock Mech & Min. Sci.*, **34**, no. 3-4, 1997a.

Tronvol, J., E. Papamichos, A. Skjarstein, and F. Sanfilippo, "Sand Production in Ultra-Weak Sandstones: Is Sand Control Absolutely Necessary?", *SPE 39042, fifth Latin American and Caribbean conf. and Exhibition*, Rio de Janeiro, Brazil, 1997b.

Tronvol, J., E. Papamichos, and N. Kessler, "Perforation Cavity Stability: Investigation of Failure Mechanisms", *Geotech. Eng. of Hard Soils-Soft Rocks*, Balkema, Rotterdam, pp. 1687-1693, 1993.

Tronvol, J., M.B. Dusseault, F. Sanfilippo, and F.J. Santarelli, "The Tools of Sand Management", *SPE 71673, SPE Annual Technical Conference and Exhibition*, New Orleans, Louisiana, 2001.

Tronvol, J., N. Morita, and F.J. Santareli, "Perforation Cavity Stability: Comprehensive Laboratory Experiments and Numerical Analysis", *SPE 24799, 67th SPE ATM*, Washington DC, 1992.

Tronvoll J., and P.M. Halleck, "Observations of Sand Production and Perforation Cleanup in A Weak Sandstone", *Proc. EUROCK' 94*, Balkema, Rotterdam, pp. 355-360, 1994.

Van den Hoek, P.J., Hertogh, G.M.M, Koijman, A.P., De Bree, Ph., Kenter, and E. Papamichos, "A New Concept of Sand Production Prediction: Theory And Laboratory Experiments", *SPE 36418, 71th SPE annual Tech. Conf.*, Denver Colorado, 1996.

Vardoulakis, I., M. Stavropoulou, and P. Papanastasiou, "Hydromechanical Aspects of the Sand Production Problem", *Transport in Porous Media*, no. 22, pp. 225-244, 1996.

Vaziri, H., B. Barree, Y. Xiao, I. Palmer, and M. Kutas: "What Is the Magic of Water in Producing Sand?", *SPE 77683, SPE Annual Technical Conference and Exhibition*, San Antonio, Texas, 2002.

Vaziri, H., and I. Palmer, "Evaluation of Open hole Cavity Completion Technique in Coalbed Methane Reservoirs", *3rd North American Rock Mechanics Symposium*, Cancun, Mexico, 1998.

Vaziri, H., X. Wang, and I. Palmer, "Wellbore Completion Technique and Geotechnical Parameters Influencing Gas Production", *the Canadian Geotechnical Journal*, no. 34, pp. 87-101, 1997.

Veeken C.A.M., Davies, D.R., Kenter, C.J., and Kooijman, A.P., "Sand Production Prediction Review: Developing an Integrated Approach", *SPE 22792, 66th Annual Tech. Conf.*, Dallas, Texas, 1991.

Vermeer, P.A., and R. de Borst, "Non-Associated Plasticity for Soils", Concrete and Rock, **29**, no. 3, pp. 1-64, 1984.

Wang, Y., C.C. Chen, and M.B. Dusseault, "An Integrated Reservoir Model for Sand Production and Foamy Oil Flow during Cold Heavy Oil Production", *SPE 69714, SPE International Thermal Operations and Heavy Oil Symposium,* Margarita, Venezuela, 2001.

Wang, Y., and M.B. Dusseault, "Sand Production Potential Near Inclined, Perforated Wellbores", *Paper 96-27, Proc. CIM 47th Annual Tech. Mtg*, Calgary, AB, 1996.

Weingarten, J.S., and T.K. Perkins, "Prediction of Sand Production in Gas Wells: Methods and Gulf of Mexico Case Studies", *SPE 24797, SPE 67th Annual Technical Conference and Exhibition*, Washington D.C., 1992.

Appendix A: Mathematical Formulation

In a basic analysis of fluid flow in a porous medium, equations of mass balance and equilibrium are solved simultaneously if the interaction between the two is to be considered. The mixture of oil-water-gas is considered as one fluid which flows through the porous medium. As long as the gas remains in occluded form, the medium can be considered fully saturated and the effective stress theory applies. Therefore, equivalent characteristics of the mixture must be used in the analysis.

Calculation Method

FLAC uses an explicit, time-marching solution scheme: the right hand side of all equations consist of known values, because the time step is chosen to be small. Therefore, information cannot physically transmit from one element to the other within that small time step.

The calculations consist of the following operations (Cundal and Board, 1988):

For all zones:

- Strain increments are derived from known nodal velocities
- New stresses are derived from strain increments by using the constitutive model

For all nodes:

- Nodal forces are derived from known stresses in surrounding zones
- Updated velocities are calculated from forces using the law of motion

Each FLAC quadrilateral is modeled as two overlaid pairs of constant stress triangles as shown in Figure 2..A.1.

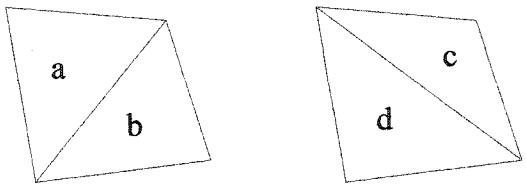

Figure 2.A.1. Overlaid pairs of constant stress triangles

Each triangle maintains its stress component independently of the other triangles. Therefore, twelve stress components are stored for each quadrilateral in plane strain mode. The forces exerted on each node are taken to be the mean of those exerted by the quadrilaterals.

Equation of Motion

The net force on a node is calculated from the summation of forces imposed by the zones surrounding the node. The force that one triangle contributes to the node is found from the stress vector acting on the edges of the triangle:

$$F_i = \frac{\sigma_{ij}[n_j^{(1)} s^{(1)} + n_j^2 s^{(2)}]}{2} \qquad [2.A.1]$$

where

At equilibrium, or steady-state flow, the net force $\sum F_i$ on a node is zero. The acceleration is integrated numerically to obtain velocities (Cundall and Board, 1988):

$$\dot{u}_i := \dot{u}_i + \left[\sum F_i - \alpha \left|\sum F_i\right| \mathrm{sgn}\left(\dot{u}_i\right)\right] \frac{\Delta t}{m} + g_i \Delta t \qquad [2.A.2]$$

where

m= inertial mass of a node (M),

g_i = gravitational acceleration (L/T2),

α = damping factor.

Strain-Hardening/Softening Mohr-Coulomb Model

Stresses are computed from deformations by using constitutive laws. The general form of the constitutive law is:

$$\sigma_{ij}^{'} = H\left(\sigma_{ij}^{'}, \varepsilon_{ij}, ...\right) \qquad [2.A.3]$$

where

H( )= the constitutive model,

ε_{ij} = the strain tensor.

Our simulations use a Mohr-Coulomb model with a consideration of cohesion, friction, dilation and tensile strength hardening or softening after the onset of plastic yield. These parameters can be defined as piecewise-linear functions of hardening parameters, measuring the plastic shear and tensile strain.

Incremental Elastic Law

The principal effective stresses and principal directions are evaluated from the effective stress tensor components and ordered so that (compressive effective stresses are negative):

$$\sigma_1^{'} \le \sigma_2^{'} \le \sigma_3^{'} \qquad [2.A.4]$$

The corresponding principal strain increments $\Delta e_1, \Delta e_2, \Delta e_3$ are decomposed as follows:

$$\Delta e_i = \Delta e_i^e + \Delta e_i^p \qquad [2.A.5]$$

where the subscripts "e" and "p" refer to elastic and plastic parts, respectively. The plastic components are zero during the elastic behaviour. The incremental expression of Hooke's law in terms of principal effective stress and strain has the form:

$$\Delta\sigma_i^{'} = \alpha_1 \Delta e_i^e + \alpha_2 (\Delta e_j^e + \Delta e_k^e) \qquad [2.A.6]$$

where

$\alpha_1 = K + 4G/3$ (F/L^2)

$\alpha_2 = K - 2G/3$ (F/L^2)

Yield and Potential Functions

The shear failure envelope is defined by the Mohr-Coulomb yield function:

$$f^s = \sigma_1' - \sigma_3' N_\varphi + 2C\sqrt{N_\varphi} \qquad [2.A.7]$$

and the tension cut-off is defined as:

$$f^t = \sigma^t - \sigma_3' \qquad [2.A.8]$$

where

φ = friction angle,

C = cohesion (F/L^2),

σ^t = tensile strength (F/L^2),

$$N_\varphi = \frac{1+\sin\varphi}{1-\sin\varphi} \qquad [2.A.9]$$

The shear potential function g^s corresponds to a non-associated flow rule and has the form:

$$g^s = \sigma_1' - \sigma_3' N_\psi \qquad [2.A.10]$$

where

ψ = dilation angle,

$$N_\psi = \frac{1+\sin\psi}{1-\sin\psi} \qquad [2.A.11]$$

The associated flow rule for tensile failure is derived from the potential function g^t with

$$g^t = -\sigma_3' \qquad [2.A.12]$$

Plastic Corrections

The shear hardening parameter is defined as (Vermeer and deBorst, 1984):

$$\Delta e^{ps} = \left(\frac{1}{2}\left(\Delta e_1^{ps} - \Delta e_m^{ps}\right)^2 + \frac{1}{2}\left(\Delta e_m^{ps}\right)^2 + \frac{1}{2}\left(\Delta e_3^{ps} - \Delta e_m^{ps}\right)^2 \right)^{\frac{1}{2}} \qquad [2.A.13]$$

where

$$\Delta e_m^{ps} = \frac{1}{3}\left(\Delta e_1^{ps} + \Delta e_3^{ps}\right) \qquad [2.A.14]$$

$\Delta e_j^{ps}, j = 1,3$ = the principal plastic shear strain increments.

The tensile hardening parameter e^{pt} measures the accumulated tensile plastic strain; its increment is defined as:

$$\Delta e^{pt} = \Delta e_3^{pt} \qquad [2.A.15]$$

The tensile hardening parameter e_3^{pt} is the increment of tensile plastic strain in the direction of the minor principal effective stress.

Friction angle, cohesion, dilation, and tensile strength are modified according to the new values of the shear and tensile strain hardening parameter.

Mechanical Parameters Hardening and Softening

In the Mohr-Coulomb hardening/softening model cohesion, dilation, and tensile strength are a strain dependent quantity of these parameters are used.

Experience shows that the experimental curves from sand testing can usually be expressed in a simple form, e.g. the relationship (Vermeer and de Borst, 1984):

$$\sin\overset{*}{\varphi} = 2\frac{\sqrt{\left(\overset{-p}{\varepsilon}\ \varepsilon^f\right)}}{\varepsilon^f + \overset{-p}{\varepsilon}} \qquad \text{for } \overset{-p}{\varepsilon} < \varepsilon^f \qquad [2.A.16]$$

$$\sin\overset{*}{\varphi} = \sin\varphi \qquad \text{for } \overset{-p}{\varepsilon} > \varepsilon^f$$

So that the mobilized friction angle gradually increases with strain to reach the limit friction angle when $\overset{-p}{\varepsilon}$ has reached the constant ε^f.

Test results have also indicated that concurrent to friction hardening, applying softening to the cohesion best models the behaviour of the material. A possible choice of this relationship is:

$$\overset{*}{C} = C \exp\left[-\left(\frac{\overset{-p}{\varepsilon}}{\varepsilon^c} \right)^2 \right] \qquad [2.A.17]$$

where

ε^c = a constant similar to ε^f in the hardening relation for the mobilised friction angle.

The hardening and softening relations for friction angles and cohesion are schematically plotted in the following Figure 2.A.2.

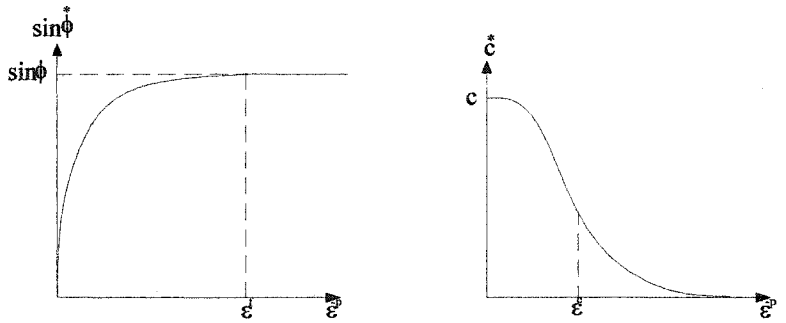

Figure 2.A.2. Schematic variation of cohesion and friction angle with plastic strain intensity

A relationship between the mobilized dilatancy angle and the effective strain has been proposed (Vermeer and de Borst, 1984).

$$\sin \overset{*}{\psi} = \frac{\sin \overset{*}{\varphi} - \sin \varphi_{cv}}{1 - \sin \overset{*}{\varphi} \sin \varphi_{cv}} \qquad [2.A.18]$$

The constant φ_{cv} is readily calculated from the limit dilatancy angle ψ and limit the friction angle φ.

$$\sin \varphi_{cv} = \frac{\sin \varphi - \sin \psi}{1 - \sin \varphi \sin \psi} \qquad [2.A.19]$$

Mass Balance Equation

The mass balance equation is presented for a single-phase (equivalent) flow.

$$\rho_f \frac{\partial \xi}{\partial t} + \phi \frac{\partial \rho_f}{\partial t} = -\frac{\partial}{\partial x_i}(q_i) + q_v \qquad [2.A.20]$$

where

q_v = the input fluid mass per unit volume ((M/L^3)/T),

ξ = the variation of volume of fluid in unit volume of porous material,

q_i = the mass discharge ((M/T)/L^2).

Transport Law

The fluid transport can be described by Darcy's law. In tensor notation it formulates:

$$v_i = -K_{ij} \frac{\partial}{\partial x_j}\left(P - \rho_f g_k x_k\right) \qquad [2.A.21]$$

where

K_{ij} = the mobility tensor (L^{3}T/M).

Constitutive Law of Fluid

The response equation for the pore fluid can be written as (Itasca Consulting Group, FLAC manual, 1998):

$$\frac{\partial P}{\partial t} = \frac{K_f}{\phi}\left(\frac{\partial \xi}{\partial t} - \frac{\partial \varepsilon_v}{\partial t}\right) \qquad [2.A.22]$$

where

K_f = the bulk modulus of the fluid (F/L^2),

ε_v = the volumetric strain of solid.

Chapter 3: Comprehensive Transient Modeling of Sand Production in Horizontal Wellbores

Publication Status: Published, SPE 84500, SPE Annual Conference and Exhibition, Denver, Colorado, Oct. 2003.

Abstract

The design of the most appropriate completion technique for a horizontal wellbore continues to be a formidable task. The choices are whether to opt for an open hole, or a cased completion; and whether to gravel pack, or otherwise there will be no need for sand production control under prospective operational conditions. This paper introduces a predictive tool that forecasts not only the initiation of sanding, but also its rate and severity in real time. All possible failure mechanisms including shear, tensile and volumetric have been included in the proposed model. Experimental data on large block tests are used to support the validity of the proposed numerical model.

A series of well-documented experiments on a large size horizontal wellbore was numerically simulated utilizing a finite difference package. The model covers the interaction between fluid flow and mechanical deformation of the medium, capturing all possible mechanisms of failure. Providing the means of encompassing the sequential nature of sanding and the direct modeling of progressive character of the cavity, the suggested model is the first to be reported using a fully coupled transient simulation approach. The removal process of the qualified elements is simulated in the model, and the criteria that are used for this process are in accordance with the physics of sand production. This numerical tool can be used to address the main factors related to sand production problems that include the conditions under which sanding takes place and how extensive if it indeed occurs.

The model shows excellent agreement with experimental results in terms of borehole deformation and sanding rates. The model predicted initiation of shear failure from the sides of the borehole and its propagation to the top and sides of the sample. Likewise, it became evident that removal of the failed material during production may trigger more sanding through development of shear failure to the formerly intact material that may continue to fail accordingly. More importantly, the agreement between the numerical and experimental well face deformation, as well as the sanding rate and volume, suggests that

an accurate prediction of sanding can be made by using the proposed numerical modeling technique. Therefore, a sound decision in completion selection and sand control strategy can be suggested. Avoiding unnecessary gravel packing, and other sand controlling and prevention techniques can be achieved by utilizing the proposed model, which in turn reduces the cost of well completion dramatically. In addition, the production decline due to gravel void throat block by fine movement can be prevented. A wide use of the proposed model is expected immediately in the oil industry.

Introduction

Sand production in the petroleum industry is a phenomenon of solid particles being produced together with reservoir fluid. This phenomenon is costing the industry billions of dollars every year. Corrosion of pipelines and other facilities, sand-oil separation costs, possible wellbore choke, environmental effects, production rate drop, and frequent work-over for clean-up operations are some examples of these expenses. On the other hand, a controlled sanding or even sand production invocation, has proved to be very effective in increasing production rates, especially in heavy oil recovery, asphalt wells and low PI wells (Dusseault, and El-Sayed, 2000, Wang, Y. and C.C. Chen, 1999, Smith, 1986).

The extent of the problem at hand is recognized by the fact that estimates indicate that seventy percent of the total world's oil and gas reserves are found in poorly consolidated reservoirs (Bianco and Halleck, 2001). Meanwhile, poorly consolidated sandstones, marked with weak existing cohesion among grains, are the most common solid producers. Sand production takes place if the material around the cavity is disaggregated and there is enough fluid flow rate to produce the grain particles. Disaggregation of the material initiates from cavity faces and propagates inside the medium. Material disaggregation can take place if the material fails under excessive drawdown or depletion, or a combination of the two. Depletion and drawdown fail the medium under either shear, tensile, or pore collapse mechanisms; or a combination of them. After failure of the rock disaggregates the material, the resulting grains are produced by the existence of enough pressure gradients in tension. Friction between the grains and capillary tension are the resisting forces against the grain movements (Vaziri et al., 2002; Morita and Boyd, 1991).

Despite the great effort to improve the technique for the prediction of sand production, field practices demonstrate that quantitatively accurate prediction of volumetric solid production is yet to be developed, especially for poorly cemented sandstones. Existing models can predict the onset of sand production and analyze cavity stability and rock failure; however, they cannot predict the volumetric production of sand over time as a function of applied stresses, fluid flow rates, and changes in water saturation.

Major sources of error in modeling sand production are due to oversimplification of physical phenomena, neglecting particular physical parameters, relying on simple mathematical models, neglecting certain unknowns, and errors in input data (Bianco and Halleck, 2001). To date, there has been no comprehensive mathematical model that considers all the mechanisms associated with sand production. The model presented in this paper takes into account different failure mechanisms that may play a role in sanding. It not only forecasts the initiation of sanding and the start of the failure, but provides the sanding volume and rate throughout the whole production process. The model is capable of giving an indication of the severity of sanding at real production time. This knowledge is crucial for completion designers to make an on time sand control plan with minimum impairment of production. The important point is the simplicity of the constitutive model that is used. The Mohr Coulomb model is one of the most recognized models for engineers whose parameters are physically sensed. By combining this model with a strain hardening/softening scheme, a powerful tool was provided which could simulate the complex behavior of the medium and the de-cementation process.

This paper attempts to numerically model the process of sanding by simulating its progressive failure and seepage associated sand release. Sanding volume and rate, as well as fluid production rate can all be estimated. Two series of experiments conducted by Kooijman et al. (1996) were simulated using this scheme. The flow rate, evolutions of stresses and deformations, as well as the real time sanding rate and volume were predicted by using the suggested model. The encouraging results of this simulation raise hopes of a promising future in the area of sanding simulation and control.

In addition, this paper explains the possible failure mechanisms associated with sanding. For that, a comprehensive model for simulating the behavior of the formation against the

applied loads in early and late life, near and far from the wellbore is presented. The significance of this numerical model is to provide a tool for better understanding and modeling of sand production by better prediction of the failure mechanism, sanding rate, and volume.

Mechanism of Sanding

Any sand production involves two distinct stages. These are the mechanical instability of the rock material and transport of particles by hydrodynamic forces to the wellbore. As sanding continues, effective stresses are redistributed around the cavity as the failed material is removed by tensile failure (Kooijman et al., 1996). This stress redistribution may in turn fail additional material that provides more grains for production. Therefore, the progressive cycle of failure-production continues until a stable geometry of cavity is formed. Figure 3.1 shows a common profile of effective stresses around an opening, such as a cavity. $\sigma_r^{'}, \sigma_\theta^{'}$, $\sigma_y^{'}$, and $\sigma_v^{'}$ in this figure stand for radial, tangential, vertical, and volumetric effective stresses, respectively. The stress component normal to the cavity face is the minimum of the principal stresses. Furthermore, it recovers more slowly than the other two components. Therefore, significant shear stresses form near the cavities, which may lead to shear failure. Once shear failure disintegrates the material in unconsolidated formations, drag forces of seepage may produce the grains. This in turn may increase development of the shear failure zone, and therefore, induce more sanding.

It is interesting to note that perforation jobs may shatter the medium subjected to the impact of shooting. Furthermore, it induces enormous shear stresses around the perforation tunnels, which may lead to their failure. Perforations further complicate the effective stress patterns around the wellbore, which may worsen the problem. Finally, the permeability damage induced by the perforation increases the pressure gradient around the cavities and, therefore, increases drag forces on grains. This adds to the possibility of grain release and initiation of cavity growth.

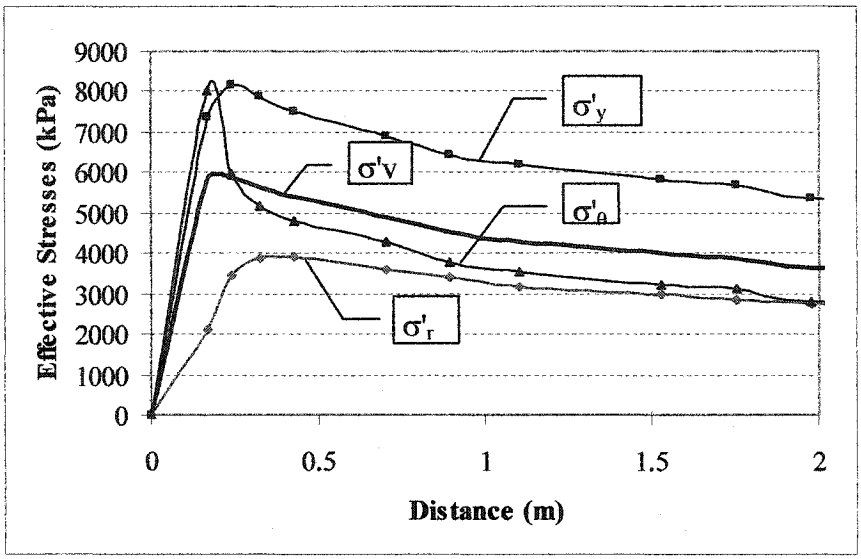

Figure 3.1. An illustration of stress profiles around a wellbore

First Stage: Failure of the Rock

Both drawdown and depletion may induce or develop the failure to the rock adjacent to any opening.

Drawdown Induced Failure

Drawdown may fail the rock under shear, tensile, or pore collapse mechanisms.

Figure 3.2 schematically shows the increment of effective stresses caused by the application of a unit drawdown assuming elasticity. It is assumed that horizontal effective stresses increase as much as 40% of vertical effective stress because of the condition of unilateral strain inside the reservoir (this percentage can differ depending on the material). Application of drawdown reduces the pore pressure in the zone around the wellbore, which in turn increases effective stresses proportionally. Increase of effective vertical and tangential stresses while radial effective stress remains at near zero, enhances shear stresses around the cavity. The closer to the wellbore, the higher the pore pressure reduction. As a result, the maximum effect of drawdown takes place in a region close to the well face.

If the material around the wellbore fails, the peak vertical and tangential stresses shift to the nearby-unfailed zone as shown in Figure 3.3. This may, therefore, develop shear failure towards the inside of the reservoir.

Inside the reservoir, an increase of drawdown equally increases vertical effective stress. Radial effective stress, however, only increases to a portion of the change of vertical stress. This is due to the fact that inside the reservoir, uniaxial strain condition prevails.

Closer to the wellbore, radial deformation may occur. As a result, near the well face, a reduced increase to effective radial stress takes place. On the well face, the effective radial stress stays at zero, while in elastic range, the maximum change occurs to the tangential and vertical stresses.

It is understood that the maximum effect of drawdown conquers the most fragile zone of the reservoir, which happens to be around the wellbore.

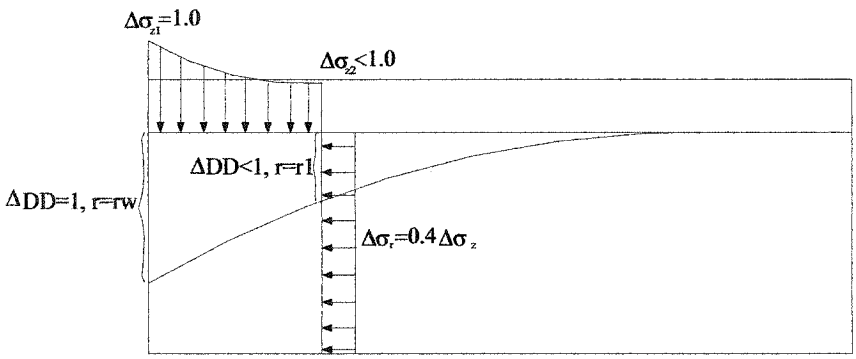

Figure 3.2. Variation of vertical and tangential effectives stresses after application of pure drawdown in an elastic medium

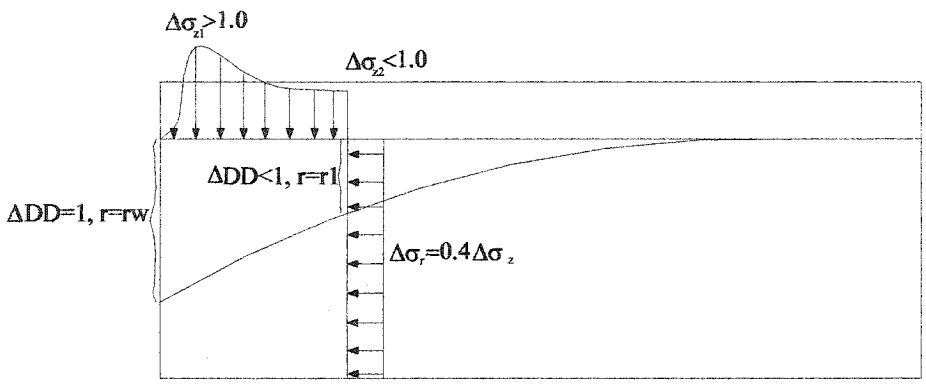

Figure 3.3. Variation of vertical and tangential effectives stresses after application of pure drawdown in an elastic-plastic medium

Depletion Induced Sanding

Depletion of the reservoir may fail the rock under shear or volumetric mechanisms.

Providing that bottom-hole pressure is unchanging, the effect of depletion, dissimilar to drawdown, is more pronounced inside the reservoir than around the wellbore. The effect of pure depletion on the variation of effective stresses is schematically shown in Figure 3.4 for an elastic medium. In this sense, depletion does not affect the stress pattern around the wellbore significantly, and therefore, does not induce more shear failure around the wellbore. Figure 3.5 also shows the same for a medium that has already entered plasticity in the immediate zone around the wellbore.

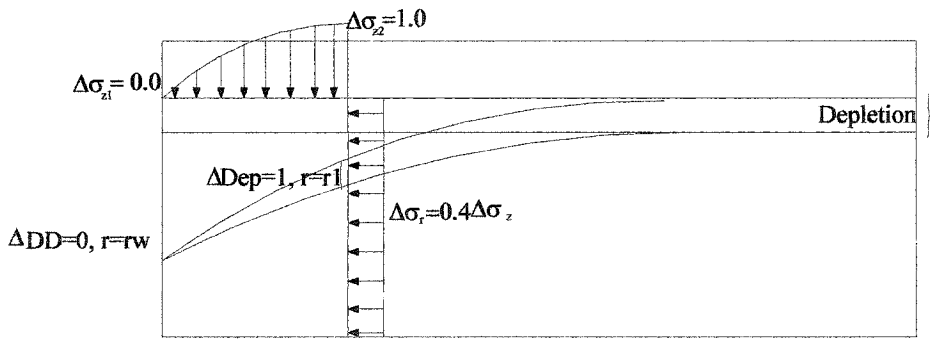

Figure 3.4. Variation of effective stresses after application of pure depletion in an elastic medium

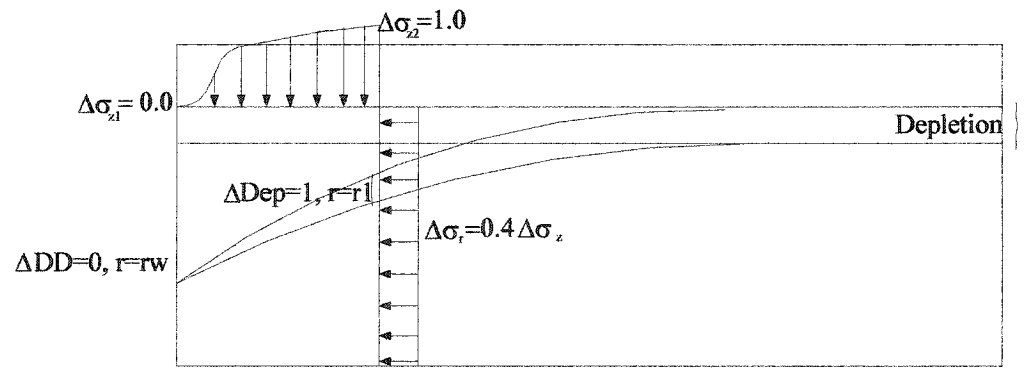

Figure 3.5. Variation of effective stresses after application of pure depletion in an elastic-plastic medium

The difference occurs, as to keep the drawdown constant, the bottom hole pressure must be reduced with the occurrence of the depletion. This is required to maintain the production rate constant (we neglect the permeability variation in the medium in this

argument). As a result, all the effects of drawdown as mentioned before reappear even in the depletion course as shown in Figures 3.6 and 3.7 for elastic and elastic-plastic cases respectively. Therefore, the effect of depletion around the wellbore is just like another drawdown of the same magnitude. As a result, the effect of depletion around the wellbore can be studied in the same way as that of drawdown. That being said, depletion has another additional effect more pronounced inside the reservoir, where drawdown has the minimum significance.

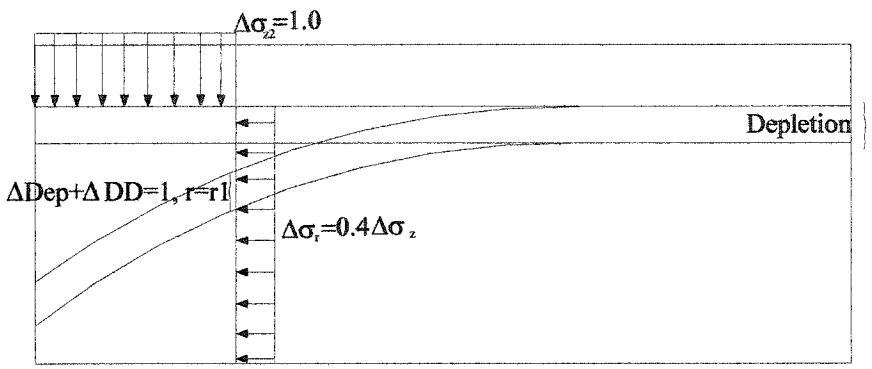

Figure 3.6. Variation of effective stresses after application of an equal quantity of depletion and drawdown in an elastic medium

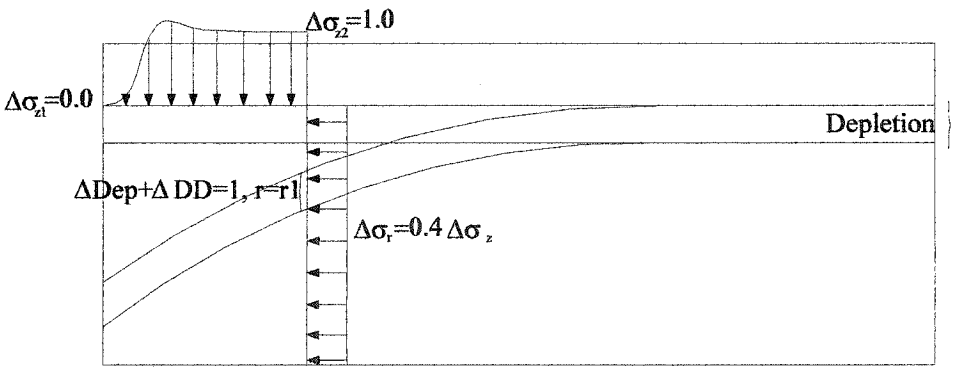

Figure 3.7. Variation of effective stresses after application of equal quantity of depletion and drawdown in an elastic-plastic medium

Second Stage: Push of Grains into the Wellbore by Seepage Forces

The grains of failed material are produced once the hold forces between them consisting of friction and capillary cohesion are smaller than drag forces induced by seepage. According to Sanfilippo et al. (1997), it is impossible to erode away the grains from sand

compacted in such a way that it has a uniaxial strength above 1 MPa. Water breakthrough destroys capillary tension while repeated shut ins and bean up may release the fine intergranular material with fluid flow that in turn loosens the grain particles. It also exerts a significant enough pressure gradient on the material that it could potentially cause tension failure. Moreover, the boosted pressure gradient applies enormous drag forces on the sand grains, which may mobilize them.

Whether sanding will occur depends on the availability of capillary cohesion (Vaziri et al., 2002), strength properties of the disaggregated rock mass (such as projected cohesion, friction), pressure gradient (drawdown and permeability), and fluid velocity.

Fundamental Mathematical Equations

The aim is to model the flow of fluid through porous media with an idealization for the case of horizontal wellbores. The flow modeling may be performed by itself, independent of the usual mechanical calculations, or it may be conducted in parallel with the mechanical modeling so as to capture the effects of fluid/solid interaction. One type of fluid/solid interaction is consolidation, in which a change of pore pressure causes displacements to occur in the solid. This type of behavior involves two mechanical effects. First, changes in pore pressure cause changes in effective stresses, which affect the response of the solid by pushing it to plastic zone for example. Secondly, the fluid in the void acts on the grain particles, and therefore inducing volume changes.

Problem Idealization

In case of horizontal wellbores, it can be assumed that displacements occur on a plane normal to the wellbore. This assumption becomes more realistic if a wellbore is absolutely horizontal and, moreover, if the medium is homogeneous. Fluid flow is also assumed to occur in the same plane.

Degrees of Freedom

In the formulation, pore pressure and solid velocities in the plane vertical to the wellbore are taken as degrees of freedom. In the case of plane strain conditions, the velocity in the third direction, parallel to the wellbore, is zero. Therefore, three independent degrees of freedom are considered.

Governing Differential Equations

In a basic analysis of fluid flow in a porous medium, equations of mass balance and equilibrium must be solved simultaneously if the interaction between the two is to be considered. The mixture of oil-water-gas is considered as one fluid which flows through the porous medium. As long as the gas remains in occluded form, the medium can be considered fully saturated and the effective stress theory applies. Therefore, equivalent characteristics of the mixture must be used in the analysis.

Balance of Momentum

The balance of momentum has the form (Bathe, 1982).

$$\frac{\partial \sigma'_{ij}}{\partial x_j} + \rho g_i = \rho \frac{d\dot{u}_i}{dt} \qquad [3.1]$$

where

$\rho = (1-\phi)\rho_s + \phi\rho_f$ = bulk density (M/L^3),

ρ_s = density of the solid phase (M/L^3),

ρ_f = density of the fluid phase (M/L^3),

σ'_{ij} = effective stress tensor (F/L^2),

$\dot{u}_i$ = solid velocity vector (L/T^2),

ϕ = porosity of the medium.

According to Terzaghi, the effective stress tensor is defined as the subtract of the tensor of total stresses and pore pressure (Das, 1993).

$$\sigma'_{ij} = \sigma_{ij} + P \qquad [3.2]$$

By convention, stresses and pore pressure are defined as negative and positive in compression, respectively.

Constitutive Law for Solid

Stresses are computed from deformations by using a constitutive law which can have a general form as follows (Desai and Siriwardane, 1984):

$$\sigma_{ij} = H(\sigma_{ij}, \varepsilon_{ij}, ...) \qquad [3.3]$$

where

H( )= the constitutive model,

ε_{ij} = strain tensor.

The selected constitutive model can be elastic, which usually does not give realistic results for unconsolidated geomaterials, or elastic-plastic. In the case of our analysis, a non-associated bilinear Mohr-Coulomb strain hardening/softening model was used.

Compatibility Equation

This equation defines the relationship between strain rate and solid velocity gradient:

$$\dot{\varepsilon}_{ij} = \frac{1}{2}\left[\frac{\partial \dot{u}_i}{\partial x_j} + \frac{\partial \dot{u}_j}{\partial x_i}\right] \qquad [3.4]$$

Mass Balance Equation

The mass balance equation is presented for a single-phase (equivalent) flow.

$$\rho_f \frac{\partial \xi}{\partial t} + \phi \frac{\partial \rho_f}{\partial t} = -\frac{\partial}{\partial x_i}(q_i) + q_v \qquad [3.5]$$

where

q_v = the input fluid mass per unit volume ((M/L^3)/T),

ξ = the variation of volume of fluid in unit volume of porous material,

q_i = the mass discharge ((M/T)/L^2).

Transport Law

The fluid transport can be described by Darcy's law. In tensor notation it formulates:

$$v_i = -K_{ij} \frac{\partial}{\partial x_j}\left(P - \rho_f g_k x_k\right) \qquad [3.6]$$

where

K_{ij} = the mobility tensor (L^3T/M).

P= pore pressure (F/L^2).

Constitutive Law of Fluid

The response equation for the pore fluid can be written as (Itasca Consulting Group, FLAC manual, 1998):

$$\frac{\partial P}{\partial t} = \frac{K_f}{\phi}\left(\frac{\partial \xi}{\partial t} - \frac{\partial \varepsilon_v}{\partial t}\right) \qquad [3.7]$$

where

K_f = the bulk modulus of the fluid (F/L^2),

ε_v = the volumetric strain of solid.

Experimental Data

Kooijman et al. (1996) performed a large scale laboratory sand production on block samples.

Sandstone blocks of 26.25cm x 26.25cm x 38 cm were tested using a varying horizontal and vertical stresses and pressures. A hole of 25.4 mm in diameter was drilled in the center parallel to long axis of the block and the fluid flowed from the external circumference to the internal hole in the course of the experiments.

Blocks were first saturated with 3% KCl brine. Next, odorless mineral spirit (OMS) was used to displace brine in order to achieve a two-phase saturation in connate brine saturation.

Two series of experiments, one with and the other without fluid flow were conducted. Experiments were carried out by applying far field stresses on the sides of the block. Applied vertical and horizontal stresses were increased keeping the ratio of vertical to horizontal stresses at two in the whole course of the experiment.

Only in the second series of experiments, OMS was poured through the sample by applying drawdown. The pressure of the central hole was kept atmospheric throughout the course of the experiment.

Material Parameters

Large blocks of weak artificial sandstones were prepared. Density, porosity, and permeability, as well as mechanical parameters of the samples were characterized. These properties are reflected in Tables 3.1 and 3.2. The rock properties as they appear in these Tables represent a weakly consolidated, highly permeable sample.

In order to capture the physics of the failure and consider the possible contribution of all of the aforementioned failure mechanisms, a bilinear Mohr-Coulomb mixed hardening/softening model was used in the simulations. A schematic of the model is depicted in Figure 3.8.

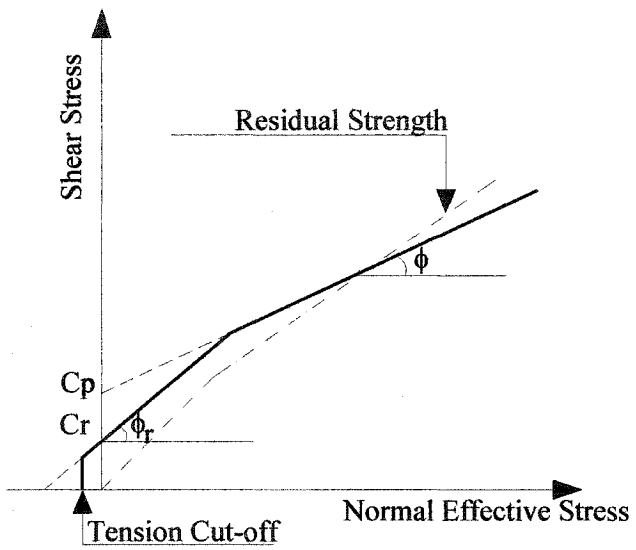

Figure 3.8. Bilinear strain hardening/softening Mohr-Coulomb model

According to the model, tensile failure takes place when stress tensor meets the tension cut-off. Shear failures occur when the stress tensor touches the shear envelope. Theoretically, shear failure may only take place adjacent to the cavity faces where there is a possibility of differential deformation taking place. Pore collapse is defined when stress content meets a volumetric yield surface, i.e. a cap.

Table 3.1. Mechanical properties of the artificial sandstone (Kooijman et al., 1996)

UCS (MPa)	Young's modulus E (MPa)	ν	C_p (MPa)	φ (degrees)	Cohesion at yield
1.1	400	0.05	0.46	37.5	0.

Table 3.2. Physical properties of the artificial sandstone (Kooijman et al., 1996)

D10/D50/D90 (Micron)	Porosity	Permeability at conf stress of 3.45 MPa (Darcy)	Oil-water plateau capillary pressure (kPa)	Capillary cohesion (kPa)
250/210/80	34-37	2-4	1.1	1.1

The mobilized friction angle is defined as a function of a hardening parameter, i. e. effective strain. Experience shows that the experimental curves can be usually expressed in a simple form as follows (Vermeer and de Borst, 1984):

$$\sin\overset{*}{\varphi} = 2\frac{\sqrt{\left(\overset{-p}{\varepsilon}\ \varepsilon^{f}\right)}}{\varepsilon^{f} + \overset{-p}{\varepsilon}} \qquad \text{for } \overset{-p}{\varepsilon} < \varepsilon^{f} \qquad [3.8]$$

$$\sin\overset{*}{\varphi} = \sin\varphi \qquad \text{for } \overset{-p}{\varepsilon} > \varepsilon^{f}$$

Therefore, the mobilized friction angle, $\overset{*}{\varphi}$, gradually increases with strain to reach the limit friction angle when $\overset{-p}{\varepsilon}$ has reached the constant ε^{f}.

Increment of $\overset{-p}{\varepsilon}$ is defined as follows:

$$\Delta e^{ps} = \left(\frac{1}{2}\left(\Delta e_1^{ps} - \Delta e_m^{ps}\right)^2 + \frac{1}{2}\left(\Delta e_m^{ps}\right)^2 + \frac{1}{2}\left(\Delta e_3^{ps} - \Delta e_m^{ps}\right)^2\right)^{\frac{1}{2}} \qquad [3.9]$$

A possible choice for cohesion-effective strain is (Vermeer and de Borst, 1984):

$$\overset{*}{C} = C\exp\left[-\left(\frac{\overset{-p}{\varepsilon}}{\varepsilon^{c}}\right)^2\right] \qquad [3.10]$$

where

ε^{c} = a constant similar to ε^{f} in the hardening relation of mobilized friction,

$\overset{*}{C}$ = the variable cohesion which starts from initial cohesion of C value (F/L^2).

Finally the mobilized dilatancy angle is defined as follows (Vermeer and de Borst, 1984):

$$\sin\overset{*}{\psi} = \frac{\sin\overset{*}{\varphi} - \sin\varphi_{cv}}{1 - \sin\overset{*}{\varphi}\sin\varphi_{cv}} \qquad [3.11]$$

where

ψ = dilatancy angle,

φ_{cv} = the friction angle of constant volume.

φ_{cv} is readily calculated from the limit dilatancy angle and limit friction angle and by using [3.11].

Tools and Assumptions

The numerical modeling was carried out using the FLAC (Itasca Consulting Group, 1998) simulator package. Sand production in this model is described in terms of the coupled mechanisms of fluid flow, stress evolution, material degradation and removal, and changing boundary conditions with time. Governing equations used in the model are formulated by [3.1] through [3.7]

A non-associated bilinear Mohr-Coulomb strain hardening/softening model was used in the analysis in which the failure envelope is a combination of two criteria along with a tension cut-off. Both bilinear shear envelope and tension cut-off can harden and soften in compliance with the hardening parameters as formulated by [3.8] through [3.11]. Hardening parameters are measures of plastic shear and tensile strains.

Sanding Criteria

The proposed model reflects the general physics of the problem; sanding takes place if the rock is directly failed in tension or the failed rock under shear falls into tension. Tensile strength and real cohesion of the rock reduces as shear failure develops in the material. This corresponds with the fact that disintegrated rock under shear failure has no or little tensile strength. After the disintegration of the material occurs by shear failure, capillary cohesion is the most important adhesive force. In the modeling, therefore, capillary cohesion has been considered as a residual cohesion.

The assumptions and procedure as used in the modeling have a significant advantage as it complies with the physics of the problem. As soon as the element, i.e. the zone, satisfies the sanding criteria, it is removed from the mesh entirely and consequently, new boundaries are defined. Only the shear failed elements that consequently succumb to tension participate in the removal process. In the model, therefore, the pattern of cavity development is visible at different stages of the loading.

Another unique feature of the model is the provision of the tools to simulate all failure mechanisms of shear, tensile, and pore collapse. Pore collapse, while substantially important in the process of sand production, has not been accounted for in the previous attempts of modeling of sand production. Showing the possible contribution of pore collapse on sand production is the subject of another paper (Nouri et al. 2003).

The Finite Difference Mesh

The considered problem consists of a sample with an inner diameter of 25.4mm and cubic dimension of 26.25cm x 26.25cm x 38cm. A section of the sample normal to the central hole was analyzed as shown in Figure 3.9. Because of the symmetry, only one quarter of the sample section was needed to be considered in the numerical modeling. The finite difference mesh includes 574 zones. Plane strain was assumed in the analyses, with solid velocities and excess pore pressure as unknown parameters. Finite difference mesh was set with finely spaced zones near the wellbore. These zones were designed to be coarser away from the wellbore so as to reduce their total number, while at the same time not compromising the accuracy of the computations.

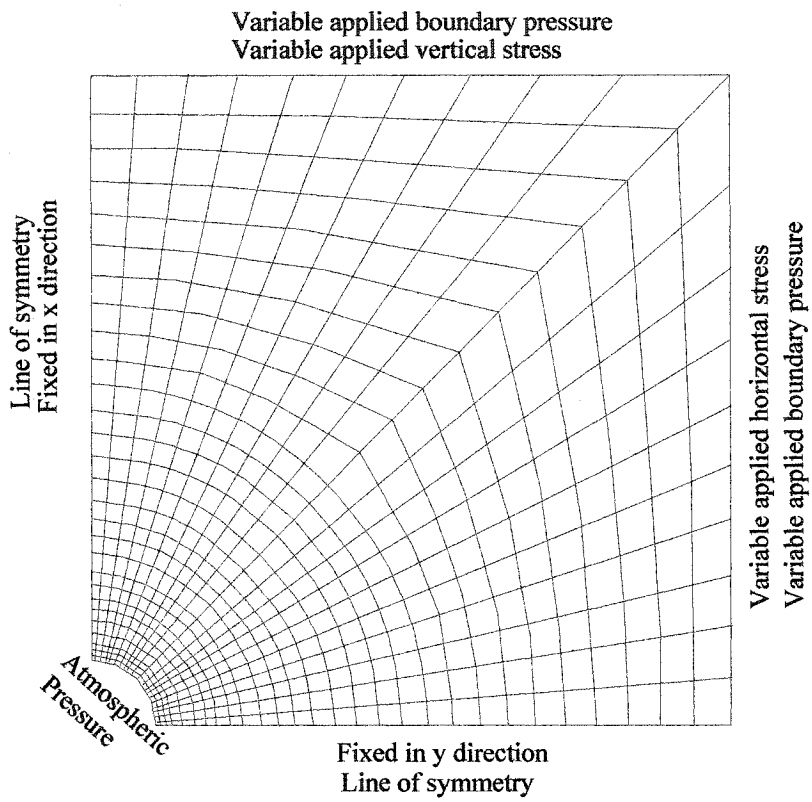

Figure 3.9. Finite difference mesh and boundary conditions

Boundary Conditions

Two sets of experiments were modeled. The first one was the standard test of open holes without any fluid flow. The objective of conducting this experiment was to verify the numerical modeling and also to obtain the necessary material parameters of the sample that are not reflected in Tables 3.1 and 3.2 and [3.1] through [3.4]. In this series of experiments, applied far field stresses were increased while keeping the ratio between vertical and horizontal stresses at a fixed value of two. Boundary conditions were defined to reflect the real testing conditions and, excluding pressure boundary conditions, they are shown in Figure 3.9. To decrease the computing time, symmetry of the geometry and loading was used to reduce the size of the geometry to one quarter. As such, vertical and horizontal displacements were fixed at the bottom horizontal and left vertical lines, respectively. At the top boundary, the variable vertical stresses were defined. A variable horizontal stress was applied at the outer right boundary.

The experiment of the second series was the repeat of the first series experiments, with the exception of the inclusion of fluid flow. Boundary conditions of this experiment are shown in Figure 3.9. Applied vertical stress on the top mechanical boundary is shown in Figure 3.10. For the flow boundaries, the central hole was kept at atmospheric pressure throughout the experiment. The top and right boundaries were also set to a fluid pressure of 172 kPa, except at two brief intervals of zero boundary pressures as shown in Figure 3.10.

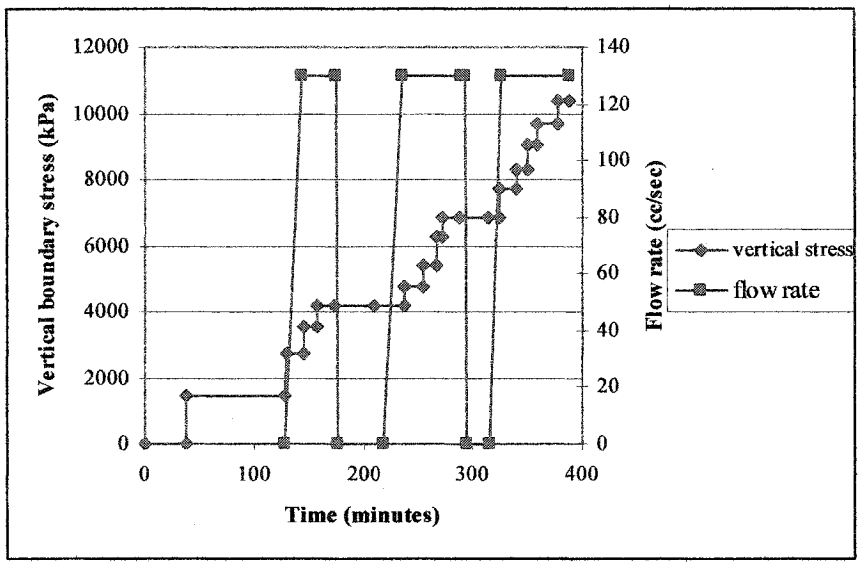

Figure 3.10. Applied vertical top boundary stress and flow rate in the second series of experiments (Kooijman et al., 1996)

Analysis Process

In the beginning, the analysis of the first series of experiments without fluid flow was conducted. In the experimental program, this phase served as a basis to decide on the stress values of subsequent flow and sand production tests. In numerical modeling, it served as a baseline to check the credibility of the constitutive law and, in general, the scheme of the numerical modeling. The mesh that was used in this modeling very well back calculated the material properties. Therefore, the same grid spacing was used in the analysis of the subsequent experiment with fluid flow.

By using the results of the first series of experiments, the second series of experiments were carried out in the presence of fluid flow.

In the analysis the initial conditions, both pore pressure and stresses, are set to zero. For both series of experiments, boundary stresses are increased such that the vertical stress increment is twice as much as the horizontal stress increment. In the case of the experiment with fluid flow, the process of loading is kept the same; in addition, fluid flow is established. A pressure of 172 kPa was also applied to the external boundary and the central hole was set to atmospheric pressure. External pressure was reduced to zero at the two middle stages.

Results and Discussions

The first series of experiments were analyzed in order to test the capability of the model to capture the behavior of the sample as observed in the process of loading. Moreover, necessary material parameters for the modeling of the second series of experiments were captured. This mainly consisted of the range of effective strain, i.e. the hardening parameter. Table 3.3 reads the material parameters as a function of the hardening parameter. The boundary values of cohesion and friction angles were used from Table 3.1. The mobilized values were calculated from [3.8] through [3.11].

The real cohesion at yield, C_r, was set to capillary cohesion. Tensile strength of the material was also set to tension cut-off, reducing to capillary tension value upon tensile failure. The tensile strength of the material was allowed to adapt with the degradation of cohesion to the maximum tension cut-off value, i.e. $C_r / \tan\varphi_r$. The boundary values of effective strain resulted from the numerical analysis of the first series of experiments. By using the material parameters as indicated in Table 3.3 and using the bilinear strain hardening/softening model, the behavior of the first series of experiments was modeled.

Table 3.3. Mechanical properties of the artificial sandstone used in the numerical modeling

ε^{-p}	C_p (kPa)	C_r (kPa)	φ (degree)	φ_r (degree)	ψ (degree)	ψ_r (degree)
0.00000	1250.0	1250.0	0.0	0.0	0.0	0.0
0.00010			11.5	13.4		
0.00025			17.7	20.7		
0.00050			23.7	27.9		
0.00086						0.0
0.00100	1152.0	1000.0	30.4	36.0		2.1
0.00157					0.0	
0.00250	750.0	400.0				
0.00350	460.0	1.1	37.5	45.0	4.0	13.8

The normal displacement of the central hole is depicted versus the vertical far field stress as shown in Figure 3.11. This figure compares the results of both experimental and numerical modeling. The agreement between the two curves is remarkable. This indicates that the essence of mechanical behavior of the medium was captured by the governing equations and the constitutive law in the numerical modeling.

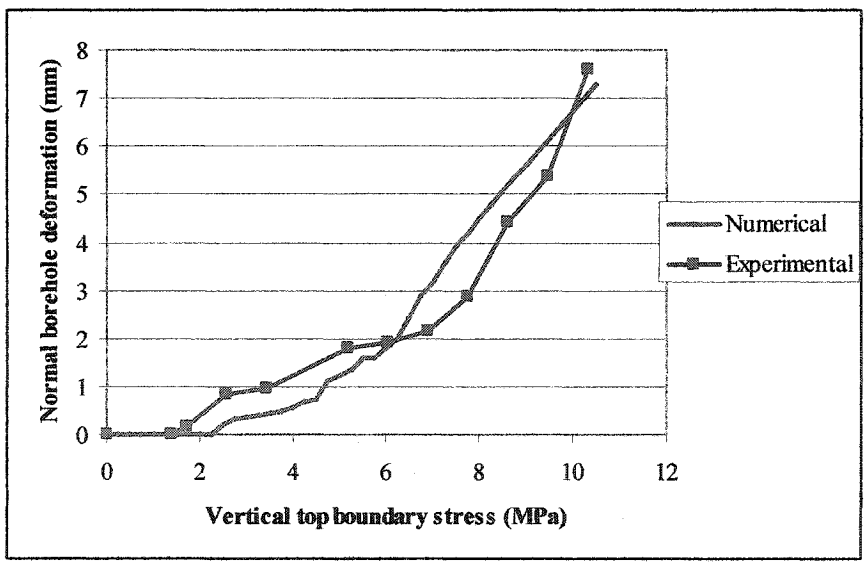

Figure 3.11. Normal borehole deformation versus top boundary stress variation from experimental and numerical modeling

Figure 3.12 compares the sand rate resulting from experimental and numerical modeling. Figure 3.13 depicts a comparison between the cumulative sanding from numerical and

experimental modeling. Since the plane strain condition was assumed in the modeling, the amount of sanding was multiplied to the length of the sample. The figures show a reasonable agreement between the experimental and numerical values. It should be noted that from any numerical analysis of sand production, obtaining knowledge on the severity of sanding should be the objective. As such, the order of magnitude of sanding rate and volume would form the bases of any decision to completion design. The outcome of our modeling not only qualitatively agreed with the experimental results, but also matched reasonably well with the experimental values in terms of sanding rate and volume. The important point is that there was no need to calibrate any parameters in the main numerical modeling of the second series of experiments. The material parameters as shown in Tables 3.1 through 3.3 were directly used, no additional adjustments were needed.

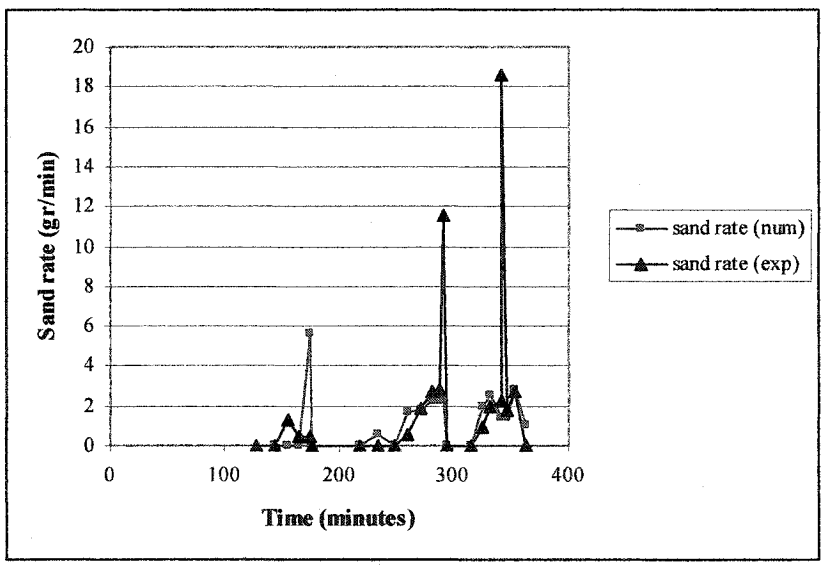

Figure 3.12. Comparison of sand rate from experimental and numerical modeling

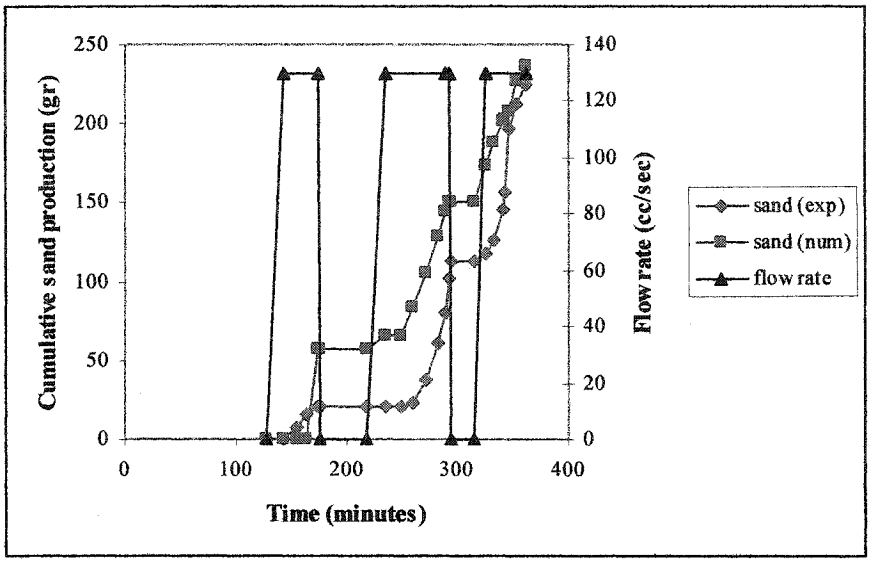

Figure 3.13. Comparison of experimental and numerical cumulative sand production

Another significance of the numerical modeling results was their agreement on the start point of failure, and removal of the material. Figure 3.14 shows the progress of the disintegrated material boundary due to failure with the increase of boundary stresses. It is realized that the most volatile point to failure is not the top point of the horizontal wellbore. Rather, the sides of the wellbore are more prone to shear failure. This is because usually the vertical stresses in the medium tend to be larger than the horizontal stresses, unless it is heavily tectonized. Since normal stress to any opening is zero, the differential stresses on the sides of the wellbore are usually higher than the top. Therefore, failure of the wellbore would usually start from the side and propagate toward the reservoir. In line with this phenomenon, horizontal deformation of the sides of the wellbore was much higher than the vertical deformation of the top point in the modeling of the first series of experiments. In addition, in the numerical modeling of the second series of experiments, the removal of the elements first affected the side elements. The notable point was also that in harmony with the experimental results, the progressive de-cemented zone almost met the boundary in the last stage of loading.

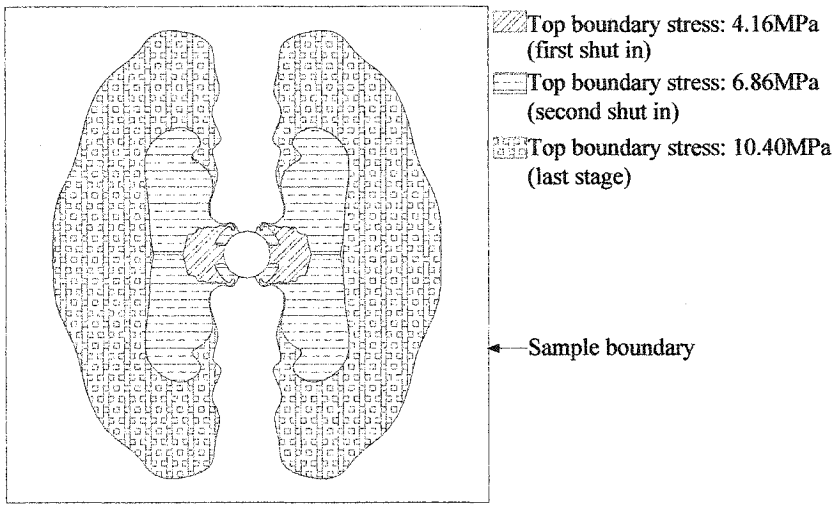

Figure 3.14. Propagation of de-cemented zone in the cross section of the sample with increasing level of loading

Conclusions

Numerical modeling correctly captured the behavior of the sample, as well as the sanding rate and volume. The ingredients of the numerical modeling were consistent with the physics of sand production. One of the major components was the bilinear strain hardening/softening Mohr-Coulomb model. This numerical model showed the power of this constitutive law in capturing the gradual degradation process of the media that could potentially lead to de-cemented material. De-cementation of the material is the first key stage to sanding and, as such, its accurate modeling is of great importance.

In modeling the rate and volume of sanding, the elimination of the elements that fulfill the removal criteria is crucial. The removal of the material induces a redistribution of the effective stresses around the cavity. This redistribution causes higher shear stresses to develop on the cavity face which may lead to more failure and de-cementation of the material. It is not an exaggeration to say that the root cause of sanding is the zero normal effective stress to the cavity face. This zero ness of effective normal stress on the cavity face paves the way to both shear and tensile failure. Even little normal effective stress would hinder shear and tensile failure. This makes the physical removal of the eligible elements necessary to any real time sand production modeling.

Another instrumental component of the modeling was the tensile criterion for the element removal. The analysis showed tensile failure on cavity face elements occurred only after shear failure degraded the material. A dynamic tensile cut off approached zero as the de-cementation process advanced. In de-cemented material on the cavity face, real mechanical cohesion, as well as effective stresses tend toward zero. In these circumstances, the consideration of capillary cohesion to resist the weak seepage forces is decisive in any real time sand production modeling.

Both numerical and experimental results indicated that in the case of horizontal wellbores, the de-cementation process initiates from the sides of the borehole. In other words, the intensity of the shear stresses is higher in these zones. Therefore, it is more likely that the removal process of the material starts from this point. Numerical modeling results conform to post-test CT cross sections along the borehole.

The rate and volume of sanding agreed reasonably well with the experimental results. This shows that the criteria used in the modeling are capturing the essence of sanding, and therefore, the use of this numerical tool in sanding prediction seems very promising.

Acknowledgements

The authors would like to thank NSERC and the Killam Trustees for their financial support.

Nomenclature

C_p = plastic projected cohesion (MPa)

C_r = plastic real cohesion (kPa)

DD= drawdown (kPa)

E= Young's modulus (kPa)

g_i = gravitational force (m/sec2)

H()= functional form of the constitutive law

K_f = bulk modulus of the fluid (kPa)

K_{ij} = the mobility tensor (m^3Sec/kg)

P= pore pressure (kPa)

q_i = the mass discharge ((kg/Sec)/m^2)

t= time (sec)

$\dot{u}_i$ = velocity in i direction (m/sec)

UCS= unconfined compressive strength (kPa)

ξ = the variation of volume of fluid in unit volume of porous material

ε^c = a constant similar to ε^f in the hardening relation for the mobilised friction angle

ε^f = effective strain associated with the limit friction angle

ε_{ij} = the strain tensor

$\bar{\varepsilon}^p$ = effective strain (hardening parameter)

ε_v = volumetric strain

ϕ = porosity of the geomaterial (%)

φ = friction angle (degree)

φ_{cv} = the friction angle of constant volume (degree)

ψ = dilatancy angle (degree)

ρ_s = density of the geomaterial (kPa)

ρ_f = density of the fluid (kg/m^3)

σ_{ij} = stress tensor (kPa)

σ'_{ij} = effective stress tensor (kPa)

σ'_r = radial effective stress (kPa)

σ'_θ = tangential effective stress (kPa)

$\sigma_y^{'}$ == vertical effective stress (kPa)

$\sigma_v^{'}$ == volumetric effective stress (kPa)

ν = Poisson's ratio

References:

Bathe, K.J., *Finite element procedures in Engineering Analysis*, Prentice-Hall, Inc., Englewood Cliffs, N. J., 1982.

Bianco, L.C.B., and P.M. Halleck, "Mechanisms of Arch Instability and Sand Production in Two-Phase Saturated Poorly Consolidated Sandstones", *SPE 68932, SPE European Formation Damage Conference*, The Netherland, 2001.

Das, B.M., *Principles of Geotechnical Engineering*, PWS Publishing Co., Boston, 1993.

Desai, C.S. and H.J. Siriwardane, *Constitutive Laws for Engineering Materials with Emphasis on Geologic Material*, Prentice-Hall Publishing Co., 1984.

Dusseault, M.B. and S. El-Sayed, "Heavy-Oil Production Enhancement by Encouraging Sand Production", *SPE 59276, SPE International Symposium on Formation Damage*, Lafayette, Louisiana, 2000.

Itasca Consulting Group, FLAC- Fast Lagrangian Analysis of Continua- User's Guide 3.4, Minneapolis, Minnesota, 1998.

Kooijman, A.P., P.J. van den Hoek, Ph. De Bree, C. J. Kenter, B.V Z. Zheng, and M. Khodaverdian, "Horizontal Wellbore Stability and Sand Production in Weakly Consolidated Sandstones", *SPE 36419, SPE Annual Technical Conference and Exhibition,* Denver, Colorado, 1996.

Morita, N., and P.A. Boyd, "Typical Sand Production Problems: Case Studies and Strategies for Sand Control", SPE *22739, 66th Annual Conference*, Dallas, TX, 1991.

Nouri, A., H. Vaziri, H. Belhaj, and R. Islam, "Effect of Volumetric Failure on Sand Production in Oil-Wellbores", *SPE 80448, SPE Asia Pacific Oil and Gas Conference and Exhibition,* Jakarta, Indonesia, 2003.

Sanfilippo F., M. Brignoli, D. Giacca, and F.J. Santarelli, "Sand Production: From Prediction to Management", *SPE 38185, SPE European Formation Damage Conference*, the Netherlands, 1997.

Smith, G.E., "Fluid Flow and Sand Production in Heavy Oil Reservoirs under Solution Gas Drive", SPE 15094, SPE California regional meeting, Oakland, California, 1986.

Vaziri, H., B. Barree, Y. Xiao, I. Palmer and M. Kutas, "What Is the Magic of Water in Producing Sand?", *SPE 77683, SPE Annual Technical Conference and Exhibition*, San Antonio, Texas, 2002.

Vermeer, P.A., and R. de Borst, "Non-Associated Plasticity for Soils, Concrete and Rock", *Heron*, **29**, no. 3, pp. 1-64, 1984.

Wang, Y., and C.C. Chen, "Improved Production and Sand (Cold) Production in Conventional and Heavy Oil Reservoirs- A Field Case and Simulation", *SPE 57290, SPE Asia Pecific improved oil recovery Conference*, Kuala Lampur, Malaysia, 1999.

Chapter 4: Experimental and Analytical Studies of Wellbore Sand Production Associated with Single- and Two-Phase Flow

Publication Status: Submitted (Submission Date: Jul. 3, 2004), Canadian Geotechnical Journal.

Abstract

The presence of a second phase in an oil-rich porous medium may tremendously change its behaviour in terms of stress distributions around the wellbore, as well as the severity of sand production. This makes the experimental and mathematical studies of the phenomena related to these effects indispensable. In this paper, laboratory sand production experiments have been performed using hollow cylinder samples simulating an open hole completion. The experiments help develop insights into the sand production mechanisms and in particular the influence of capillary forces. While extensive research has been conducted on sanding mechanisms (shear and pore collapse) using triaxial cells, very few large-scale sand production experiments have been performed with scaled wellbore models to more accurately represent field conditions. Such results are also very useful for verifying theoretical concepts and validating mathematical models, such as the one presented in this paper.

Experiments were conducted on hollow cylinder samples of open hole completion with single- and two-phase pore fluids involving both fine and coarse grained sandstone. Moreover, a full investigation was carried out to characterize the yield envelopes of the material. A formulation is presented which quantifies seepage forces on grains. In this formulation, an estimation of the required real cohesion for a safe production is provided which can be compared with the cohesion that capillarity offers.

The investigations indicated that the presence of a second phase could remarkably change the behaviour of the media in terms of sand production. A small percentage of water content greatly stabilizes the disaggregated fine grained sandstone while the effect fades as the constituent grains get coarser. Moreover, if the saturation level of the second phase is more than a threshold, the capillarity issue again looses its importance. The findings are considered useful in determining the most cost-effective completion options and estimating safe operational limits.

Introduction

It has typically been reported that the onset of sand production is observed at water breakthrough (Tronvol et al., 2001, Vaziri el al, 2002). Han and Dusseault (2002) and Vaziri et al. (2002) proposed the many possible mechanisms that may hasten the instability depending on the degree of water saturation and the cement mineralogy. For instance, water changes the multi-phase flow behaviour by changing the relative permeability. Water can also weaken the sandstone whose constituents react to water, e.g. shale, some clay minerals, and carbonate cementation. While the aforementioned effects have some influence, in many situations it is difficult to determine any link between such mechanisms and an immediate sanding following a water-cut. Numerous studies have linked the immediate instability of the grains upon water breakthrough to the destruction of capillary induced cohesion between the grains.

Bianco and Halleck (2001) performed several experiments on poorly consolidated sandstones subjected to water influx. In their experiments, confining pressure was kept constant during the test, while single- and two-phase experiments were performed. Two-phase experiments were conducted at two different levels of flow rate. According to the results, single-phase saturated sands did not develop enough cohesive strength to support a stable arch and sand was produced massively. However, a small increase in the wetting phase saturation developed enough cohesive strength to stabilize an arch, reducing sand production. Lower connate water content increased the level of flow rate to induce sanding.

Han and Dusseault (2002) presented a model to evaluate the magnitude of capillary cohesion as well as the behaviour of the medium with an increasing level of water saturation. They concluded that the order of magnitude of capillary cohesion is the same as seepage forces. Therefore, this effect should not be neglected. Moreover, the capillary cohesion degrades very quickly with the increase of water saturation. The most degradation of the capillary cohesion occurs within the first small percentage, say 5%, of water saturation. The possibility of chemical reactions with water breakthrough was also discussed, but it was observed that capillary changes play a dominant role, while, chemical reactions may become an issue in the long term.

Skjarstein et al. (1997) performed a few experiments on semi hollow cylinder samples. For a single-phase fluid flow, the initial saturating fluid was oil with a later flow of oil, or instead, brine with a second stage of brine flow. They concluded that for a few samples with smectite/Illtite minerals in cement, the strength of the material significantly dropped with the flow of water. The effect is different for different salts (cat ions). Therefore, the chemical reactions degrade the material if there are sensitive clays to the water that is injected to the medium. The natural formation water is expected to be in chemical balance with the formation rock. The degradation process by water is, therefore, the only mechanism whereby injected water for enhanced oil recovery is incompatible with the rock constituents. As an example, in the case of Red Wildmoor sandstone, Skjarstein et al. (1997) reported that the mineral was little affected by NaCl based brine, while it was appreciably degraded by a KCl based brine. Therefore, if the reservoir of this medium has a connate water of NaCl base, and KCl based brine is injected to it, the degradation process will occur.

Han et al. (2002) studied the effect of chemical incompatibility between injected water and cement bonds. They concluded that this effect by itself could not induce material disaggregation; nevertheless, it may degrade the material. This, in turn, could hasten its failure and, therefore, increase the possibility of sand production. How pronounced this effect would be depends on the amount of clay in the structure, the salinity of the formation/injected water, and the type of clay.

In this paper, a series of open hole hollow cylinder samples with two different grain size distributions are considered. Experiments are conducted using both single- and two-phase flow conditions. A formulation is presented for a quick check of sand production. This formulation is applied to the experimental results and the validity of its prediction is examined.

Experimental Method

Getting sandstone samples from the field is usually expensive and difficult. Weakly-consolidated sandstone is particularly difficult to core in the oil-wells and recover to the surface undisturbed. Moreover, in experimental studies, the use of consistent samples is preferable, increasing the likelihood that the results obtained would be reproducible in

future or ongoing research. For the samples that are extracted from the quarries, a quick spatial change of physical and mechanical properties are common. This inconsistency usually introduces difficulties in the interpretation of the results. Therefore, it was decided to manufacture sandstone samples that can closely represent formation sandstone.

Hollow Cylinder Sample Preparation

Synthetic samples were manufactured for both material characterization and sand production experiments. For the sand production experiments, hollow cylinder samples were cast.

Material Composition

The manufacturing of synthetic sandstone employs sand with Portland cement and water. The material composition for preparing the samples consisted of a cement/sand weight ratio of 0.11 and water/cement weight ratio of 1.25.

Grain Size Distribution of the Sand Used in Sample Making

The sandstone samples are made of a mixture of one of the two sand grain size distributions, Portland cement, and water. Two grain size distributions of the Silica sand grains, namely coarse and fine grain, ranged between 70 to 600 μm and 37.5 to 260 μm respectively as shown in Figure 4.1.

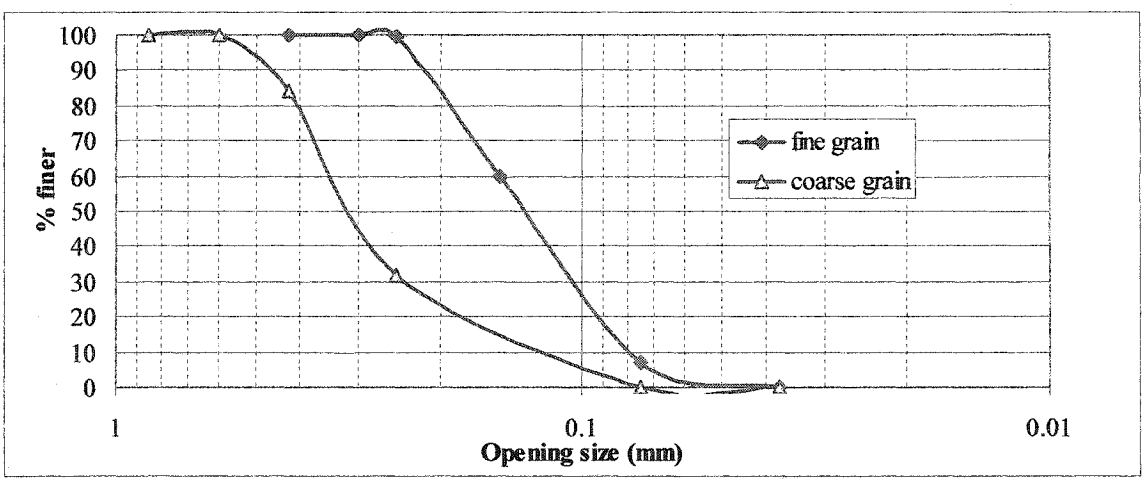

Figure 4.1. Two grain size distributions of the sand used in synthesizing the samples

Manufacturing Process

Sand, cement, and water are mixed into slurry, and then slightly pre-compacted when packed by a spatula into a mould and vibrated by gentle hits. To prevent the formation of distinct layers, the top of each layer was ploughed by the spatula.

Two grain size distributions, fine and coarse, were used in preparation of the Hollow Cylinder Samples (HCS). Therefore, effects of grain size on general sample behaviour and specifically on sand production were monitored. Casting was performed in an aluminium mould with a 125 mm inside diameter and a central rod which created the central hole. After each casting, the sample remained in the mould for 3 days. It was then taken out of the mould and put in water for 18 days at ambient temperature. After this, the sample was put in an oven set to 50 ^{o}C. All of the samples were ground at both ends and epoxy was applied in order to make a stiff smooth cap at each end. The sample was kept dry in the oven before it was again saturated before the start of each experiment.

Stringent quality control was implemented during the casting to obtain uniform material properties in each HCS as well as from one sample to the next. The process of sample making was consistent for all the samples in order to make sure that they would provide reproducible results.

Sample Saturation

Samples were saturated in a container under vacuum pressure. In the case of single-phase flow, samples were either saturated by Odourless Mineral Spirits (OMS) or water. In the case of two-phase flow, the samples were first saturated by water. Subsequently, OMS was flown through the sample and reduced the water saturation of the sample to connate water content.

Physical Properties of the Samples

Physical properties of the synthetic samples which were used in the experiments are listed in Table 4.1.

Table 4.1. Physical properties of the synthetic sandstone

	D10/D50/D90 (Micron)	γ_d (kg/m^3)	γ_{sat} (kg/m^3)	Porosity	Initial Permeability (md)	S_{wres} (%)
First coarse grained single-phase	120/300/500	-	-	-	1000	-
Second coarse grained single-phase	120/300/500	1670	2044	37.5	3800	-
Coarse grained two-phase	120/300/500	1570	1982	41	1000	52
First fine grained single-phase	80/130/220	1504	1942	43.7	3200	-
Second fine grained single-phase	80/130/220	1503	1941	43.7	1600	-
Fine grained two-phase	80/130/220	1476	1923	44.7	1500	40

A thin section was manufactured from a coarse-grained synthetic sandstone sample. The photomicrograph of this thin section is shown in Figure 4.2 under cross-polarized light. The grain shape is angular to sub-angular, and the grain size distribution is confirmed to be well sorted.

Figure 4.2. Microphotograph of a thin section under cross-polarized light; field of view is 11 mm

Mechanical Properties of the Samples

Table 4.2 summarizes the mechanical properties of the fine and coarse grained synthetic sandstones including a characterization of the Mohr-Coulomb shear envelope.

Table 4.2. Mechanical properties of the fine and coarse grained synthetic sandstone

	UCS (MPa)	Young's modulus E (MPa)	ν	C_p (kPa)	C_r (kPa)	φ (degrees)	φ_r (degrees)
Coarse grained	2.1	400	0.05	810	480	34	39
Fine grained	1.03	-	-	1230	425	26	38

Experimental Set-Up

Test equipment includes a loading unit, flow set-up, sanding measurements unit, and instrumentation. A picture of this set-up is shown in Figure 4.3.

Each sample is confined in a chamber similar to a consolidation assembly. This set-up creates a condition similar to what is in reality in a reservoir, where no lateral movement is allowed. The outer radial pressure, therefore, is accordingly adjusted to the axial load, and its value depends on the material and the stress path.

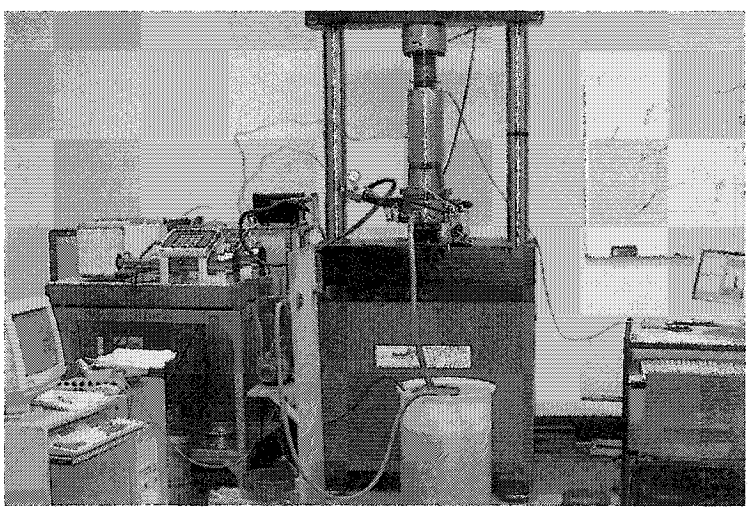

Figure 4.3. Photograph of the set-up used in sand production experiments

A schematic of the consolidation chamber is depicted in Figure 4.4. A steel hard shell of 12 mm in thickness restrains a hollow cylinder sample that is surrounded by a 7.5 mm

thick gravel pack. A top platen slides inside the chamber and transfers the load from the top piston to the sample. The top platen is sealed by two rows of O-rings.

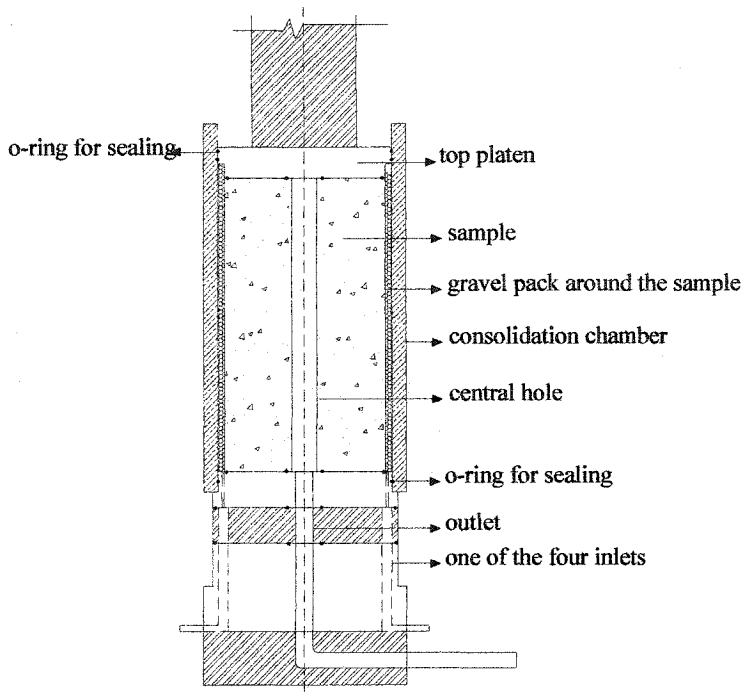

Figure 4.4. A schematic of configuration of the consolidation chamber

Loading Unit

The axial loading unit can apply up to 250 kN of force. It is designed with feedback control and continuous displays of axial load and platen displacement, and an IEEE computer interface with built-in stepping motor.

Flow Unit

Figure 4.5 shows a schematic of the fluid flow unit. The flow system was set up to supply a radial inward flow. A positive displacement pump was used for supplying fluid flow during the test. A manifold was used to divide the flow after the pump to four vessels in the base plate of the cell. Fluid was injected through the four tubes to small holes in the circumference of the bottom platen.

The fluid was supplied to the pump from a tank with nearly 200 litre volume capacity. To generate a radial flow, a highly permeable zone of gravel-pack was deployed around

the sample. This system diverted the axial flow in the permeable zone to radial in the sample.

The fluid and any produced sand were collected by the wellbore in the centre of the sample. The wellbore was connected to the outlet and was kept at atmospheric pressure during the test.

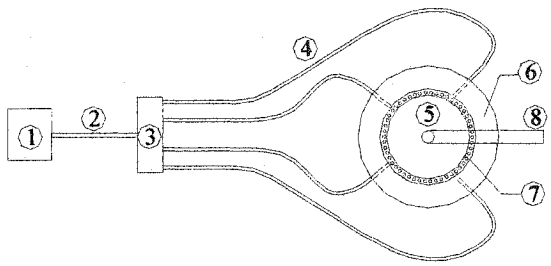

1- Positive pump
2- Main tubing between the pump and the division box
3- Manifold
4- One of the four tubings between the division box and the base
5- Bottom platten on which the sample sits
6- Base of the set-up
7- Small holes connected to the four vessles by a round channel
8- Flow outlet

Figure 4.5. A schematic of configuration of the fluid flow vessels

Sand Measurements Unit

From the sieve analysis results, grains were distributed in the range of 0.0375-0.26 mm for fine grain and 0.07-0.60 mm for coarse grain distribution as shown in Figure 4.1. Therefore, a sieve #400 was sufficient to entrap practically 100% of the produced material. The sieves sat on a tripod inside the tank. A pair of sieves was used and a digital balance weighed the produced sand.

By interchanging the sieve as often as required, the amount of the produced sand during consecutive time intervals could be measured. The produced sand was weighed at regular time intervals.

Instrumentation

Both axial load and displacements were measured by built-in transducers on the loading frame. A dial gauge pressure measurement unit with a maximum pressure capacity of 688 kPa (100 psi), as well as a digital pressure transducer, were connected to the manifold to precisely measure the fluid pressure in the box. Moreover, a pressure transducer was connected to the cylinder shell to directly measure the fluid pressure around the sample.

Two flow-meters were connected to the tubing of fluid supply. The minimum and maximum measurable flow rates with this device were 3 and 250 cm3/second respectively.

Gravel-Pack between the Sample and the Chamber

Gravel was placed between the sample and the chamber in a 7.5 mm gap as shown in Figure 4.6. The gravel pack created a highly permeable zone around the sample. Two types of gravel, one coarse ranging between 2 to 6 mm, and another fine between 0.5 to 2.5 mm were used in the experiments. Grain size distributions of the two are shown in Figure 4.7. The coarse grain size distribution was used in the first experiment deploying a coarse grained sample and single-phase flow. It was also used in the two-phase experiment of a coarse grained sample. In the rest of the experiments the fine grained gravel pack was used. This was to reduce the friction between the gravel-pack and the sample, as well as between the gravel-pack and the chamber. According to calibration experiments, this switch did not make a great difference.

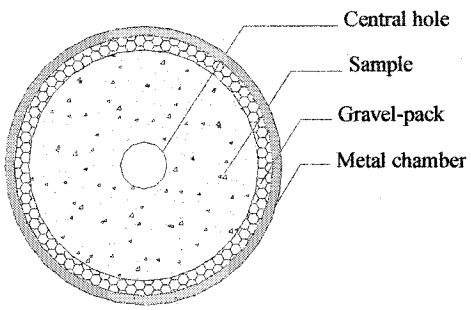

Figure 4.6. A cross section of the chamber containing the sample and the gravel-pack

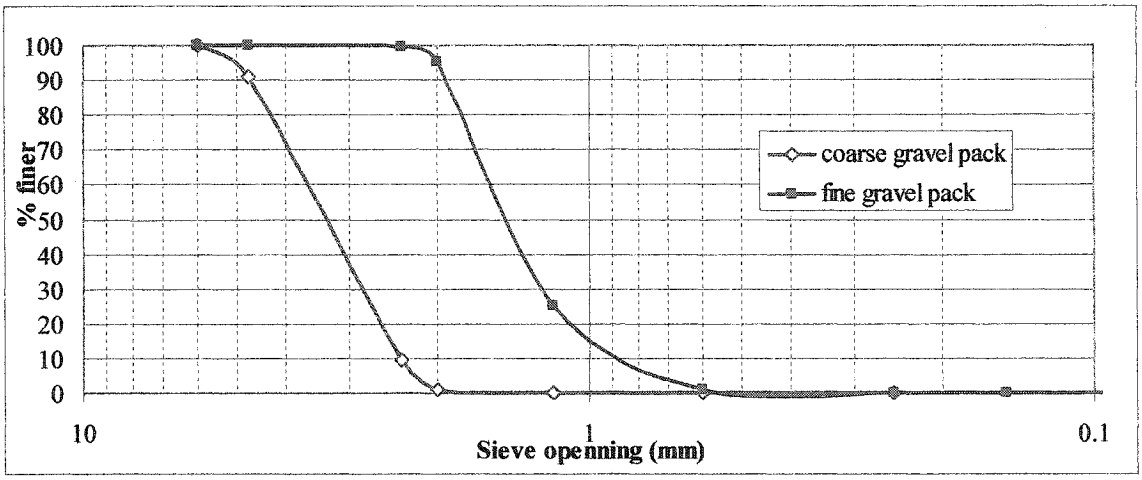

Figure 4.7. Grain size distribution of the coarse and fine gravel pack around the sample in the consolidation chamber

Testing Procedure

First, a saturated sample was placed in the chamber and was positioned in the axial loading frame as shown in Figure 4.4. Each sample was laid on the bottom platen which contained small circumferential holes. The cylindrical steel shell was slipped down, then firmly secured by sliding around a bottom platen. An o-ring sealed the gap between the platen and the shell. Gravel grains were packed in the circumferential gap between the sample and the hard shell, and filled to the top of the sample. The top platen was then slipped down and laid on top of the sample. The top platen was also sealed with two rows of o-rings. Subsequently, controllers and the tubing system were connected.

Each experiment started with a gradual increase in axial stress. The high flow rate pump was started and the flow rate was increased to its designed level. The flow was established when it was expected that the sample was still in elastic range. Throughout each experiment, the pressure of the central hole was kept atmospheric.

As the drag forces of seepage produced the disaggregated material, the produced sand was collected on a sieve and weighed on a regular basis.

Observations of the Experiments

The observations of the experiments on coarse and fine grained samples are elaborated upon in the following paragraphs.

Experiments on Fine Grained Samples

Two experiments on fine grained samples with single-phase flow, and an experiment on a similar sample with two-phase flow were conducted. Water was used for both saturation and flow through the samples in single-phase experiments. In the two-phase experiment, water was used for saturation and OMS was used as the flowing fluid.

First Experiment on Fine Grained Samples with Single-Phase Flow

Figure 4.8 illustrates a graph of several parameters as a function of axial deformation.

An initial concavity in the curve of the axial loading-deformation is observed, which is attributed to the gradual closure of the fissures in the sample and the gaps between the platens and the sample at the onset of the loading.

As Figure 4.8 shows, the flow rate was established at an axial stress of about 1500 kPa, and the peak of flow rate occurred at an axial stress of 4000 kPa. A rather steep slope of sanding in the beginning indicates that a flow rate of 30 cc/sec was not strong enough to push the disaggregated material into the central hole. After the flow rate peaked, it was kept almost constant for the rest of the experiment. Sanding showed an exponentially increasing rate with the increase of the axial loading.

Additionally, Figure 4.8 indicates an increasing permeability of the sample throughout the test.

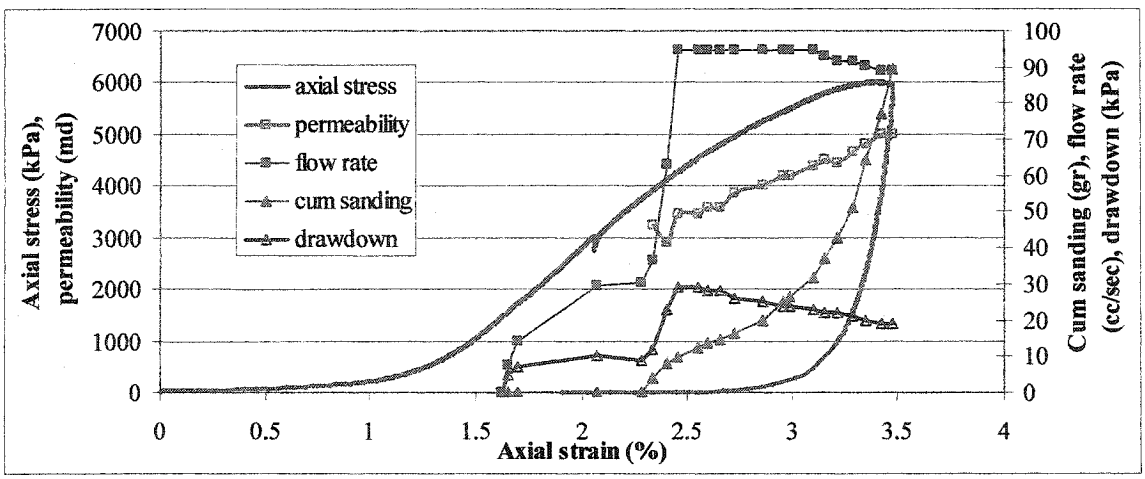

Figure 4.8. Experimental results of sand production experiment on fine grained samples with single-phase flow

Second Experiment on Fine Grained Samples with Single-Phase Flow

This experiment was a repeat of the previous experiment. Figure 4.9 indicates the same peak of axial stress and axial strain, and the same amount and trend for sanding as the previous experiment, which proves the reproducibility of the results. Sand production started at an axial stress of nearly 4000 kPa with an exponential increase in its rate. Figure 4.9 shows a trend of increasing permeability throughout the experiment.

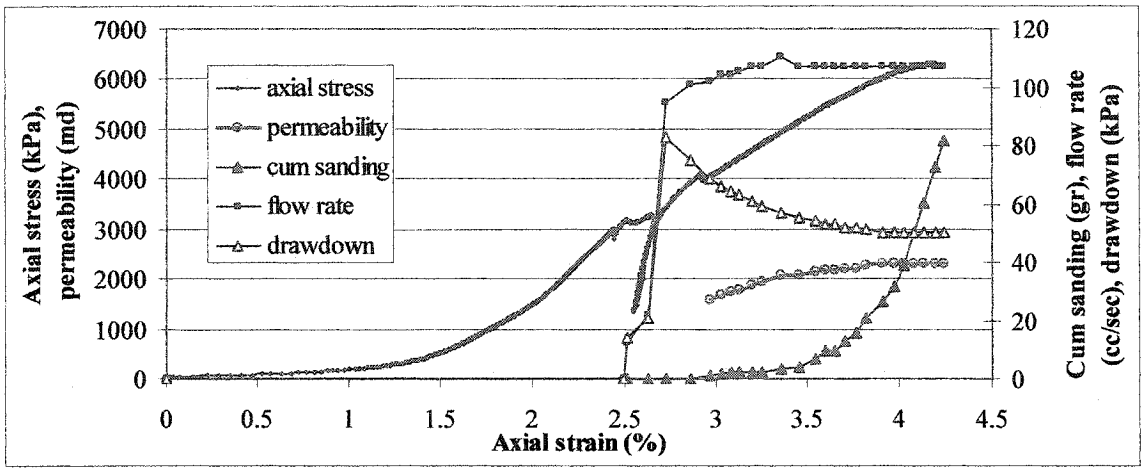

Figure 4.9. Experimental results of the sand production experiment on fine grained samples with single-phase flow

Experiment on Fine Grained Samples with Two-Phase Flow

This is a repeat of the previous experiment, except that the flowing fluid was different from the saturating fluid. OMS was used as the flowing fluid and water as the saturating fluid. OMS flow could partly sweep the saturating water. A steady OMS flow with only traces of water indicated that water saturation had decreased to a connate water level.

A comparison of the graphs of Figure 4.10 with the similar ones of single-phase experiments indicates a two fold decrease in sanding volume, although the axial stress shows a decrease from nearly 6000 kPa to 4800 kPa due to a slightly weaker sample. The trend of sanding with an initially small rate growing exponentially to the end of the experiment, confirms the same trend as was observed in single-phase experiments.

Moreover, an increasing trend of permeability in the course of shear failure repeats the observations of the single-phase experiments.

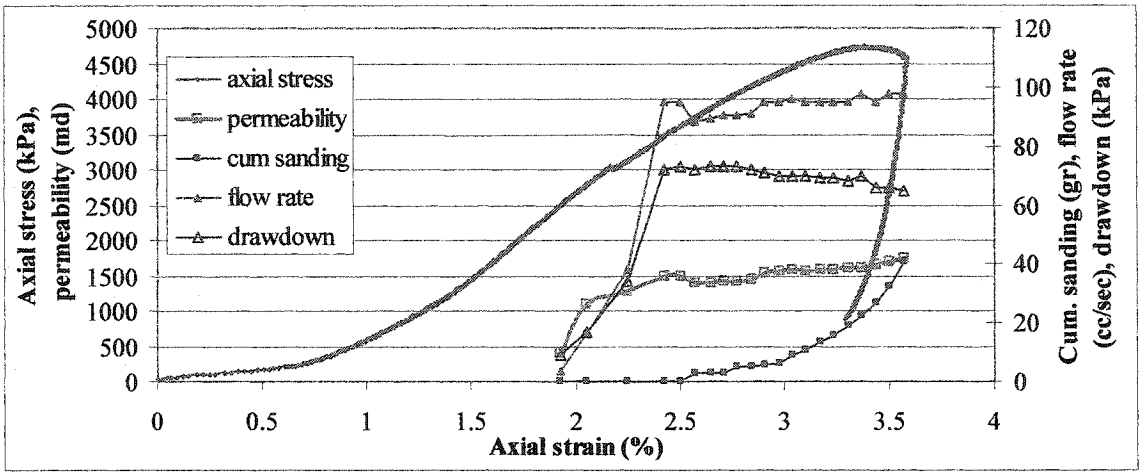

Figure 4.10. Experimental results of the sand production experiment on fine grained samples with two-phase flow

Comparison of the Grain Size Distribution of the Original and Produced Sand

Figure 4.11 depicts the sieve analysis of the original sand grains that were used for fabricating the artificial sandstones and compares it with the produced sand of both single- and two-phase flow experiments. A comparison of the grain size distribution of the produced sand of the single-phase experiments with that of the two-phase shows a slight increase in the size of particles produced from the two-phase experiment.

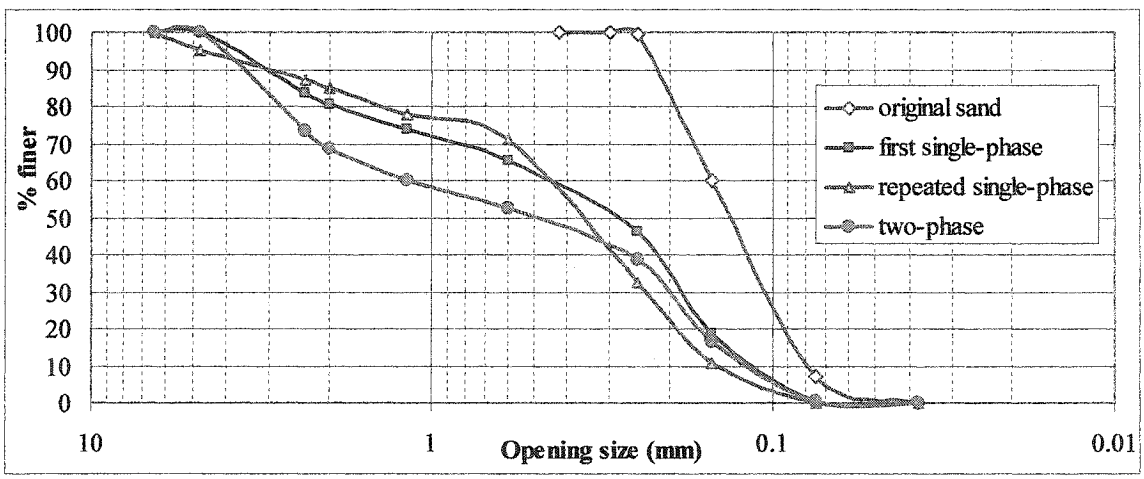

Figure 4.11. A comparison of the grain size distribution of the original fine sand and the produced sand from the series of experiments on fine grained samples

Experiments on Coarse Grained Samples

Two experiments with single-phase flow and an experiment with two-phase flow were conducted. In one of the experiments with single-phase flow OMS was used, and in the other water was used as the saturation and flowing fluid. In the two-phase experiment, water saturated the sample and OMS was used as the flowing fluid.

First Experiment on Coarse Grained Samples with Single-Phase OMS Flow

A typical response is observed in the beginning of the loading as shown in Figure 4.12 in which a rather large deformation occurs.

Figure 4.12 shows that the permeability of the sample increased throughout the experiment. Sanding started at an axial strain of nearly 1.3% and at an axial strain of about 2.2% sanding accelerated. At a higher deformation level, where the stress-deformation curve flattened off, the sanding activity showed a dramatic increase.

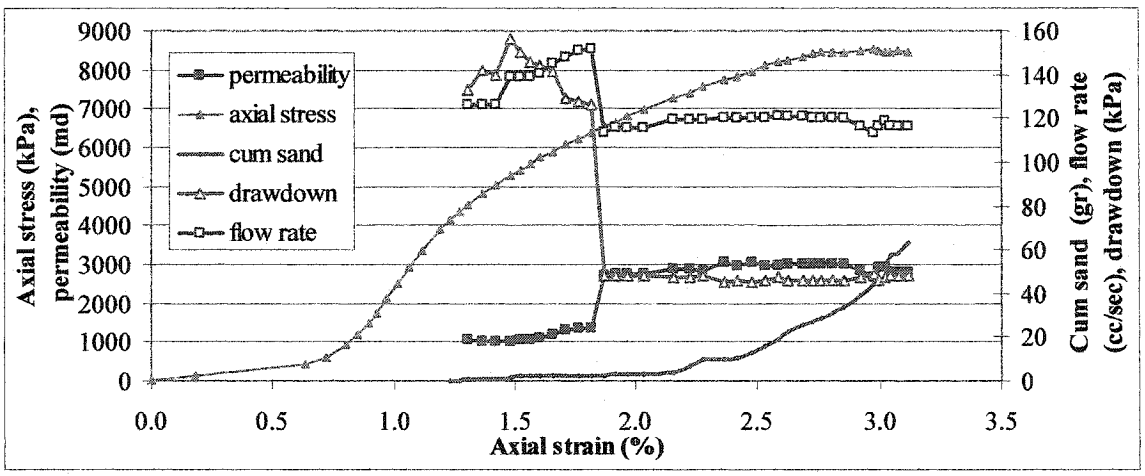

Figure 4.12. Experimental results of sand production experiment on coarse grained samples with single-phase flow

Figure 4.13 shows a picture of the top of the sample after the experiment terminated. In this experiment, the sanding was concentrated to the top of the sample, and absolutely no sanding took place from anywhere else along the borehole. This observation can be explained by the phenomenon of strain localization in an initially weak zone and the development of the shear bands from that region.

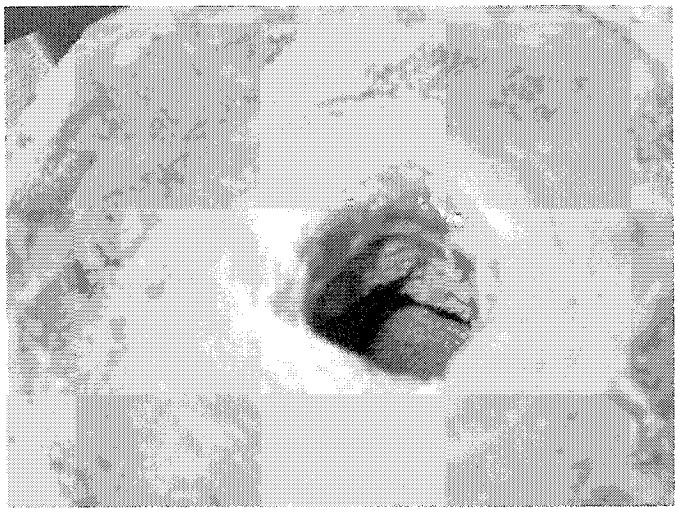

Figure 4.13. A picture from the top of the sample showing the cavities around the hole

Second Experiment on Coarse Grained Samples with Single-Phase Flow

This is a repeat of the previous experiment. Axial loading was increased steadily, and flow rate started at an axial stress of nearly 4 MPa. Figure 4.14 shows that sand production started at an axial stress of 7 MPa and its rate increased exponentially. Moreover, an increasing trend of permeability during the experiment confirms the previous observations.

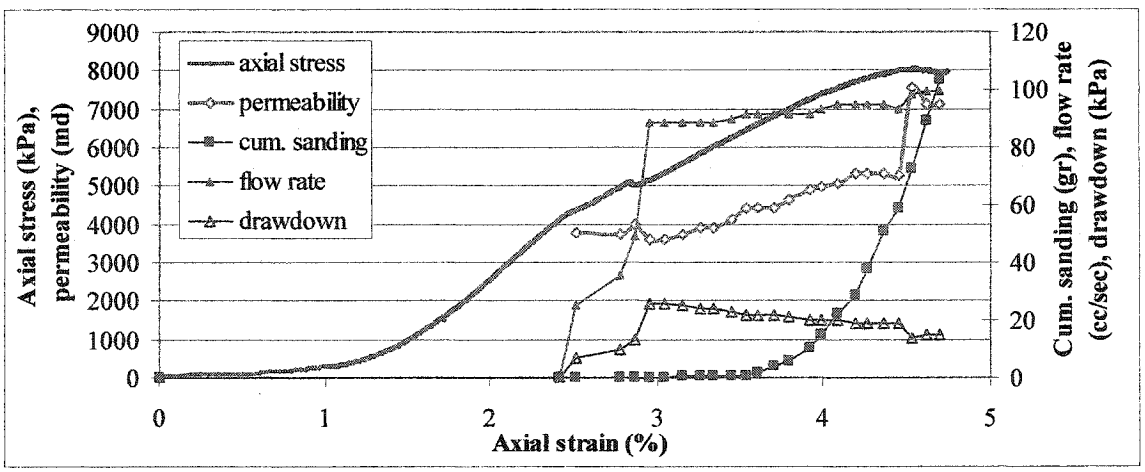

Figure 4.14. Experimental results of a sand production experiment on coarse grained samples with single-phase flow

Experiment on Coarse Grained Samples with Two-Phase Flow

This experiment is a repeat of the previous experiments on coarse grained samples the only difference being that OMS was passed through the sample which was initially saturated with water.

Figure 4.15 shows the curves of cumulative sanding and the corresponding axial stress versus axial deformation. Sanding started at an axial stress of about 6500 kPa and later, its rate increased throughout the experiment. At the peak of the axial stress-deformation curve, the rate of sanding showed a remarkable increase. A comparison of the graphs of Figure 4.15 with the corresponding graphs of the experiment with single-phase flow shows both started producing sand at similar axial strain and stress levels and, more importantly, produced the same amount of sanding. Therefore, the second phase in coarse grained samples produced little capillary cohesion and played no role in deterring sand production.

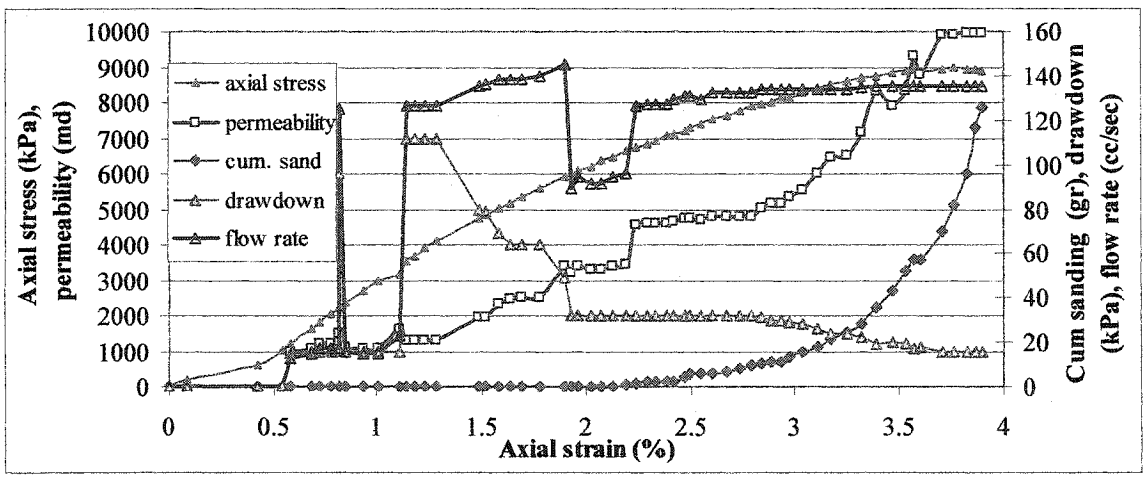

Figure 4.15. Operational conditions as well as the results of the experiment

Figure 4.16 shows a picture of the sample from its top, the only location where it produced sand.

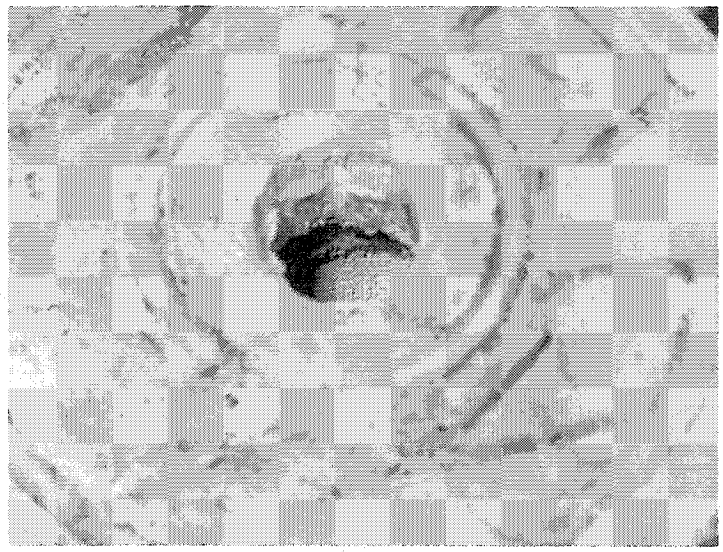

Figure 4.16. A picture from the top of the sample showing the cavities around the hole

Comparison of the Grain Size Distribution of the Original and Produced Sand

Figure 4.17 depicts the sieve analysis of the original sand grains that were used for fabricating the artificial sandstones and compares it with the produced sand of both single- and two-phase flow experiments. A comparison of the grain size distribution of the produced sand of the single-phase experiments with that of the two-phase shows a slight increase in the size of small particles produced from the two-phase experiment. In the top portion, however, the same distribution results from both single- and two-phase experiments.

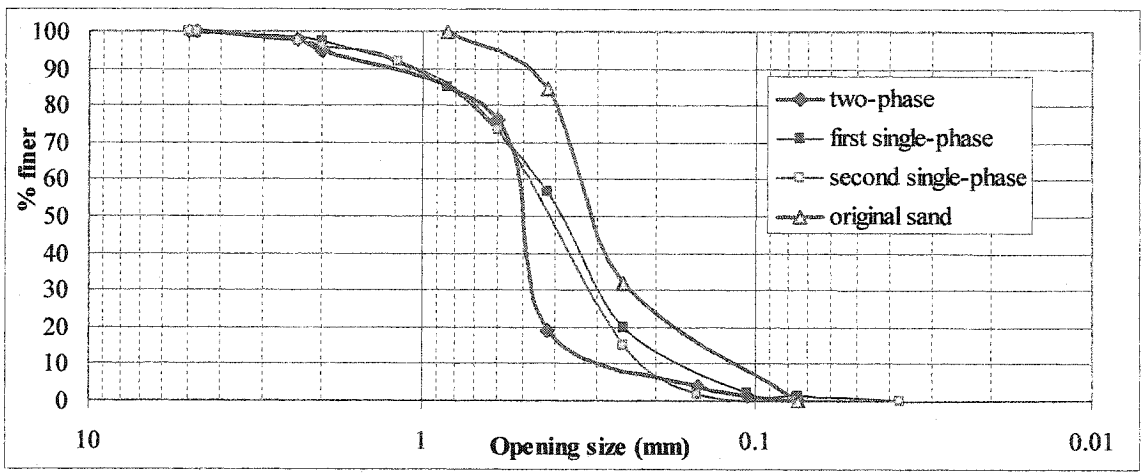

Figure 4.17. A comparison of the grain size distribution of the original coarse sand and the produced sand from the series of experiments on coarse grained samples

Analytical Studies

A formulation is developed which combines an equilibrium equation and a formulation of capillary cohesion. The formulation is valid for the disaggregated material around a cavity. Therefore, the material properties which are used in this formulation should be for the degraded material rather than the original intact rock.

Mathematical Formulation of Seepage Forces and Capillary Induced Resistance

The stability criterion can be expressed in terms of the normalized drawdown induced pressure gradient at the cavity wall which formulates:

$$g_{pn} = \partial P / \partial(r / r_w) r = r_w \qquad [4.1]$$

where

r = radius of investigation (L),

r_w = radius of the cavity (L).

For a cylindrical geometry of cavity, stress equilibrium states:

$$\partial\sigma_r / \partial r = (\sigma_\theta - \sigma_r) / r \qquad [4.2]$$

where

σ_r = radial total stress (F/L^2),

σ_θ = tangential total stress (F/L^2).

At $r = r_w$:

$$\sigma_r = \sigma_r' + P = P \qquad [4.3]$$

$$\sigma_\theta = \sigma_\theta' + P \qquad [4.4]$$

Which reduces [4.1] to:

$$\partial\sigma_r / \partial(r / r_w) + \partial P / \partial(r / r_w) = \sigma_\theta \qquad [4.5]$$

A tensile radial stress develops if $\partial\sigma_r / \partial(r / r_w)$ is near zero or:

$$g_{pn} \geq \sigma_{\theta}(r = r_w) \qquad [4.6]$$

Since σ_r at the cavity wall is zero, the maximum σ_θ at the same location is limited by the Unconfined Compressive Strength (σ_{UCS}). Hence:

$$\sigma_{\theta} \leq \sigma_{UCS} \qquad [4.7]$$

and:

$$g_{pn} = {}^{\partial p}/_{\partial(r/r_w)} = \sigma_{UCS} \qquad [4.8]$$

This equation sets an upper limit to the pressure gradient.

σ_{UCS} can be elaborated by friction angle and cohesion:

$$\sigma_{UCS} = \frac{2C_r \cos\varphi}{1-\sin\varphi} \qquad [4.9]$$

where

φ = friction angle,

C_r = real cohesion (F/L^2).

Therefore:

$${}^{\partial p}/_{\partial(r/r_w)} = \frac{2C_r \cos\varphi}{1-\sin\varphi} \qquad [4.10]$$

For a stable condition (no material movement):

$$C_r \geq \frac{(1-\sin\varphi)}{2\cos\varphi} {}^{\partial P}/_{\partial(r/r_w)} \qquad [4.11]$$

The pressure gradient can be related to pressure drawdown:

$$\Delta P_{dd} = {}^{\partial P}/_{\partial(r/r_w)} \log(r_e/r_w) \qquad [4.12]$$

where

r_e = the external diameter (L).

In this equation the assumption of uniform permeability is used. [4.11] can be elaborated in terms of the pressure drawdown:

$$C_r \geq \frac{1-\sin\varphi}{2\cos\varphi}\frac{\Delta P_{dd}}{\log(r_e/r_w)} \qquad [4.13]$$

Alternatively [4.11] can be written in terms of fluid flow rate.

$$\frac{\partial P}{\partial\left(\frac{r}{r_w}\right)} = \frac{Q\mu}{2\pi kh} \qquad [4.14]$$

where

μ = viscosity of the fluid (F/(LT)),

h = height of the pay zone (L),

Q = fluid flow rate (L^3/T),

k = intrinsic permeability (L^2).

Therefore:

$$C_r \geq \frac{(1-\sin\varphi)}{4\cos\varphi}\frac{Q\mu}{\pi kh} \qquad [4.15]$$

In case of total disaggregation, capillary cohesion is the only responsible defensive agent. Otherwise, it is a combination of real cohesion from cementation and capillary cohesion (Han et al., 2002).

$$\sigma_{UCS} = \lambda\frac{1-\phi}{\phi}\frac{\sin\varphi}{1-\sin\varphi}\frac{F_c}{2R^2}$$

$$F_c = \pi x^2 \Delta P_{capillary} \qquad [4.16]$$

$$x = R\sin\alpha$$

where

ϕ = porosity,

R = average grain diameter (L),

F_c = cohesion force (F),

α = water volume angle,

$\Delta P_{capillary}$ = capillary pressure (F/L^2),

λ = a factor accounting for the effect of the non-uniform grain distribution on the rock strength.

A value of $\lambda = 6-8$ has been suggested for packs of narrowly distributed sand and a range of 1.9-14.5 for wider distributions. We assume a value of $\lambda = 7$ for later calculations.

By elaborating σ_{UCS} in terms of cohesion and friction angle and replacing in [4.16], capillary cohesion can be related to capillary pressure:

$$C_c = -\lambda \Delta P_{capillary} \frac{(1-\phi)}{\phi} \tan\varphi \frac{\pi \sin^2 \alpha}{4} \qquad [4.17]$$

where

C_c = capillary cohesion (F/L^2).

Assuming that the shape of the liquid bridge is a toroid characterized by radii x_p and r, a commonly accepted formula to calculate capillary pressure across the liquid water bridge has been developed (Han et al., 2002):

$$\Delta P_{capillary} = \gamma\left(\frac{1}{x_p} - \frac{1}{r}\right) \qquad [4.18]$$

where

γ = surface tension between two fluids (F/L),

$x_p = R \sin\alpha$

$$r = \frac{1-\cos\alpha}{\cos\alpha} R \qquad R = D_{50} \qquad [4.19]$$

On the other hand, assuming uniform grade distribution, the expression for water saturation becomes (Han et al., 2002):

$$\phi S_w = \frac{-\alpha}{2} + \sin\alpha - \frac{1}{4}\sin 2\alpha - \frac{(1-\cos\alpha)^2}{1+\cos 2\alpha}\left[\frac{\pi}{2} - \alpha - \frac{\sin 2\alpha}{2}\right] \qquad [4.20]$$

where

S_w is water saturation.

In the process of estimation of the stability of the de-cemented grains, first α is estimated from [4.20], knowing the water saturation and porosity. Then r and x_p are calculated from [4.19]. Capillary pressure is estimated by [4.18] by knowing the surface tension between the water and the oil. This is used in [4.17] and compared with [4.15] to evaluate the stability of the grain.

Estimation of Capillarity Effect in the Experiments

Tables 4.3 and 4.4 estimate the capillary cohesion and the drawdown associated with the onset of sanding in the fine and coarse grained samples respectively.

In the calculations, a mean grain size of 0.12 mm was used which is based on the graph of Figure 4.1. The porosity of the sample in the beginning measured 44%. The friction angle of the material is estimated to be about 45o. Although not measured, it is estimated that the interfacial tension between water and oil is about 0.03 N/m (Berg, 1975).

In the two-phase experiment on fine grained sandstone, a 40% of residual water saturation was evaluated. This calculation was based on the amount of initial water and the amount of water which was displaced by the flow of OMS. As seen in Table 4.3, this saturation is above the 33.3% level at which capillarity effect disappears.

Table 4.3. Calculation sheet of capillary cohesion and the level of drawdown at the onset of sanding for fine grain sandstone

S_w (%)	α (rad)	x_p (m)	r (m)	P_c (kPa)	C_c (kPa)	P_{dd} (kPa)
0.10	0.115	1.38E-05	7.98E-07	-35.42	3.44	27.47
0.50	0.2	2.38E-05	2.44E-06	-11.03	3.21	25.65
1.00	0.2565	3.04E-05	4.06E-06	-6.41	3.04	24.29
5.00	0.468	5.41E-05	1.45E-05	-1.52	2.28	18.23
10.00	0.613	6.9E-05	2.67E-05	-0.69	1.68	13.42
20.00	0.8088	8.68E-05	5.38E-05	-0.21	0.82	6.53
30.00	0.9544	9.79E-05	8.76E-05	-0.04	0.18	1.42
33.28	0.996	0.000101	0.000101	0.00	0.00	0.00

The same result is repeated for the coarse grained sample as seen in Table 4.4. In the calculations, a mean grain size of 0.31 mm was used which is based on the graph of Figure 1. The porosity of the sample in the beginning measured 39%. According to calculations, connate water content of the coarse grained sample was 50%. This was well above a saturation level of 33.3% at which capillarity disappears.

Table 4.4. Calculation sheet of capillary cohesion and the level of drawdown at the onset of sanding for coarse grained sandstone

S_w (%)	α (rad)	x_p (m)	r (m)	P_c (kPa)	C_c (kPa)	P_{dd} (kPa)
0.10	0.115	3.56E-05	2.06E-06	-13.71	1.64	13.07
0.50	0.2	6.16E-05	6.31E-06	-4.27	1.53	12.20
1.00	0.257	7.88E-05	1.05E-05	-2.47	1.45	11.55
5.00	0.468	0.00014	3.73E-05	-0.59	1.09	8.67
10.00	0.613	0.000178	6.9E-05	-0.27	0.80	6.39
20.00	0.8087	0.000224	0.000139	-0.08	0.39	3.11
33.28	0.996	0.00026	0.00026	0.00	0.00	0.00

Results and Discussions

Localization of Plasticity and Concentrated Sanding

In most of the experiments, sand production was concentrated at the top portion of the samples. This was mainly due to the fact that a small portion of axial loading is absorbed by friction in both the contacts of the sample and the gravel-packing, and also the latter and the hard shell chamber. Calibration was conducted to evaluate the magnitude of this

effect. The results indicated that the bottom portion of the sample contained an axial stress of 500 kPa less than that for the top section.

A possible reason is the localization of strain softening. The material around the borehole holds little radial stresses which enhances the likelihood of strain softening in that region. If strain softening initiates from a first weak zone, that zone will carry less stress. Load equilibrium, on the other hand, necessitates a redistribution of the stresses, and this process causes more stress to transfer in the neighbouring zones. This causes the weak zone and its neighbouring area to undergo more deformation and develop the zone of strain softening. This process is responsible for localization in a strain-softening material. This logic supplies enough reason as to why sanding occurred in only a limited region. As sanding continued, the strain localization induced more deformation of the adjacent zones and further strain softening. Localized strain softening, therefore, localized the sanding.

Effect of Capillarity

The effect of capillarity can be studied by comparing the graph of sanding in the experiment with two-phase flow and the corresponding graphs of the experiment with single-phase flow. For the coarse grained samples, both single- and two-phase flow experiments started producing sand at similar axial strain and stress levels. Figures 12, 14, and 15 can be used to compare the amount of sanding in single- and two-phase flow experiments. No alleviation in sanding volume resulted as a consequence of the two-phase condition. Therefore, the second phase in coarse grained samples produced little capillary cohesion and played no role in delaying sand production. This observation is in line with the calculations of capillarity effect as reflected in Table 4.4.

As for the fine grained samples, an alleviated amount of sanding was observed in the experiment with single-phase flow. However, the rate of sanding was still considerable.

According to the calculation sheet of capillarity effect of Table 4.3, the average connate water content of the experiment with two-phase flow is higher than the level at which capillarity effect vanishes. Therefore, it cannot be said that the alleviated amount of sanding was a result of capillarity or other effects in place. However, it is possible that the amount of residual water in the neighbourhood of the wellbore can be lower than the

rest of the sample. This is because in the vicinity of the wellbore, oil flow can more easily displace the residual water to the wellbore.

Tables 4.3 and 4.4 indicate that the critical drawdown pressure associated with the onset of sanding for fine and coarse grained samples at 5% of water saturation are 8.67 kPa and 18.2 kPa for coarse and fine grained samples, respectively. These are less than the minimum drawdown levels that were applied in the experiments, which was 20 kPa, in reference to Figures 8 through 10, 12, 14, and 15. Therefore, the applied drawdown was higher than the critical drawdown at such a low water saturation level. This minimizes the possible role of capillarity in the experiments.

Increasing Permeability Trend

All of the single- and two-phase experiments of both fine and coarse grained samples showed a trend of increasing permeability throughout the experiment. There are mainly two sources of this increase. They are, first, dilation of the material in the course of shear failure and, second, the removal of the material as a result of sand production. As sanding only removes the surface material, its effect on the increasing permeability is expected to be of minor importance, and the dilation plays the predominant role in the increasing trend of permeability.

Analysis of the Produced Sand

A comparison of the grain size distribution of the produced sand of the single-phase experiments on fine grained samples with that of the two-phase shows a slight increase in the size of particles produced from the two-phase experiment. In other words, the adhesion force of capillarity could bond some of the fine particles together.

Furthermore, the same comparison for coarse grained samples shows a slight increase in the size of small particles produced from the two-phase experiment. In the top portion, however, the same distribution results from both the single- and two-phase experiments. In other words, the adhesion force of the capillary cohesion in the coarse sand was not enough to combine larger particles together.

Conclusion

Sand production experiments were conducted on large-scale hollow cylinder samples which used weakly consolidated synthetic sandstone and single-as well as two-phase

flow. The central hole was an open hole and the samples used fine and coarse grain size distributions for the constituent grains. A formulation was proposed which could analytically predict the stability of the disaggregated grains in single-and two-phase fluid flow condition.

The predictions of the formulation were in line with the observations of the experiments. The experiments showed that the coarse-grained sample with two-phase pore fluid flow produced the same amount of sand as single-phase flow did. Additionally, a high saturation of connate water content in the fine grained samples highly declined the capillary cohesion.

The proposed formulation of capillarity and critical drawdown associated with sanding showed that capillarity faded quickly as connate water saturation increased. It also weakened as constituent grains of the medium got coarser. The predictions of the analytical analyses matched the observations of the experiments.

The presented formula helps the operators in quick estimation of operational limits in order to achieve safe production limits.

Nomenclature

C_c = capillary cohesion. (kPa)

C_r = real cohesion (kPa)

F_c = cohesion force (kN)

h = height of the pay zone (m)

Q = fluid flow rate (m^3/sec)

r = the radius of investigation (m)

r_e = external radius (m)

r_w = cavity radius (m)

R = average grain diameter (m)

S_w = water saturation

α = water volume angle (rad)

$\Delta P_{capillary}$ = capillary pressure (kPa)

φ = friction angle (degree)

ϕ = porosity

γ = surface tension between two fluids (N/m)

k = intrinsic permeability (m^2)

λ = a factor accounting for the effect of the non-uniform grain distribution on the rock strength

μ = viscosity of the fluid (kN/(m.sec))

σ_r = radial total stresses (kPa)

σ_θ = tangential total stresses (kPa)

σ_{UCS} =Unconfined Compressive Strength (kPa)

Acknowledgements

The authors would like to thank NSERC, and the Killam trustees for their financial support.

References

Bianco, L.C.B., and P.M. Halleck, "Mechanisms of Arch Instability and Sand Production in Two-Phase Saturated Poorly Consolidated Sandstones", *SPE 68932, SPE European Formation Damage Conference*, the Netherland, 2001.

Berg, R. R., "Capillary Pressures In Stratigraphic Traps", *Bull. Amer. Assoc. Petrol. Geol.*, **59**, no. 6, pp. 939-956, 1975.

Han, G., and M.B. Dusseault, "Quantitative Analysis of Mechanisms for Water-Related Sand Production", *SPE 73737, SPE Symposium and Exhibition on Formation Damage*, Lafayette, Louisiana, 2002.

Skjarstein, A., J. Tronvoll, F.J. Santarelli, and H. Joranson, "Effect of Water Breakthrough on Sand Production: Experimental and Field Evidences", *SPE 38806, SPE Annual Conference and Exhibition*, San Antonio, Texas, 1997.

Tronvol, J., M.B. Dusseault, F. Sanfilippo, and F.J. Santarelli, "The Tools Of Sand Management", *SPE 71673, SPE Annual Technical Conference and Exhibition*, New Orleans, Louisiana, 2001.

Vaziri, H., B. Barree, Y. Xiao, I. Palmer, and M. Kutas: "What Is the Magic of Water in Producing Sand?", *SPE 77683, SPE Annual Technical Conference and Exhibition*, San Antonio, Texas, 2002.

Chapter 5: Physical Modeling of Sand Production from a Supported Wellbore in Weakly Consolidated Sandstone

Publication Status: Submitted (Submission Date: Jul. 5, 2004), Geotechnical Testing Journal.

Abstract

Deployment of expandable technology for sand control is experiencing rapid growth. While several expandable systems have been developed, assessment of their long-term performance and effectiveness has not. To alleviate some concerns and uncertainties, criteria are provided in this paper for assessing the possibility of sanding in wellbores that employ expandable completions and to illustrate an in-depth understanding of the mechanism under which expandable screens may prevent sand grain mobilization.

To investigate these issues, a series of experiments were conducted using hollow cylinder synthetic sandstone samples involving both fine- and coarse-grained sands. A stiffener of two different opening sizes supported the central hole to check if sanding takes place and if so, how great the influence of the opening size relative to the grain size is in dictating the operational limits.

The experiments on weakly-consolidated sandstones showed that expandable completions were successful in preventing any shear failure around the wellbore. Under excessive drawdown/depletion, pore collapse proved to be a plausible failure mechanism in the material. Nevertheless, much less sanding occurred and this improvement was attributed to grain-to grain friction, enhancements of effective stresses at the wellface, and some degree of conservation of the original structure of the material.

Introduction

Several expandable techniques have been implemented by the oil industry (Van Buren et al., 1999; Metcalfe and Whitelaw, 1999; Hackworth et al., 2003; Echols et al., 2002; Cuthbertson et al., 2003), and their application is experiencing a rapid growth. These completion techniques are supposed to leave no gaps between the liner and the formation and, as such, avoid shear failure and disaggregation of the material around the wellbore. Although expandable completion techniques have been used in over 1000 wellbores (Gilmer and Emerson, 2004), few experimental research studies have been reported on

their interaction with the surrounding medium, in terms of their impact on productivity, and possible failure of the medium and its mechanism.

Since, no gaps should be left between the expandable structure and the wellface, radial effective stresses should build up in the medium around the well, which makes pore collapse a likely mechanism. Pore collapse has been investigated in the studies related to land subsidence (Lawrence et al., 1991; Hamilton and Shafer, 1991; Soares and Ferreira, 2002; Ditzhuijzen et al., 1984; Smits et al., 1986) and sand production (Nouri et al. 2003). However, its possible role in the medium around the wellbore supported by expandable completions remains unknown.

Another effect of supporting the wellbores by expandable completions is an unknown level of permeability and porosity reduction around the wellbore. A few authors studied permeability damage in the formation during its pressure depletion (Belhaj et al., 2002; Ruistuen et al., 1996; Schutjens et al., 2001). There is nothing reported on the effect of the liner-medium interaction in terms of permeability damage.

This paper bridges a gap in the literature on how a general reticulated expandable completion works. In these experiments, hollow-cylinder large-scale samples were used. A perforated stiffener (liner) in the central hole represented a general expandable completion including a network of small holes. The reason the name "stiffener" is given to the liner is to highlight the mechanical support it provides to the wellbore.

Objectives of the Experiments

The objective of this study is to conduct fundamental research on various aspects of the interaction between an expandable completion and a weakly consolidated medium. Among the main effects to take into account was the possible pore collapse of the medium during production. There was uncertainty regarding the possible effects of pore collapse on the severity of the damage to the rock. Moreover, it was not clear if the pore collapse could degrade the material to the level of the constituent grains supplying a source for sand production. Another objective was to investigate the level of the possible effect of an expandable completion on productivity of a wellbore.

Experiment Preparations

Getting sandstone samples from a field is usually expensive and difficult. Weakly-consolidated sandstones are especially difficult to core in the oil-wells and recover to the surface undisturbed. Moreover, in experimental studies, the use of consistent samples is preferable, increasing the likelihood that the results obtained would be reproducible in future or ongoing research. Samples recovered from quarries often do not have the required material properties (e.g. weakly consolidated), introducing difficulties in the interpretation of the results. Therefore, it was decided to fabricate synthetic sandstone samples that could closely represent the targeted formation sandstone.

Hollow Cylinder Sample Preparation

The synthetic samples were made for both material characterization and sand production experiments. For the sand production experiments, Hollow Cylinder Samples were cast. In each sample, a stiffener along the sample length supported the central hole. The stiffeners were perforated by a mesh of small holes. The stiffeners are intended to simulate expandable completion techniques representing a real downhole situation.

Material Composition

The synthetic sandstone samples were manufactured using silica sand, Portland cement binder, and water. The material composition for preparing the samples consisted of a cement/sand weight ratio of 0.11 and a water/cement weight ratio of 1.25.

Grain Size Distribution of the Sand Used in Sample Making

Two grain size distributions of the silica sand, namely coarse and fine grained ranged between 100 to 1000 μm and 30 to 300 μm, respectively as shown in Figure 5.1.

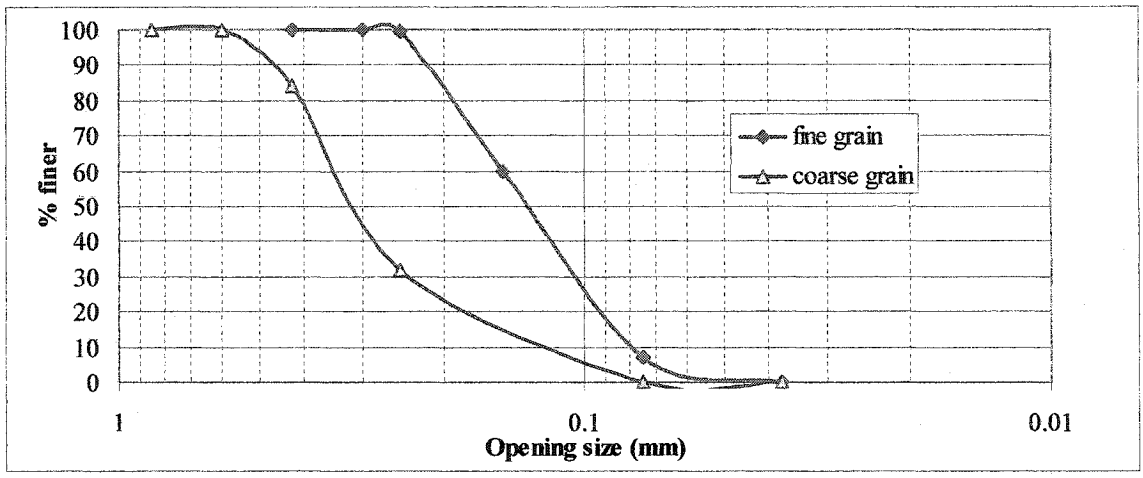

Figure 5.1. Two grain size distributions of the sand used in synthetic samples

Hollow Cylinder Sample Preparation

The Hollow Cylinder Samples (HCS) were prepared using the synthetic sandstone mixture described above. The sand, cement, and water were mixed into slurry, and then slightly pre-compacted when packed by a spatula into a mould and vibrated by gentle hits. To prevent the formation of distinct layers, the top of each layer was ploughed by the spatula. Casting was performed in an aluminium mould with a 125 mm inside diameter and a central rod which supported the stiffener in the centre. After each casting, the sample remained in the mould for 3 days. It was then removed from the mould and put in water for 18 days at ambient temperature. After this, the sample was put in an oven set to 50 oC. All of the samples were ground at both ends and epoxy was applied in order to make a stiff smooth cap at each end. The sample was kept dry in the oven before it was again saturated, before the start of each experiment.

Stringent quality control was implemented during the casting to obtain uniform material properties in each HCS as well as from one sample to another.

Sample Saturation

Samples were saturated in a container under vacuum pressure. Samples were either saturated by Odourless Mineral Spirits (OMS) or by water.

Experimental Set-Up

The test equipment included the loading unit, the flow set-up, sanding measurements unit and instrumentation. A picture of this set-up is shown in Figure 5.2.

This set-up has been designed in such a way that it resembles the real field conditions. It uses a hollow cylinder sample whose central hole simulates the wellbore, and the body of the sample replicates the reservoir. The sample is a scaled down version of the reservoir. As such, a smaller central hole needs a thinner body for the stresses to form a mature profile, similar to what forms in a full scale situation. The sample is restrained in the lateral boundary which creates a condition similar to what would be found in the field, where no lateral movement is allowed.

The axial loading is applied from the top of the sample. The outer radial pressure adjusts itself accordingly to the axial load, as the sample is confined laterally in a chamber similar to a consolidation assembly. The value of radial stresses depends on the material and the stress path.

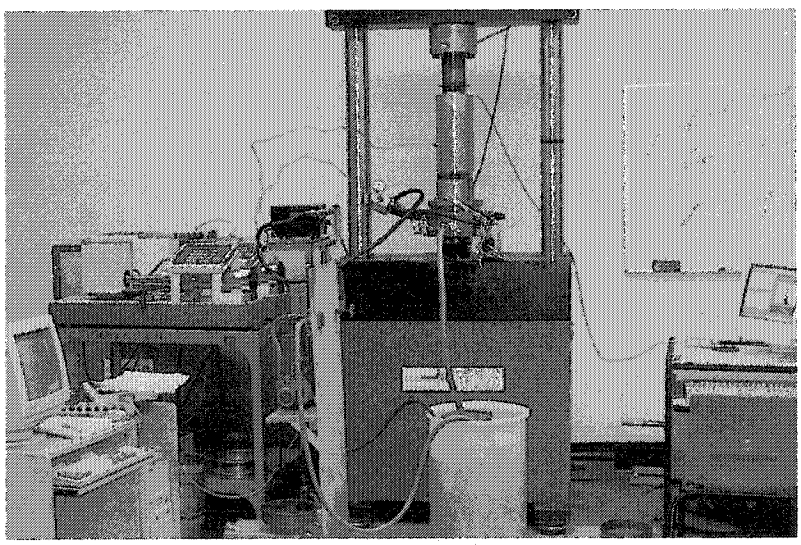

Figure 5.2. Photograph of the set-up used in sand production experiments

A schematic of the consolidation chamber is depicted in Figure 5.3. A steel hard shell of 12 mm in thickness restrains a hollow cylinder sample that is surrounded by a 7.5 mm thick gravel pack. A top platen slides inside the chamber and transfers the load from the top piston to the sample. The top platen is sealed by two rows of O-rings. The centre of the top platen is provided with a hole to the half thickness of the platen in order to

provide room to accommodate the stiffener. This prevents any possible direct transfer of the load from the platen to the stiffener.

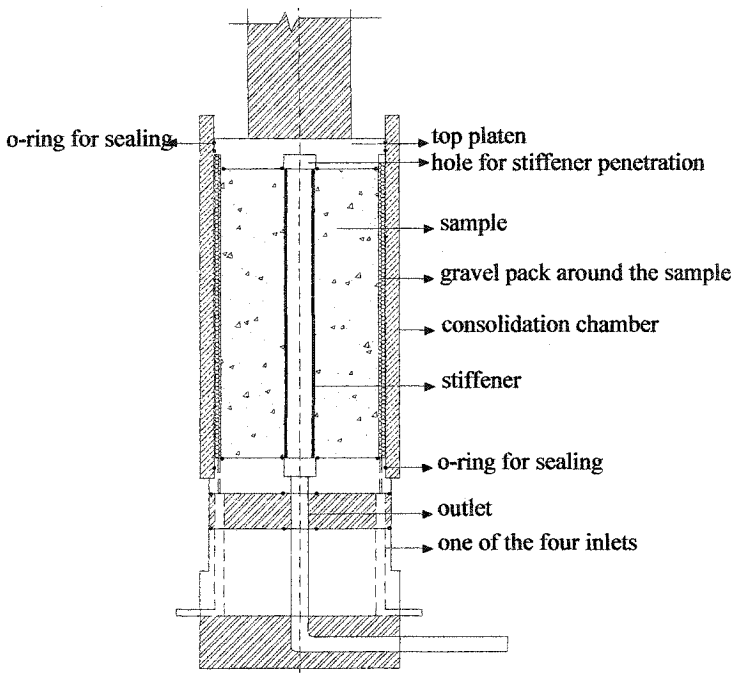

Figure 5.3. A schematic of configuration of the consolidation chamber

Loading Unit

The axial loading unit can apply up to 250 kN of force. It is designed with feedback control and continuous displays of axial load and platen displacement. Continuous corrections are applied to platen displacement by the servo-control system to correct for deflections of the frame and loading platens.

Flow Setup Unit

Figure 5.4 shows a schematic of the fluid flow unit. The flow system was set up to supply a radial inward flow. A positive displacement pump was used for supplying fluid flow during the test. A manifold was used to divide the flow from the pump to four vessels in the base plate of the cell. Fluid was injected through the four tubes to small holes in the circumference of a platen on which the sample sits.

The fluid was supplied to the pump from a tank with nearly 200 litre volume capacity. To generate radial flow, a highly permeable zone of gravel-pack was used around the

sample. This system diverted the axial flow in this permeable zone to radial in the sample.

The fluid and any produced sand were collected by the wellbore in the centre of the sample. The wellbore was connected to the outlet and was kept at atmospheric pressure during the test.

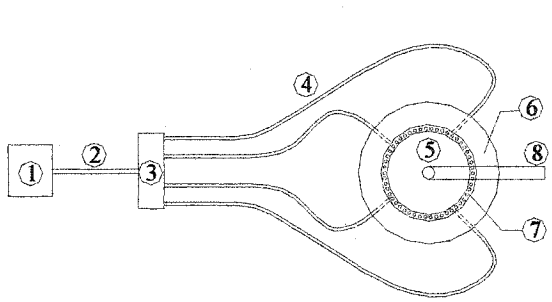

Figure 5.4. A schematic of configuration of the fluid flow vessels

Sand Measurements Unit

From the sieve analysis results, grains are distributed in the range of 0.0375-0.26 mm for fine grain distribution, and 0.07-0.6 mm for coarse grain distribution, as shown in Figure 5.1. Therefore, a sieve #400 (aperture size of 0.0375 mm) would suffice to entrap practically 100% of the produced material. The sieves sit on a tripod inside the tank. A pair of sieves was used and a digital balance weighed the produced sand.

By interchanging the sieve as often as required, the amount of the produced sand during consecutive time intervals could be measured. The produced sand was normally weighed at regular time intervals.

Instrumentation

Both axial load and displacements were measured by built-in load and displacement transducers on the loading frame. A dial gauge pressure measurement unit with a maximum pressure capacity of 690 kPa (100 psi), as well as a digital pressure transducer were connected to the manifold to precisely measure the fluid pressure in the box. Moreover, a pressure transducer was connected to the cylinder shell to directly measure the drawdown pressure.

Two flow-meters were connected to the tubing of fluid supply. The minimum and maximum measurable flow rates with this device were 3 and 250 cm3/second respectively.

Gravel-Pack between the Sample and the Chamber

The gravel was placed between the sample and the chamber in a 7.5 mm gap as shown in Figure 5.5. Two types of gravel, one coarse ranging between 2 to 6 mm, and another fine between 0.5 to 2.5 mm were used in the experiments. Grain size distributions of the two are shown in Figure 5.6.

The coarse gravel-pack was used in the first experiment on the coarse grained sample. Later the fine grained distribution was used in the second and third experiments on coarse grained and fine grained samples, respectively. The reason for this switch was to reduce the friction between the gravel-pack and the sample as well as between the gravel-pack and the chamber.

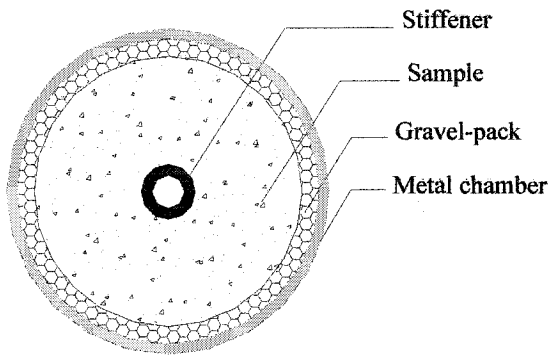

Figure 5.5. A cross section of the chamber containing the sample and the gravel-pack

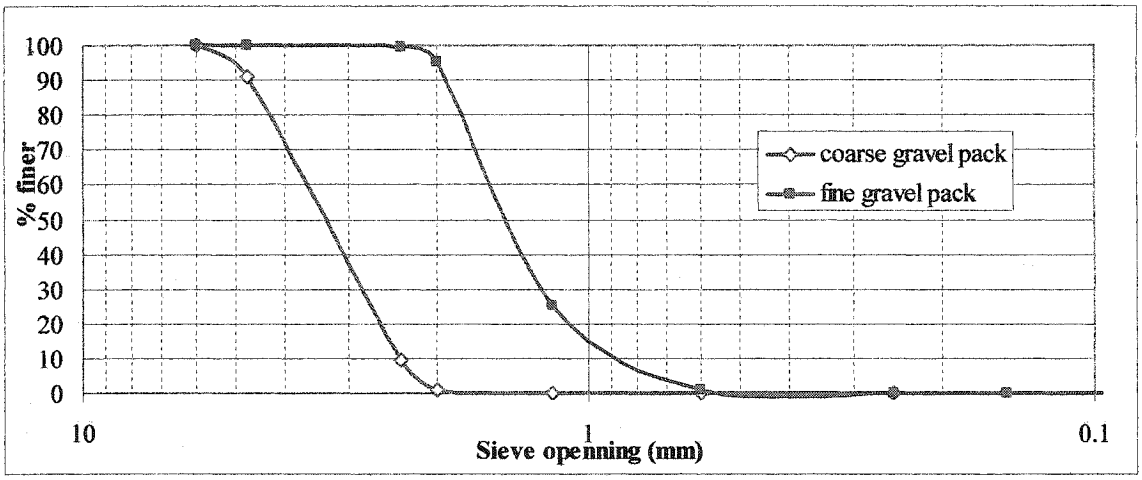

Figure 5.6. Grain size distribution of the coarse and fine gravel pack around the sample in the consolidation chamber

The Supporting Structure of the Wellbore (Stiffener)

The size of the perforations of the stiffener was designed such that if material was disaggregated by pore collapse, individual grains could pass through the perforations into the central hole. Two series of stiffeners used different patterns of perforations, as illustrated in Figure 5.7. They included perforations with diameters of 2.5mm (fine mesh) and 5mm (coarse mesh).

For the fine grain sand, an opening size of 5 mm indicates it is 42 times larger than the mean grain size ($42D_{50}$). This figure is 16 times ($16D_{50}$) for the coarse grain distribution.

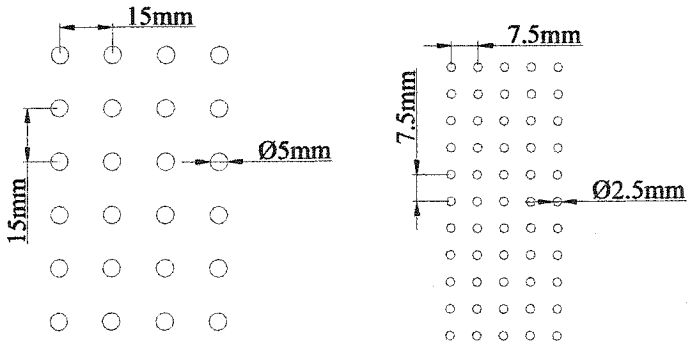

Figure 5.7. Coarse and fine perforation mesh on the stiffener

Material Characterization

Physical Properties

The physical properties of the artificial samples are listed in Table 5.1.

Table 5.1. Physical properties of the artificial sandstone

	D10/D50/D90 (Micron)	Dry Density (kg/m^3)	Saturated Density (kg/m^3)	Porosity	Initial Permeability (md)	Specific gravity
Coarse sand	120/300/500	1610	1980	36-40	3600	2.67
Fine sand	80/130/220	1645	2030	38-39	2600	2.67

A thin section was manufactured from a coarse-grained synthetic sandstone sample. The photomicrograph of this thin section is shown in Figure 5.8 under cross-polarized light. The grain shape is angular to sub-angular and the grain size distribution is confirmed as being well sorted.

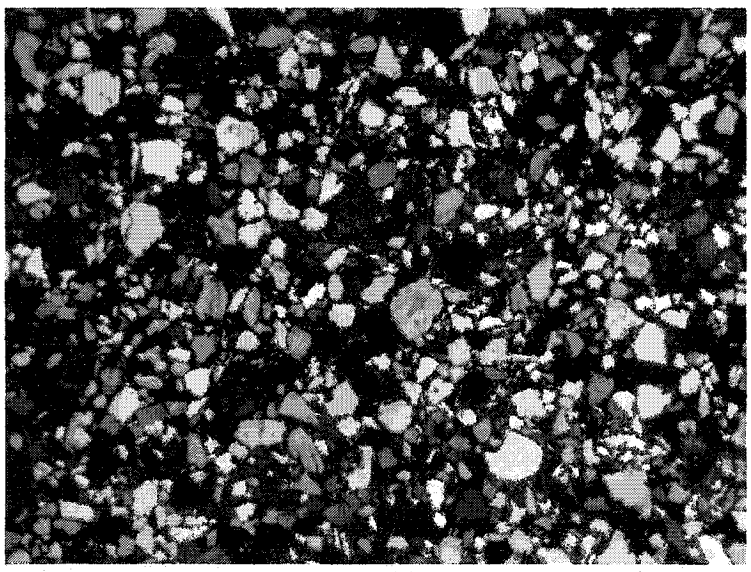

Figure 5.8. Microphotograph of a thin section under cross-polarized light; field of view is 11 mm

Mechanical Properties

Table 5.2 summarizes the mechanical properties of the synthetic sandstones including Mohr-Coulomb parameters.

Table 5.2. Mechanical properties of the artificial sandstone

	UCS (MPa)	Young's modulus E (MPa)	ν	C_p (kPa)	C_r (kPa)	φ (degrees)	φ_r (degrees)	Cap pressure (MPa)
Coarse grained	2.1	400	0.05	810	480	34	39	4
Fine grained	1.03	-	-	1230	425	26	38	-

The Testing Procedure

Three sand production experiments were conducted on hollow cylinder samples supported in the central hole by a stiffener. All the experiments were conducted under a single-phase fluid flow condition.

The first experiment was conducted on a coarse grain sample including a stiffener of fine mesh. In the second experiment, a coarse grain sample with a stiffener of coarse mesh was used. The third experiment repeated the second experiment on a fine grain sample.

Sample Placement

Each sample was laid on the bottom platen which contained the small circumferential holes. The cylindrical steel shell was slipped down a bottom platen, and an O-ring sealed the gap between the platen and the shell. Gravel grains were packed in the circumferential gap between the sample and the hard shell and filled to the rim. The top platen was then slipped down and laid on top of the sample. The top platen was also sealed with two rows of O-rings as shown in Figure 5.3.

Test Conduct

During simulated production, axial stress was increased gradually. Subsequently, drawdown was applied to the fluid flow. The produced sand, if any, was collected and regularly weighed. The pressure of the central hole was kept atmospheric at all times.

In the first experiment, the bottom of the stiffener sat on the bottom platen. Therefore, it was expected that a gradual transfer of the axial loading to the stiffener took place. As a result, even though the top portion of the sample carried the full load, it carried less and less load as its bottom was approached. This was rectified in the subsequent experiments. In the second experiment, the stiffener did not touch the bottom platen. The bottom

platen was modified to provide room for a relative displacement of the stiffener as much as 25 mm. This design is illustrated in Figure 5.9.

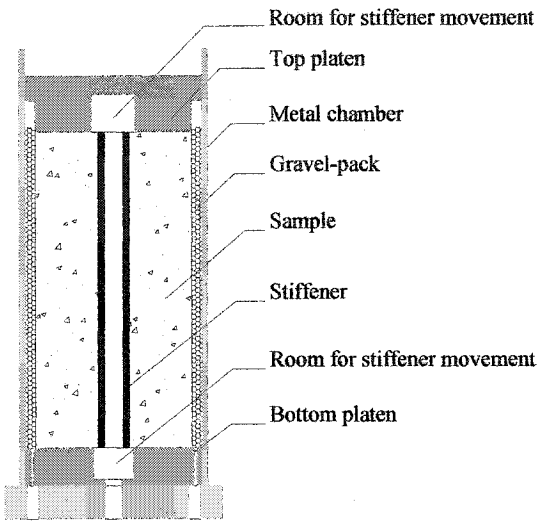

Figure 5.9. The central cavities provided in the bottom and top platen to accommodate relative movement of the sample and the stiffener

Observations of the Experiments

The observation of the experiments on coarse grained sample-fine mesh and coarse grained sample-coarse mesh, and fine grain sample-coarse mesh are elaborated upon in the subsequent paragraphs.

Experiment #1 - Observations of the Experiment on Coarse Grained Samples with Fine Mesh Stiffeners

OMS was used for both the initial saturation, as well as for flow establishment in the sample of this experiment. To prevent the direct transfer of the axial load to the stiffener upon relative deformation of the sample and the stiffener, a space of 30 mm in diameter and 25 mm deep was used in the centre of the top platen. In this experiment the stiffener sat on the bottom platen.

The presence of the stiffener caused radial stresses to build up around the wellbore which enhanced mean effective stresses in that region. It is believed that a gradual pore collapse rather than an abrupt one took place as a result of the stress gradients along the sample.

The pore collapse started from the top portion where the whole load was transferred to the sample and gradually developed downward.

As shown in Figure 5.10, axial load was applied and gradually increased where no lateral deformation was allowed at the side boundaries of the sample. A concavity of the curve in the beginning of the experiment led to stiffer behaviour at an axial stress level of nearly 1000 kPa. The axial loading continued to an axial stress of nearly 15 MPa where the slope was drastically changed. This change can be attributed to full separation of the sample from the stiffener which transfers most of the axial loading to the sample. As Figure 5.10 indicates, no sand was produced which signifies a 100% success to the application of the stiffener in eliminating sand production in this experiment.

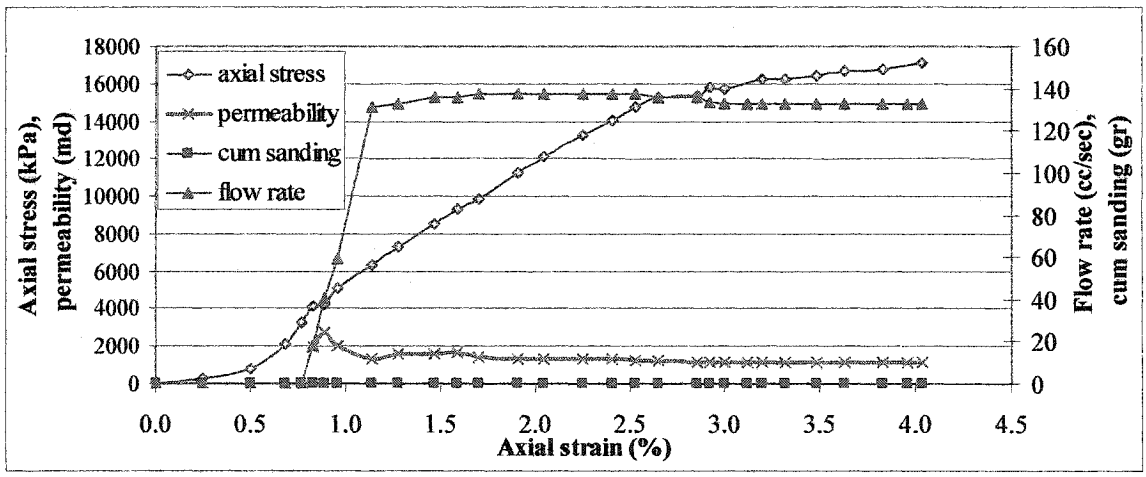

Figure 5.10. Axial loading vs. axial deformation

Figure 5.11 shows a graph including the curves of flow rate and drawdown as well as the overall permeability. This graph shows a gradual decrease in permeability, which is a result of compaction of the sample as mean effective stresses increase. Permeability ranges across a broad spectrum, including values of several orders of magnitude. Therefore the scale of the permeability damage as observed in Figure 5.11 is not very significant. The slight decline of permeability can be compensated for by adjusting the drawdown.

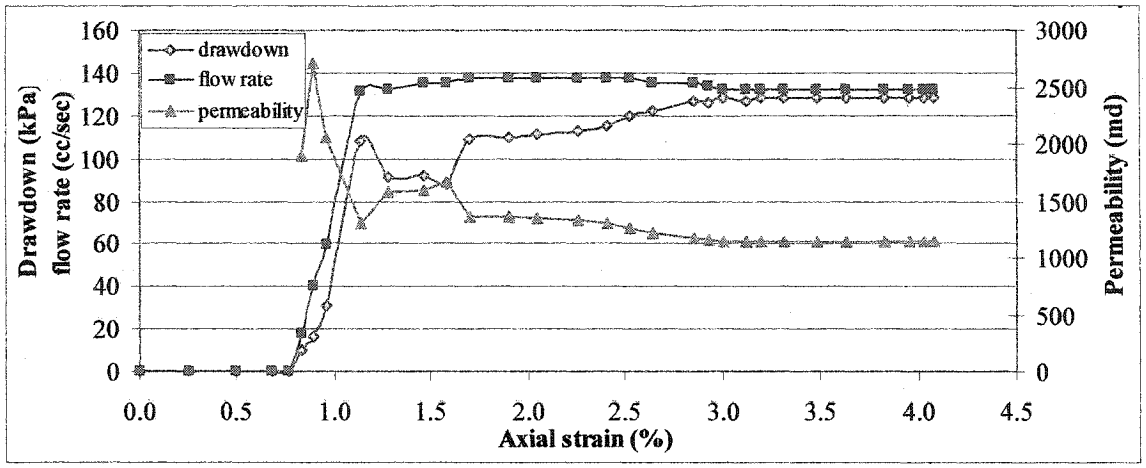

Figure 5.11. Flow rate and drawdown vs. axial deformation

Experiment #2: Observations of the Experiment on Coarse Grained Samples with Coarse Mesh Stiffeners

The experiment began with a gradual increase in axial stress as shown in Figure 5.12. Fluid flow was started at an axial stress of 1500 kPa and was gradually increased. Axial stress was increased to a final level of 18 MPa. Beyond this state, abrupt deformations of the sample induced sudden decreases in axial stress. At this stage, the experiment was terminated.

Figure 5.12 shows that even though the sample shortened as much as 10% (25 mm) and the axial stress increased to more than 18 MPa, little sand was produced (as low as 10 g throughout the experiment), although the aperture size of stiffener was 6 and 16 times larger than the maximum and mean grain sizes, respectively.

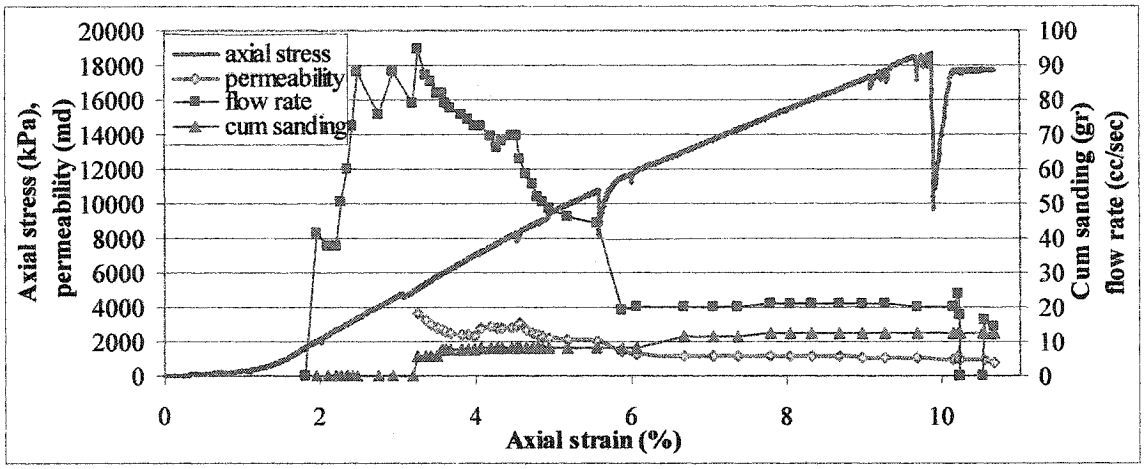

Figure 5.12. Axial stress, flow rate and cumulative sanding versus axial deformation

Figure 5.13 indicates a general trend of decline for permeability throughout the experiment. This can be attributed to the restraint of the sample from lateral deformation. The restraint is enforced by the gravel pack surrounding the sample, and by the stiffener in the centre of the sample. This condition resulted in a gradual increase in mean effective stresses in the sample as axial stress increases. As the sample undergoes gradual compaction, permeability declines accordingly.

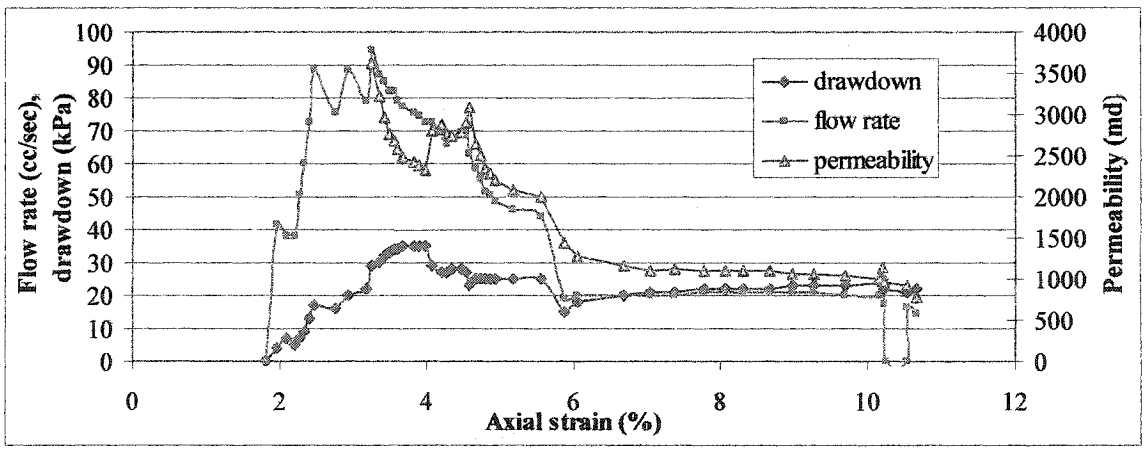

Figure 5.13. Flow rate, drawdown and permeability vs. axial deformation

Figure 5.14 shows a picture of the sample after the test. The sample underwent a compaction of as much as nearly 25 mm relative to the stiffener. Table 5.3 indicates that the mean effective stress met the failure cap at less than 4 MPa meaning the sample

underwent pore collapse. When pore collapse occurs, the grain cementing is broken and sand grains contact each other resulting in volume shrinkage. Nevertheless, Figure 5.14 shows that the sample was still intact after the experiment was complete. Furthermore, as Figure 5.12 indicates, little sand was produced from a rock at the state of pore collapse. This indicates that any sanding criterion in the presence of an expandable completion should be set irrespective of the considerations of pore collapse. It is only if the arch effect is not sufficient as a result of large aperture size and high flow rates that sand may be produced in the presence of the stiffener.

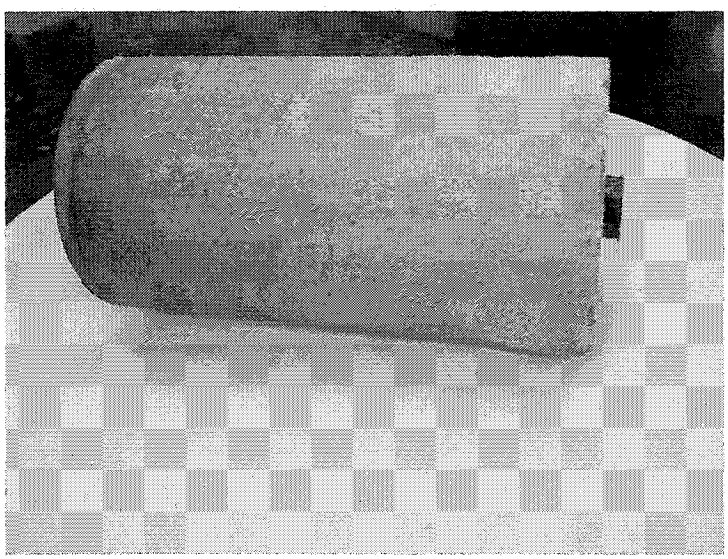

Figure 5.14. A picture of the sample after the test and its relative deformation with respect to the stiffener

Experiment #3: Observations of the Experiment on Fine Grained Samples with Coarse Mesh Stiffeners

A fine grained sample was used in this experiment, where the aperture size of the holes in the stiffener was 5 mm. Therefore, the opening size was $42D_{50}$ and 20 times the maximum grain size.

As seen in Figure 5.15, the experiment started with a gradual increase in axial stress. Later, fluid flow was started and quickly increased to a steady rate of nearly 110 cc/sec. A small but steady rate of sand production started and continued to the end of the experiment. Therefore, the stiffener with such drastic differences of grain and aperture

sizes of the holes was not able to completely eliminate the sanding issue; however, it was successful in substantially reducing the sanding rate.

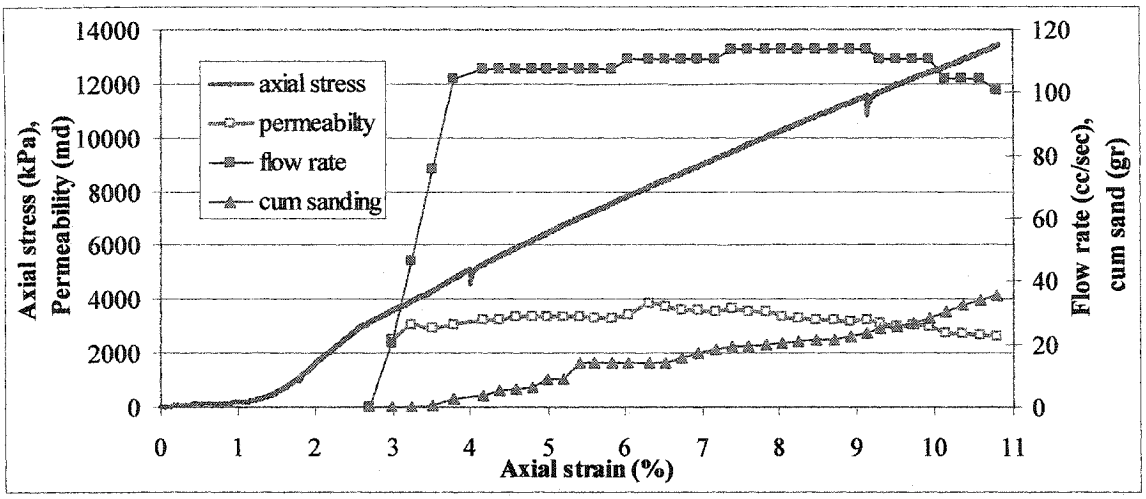

Figure 5.15. Axial stress, flow rate and cumulative sanding versus axial deformation

Figure 5.16 indicates a slighter declining trend for permeability for this experiment in comparison to the previous ones. The decreasing permeability is again related to the compaction associated with the rise of effective mean stresses in the sample. As in this experiment, the relative difference of the sizes of the fine grain sand and the aperture size of the stiffener was drastic; some cavity growth and dilation associated with pockets of shear failure at the openings enhanced the permeability. Therefore, the permeability curve of Figure 5.16 reflected a combination of compaction in the body of the sample as loading increased, dilation of the material at the cavity faces as they underwent shear failure, and cavity growth as sand was produced.

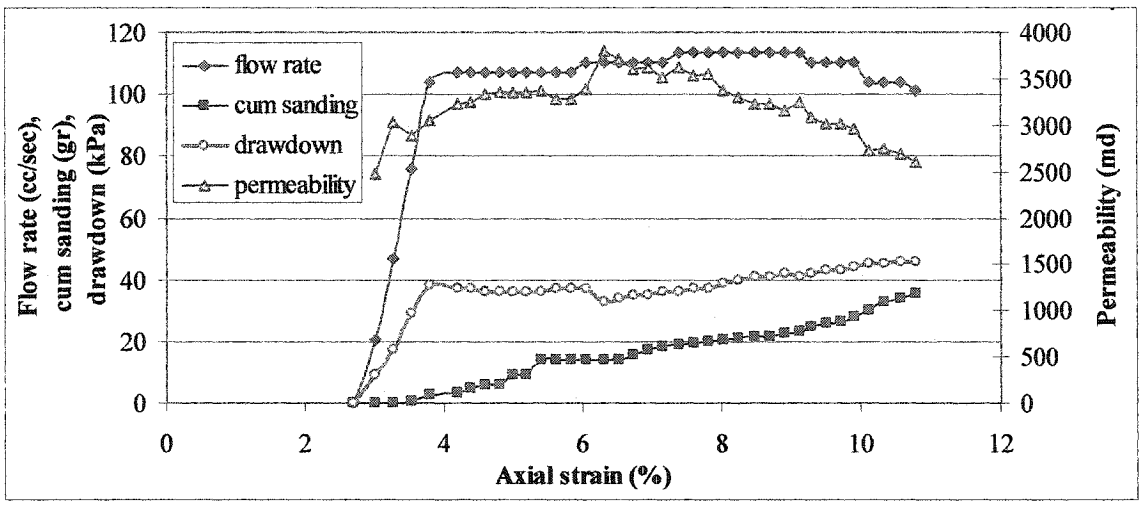

Figure 5.16. Flow rate, drawdown and permeability vs. axial deformation

Figure 5.17 shows a picture of the sample after the test. A relative deformation of the sample with respect to the central stiffener was the indicator of sample compression. Such high compaction took place in the aftermath of pore collapse. Nevertheless, the sample retained its integrity and was not reduced to its constituent grains. Confirming the previous observations of the experiment using coarse grained samples, pore collapse should not be considered as the disaggregator of the solid material and the direct inducer of sand production.

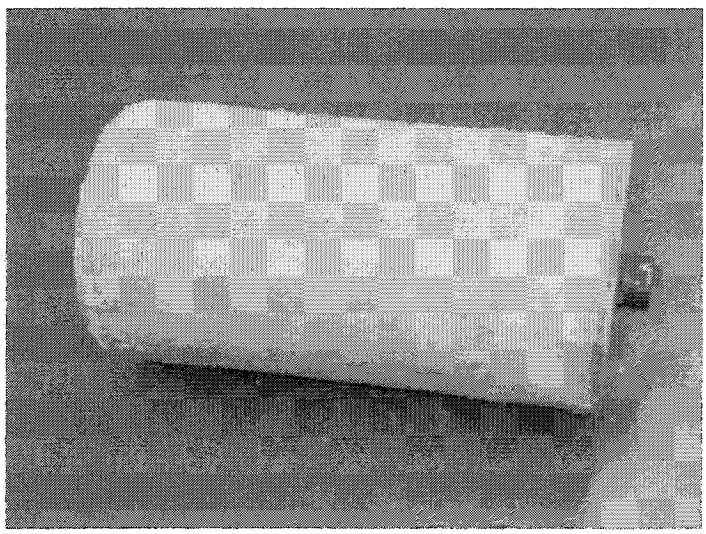

Figure 5.17. A picture of the fine grained sample after the test and its relative deformation with respect to the stiffener

Results and Discussions

General Observations

Table 5.3 summarizes the sand production experiments of fine and coarse grained samples with fine and coarse mesh sizes. In summary, an opening size of nearly 10 times the mean grain size did not produce any sand. Increasing this ratio to nearly 20 induced only traces of sanding. A 40-times ratio induced a small rate of sand production. In the two cases with stiffeners of coarse mesh, however, the sanding was transient and upon the formation of stable arches and under the same loading conditions, sanding ceased. Therefore for a single-phase flow condition which is far more critical than a two-phase, the installation of the stiffener greatly alleviated the sanding problem.

Table 5.3. A summary of the grain size distribution and the perforation sizes

Experiment	D_{max} (mm)	D_{min} (mm)	D_{50} (mm)	Aperture D (mm)	D/D_{max}	D/D_{50}	Comments
No.1 (coarse)	0.60	0.07	0.31	2.5	4.2	8	No sanding
No.2 (coarse)	0.60	0.07	0.31	5	8.4	16	Traces of sanding
No.3 (fine)	0.26	0.0375	0.12	5	20	42	Small rate of sanding

Effect of Pore Collapse

In the sand production experiments, mean effective stresses exceeded the cap pressure (less than 4 MPa). Therefore, the samples underwent pore collapse in the initial stages of the loading. However, only a small volume of sand, if any at all, was produced.

When pore collapse occurs, the grain cements break and sand grains contact each other, resulting in volume shrinkage. This shrinkage increases the interlock of the grains with one another. Although the sample has volumetrically failed, the structure of the material is preserved. In addition, high effective stresses build up in the sample adjacent to the stiffener because it is restrained from lateral movement. As a result of friction mobilization, the individual grains cannot move easily. This inter-granular frictional resistance is boosted by the increased level of interlock of the grains by compaction.

In conclusion, sanding criterion in the presence of any expandable completion should be set irrespective of the pore collapse. Little sand may be produced from a rock in a state of pore collapse.

Is Shear Failure Possible?

The major achievement of the stiffener is its elimination of shear failure in the vicinity of the wellbore. In any unsupported wellbore, shear failure is the main failure mechanism, and it is provoked by sharp contrasts between normal stresses and the two other components of the principal stresses. Effective normal stresses build up at the supported well face, and their magnitude is directly related to the liner's stiffness. As normal stresses build up, the possibility of shear failure is lessened. If the opening size is too large, local shear failure may occur in the material at the opening location. Therefore, small amounts of sanding may be produced before stable arches develop.

The Effect of Arch Formation in Cavity Stability

Arching is another stability mechanism. Sand production develops small cavities at the openings, which stabilizes the material in the vicinity of the cavity by changing the pattern of the load transfer to compressional. The compressional stresses between the grains mobilize frictional resistance between them which adds to their stability. Any increased level of drawdown or depletion of the reservoir may produce a small amount of sand, and thereby, induce a limited growth to the arch size.

The Possible Effect of the Stiffener on Productivity

There is a general observation of declining permeability and porosity during the rise of drawdown and depletion. Any increase in mean effective stresses leads to compaction of the material, and in return decreases its porosity and permeability.

Conclusion

Sand production experiments were conducted on large-scale hollow cylinder samples which were made of weakly consolidated synthetic sandstones. The central hole of all of the samples was supported by a stiffener (a metal liner that in these experiments represented a general reticulated expandable completion technique), which contained a mesh of small holes. Two types of samples were used in the experiments; one of them used fine-grained and the other coarse-grained sand. Two patterns of meshes were deployed for the stiffeners one of them used fine and the other a coarse network of small holes. Single-phase flow was established in all of the experiments.

Based on experimental results, this paper evaluated the various aspects of the interaction between a supported wellbore and a weakly consolidated medium.

The stiffener proved that it was capable of eliminating shear failure in the material around the well. Shear failure has been reported to be the main culprit in almost all sanding issues.

One possible consequence of using a stiffener to support a wellbore is pore collapse of the medium during production. There was an unknown influence of this mode of failure on the severity of the damage to the rock. The experiments showed that a sample in the state of pore collapse retains its structure. In addition, the interlock between the grains is enhanced as the material compacts. This addressed the initial uncertainty as to whether the pore collapse could degrade the material to its constituent grains which could supply the material for sand production. The experiments showed that the material in the state of pore collapse produced little sand.

The experiments also examined the possible local shear and tensile failure of the material behind the apertures. The general observation was that the stiffeners highly alleviated the amount of the produced sand. The magnitude of sanding, if any at all, depended on the aperture size. If the opening size was too large, local shear failure might occur in the material at the opening location. Therefore, a limited amount of sanding might be produced prior to the development of stable arches. In the experiments, an aperture size of 4.2 and 8 times the maximum and mean grain size, respectively, produced no sand at all, even in excessive effective stress conditions. An aperture size of 8.4 and 16 times of maximum and mean grain sizes produced traces of sand, and an aperture size of 20 and 42 times the maximum and mean grain sizes produced a small rate of sanding. This shows the remarkable ability of the stiffener in hampering the sanding rate.

Evaluating the level of possible effects of a supported wellbore on productivity was another objective of the paper. As expected, while the sample compacted, its porosity and permeability decreased. However, supporting a wellbore provides greater operational limits which can compensate the loss of permeability.

Nomenclature

C_p = plastic projected cohesion (kPa)

C_r = plastic real cohesion (kPa)

DD= drawdown (kPa)

E=Young's modulus (kPa)

UCS= unconfined compressive strength (kPa)

ϕ = porosity of the geomaterial

φ = friction angle associated with the high stress portion of the bilinear envelope (degree)

φ_r = friction angle associated with the low stress portion of the bilinear envelope (degree)

ν = Poison's ratio

Acknowledgements

The authors would like to thank NSERC, and the Killam trustees for their financial support.

References:

Belhaj, H.A., A. Nouri, H.H. Vaziri, S.D. Butt, and M.R. Islam: "Experimental Determination of the Effect of Pore Collapse on Permeability and Porosity of Sandstone Reservoirs," *proc., PAPG-SPE Annual Technical Conference*, Karachi, Pakistan, 2-4 November 2002.

Cuthbertson, R.L., A. Green, J.A. Dewar, and B.D. Truelove, "Completion of an Underbalanced Well Using Expandable Sand Screen for Sand Control", *SPE/IADC 79792, SPE/IADC Drilling Conference*, Amsterdam, the Netherlands, 2003.

Ditzhuijzen P.J.D., and J.A. Waal, "Reservoir Compaction and Surface Subsidence in the Central Luconia Gas bearing Carbonates, Offshore Sarwak, East Malaysia", *SPE 12400, SPE 5th Offshore South East Asia Conference*, Singapore, 1984.

Echols, R., J. Gano, P. Shy, C. Tuckness, H. Zhang, and D. Campo, "Development and Testing of an Expandable Sand Screen and Expansion Tool", *SPE 73750, SPE International Symposium and Exhibition on Formation Damage Contro*l, Lafayette, Louisiana, 2002.

Gilmer, M., B. Emerson, "World's First Completion Set Inside Expandable Screen", *IADC/SPE 87201, IADC/SPE Drilling Conference*, Dallas, TX, 2004.

Hackworth, M., C. Johnson, J. Heiland, J. McClukin, D. Eubank, M. Kemp. L.M. Schetky, and P.S. Smith, "Development and First Aplicaion of Bistable Expandable Sand Screen", *SPE 84265, SPE Annual Conference and Exhibition*, Denver, Colorado, 2003.

Hamilton, J.M., and J.L. Shafer, "Measurement of Pore Compressibility Characteristics in Rock Exhibiting Pore Collapse and Volumetric Creep", *SCA Conference*, Paper Number 9124, 1991.

Lawrence W.T., D.W. Rhett, and H.E. Farrell, "Effect of Reservoir Depletion and Pore Pressure Drawdown on *In situ* Stress and Deformation in the Ekofisk Field, North Sea", *Rock Mechanics and Multidisiplinary Science*, Balkema, Rotterdom, 1991.

Metcalfe, P., and C. Whitelaw, "The Development of the First Expandable Sand Screen", *SPE 11032, Offshore Technology Conference*, Houston, TX, 1999.

Nouri, A., H. Vaziri, H. Belhaj, and R. Islam, "Effect of Volumetric Failure on Sand Production in Oil-Wellbores", *SPE 80448, SPE Asia Pacific Oil and Gas Conference and Exhibition,* Jakarta, Indonesia, 2003.

Ruistuen, H., L.W. Teufel, and D. Rhett, "Influence Of Reservoir Stress Path on Deformation and Permeability of Weakly Cemented Sandstone Reservoir", *SPE 36535, SPE Annual Technical Conference and Exhibition*, Denver, Colorado,1996.

Schutjens, P.M.T.M., T.H. Hanssen,, M.H.H. Hettema, J. Merour, J.Ph. de Bree, J.W.A. Coremans, and G. Helliesen, "Completion-Induced Porosity/Permeability Reduction in Sandstone Reservoirs. Data and Model for Elasticity-Dominated Deformation", *SPE 71337, SPE Annual Technical Conference and Exhibition,* New Orleans, Louisiana, 2001.

Smits R.M.M., A. Waal, and J.F.C. Kooten, "Prediction of Abrupt Reservoir Compaction and Surface Subsidence Due to Pore Collapse in Carbonates", *SPE 15642, 61th Annual SPE Conference*, New Orleans, LA, 1986.

Soares A.C., and F.H. Ferreira, "An Experimental Study for Mechanical Formation Damage", *SPE 73734, SPE International Symposium and Exhibition on Formation Damage Control*, Lafayette, Louisiana, 2002.

Van Buren, M., L. van den Broek, and C. Whitelaw, "Trial of an Expandable Sand Screen to Replace Internal Gravel Packing", *SPE/IADC 57565, SPE/IADC Middle East Drilling Technology Conference*, Abu Dhabi, UAE, 1999.

Chapter 6: Physical and Analytical Studies of Sand Production from a Supported Wellbore in Unconsolidated Sand Media with Single- and Two-Phase Flow

Publication Status: Submitted (Submission Date: Jul. 6, 2004), Journal of Canadian Petroleum Technology.

Abstract

Use of expandable technology for sand control has rapidly grown in recent years. While several expandable systems have been developed, assessment of their long-term performance and effectiveness has hitherto not been objectively completed. To address some of the concerns and uncertainties on this front, this paper provides criteria for assessing whether sanding has the possibility to occur in the wellbores that are completed by expandable completion techniques. It also provides an in-depth understanding of the mechanism under which expandable screens control mobilization of sand grains. By the same token, it reviews the possibility of sand production in wellbores completed by this technique.

A series of experiments were conducted using hollow cylinder fine and coarse grained unconsolidated samples to investigate the issues involved. A stiffener supported the central hole which is representative of a general expandable completion technique containing a network of small perforations. This was to verify whether sanding can take place when the wellbore is supported by the stiffener and if so, what influence the opening size relative to the grain size has in dictating the operational limits. Experiments were conducted on both single- and two-phase flow media. This was to explore the possible effect of a second phase in sand production in the presence of the stiffener.

Experiments on unconsolidated sandstones showed that the friction between the grains mobilized by high normal stresses at grain to grain contacts plays a major role in preventing sand production. The aperture size of the liner is another important factor in providing the possibility of grain mobilization. The experiments confirm that even with a large aperture size of an order of magnitude greater than the maximum grain size, sanding did not take place under routine operational conditions in a two-phase medium. On the contrary, instant sanding from the sand-pack in single-phase experiments took place which emphasized the important role of capillarity.

Introduction

Several expandable techniques have been implemented by the oil industry (Van Buren et al., 1999; Metcalfe and Whitelaw, 1999; Hackworth et al. 2003; Echols et al. 2002; Cuthbertson et al., 2003), and their application is experiencing a rapid growth. Although expandable completion techniques have been used in over 1000 wellbores (Gilmer and Emerson, 2004), few experimental research studies have been reported on their interaction with the medium around them. This paper bridges a gap in the literature on several important issues surrounding the supported wellbores.

This research used unconsolidated sandstone in a comprehensive experimental program. The importance of studying the response of unconsolidated and weakly consolidated sandstones to an expandable completion technique is realized by indications of some estimation that show approximately seventy percent of the total world's oil and gas reserves are found in poorly consolidated reservoirs (Bianco and Halleck, 2001).

This paper presents an insight into hollow cylindrical experimental implementation of an expandable completion and uses both single-and two-phase fluid flow. Field observations have indicated strong ties between sand production and water influx (Skjarstein et al., 1997; Tronvol et al., 2001; Vaziri el al, 2002; Han and Dusseault, 2002; Bianco and Halleck, 2001). A formulation is suggested for a sound and simple evaluation of the stability of unconsolidated media in single- and two-phase flow conditions. The validity of the formulation is examined by the experimental observations.

Hollow cylinder large-scale samples made of non-cemented sandstone were used in the experiments. A perforated stiffener (liner) in the central hole represented a general reticulated expandable completion. The reason the name "stiffener" is given to the liner is to emphasize the mechanical support it provides to the wellbore. Two different grain size distributions were deployed in the experimental program, one representing fine-grained and another coarse-grained media.

Relevance of the Experiments

When it comes to sand production, general non-cementation provides the worst condition in any reservoir. There may be two different sources of non-cementation. First, it is

found in absolutely unconsolidated sandstones (the level of consolidation is defined based on the degree of cementation). Secondly, material failure under excessive loading conditions may degrade a rock type material to soil type.

No disaggregation related to shear failure can possibly occur in supported wells since the chance of a general shear failure is eliminated in the presence of the stiffener. pore collapse is a possible failure mechanism around a supported wellbore. When pore collapse occurs, the grain cement bonds break and sand grains contact each other resulting in volume shrinkage.

Experimental Set-Up

Testing equipment included the loading unit, the flow set-up unit, sanding measurements unit and instrumentation. A picture of this set-up is shown in Figure 6.1.

The sample is confined in a chamber very similar to a consolidation assembly. This set-up creates a similar condition to reality where no lateral movement is allowed. The outer radial pressure is accordingly adjusted to the axial load, and its value depends on the material and the stress path.

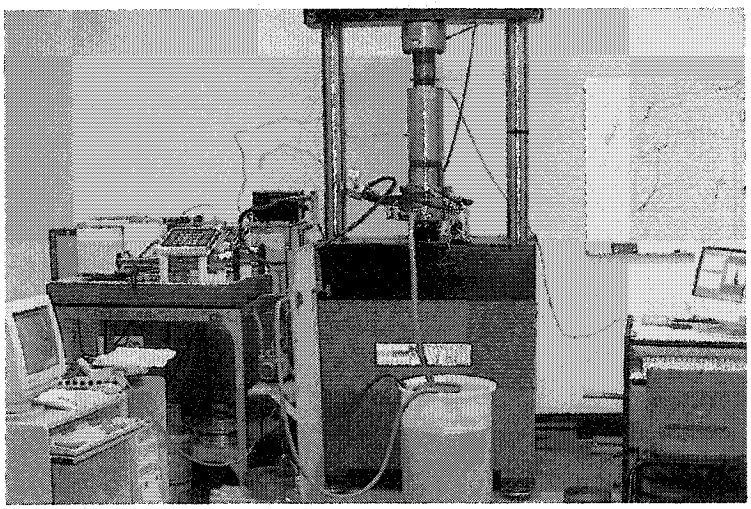

Figure 6.1. Photograph of the set-up used in sand production experiments

A schematic of the consolidation chamber is depicted in Figure 6.2. A steel hard shell of 12 mm in thickness restrains a hollow cylinder sample that is surrounded by a 7.5 mm thick gravel pack. A top platen slides inside the chamber and transfers the load from the

top piston to the sample. The top platen is sealed by two rows of O-rings. The centre of the top platen is provided with a hole to its half thickness in order to provide room for the stiffener to be accommodated. This prevents any direct transfer of the load from the platen to the stiffener.

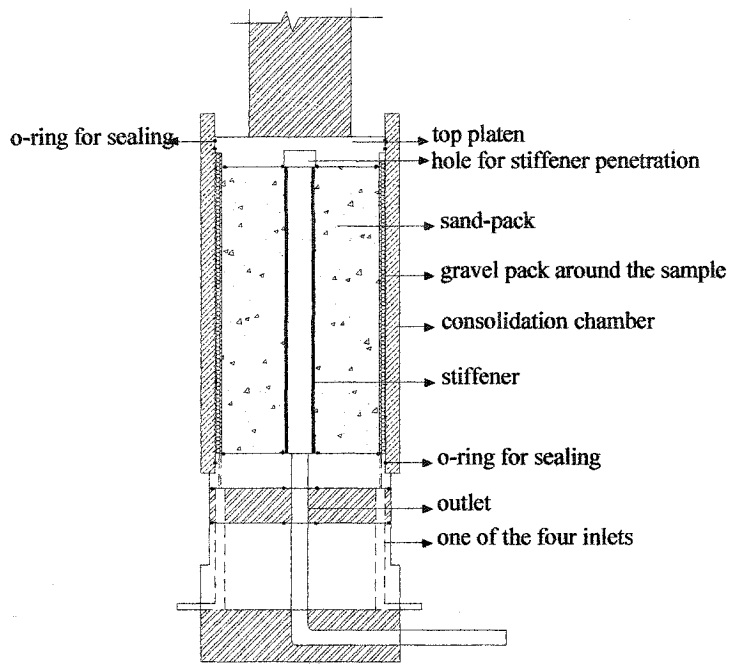

Figure 6.2. A schematic of configuration of the consolidation chamber

Loading Unit

The axial loading unit can apply up to 250 kN of force. It is designed with feedback control and continuous displays of axial load and platen displacement, and an IEEE computer interface with built in stepping motor.

Flow Setup Unit

Figure 6.3 shows a schematic of the fluid flow unit. The flow system was set up to supply a radial inward flow. A positive displacement pump was used for supplying fluid flow during the test. A manifold was used to distribute the flow from the pump to four vessels in the base plate of the cell. Fluid was injected through the four tubes to small holes in the circumference of the bottom platen, and from there to the permeable zone which surrounds the sample.

The fluid was supplied to the pump from a tank with an approximately 200 litre volume capacity. To generate a radial flow, a highly permeable zone of gravel-pack was deployed around the sample. This system diverted the flow in axial direction within the permeable zone to radial flow in the sample.

The fluid and any produced sand were collected by the wellbore in the centre of the sample. The wellbore was connected to the outlet and was kept at atmospheric pressure during the test.

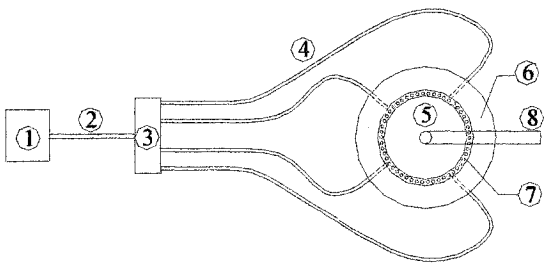

1- Positive pump
2- Main tubing between the pump and the division box
3- Manifold
4- One of the four tubings between the division box and the base
5- Bottom platten on which the sample sits
6- Base of the set-up
7- Small holes connected to the four vessles by a round channel
8- Flow outlet

Figure 6.3. A schematic of configuration of the fluid flow vessels

Sand Measurements Unit

From the sieve analysis results, grains are distributed in the range of 0.0375-0.26 mm for fine grain distribution, and 0.070-0.60 mm for coarse grain distribution as shown in Figure 6.4. Therefore, a sieve #400 would suffice to entrap practically 100% of the produced material. The sieves sit on a tripod inside the tank. A pair of sieves was used and a digital balance was used to weigh the produced sand.

By interchanging the sieve as often as required, the amount of the produced sand during consecutive time intervals could be measured. The produced sand was weighed at regular time intervals.

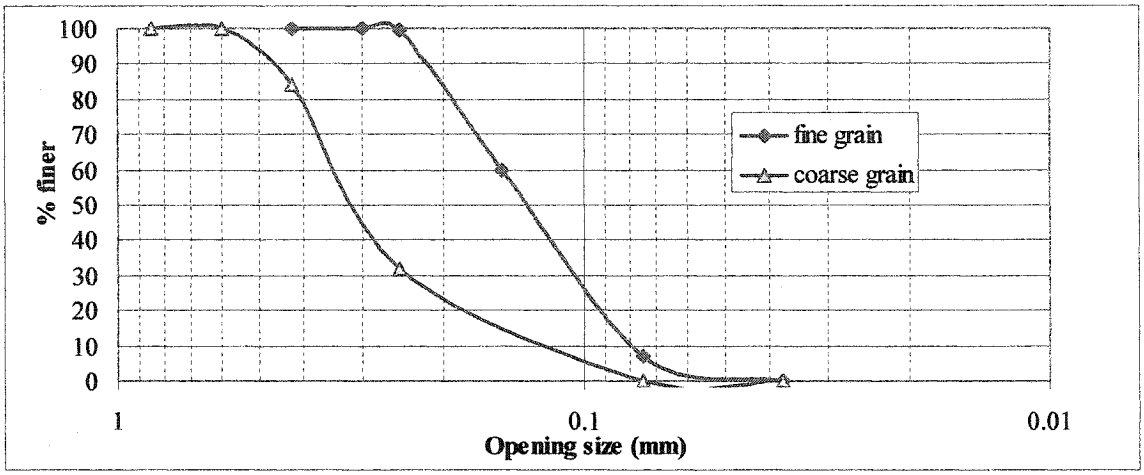

Figure 6.4. Grain size distributions of the fine and coarse sand used in sand-pack samples

Instrumentation

Both axial load and displacements were measured by built-in transducers of the loading frame. A dial gauge pressure measurement unit with a maximum pressure capacity of 688 kPa (100 psi), as well as a digital pressure transducer, were connected to the manifold to precisely measure the fluid pressure in the box. Moreover, a pressure transducer was connected to the cylinder shell to directly measure the fluid pressure around the sample.

Two flow-meters were connected to the tubing of fluid supply. The minimum and maximum measurable flow rates with these devices were 3 and 250 cm^3/seconds respectively.

Gravel-Pack between the Sample and the Chamber

Gravel was placed between the sample and the chamber in a 7.5 mm gap as shown in Figure 6.5. The gravel pack created a highly permeable zone around the sample. Grain size distribution of the gravel is shown in Figure 6.6.

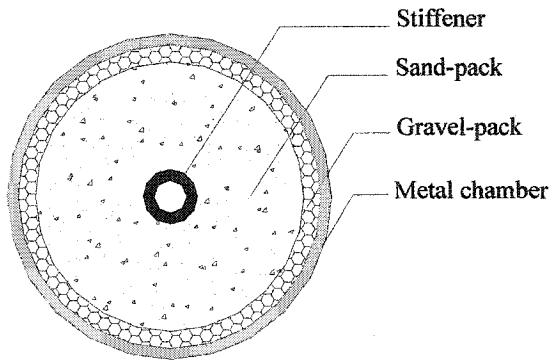

Figure 6.5. A cross section of the chamber containing the sample and the gravel-pack

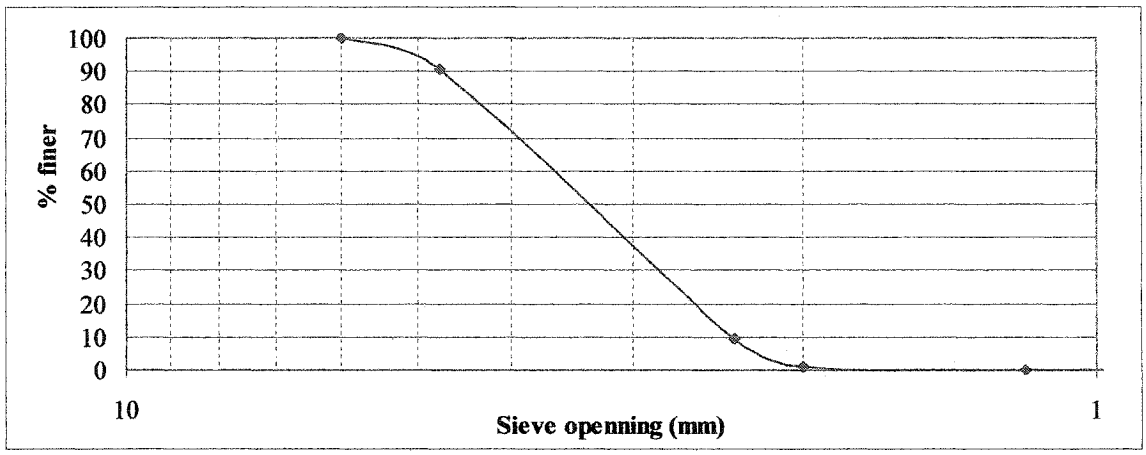

Figure 6.6. Grain size distribution of the gravel pack placed around the sample

The Supporting Liner (Stiffener) Structure

Table 6.1 compares the aperture size of the stiffener with some indicative grain sizes of the sand. 2.5 mm of diameter was used for the perforations of the stiffener whose pattern is shown in Figure 6.7. The aperture size was designed to be several times larger than the maximum size of the grain. This was to ensure that individual grains could pass through into the central hole. The perforations were at 45° of angular phasing. In the axial direction, they were 7.5 mm centre to centre apart.

Table 6.1. A summary of the grain size distribution and the perforation sizes

Experiment	D_{max} (mm)	D_{min} (mm)	D_{50} (mm)	Opening size D (mm)	D/D_{max}	D/D_{50}	Comments
Coarse grain	0.60	0.07	0.31	2.5	4.2	8	No sanding
Fine grain	0.26	0.0375	0.12	2.5	10	21	Small rate of sanding

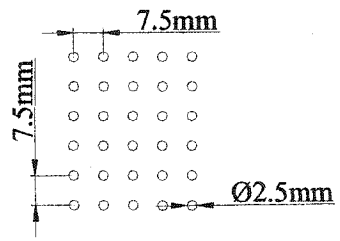

Figure 6.7. Coarse and fine perforation mesh on the stiffener

Sample Preparation

Sand-pack samples were sized 125 mm in diameter and 250 mm in height. The central hole of the samples was supported by a perforated stiffener along the sample height. They intended to simulate a general reticulated expandable completion technique in a real downhole situation.

Grain Size Distribution of the Sand-Pack

Two different grain size distributions, namely coarse and fine grain, were used to prepare the sand-packs. The grain size of coarse and fine sand ranged between 0.07 to 0.6 mm and 0.0375 to 0.26 mm respectively. Their grain size distribution is depicted in Figure 6.4.

Sample Making Procedure

The following routine was used in preparing the samples:

- A thin sheet of plastic sliding frame was used to separate the sand from the surrounding gravel pack. The sand and gravel packs were deposited simultaneously as shown in Figure 6.8.
- Gravel grains were placed between the sliding frame and the chamber. Sand with a moisture content of 0.03 was placed inside the sliding frame in thin lifts (about 5cm). The stiffener was placed in the centre. The central hole of the stiffener was plugged to prevent sand grains from being poured in.
- As shown in Figure 6.8, the stiffener was secured by a bushing fit into the central hole of the bottom platen. To keep the stiffener straight, it was fixed at a second point by a plate that was used to apply axial loading to compact each lift.
- The thin sliding frame was pulled out and the lift was then vertically compacted under 5150 kPa (750 psi) of axial loading. The load was applied to a platen on

the top of the lift which covered the area of both sand and gravel as shown in Figure 6.8.

- To ensure the homogeneity of the sample, the interfaces were roughened to guarantee a good connection between the layers.
- The compaction and subsequent deposition of the remaining lifts took place.
- A disk of sample size with a central hole of stiffener diameter was used at the top of the sample to ensure that no sand could escape from the top during the testing.

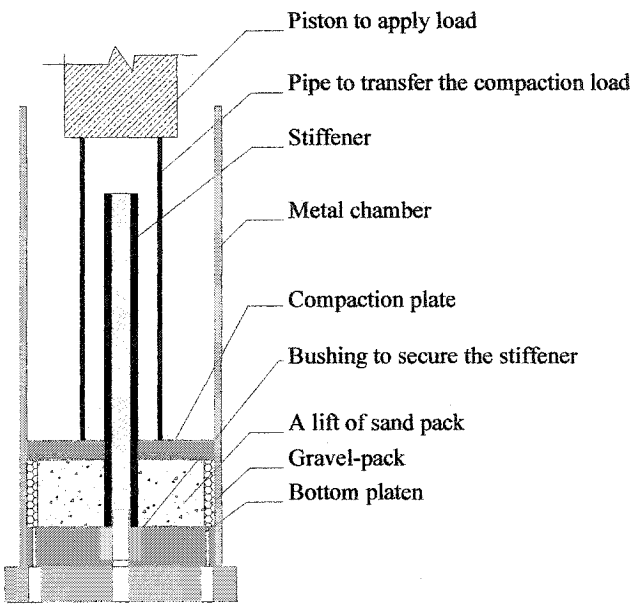

Figure 6.8. A cross section of the chamber with a lift of sand pack and the compaction device

Physical Properties

The physical properties of the unconsolidated sandstone samples used in the experiments are shown in Table 6.2.

Table 6.2. Physical properties of the coarse and fine sand-pack

	D10/D50/D90 (Micron)	Dry Density (kg/m^3)	Saturated Density (kg/m^3)	Initial porosity	Permeability (Da)	Specific gravity
Coarse sand	120/300/500	1397	1528.2	47.7-50.0	30	2.67
Fine sand	80/130/220	1340	1850	50.5	2.1-4.5	2.67

Sand Production Experiments

Table 6.3 summarizes the test plan. Four two-phase and three single-phase experiments were performed. Two of the two-phase experiments were conducted on coarse grained sand packs and the remaining two were performed on fine grained sand-packs. Water-cut was induced in one of the two-phase experiments on each fine and coarse grained sand-pack. In all of the two-phase experiments, the samples were compacted water-wet and later Odourless Mineral Spirits (OMS) were flown through them.

In the second series, three single-phase experiments were conducted on fine grained sand-packs. In two of the experiments, water was used for both saturation and seepage. To examine the possible effect of chemical reactions of water and sand in the results, the experiment on fine grained single-phase sample was repeated by using OMS for both compaction and seepage.

Table 6.3. Test plan on sand-pack samples

	Two-phase		Single-phase	
	Without water-cut	With water-cut	Water saturated	OMS saturated
Coarse grain	1	1	0	0
Fine grain	1	1	2	1

Testing Chronology

The following procedure was used in the experiments.

- The axial loading was increased gradually on the sample under no lateral deformation. The axial loading reached a peak of 10330 kPa (1500 psi) and was then kept constant for the rest of the testing.
- The stresses were allowed to equilibrate for a few hours.
- The flow system was set up to supply radial inward flow through the four tubes in the base, which connected to several small holes underneath the gravel pack. The radial flow was increased gradually while the wellbore was kept at atmospheric pressure during the test.
- Any produced sand was collected on a sieve and regularly weighed throughout the test.

Experiment on a Coarse Grained Sand-Pack, Two-Phase Flow without Water-Cut

Figure 6.9 provides a general picture of the loading sequence and the sample reaction. The initial bell shape curve is a result of the initial closure of the gaps between the sample and platens. The axial stress continues to rise and after the axial stress hits the peak, it is kept constant for the rest of the test. Initially, some small deformations take place in the sample under the constant loading and after a few hours any more deformations would be infinitesimal. At this stage OMS flow is started and gradually increased. As shown in Figure 6.9, at low flow rates, little deformation in the sample was registered. Moreover, only traces of sand were produced.

As the flow rate increased to about 75 cc/sec, the deformation rate increased, and accelerated as the flow rate approached 100 cc/sec. At a flow rate of 95 cc/sec, a small sand burst occurred which is simultaneous to a rather quick deformation and slight temporary decrease of axial loading. This may be associated with the possible collapse of the small cavities that were formed behind the openings of the stiffener in the wake of the increased flow rate.

At a flow rate of nearly 125 cc/sec, a massive sanding took place and, consequently, the sample showed an abrupt deformation. At the same time, axial stress levels sharply dropped reacting to the quick deformation of the sample. The pump was at this stage stopped and the stress level was allowed to rebound to the level prior to the massive sanding. Subsequently, the pump was again started and the flow rate was again gradually increased to 100 cc/sec. The reason for conducting this stage was to find out if the material could be stabilized in the wake of massive sand production. At this phase, in agreement with the initial stage of sand production, an increased sanding rate was registered. This indicates upon clean-up of the wellbore, oil production can be resumed to an operational limit close to the previous record before any massive sanding occurred, provided all other conditions remained the same.

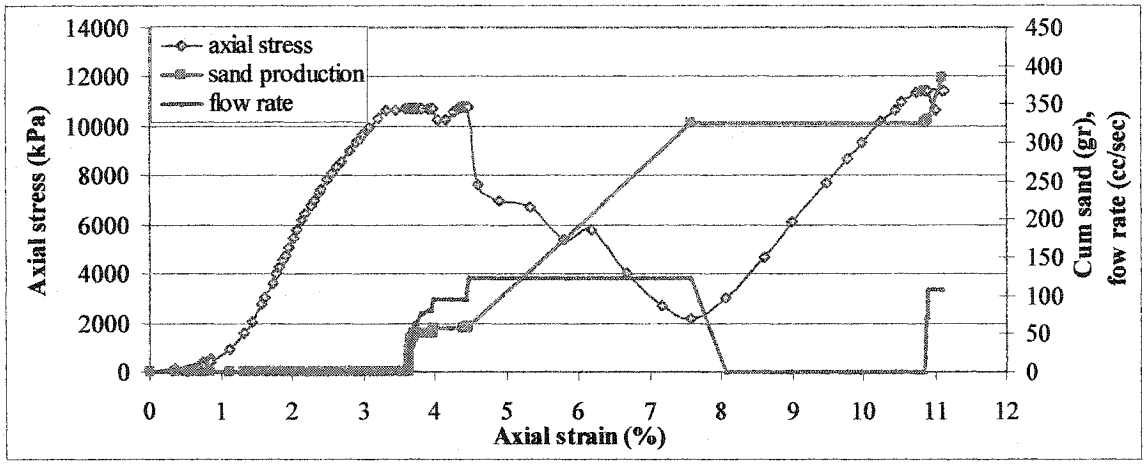

Figure 6.9. Axial stress, cumulative sanding and flow rate vs. axial deformation

Figure 6.10 shows the curves of cumulative sand production, axial strain and flow rate versus time after the 24th hour when the flow was started. According to this graph, traces of sand were detected at relatively low flow rates. At this stage, the small sand production indicated that arches were growing as flow rate was increasing. This enlargement decreased the pressure gradient and created stable arches. Radial effective stresses induced by the stiffener mobilized the friction between the grains. This, in combination with the arching effect and capillarity, was considered to be responsible for cavity stability.

As fluid flow increases, a more or less step-like sanding pattern is observed. At the same time, very small deformations were recorded. Finally, a considerable sanding rate and sample deformation led to a massive sanding associated with large deformations, which indicated a collapse of cavities.

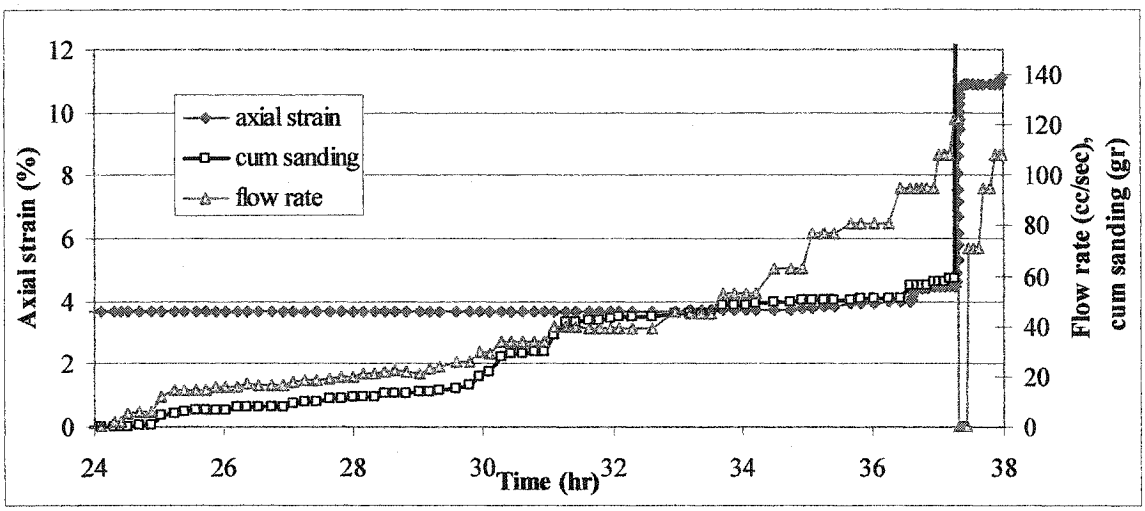

Figure 6.10. Deformation, cumulative sanding and flow rate vs. time

Experiment on Coarse Grained Sand-Packs, Two-Phase Flow with Water-Cut

To prove the repeatability of the results of the previous experiment and, moreover, to study the response of the coarse grained sand-packs to water-cut, another experiment was conducted. Figures 6.11 and 6.12 illustrate the results of this test.

According to Figure 6.11, no change in axial deformation was registered at flow rates up to approximately 120 cc/sec. However, this range of flow rates induced small amount of sand production. Sand production without axial deformation can be explained by the development of stable arches during the production of small amounts of sands. It was only at flow rates above 120 cc/sec that arches collapsed and sanding rate showed a significant boost. This brought about extensive axial deformation of the sample. The flow rate of 120 cc/sec associated with massive sanding agrees with the outcome of the previous experiment.

After the massive sanding, the flow rate was reduced to zero and the sample was allowed to equilibrate under the applied axial loading. At the next stage, a water-cut was induced. At a very small flow rate, massive sanding occurred and the sample showed an extensive deformation. This observation showed the importance of capillarity in arch stability in non-cemented material.

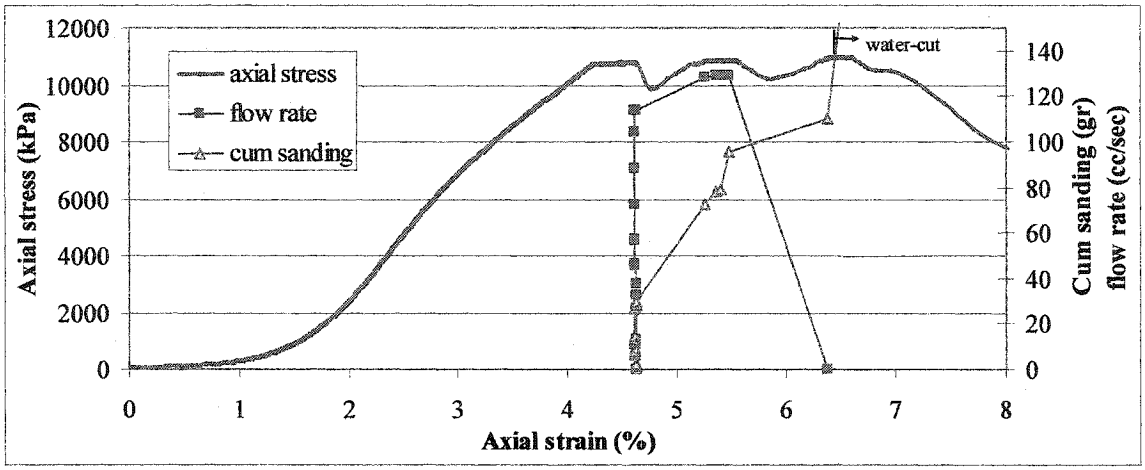

Figure 6.11. Axial stress, cumulative sanding and flow rate vs. axial deformation

To better illustrate the response of the sample to the loading and fluid flow, Figure 6.12 shows the curves of sanding, flow rate, and axial deformation versus time from start of the test. Only that part of the test after the fluid flow establishment is shown in this figure, which shows that at small flow rates, small rates of sanding were recorded and the sample experienced little deformation. Massive sanding and accordingly step-like deformations took place at a flow rate of 120 cc/sec and, moreover, at the water-cut which was induced at the end of the testing.

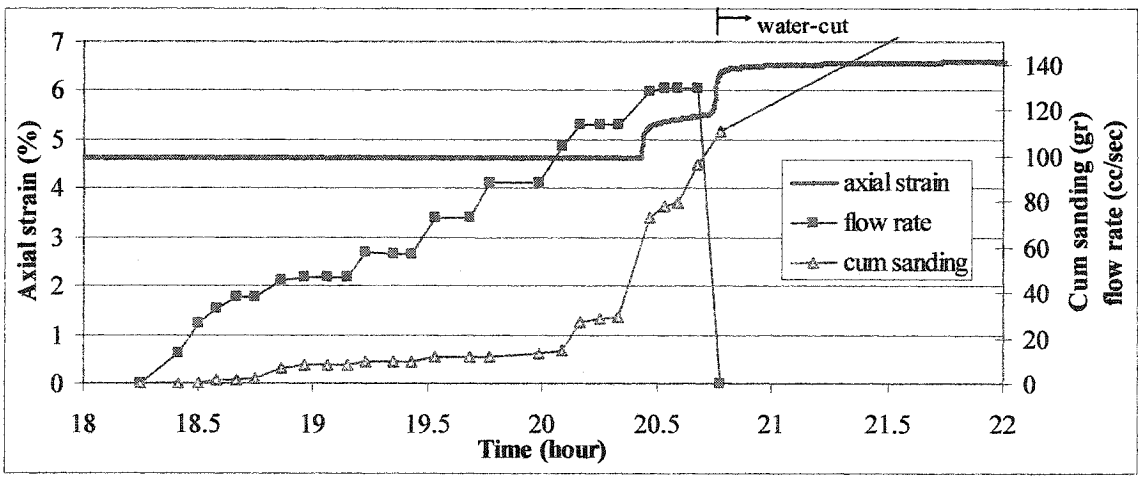

Figure 6.12. Deformation, cumulative sanding and flow rate vs. time

Experiment on Fine Grained Sand-Packs with Two-Phase Flow, without Water-Cut

The experimental procedure was similar to the one on coarse grained samples, as shown in Figure 6.13. Initially, axial stress was increased gradually to 10350 kPa (1500 psi) in 2 hours. The sample was left under constant loading for another 10 hours. Subsequently, fluid flow was established and the flow rate was gradually increased. At the time that fluid flow was increasing, axial loading remained constant. Massive sanding took place when fluid flow reached a critical limit and, subsequently, it was reduced to zero. Fluid flow was later re-established beginning with small rates and gradually increasing.

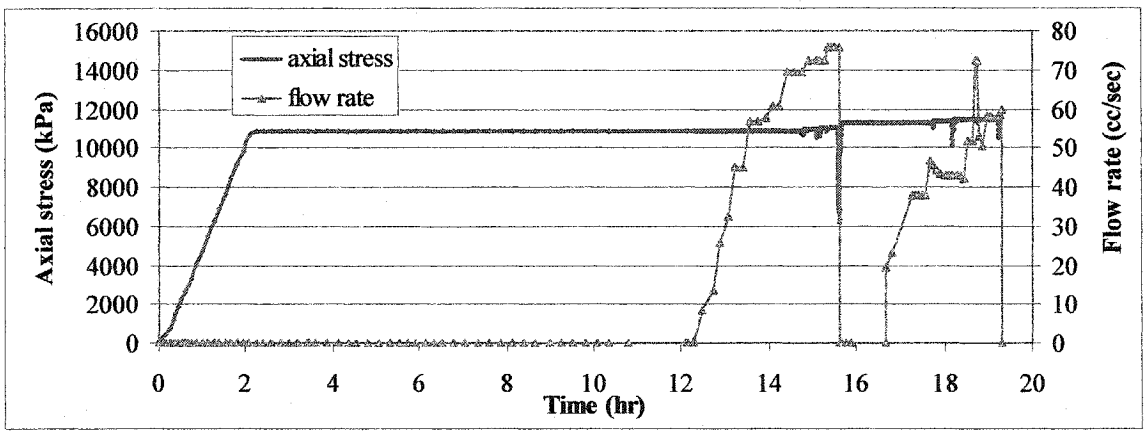

Figure 6.13. Operation conditions of the test on fine grained sand-pack

As depicted in Figure 6.14, a division is observed in the axial stress-deformation curve at an axial stress of 5200 kPa, which reflects the precompaction pressure of the same level.

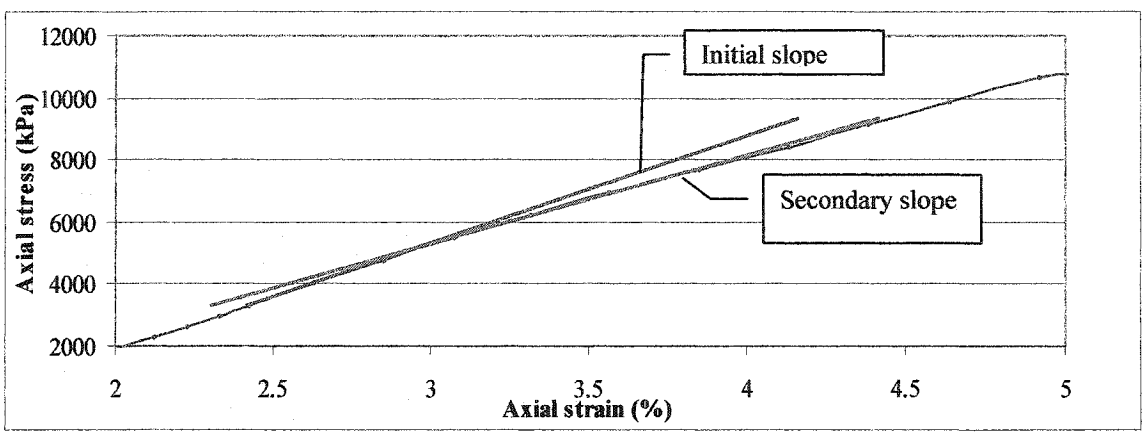

Figure 6.14. Pre-compaction level of the sand-pack

Figure 6.15 shows a step-like pattern in the sand production curve, which infers development and stabilization of small cavities after each sanding. Upon the increase in flow rate, more sanding may take place, causing gradual enlargement of cavities. A flow rate of 75 cc/sec was a critical limit associated with arch instability. Figure 6.15 indicates, a massive sanding leading to a rapid decline in axial loading and an extensive deformation followed a few smaller sand bursts. Subsequently, the pump was shut off and the axial stress was allowed to rebound to initial level.

Figure 6.15 indicates an increase in the permeability of the sample at small rates of sand production. As the sanding rate increases, permeability starts a declining trend. The decline of permeability steps up at the onset of an extensive deformation causing massive sand production. The more massive the sanding and deformation, the greater the decline in permeability. After each stabilization post massive sanding, permeability resumes another enhancing trend.

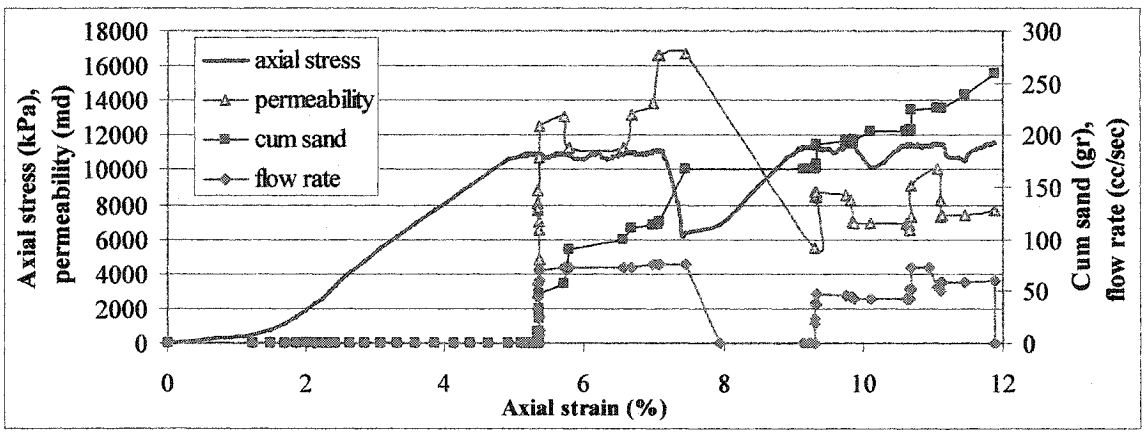

Figure 6.15. Test results of the experiment on fine grained sand-packs with two-phase flow, without water-cut

Figure 6.16 depicts the response of sand production to fluid flow rate and its correspondence to axial deformation. This graph shows no sanding up to a flow rate of nearly 30 cc/sec. In a range of flow rate between 30 cc/sec to 60 cc/sec, only traces of sanding were produced which was associated with very small axial deformation. Above this flow rate, the sanding rate increased and with that the cavities grew. The cavities grew to a size that could not maintain their stability, and were collapsed periodically. Each collapse of the cavities corresponded with a quick settlement in the sample and a

temporary reduction in axial stress as shown in Figure 6.15. At a flow rate of about 75 cc/sec, a massive continuous sanding took place.

After the fluid flow was re-established, sanding occurred at a flow rate of nearly 50 cc/sec and massive sanding took place at a flow rate of 75 cc/sec in agreement with the previous observations.

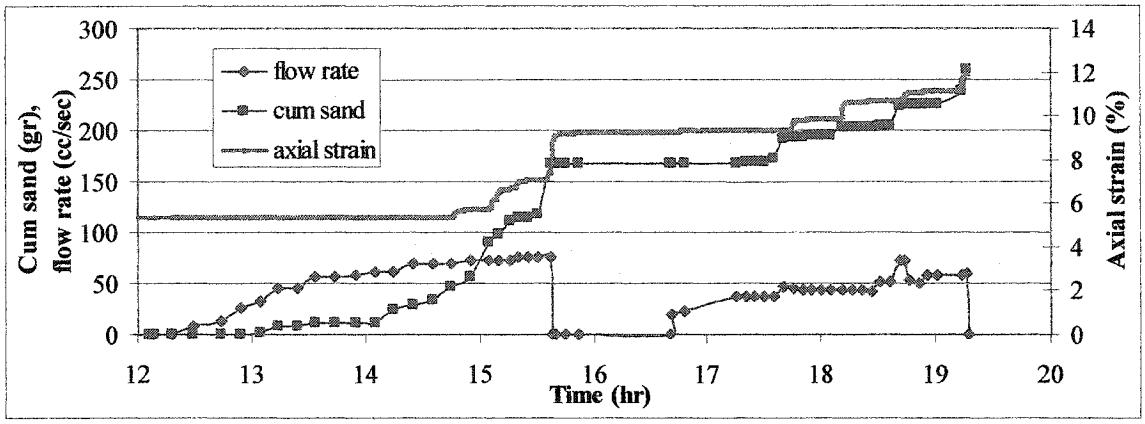

Figure 6.16. Cumulative sanding, flow rate and axial strain vs. time

Sand-Pack of Two-Phase Flow, Fine Grain Distribution, with Water-Cut

This experiment is a repeat of the previous experiment. The only difference was that at the end of this experiment, a water-cut was induced.

Figure 6.17 shows the different stages of the loading after the start of the fluid flow. The experiment was started with a gradual increase of axial stress from zero to 10330 kPa and was kept constant for the rest of the experiment. After the sample was under the peak axial loading for nearly 18 hours, OMS flow began and the flow rate was gradually increased. A small rate of sanding started at a flow rate of 30 cc/sec and its rate was dramatically increased at a flow rate of 100 cc/sec. At the end of the experiment the flow rate was decreased to 20 cc/sec and the sample was allowed to stabilize. Subsequently, a water cut was induced.

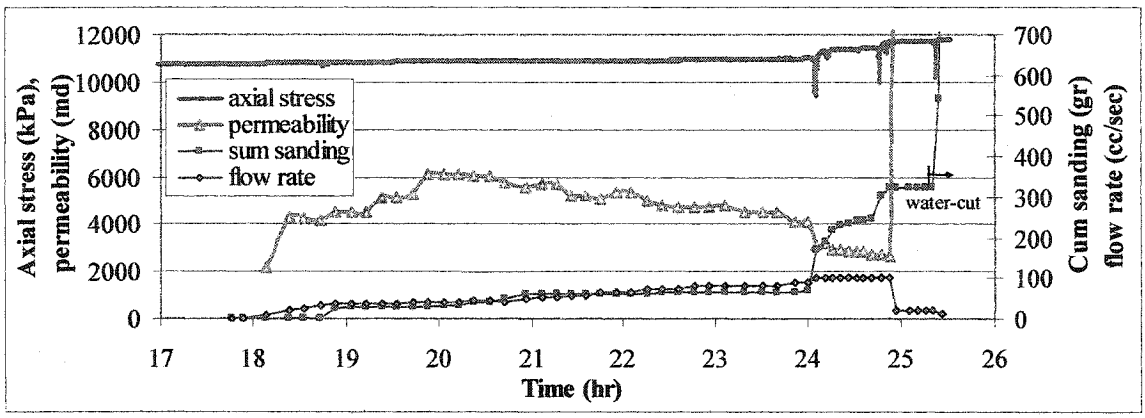

Figure 6.17. Operation conditions and cumulative sand in the interval of after starting the fluid flow

Figure 6.18 shows axial stress as well as cumulative sanding, permeability and flow rate versus axial deformation. Figure 6.19 shows the same graph but in the certain range of axial deformation between 4% to 8%. This is to magnify the results in an important portion of the experiment before a massive sanding took place. According to Figure 6.19, no sanding occurred up to a flow rate of 37 cc/sec. Any sanding in the range of flow rate between 37-88 cc/sec was transient and small. Each sanding ended with arch re-stabilization. This enabled the sample to take even higher flow rates without any further sanding at slightly higher flow rates. Figure 6.19 shows that as the flow rate approached 100 cc/sec, sanding activities increased. This is marked, as Figure 6.18 indicates, with a quick increase in axial deformation in the range of 6.5% to 13%. Moreover, intermittent drops of axial stress as a result of massive sanding and a temporary re-stabilization is another characteristic of this segment.

Figures 6.17 through 6.19 indicate similar performances of permeability as observed in the previous experiment.

Water-Cut Induced Sand Production

In the next stage, the fluid flow was decreased from 100 cc/sec to nearly 18 cc/sec. The sample was allowed to stabilize. In this interval sanding was reduced to zero. Subsequently, a water-cut was induced and under such a low flow rate, a massive amount of sand was produced as shown in Figure 6.20. This observation stresses the important

role of capillary-induced cohesion in maintaining the integrity of the material and stabilizing the arches.

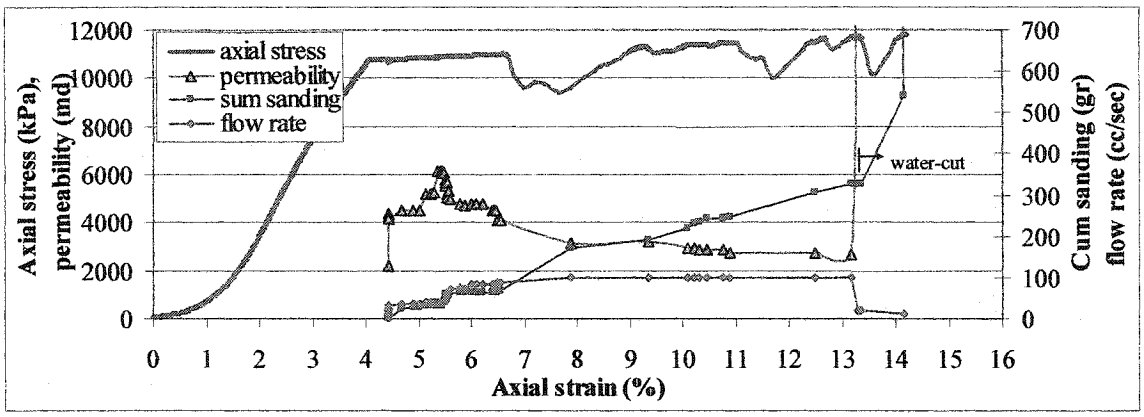

Figure 6.18. Operation conditions, permeability and cumulative sand versus axial deformation

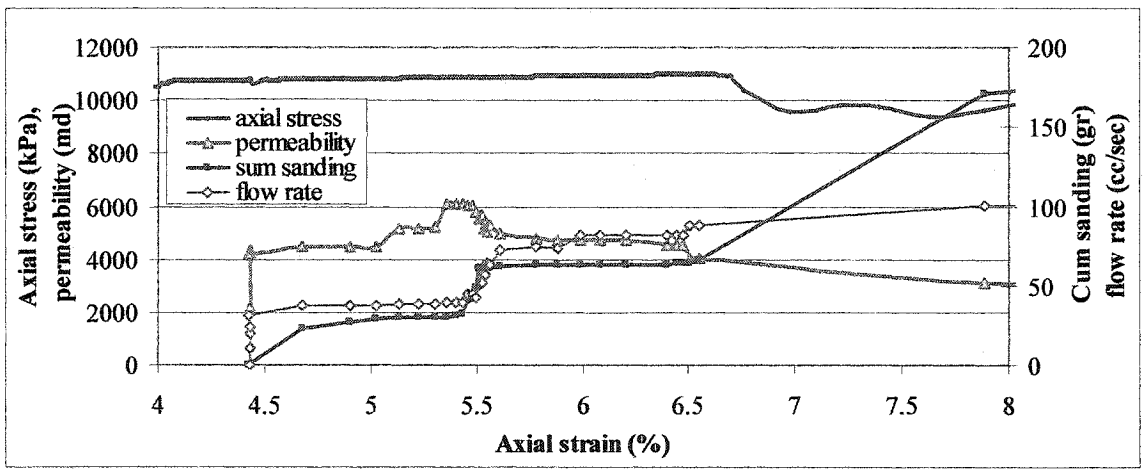

Figure 6.19. Operation conditions and cumulative sand versus axial deformation in the interval of after starting the fluid flow

Experiments on Fine Grained Sand-Pack, Single-Phase Flow

Two single-phase experiments were conducted on fine grained sand-packs. In these two experiments water was used for compaction. Water was also used to flow through the sample during the experiment. The same experiment was repeated to confirm that the

results were reproducible and were not an artefact of the possible experimental deficiencies.

The third single-phase experiment was conducted to examine the possible role of chemical reactions of water and sand minerals. In this experiment, OMS was used for both compaction and the main testing stage.

First Experiment on the Sample with Single-Phase Water Flow

As shown in Figure 6.20, axial loading was gradually increased to 10330 kPa and was kept under this load for 7 hours. Next, water flow was established and it was observed that with a very small flow rate (only drips of water flow), massive sanding took place. As soon as massive sanding started, an abrupt deformation was induced. Consequently, axial stress was sharply reduced. The pump was shut off to let the axial stress rebound to the set value. To re-examine the phenomenon, the pump was restarted. The same observation was repeated for the second and third time as seen in Figure 6.18.

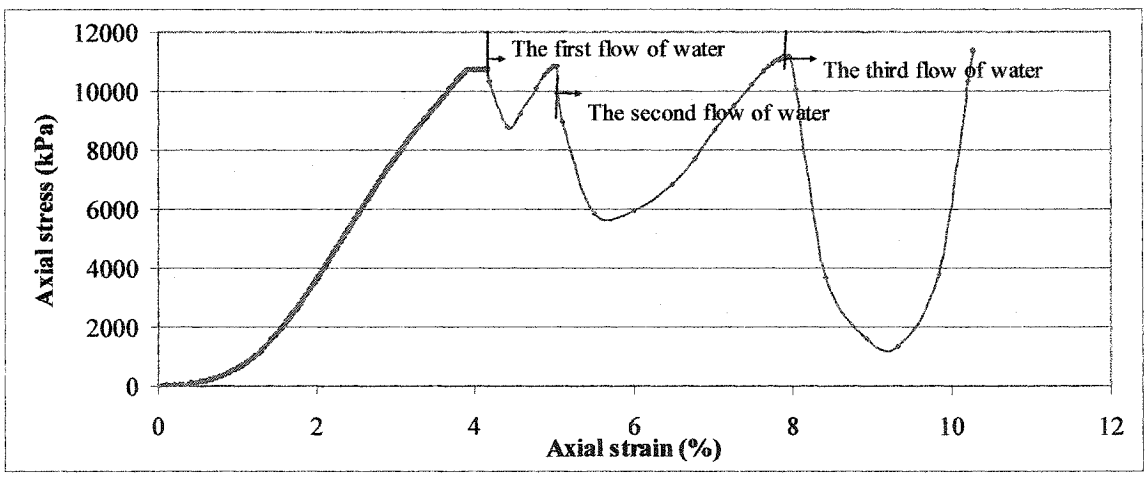

Figure 6.20. Axial stress-deformation of the first single-phase sand production experiment

Second Experiment on the Sample with Single-Phase Water Flow

The same observations as the previous experiment were repeated. Only a very small flow rate was enough to induce massive sanding as shown in Figure 6.21. Massive sanding caused an abrupt deformation of the sample, which in return, dropped the axial stress.

Next, it was decided to establish an oil flow through the sample, hoping that a two-phase medium might be established and the massive sanding might stop. A small oil flow rate

as much as 13 cc/sec was started. The oil flow initially swept the water in the medium. The sweep of water before establishing any steady-state oil flow continued the massive sanding. At this time, the volume ratio of the passing fluid measured 10% sand, 2.5% oil, and 87.5% water. After the stiffener touched the top platen, the experiment was terminated and unloading process commenced.

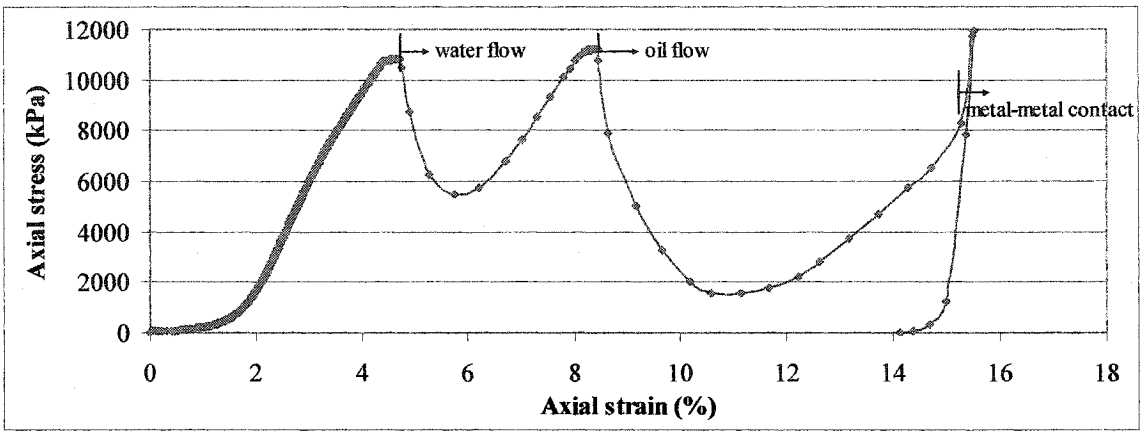

Figure 6.21. Axial stress-deformation of the second single-phase sand production experiment

Experiment on the Sample with Single-Phase OMS Flow

This experiment was conducted to confirm that the massive sanding of the previous single-phase experiments occurred due to single-phase flow rather than a possible chemical reaction of water with the material. The sample with an OMS content of 3% was compacted in several lifts. The axial stress was gradually increased to 10330 kPa and this process took two hours. The axial stress was kept constant for nearly 20 hours.

In the next stage, a flow of OMS was established. In agreement with the other two single-phase experiments, massive sanding occurred under a very small flow of oil. This is marked by the first abrupt change of axial stress and deformation in Figure 6.22. At this stage, the pump was shut off and the axial stress was allowed to rebound to the set value. Another flow of oil repeated the same observation.

Subsequently, it was decided to flow water through the sample. A water flow rate as low as 5 cc/min induced an immediate massive sanding. The produced flow contained more than 95% oil and only 5% of water, indicating that the system was still far from a steady

state. Therefore, even though water was getting injected, the OMS which had originally saturated the sample was being produced. The water flow was then increased to 17 cc/min. Initially the produced fluid contained more than 90% OMS which very soon increased to 225 cc/min. Concurrently, the composition of the produced fluid changed to 70% water, 12% oil and 18% sand. This rapid increase in flow rate along with the composition change of the produced fluid suggests that viscous fingering took place. Massive sand production at this stage marked an end to the experiment.

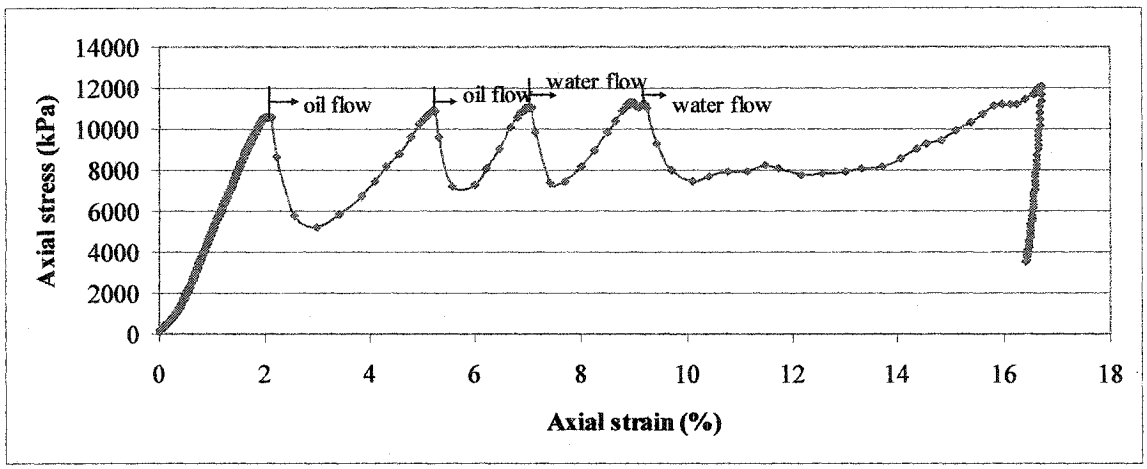

Figure 6.22. Axial stress-deformation of the third single-phase sand production experiment

Analytical Evaluation of the Capillarity and Arch Stability

A straightforward formulation is derived in the following which can be applied for a quick estimation of arch stability. The formulation covers both single-and two-phase fluid flow. It can be directly applied for an estimation of cavity stability in unconsolidated media or, instead, it can be used for the same purpose in weakly consolidated material disaggregated by shear or tensile failure.

Mathematical Formulation of Seepage Forces and Capillary-Induced Resistance

The stability criterion can be expressed in terms of the normalized drawdown induced pressure gradient at the cavity wall which formulates:

$$g_{pn} = \partial P / \partial (r / r_w) r = r_w \qquad [6.1]$$

where

r = radius of investigation (L),

r_w = radius of the cavity (L).

For a cylindrical geometry of cavity, stress equilibrium states:

$$\partial\sigma_r / \partial r = (\sigma_\theta - \sigma_r) / r \qquad [6.2]$$

where

σ_r = radial total stress (F/L^2),

σ_θ = tangential total stress (F/L^2).

At $r = r_w$:

$$\sigma_r = \sigma_r' + P = P \qquad [6.3]$$

$$\sigma_\theta = \sigma_\theta' + P \qquad [6.4]$$

which reduces [6.2] to the following at the face of the cavity:

$$\partial\sigma_r' / \partial(r / r_w) + \partial P / \partial(r / r_w) = \sigma_\theta' \qquad [6.5]$$

As tensile failure develops near the cavity, $\partial\sigma_r' / \partial(r / r_w)$ approaches to zero or:

$$g_{pn} \approx \sigma_\theta'(r = r_w) \qquad [6.6]$$

Since σ_r' at the cavity wall is zero, the maximum σ_θ' at the same location is limited by the Unconfined Compressive Strength (UCS). It must be noted that the UCS of the degraded material at the face of the well is to be used rather than the UCS of the intact material. Hence:

$$\sigma_\theta' \le \sigma_{UCS} \qquad [6.7]$$

and:

$$g_{pn} = \partial p / \partial(r / r_w) = \sigma_{UCS} \qquad [6.8]$$

This equation sets an upper limit to pressure gradient.

σ_{UCS} can be elaborated by friction angle and cohesion:

$$\sigma_{UCS} = \frac{2C_r \cos\varphi}{1-\sin\varphi} \qquad [6.9]$$

where

φ is friction angle and C_r is real cohesion (friction angle and cohesion of the degraded material).

Therefore:

$$\partial p / \partial(r / r_w) = \frac{2C_r \cos\varphi}{1-\sin\varphi} \qquad [6.10]$$

For a stable condition (no material movement):

$$C_r \geq \frac{(1-\sin\varphi)}{2\cos\varphi} \partial P / \partial(r / r_w) \qquad [6.11]$$

Pressure gradient can be related to pressure drawdown:

$$\Delta P_{dd} = \partial P / \partial(r / r_w) \log(r_e / r_w) \qquad [6.12]$$

where

r_e = external diameter (L).

In this equation the assumption of uniform permeability is used. [6.11] can be written in terms of the pressure drawdown:

$$C \geq \frac{1-\sin\varphi}{2\cos\varphi} \frac{\Delta P_{dd}}{\log\left(\frac{r_e}{r_w}\right)} \qquad [6.13]$$

Alternatively [6.11] can be written in terms of fluid flow rate.

$$\frac{\partial P}{\partial\left(\frac{r}{r_w}\right)} = \frac{Q\mu}{2\pi k h \chi} \qquad [6.14]$$

where

μ = viscosity of the fluid (F/(LT)),

h = height of the pay zone (L),

Q = fluid flow rate (L^3/T),

χ = ratio of the total opening area to the total area of the wellbore,

k = intrinsic permeability (L^2).

$$C_r \geq \frac{(1-\sin\varphi)}{4\cos\varphi}\frac{Q\mu}{\pi k h \chi} \qquad [6.15]$$

In case of a complete disaggregation, or in case of the sand-pack, capillary cohesion is the only responsible cohesive agent, and in the absence of normal stresses in material in strain softening conditions it is the only defensive agent. Otherwise, it is a combination of the material real cohesion and capillary cohesion (Han et al., 2002).

$$\sigma_{UCS} = \lambda\frac{1-\phi}{\phi}\frac{\sin\varphi}{1-\sin\varphi}\frac{F_c}{2R^2}$$

$$F_c = \pi x^2 \Delta P_{capillary} \qquad [6.16]$$

$$x = R\sin\alpha$$

where

ϕ = porosity,

R = average grain diameter (L),

F_c = cohesion force (F),

α = water volume angle,

$\Delta P_{capillary}$ = capillary pressure (F/L^2),

λ = a factor accounting for the effect of the non-uniform grain distribution on the rock strength.

A value of $\lambda = 6-8$ has been suggested for packs of narrowly distributed sand and a range of 1.9-14.5 for wider distributions. We assume a value of $\lambda = 7$ for later calculations.

By elaborating σ_{UCS} in terms of cohesion and friction angle and replacing in [6.16], capillary cohesion can be related to capillary pressure:

$$C_c = -\lambda \Delta P_{capillary} \frac{(1-\phi)}{\phi} \tan\varphi \frac{\pi \sin^2 \alpha}{4} \qquad [6.17]$$

where

C_c = capillary cohesion (F/L^2).

Assuming that the shape of the liquid bridge is a toroid characterized by radii x_p and r, a commonly accepted formula to calculate capillary pressure across the liquid water bridge has been developed (Han et al., 2002):

$$\Delta P_{capillary} = \gamma\left(\frac{1}{x_p} - \frac{1}{r}\right) \qquad [6.18]$$

where

γ = surface tension between two fluids (F/L),

$x_p = R \sin\alpha$

$$r = \frac{1-\cos\alpha}{\cos\alpha} R \qquad R = D_{50} \qquad [6.19]$$

On the other hand, assuming uniform grade distribution, the expression for water saturation becomes (Han et al., 2002):

$$\phi S_w = \frac{-\alpha}{2} + \sin\alpha - \frac{1}{4}\sin 2\alpha - \frac{(1-\cos\alpha)^2}{1+\cos 2\alpha}\left[\frac{\pi}{2} - \alpha - \frac{\sin 2\alpha}{2}\right] \qquad [6.20]$$

where

S_w is water saturation.

Implementation Process of the Formulation

The presented formulation can be used to evaluate the capillary cohesion. It can also be used to estimate the level of drawdown at the onset of sanding.

In estimating the stability of de-cemented grains, α is first estimated from [6.20] knowing the water saturation. Then r and x_p are calculated from [6.19]. Capillary pressure is estimated by [6.15], knowing the surface tension between the water and the oil. This is used in [6.17] to evaluate the capillary cohesion. The level of drawdown that the sample can take before the onset of sanding is evaluated by [6.13].

Evaluation of the Level of Drawdown at the Onset of Sanding in Fine Grained Sand-Packs

Table 6.4 estimates the capillary cohesion and the drawdown associated with the onset of sanding implementing the presented formulation. In the calculations, a mean grain size of 0.12 mm was used which is based on the graph of Figure 6.4. The porosity of the sand-pack in the beginning measured 51%. During the experiment this value gradually decreased to an average value of nearly 45%. At the onset of sanding, the average porosity of the sample was nearly 49%, which is used in the calculations. A sand-pack with a porosity of nearly 50% and dry density of 1340 kg/m^3 is considered loose (Das, 1997). Therefore, the friction angle of the material is estimated to be about 35°. Although not measured, it is estimated that the interfacial tension between water and oil is about 0.03 N/m (Berg, 1975).

Table 6.4. Calculation sheet of capillary cohesion and the level of drawdown at the onset of sanding for fine grained sand-packs

S_w (%)	α	x_p (m)	r (m)	P_c (kPa)	C_c (kPa)	P_{dd} (kPa)
0.10	0.115	1.38E-05	7.98E-07	-35.42	1.87	11.44
0.50	0.2	2.38E-05	2.44E-06	-11.03	1.74	10.68
1.00	0.257	3.05E-05	4.08E-06	-6.38	1.65	10.11
3.00	0.386	4.52E-05	9.53E-06	-2.48	1.41	8.64
5.00	0.468	5.41E-05	1.45E-05	-1.52	1.24	7.59
7.00	0.533	6.1E-05	1.93E-05	-1.06	1.10	6.72
8.31	0.57	6.48E-05	2.25E-05	-0.87	1.01	6.20
10.00	0.613	6.9E-05	2.67E-05	-0.69	0.91	5.59
20.00	0.809	8.68E-05	5.39E-05	-0.21	0.44	2.72
30.00	0.9544	9.79E-05	8.76E-05	-0.04	0.10	0.59
33.28	0.996	0.000101	0.000101	0.00	0.00	0.00

Table 6.4 clarifies the effect of the saturation level on capillary cohesion. It indicates that capillary cohesion quickly fades as the saturation percentage of the connate water increases. According to Table 6.4, a capillary cohesion of nearly 1.01 kPa is estimated for a water content of 0.03, which translates to a saturation level of 8.3%. Moreover, the corresponding level of drawdown at the onset of sanding was estimated to be around 6.20 kPa. In the experiment on one of the two-phase experiments, which was conducted without inducing water-cut, sanding onset occurred at a drawdown of about 6 kPa, concluded from Figure 6.23. In a similar experiment, which was conducted with a water-cut induced, a drawdown of 8 kPa was concluded, as shown in Figure 6.24. Therefore, the level of the experimental drawdown associated with the onset of sanding is in reasonable agreement with the one estimated analytically.

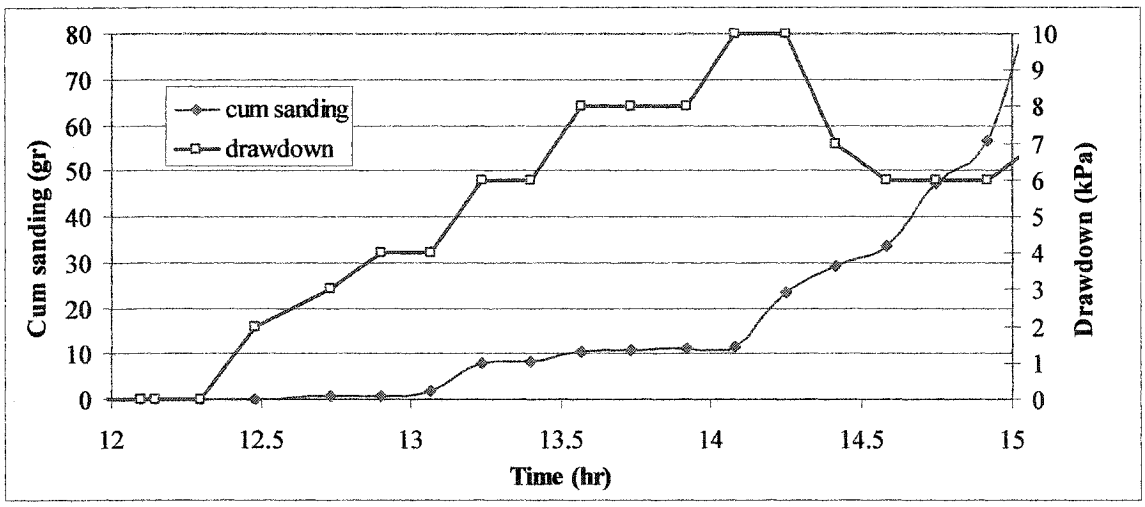

Figure 6.23. Cumulative sanding and drawdown in the two-phase experiment on fine grained sand-pack without water-cut

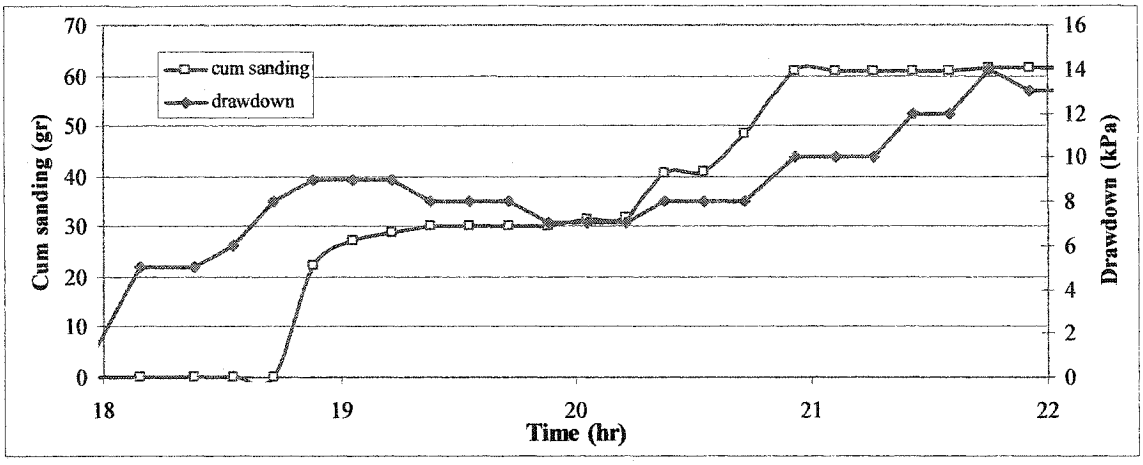

Figure 6.24. Cumulative sanding and drawdown in the two-phase experiment on fine grained sand-pack with water-cut

Evaluation of the Level of Drawdown at the Onset of Sanding for the Coarse Grained Sand-Pack

Table 6.5 estimates the capillary cohesion and the drawdown associated with the onset of sanding for the coarse grained sand-pack. The sand-pack was compacted at a water content level of 3%. This translates to a saturation level of 7.9%. Table 6.5 suggests that at this level of saturation a capillary cohesion of 0.42 kPa exists between the grains and this produces a safe drawdown limit of 2.59 kPa. A friction angle of 35° and porosity of 50%, which reduces to 47.7% at the onset of sanding was used in the calculations.

Table 6.5. Calculation sheet of capillary cohesion and the level of drawdown at the onset of sanding for coarse grain sand-packs

S_w (%)	α	x_p (m)	r (m)	P_c (kPa)	C_c (kPa)	P_{dd} (kPa)
0.10	0.115	3.55715E-05	2.0612E-06	-13.71	0.76	4.67
0.50	0.2	6.15875E-05	6.305E-06	-4.27	0.71	4.36
1.00	0.257	7.87959E-05	1.0527E-05	-2.47	0.67	4.12
3.00	0.386	0.000116711	2.4621E-05	-0.96	0.58	3.52
5.00	0.468	0.000139842	3.735E-05	-0.59	0.51	3.10
7.00	0.533	0.000157517	4.9927E-05	-0.41	0.45	2.74
7.90	0.559	0.000164405	5.5658E-05	-0.36	0.42	2.59
10.00	0.613	0.00017835	6.9008E-05	-0.27	0.37	2.28
20.00	0.809	0.000224315	0.00013913	-0.08	0.18	1.11
30.00	0.955	0.000253057	0.0002267	-0.01	0.04	0.24
33.28	0.996	0.000260184	0.00026021	0.00	0.00	0.00

The results of this calculation are in line with the observations of the experiment. According to Figure 6.25, a small sanding occurred at a drawdown of 1.9 kPa which is in reasonable agreement with the predictions of the analytical analysis.

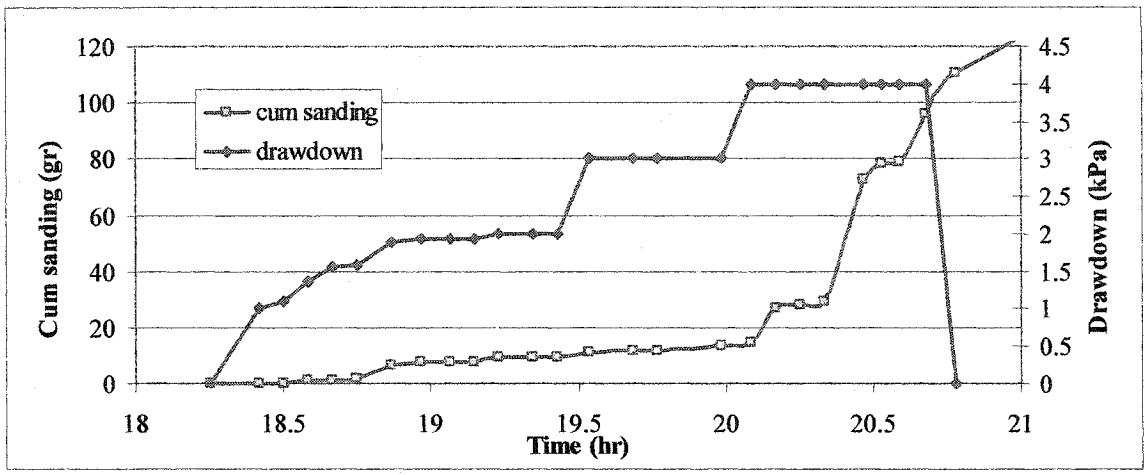

Figure 6.25. Cumulative sanding and drawdown in the two-phase experiment on coarse grained sand-packs with water-cut

Results and Discussions

Sand production from a supported wellbore in an unconsolidated medium was studied. New phenomenological evidence was collected in a series of unprecedented experiments, improving our understanding of the possible sand production mechanism from the wellbores in unconsolidated media. Two different series of experiments were conducted in single- and two-phase flow conditions. The effects of changing the fluid flow velocity were also comprehensively analysed.

Sanding in Two-Phase Flow State

Table 6.6 summarizes some indicative grain size parameters and compares them to the opening size. In the case of the fine grained sand-pack, an opening size of 10 times larger than the maximum grain size guarantees that any individual grain can easily pass through.

Table 6.6. A summary of the grain size distribution and the perforation sizes

Experiment	D_{max} (mm)	D_{min} (mm)	D_{50} (mm)	Aperture size D (mm)	D/D_{max}	D/D_{50}
No.1&2 (coarse grained)	0.60	0.07	0.31	2.5	4.2	8
No.3&4 (fine grained)	0.26	0.0375	0.12	2.5	10	21

Table 6.7 summarizes the benchmark parameters as recorded in the series of two-phase experiments. From this table, the coarser sand-pack was stiffer than the fine-grain sample. It deformed only as much as an average of 2.8%, as opposed to an average of 3.6% for the fine-grain sample in a similar loading pattern.

The onset of sanding, according to the second column, occurred at a similar flow rate for the coarse sample. However, the coarse grained samples produced massive sanding at a higher flow rate than the fine grained samples. Moreover, the onset of material deformation in the coarse grained sample occurred at a higher flow rate. The onset of deformation is an indication of the collapse of one or several of the unstable arches.

Table 6.7. Fluid flow at different benchmarks

	Net axial strain in peak stress before the start of the fluid flow (%)	Fluid flow at the onset of sanding (cc/sec)	Fluid flow at the onset of deformation (cc/sec)	Fluid flow at the onset of massive sanding (cc/sec)
First coarse grained sample	2.3	12	95	122
Second coarse grained sample	3.2	45	120	120
First fine grained sample	4	45	69	61-75
Second fine grain sample	3.2	37	72	88-100

The experimental results on samples with two-phase flow indicated that the stiffener was capable of efficiently holding back the non-cemented sand grains under high flow rates. The mechanism of sand production in the sand-pack is related to the interaction between the fluid and the sand causing hydromechanical instabilities, which manifested in transporting particles due to the seepage forces. Washing-out of the particles increases the porosity of the intact matrix, changes the geometry of the macroscopic structures, and

may cause a readjustment of the intergranular forces, all leading to a redistribution of stresses and further damage of the medium.

The results showed that upon a small transient sand production, stable arches were formed for each step of fluid flow increase. Beyond a certain limit, the sample showed an obvious higher deformation activity. This was related to possible collapses of the arches behind the openings, which subsequently formed larger arches. As flow rate increased, the deformation rate enlarged. Eventually, massive sanding put a limit to the flow rate that the sample could take.

In a flow of immiscible fluid through unconsolidated granular media, cohesion due to capillary forces must be the most important adhesive force acting at the grain scale. Because of the particulate nature of unconsolidated sandstones, the influence of the contact bonding mechanism between particles is extremely important. This mechanism is fully coupled with the mechanical and hydromechanical instabilities in granular media since small changes in cohesive bonding correspond to substantial changes in the mechanical and hydrodynamical response. The proposed formulation can be used to better describe the role of capillary cohesion in arch stability. According to [6.11], no cohesion means no tolerance to any pressure gradient. The importance of friction comes next to the cohesion. According to [6.11], with no mobilized friction, still there is a chance of arch stability in low pressure gradients; although, increasing friction enhances the stability. Capillary cohesion helps in developing some tangential effective stresses which in return mobilizes some friction which, in return, boosts the stability of the arch.

A reasonable agreement between the predictions of the suggested formulation in single- and two-phase flow conditions was evident for both fine and coarse grained sand-packs. Simple and straightforward implementation processes of the formula with a minimum number of the required parameters suggest a very efficient and quick check of the operational conditions leading to sand production.

Single-Phase Flow in Fine Sand-Packs

All of the single-phase experiments that were conducted on unconsolidated sand-packs proved no stable arches could form. Capillary cohesion, albeit minimal, is sufficient to delay sand production.

The experiment on the sand-pack compacted OMS wet with flow of OMS in the subsequent stage proved that the lack of capillarity was the main culprit. This ruled out the possibility of any aggravating effect of water on the sand minerals including the possibility of chemical reactions.

Performance of Permeability in Two-Phase experiments

At small rates of sand production, a trend of increasing permeability was observed. After each massive sanding, permeability declined, and the level of each decline was consistent with the magnitude of sanding.

The enhancement of permeability can be associated with the formation of stable arches and, consequently, an increased level of exposure area for the fluid flow discharge. As massive sanding occurs, arches collapse and the sample undergoes a compaction process. Both the loss of some of the exposure area and compaction of the sample are responsible for the reduction of the permeability. The more massive the sanding, the more extensive the collapse of arches and compaction and, therefore, the higher the loss of permeability.

Conclusions

A number of large scale sand production experiments were conducted on hollow cylinder samples. The samples used loose compacted sand-packs, with a high porosity and permeability. The central hole of all of the samples was supported by a stiffener (a metal liner that was a representative of a general reticulated expandable completion), which contained a mesh of small holes. Single-and two-phase flow were used in two series of experiments; one of them deployed fine- grained and the other coarse-grained sand-packs. Fine-grained sand-packs constituted sand grains whose maximum size was 10 times smaller than the opening size.

The experiments were to test the ability of an expandable completion in alleviating sand production in the worst possible condition: unconsolidated sandstone media, i.e. no cementation between the grains.

In all of the experiments with single-phase flow in fine grained sand-packs, massive sanding took place at small flow rates. The response was, however, totally different in the case of two-phase flow, keeping all other variables similar. As a result, capillarity played a determining role in holding the grains together and preventing their release.

Therefore, the stiffener alone could not hold back fine grained non-cemented material, however, an additional phase inflow did.

All of the experiments in two-phase flow conditions showed a step-like sanding. Each small sand production developed the cavities which formed behind the apertures of the stiffener. An arching effect in the presence of capillary cohesion stabilized the cavities until/unless more flow rates were applied. Development of the cavities continued until a critical flow rate caused them to collapse. Massive sanding followed the collapse of the cavities.

A very straightforward formula was presented in this paper which could estimate the onset of sanding from the media around a wellbore under single- and two-phase flow. A remarkably close prediction of the drawdown associated with sanding proved the usefulness of the formula in providing a quick and reliable estimate of the safe operational conditions.

Nomenclature

C_c = capillary cohesion (kPa)

C_r = real cohesion (kPa)

F_c = cohesion force (kN)

h = height of the pay zone (m)

Q = fluid flow rate (m^3/sec)

r = radius of investigation (m)

r_e = external radius (m)

r_w = cavity radius (m)

R = average grain diameter (mm)

α = water volume angle (rad)

β = ratio of the total opening area to the total area of the wellbore

$\Delta P_{capillary}$ = capillary pressure (kPa)

φ = the friction angle (degree)

ϕ = porosity

γ = surface tension between two fluids (N/m)

k = intrinsic permeability (m^2)

λ = a factor accounting for the effect of the non-uniform grain distribution on the rock strength

μ = viscosity of the fluid (kN/(m.sec))

σ_r = radial total stresses (kPa)

σ_θ = tangential total stresses (kPa)

σ_{UCS} =Unconfined Compressive Strength (kPa)

Acknowledgements

The authors would like to thank NSERC, and the Killam trustees for their financial support. Gary Zatzman's efforts in reviewing the manuscript of the paper are appreciated.

References:

Berg, R.R., "Capillary Pressures in Stratigraphic Traps", *Bull. Amer. Assoc. Petrol. Geol.*, **59**, no. 6, pp. 939-956, 1975.

Bianco, L.C.B., and P.M. Halleck, "Mechanisms of Arch Instability and Sand Production in Two-Phase Saturated Poorly Consolidated Sandstones", *SPE 68932, SPE European Formation Damage Conference*, The Netherland, 2001.

Cuthbertson, R.L., A. Green, J.A. Dewar, and B.D. Truelove, "Completion of an Underbalanced Well Using Expandable Sand Screen for Sand Control", *SPE/IADC 79792, SPE/IADC Drilling Conference*, Amsterdam, the Netherlands, 2003.

Das, B.M., *Principles of Geotechnical Engineering*, Fourth Edition, PWS-KENT Publishing Company, 1998.

Echols, R., J. Gano, P. Shy, C. Tuckness, H. Zhang, and D. Campo, "Development and Testing of an Expandable Sand Screen and Expansion Tool", *SPE 73750, SPE International Symposium and Exhibition on Formation Damage Contro*l, Lafayette, Louisiana, 2002.

Gilmer, M., and B. Emerson, "World's First Completion Set Inside Expandable Screen", *IADC/SPE 87201, IADC/SPE Drilling Conference*, Dallas, TX, 2004.

Hackworth, M., C. Johnson, J. Heiland, J. McClukin, D. Eubank, M. Kemp. L.M. Schetky, and P.S. Smith, "Development and First Aplicaion of Bistable Expandable Sand Screen", *SPE 84265, SPE Annual Conference and Exhibition*, Denver, Colorado, 2003.

Han, G., and M.B. Dusseault, "Quantitative Analysis of Mechanisms for Water-Related Sand Production", SPE 73737, *SPE Symposium and Exhibition on Formation Damage*, Lafayette, Louisiana, 2002.

Metcalfe, P., and C. Whitelaw, "The Development of the First Expandable Sand Screen", *SPE 11032, Offshore Technology Conference*, Houston, TX, 1999.

Skjarstein, A., J. Tronvoll, F.J. Santarelli, and H. Joranson, "Effect of Water Breakthrough on Sand Production: Experimental and Field Evidences", *SPE 38806, SPE Annual Conference and Exhibition*, San Antonio, Texas, 1997.

Tronvol, J., M.B. Dusseault, F. Sanfilippo, and F.J. Santarelli, "The Tools Of Sand Management", *SPE 71673, SPE Annual Technical Conference and Exhibition*, New Orleans, Louisiana, 2001.

Van Buren, M., L. van den Broek, and C. Whitelaw, "Trial of an Expandable Sand Screen to Replace Internal Gravel Packing", *SPE/IADC 57565, SPE/IADC Middle East Drilling Technology Conference*, Abu Dhabi, UAE, 1999.

Vaziri, H., B. Barree, Y. Xiao, I. Palmer, and M. Kutas: "What Is the Magic of Water in Producing Sand?", *SPE 77683, SPE Annual Technical Conference and Exhibition*, San Antonio, Texas, 2002.

Chapter 7: Summary and Conclusions

Introduction

This thesis discussed the sanding issue and the conditions leading to sand production. According to our understanding of the physics of the problem, a numerical modeling scheme was presented which could foresee the onset as well as the continuous process of sand production. A completion technique was proposed which could eliminate the sanding issue. The interaction of the completion and the medium around the wellbore was examined using a series of experiments on samples with different levels of consolidation. Single- and two phase fluid flow was passed through samples that used two different grain size distributions. Samples with both supported and unsupported central holes were studied in the experiments in which boundary stresses and fluid flow rate could be varied during the test. A simple and straightforward analytical methodology was suggested which could predict the onset of sanding in single- and two-phase flow conditions. The predictions of this analytical technique were compared to the observations of the sand production experiments.

Numerical Modeling of Sand Production

The FLAC simulator package was tailored to use our assumptions and understanding of the physics of sand production and was used in the numerical modeling.

Assumptions, and Techniques Used in the Modeling

Axial symmetry for the vertical and plane strain for the horizontal wells were assumed in the simulations. By combining a Mohr-Coulomb model with a strain hardening/softening scheme, a powerful tool was provided which could simulate the complex behavior of the medium and the disaggregation process.

Another instrumental component of the modeling was the tensile criterion for the removal of the elements. The analysis showed tensile failure on cavity face elements occurred only after shear failure degraded the material. A softening tensile cut-off was used as material was de-cemented. In de-cemented material on a cavity face, real cohesion as well as effective stresses tends to zero.

In modeling severity of sanding, the conduct of the elimination of the elements that fulfill the removal criteria seemed crucial. This feature redistributes the effective stresses around the cavity which may further develop shear failure.

The Suitability of the Suggested Numerical Model

The proposed numerical modeling well captured the behavior of the samples as well as sanding rate and volume. The numerical modeling showed that a bilinear Mohr-Coulomb model equipped with strain hardening/softening adequately captured the gradual degradation process of the media that may eventually lead to de-cemented material. De-cementation of the material is the first key stage to sanding and, as such, its accurate modeling is of great importance.

The predictions of volume of sanding by the numerical modeling agreed reasonably well with the experimental results. This shows that the criteria used in the modeling captured the essence of sanding, and therefore, the use of this numerical tool in sanding prediction seems very promising.

The Fundamental Condition Leading to Sanding

Numerical analysis, along with the experimental modeling using open hole showed that under the usual operational practices, shear failure is the main mechanism which may fail and disaggregate the media around the wellbore. According to numerical modeling, a tensile failure seems to be a necessity for the disaggregated material to be washed out.

Both shear and tensile failure occur because of one fundamental condition, and that is the status of zero effective normal stress at the well face (in general on cavity face).

How to Eliminate the Necessary Condition for Sanding?

For shear and tensile failure to be eliminated, radial stresses must build up on the wellface. For this, the wellbore must be supported by a solid structure.

The Proposed Completion Technology

To support the wellbore and at the same time establish a high flow rate, an expandable screen must be implemented. Here the idea of FRC expandable comes into view. This completion, while flexible in the beginning, is lowered and expanded by inflation. It is, subsequently cured by the heat of the reservoir forming a solid structure with the required

strength and stiffness. It also contains a mesh of holes with the required aperture size, allowing a continuous flow of oil.

Interaction of the Proposed Completion Technique with the Medium: Possibility of Material Failure Surrounding the Wellbore

By using the proposed technique, the general shear and tensile failure of the open hole cavity is eliminated. The next question is the possible effect of pore collapse as well as local shear and tensile failure of the material behind the apertures. As a result of a high radial effective stress, pore collapse seems plausible.

Is Pore Collapse Important in Sanding?

Extensive research was conducted on studying pore collapse and its effect on the integrity of the material. The experimental results and literature survey, as detailed in Appendix D, showed that first, for pore collapse, i.e. pore collapse, to take place in the effective stresses of regular conditions, the material must be weakly consolidated.

Secondly, even if the material failed under pore collapse, the experiments on both small samples used for material characterization, as well as HCS with a central stiffness, used in sand production experiments, showed that this mode of failure did not destroy the integrity of the material. In fact, as a result of a compaction phase in the aftermath of pore collapse, the interlock between the grains is enhanced. This in return may provide a greater stability.

Are Shear and Tensile Failure Plausible?

To examine the possible local shear and tensile failure of the material behind the apertures, a few experiments were conducted with two sizes of aperture in stiffeners and two grain size distributions for the constituent sand of the material. The experiments showed that the use of stiffener highly alleviated the amount of the produced sand. The magnitude of sanding, if any at all, depended on the aperture size. If the opening was too large, local shear failure might occur in the material at the aperture location. Therefore, a limited amount of sanding may be produced before stable arches develop.

In the experiments, an aperture size of 4.2 and 8 times the maximum and mean grain size, respectively, produced no sand at all even in excessive effective stress conditions. An aperture size of 8.4 and 16 times the maximum and mean grain sizes produced traces of

sand, and an aperture size of 20 and 42 times the maximum and mean grain sizes produced a small rate of sanding. This shows the remarkable ability of the stiffener in altering the mode of failure of the medium around the wellbore and, therefore, greatly enhancing the operational limits.

Sanding from Supported Well versus an Open hole

Figure 7.1 compares the measurements of cumulative sanding form the different tests with the stiffener completion as well as the ones which use an open hole. According to this figure, the stiffener either eliminated or highly alleviated the level of sanding as compared to the cases of the samples which use an open hole.

Furthermore, the stiffener highly increased the level of deformability of the sample. This implies that greatly harsher operational conditions can be applied before any major sanding is realized.

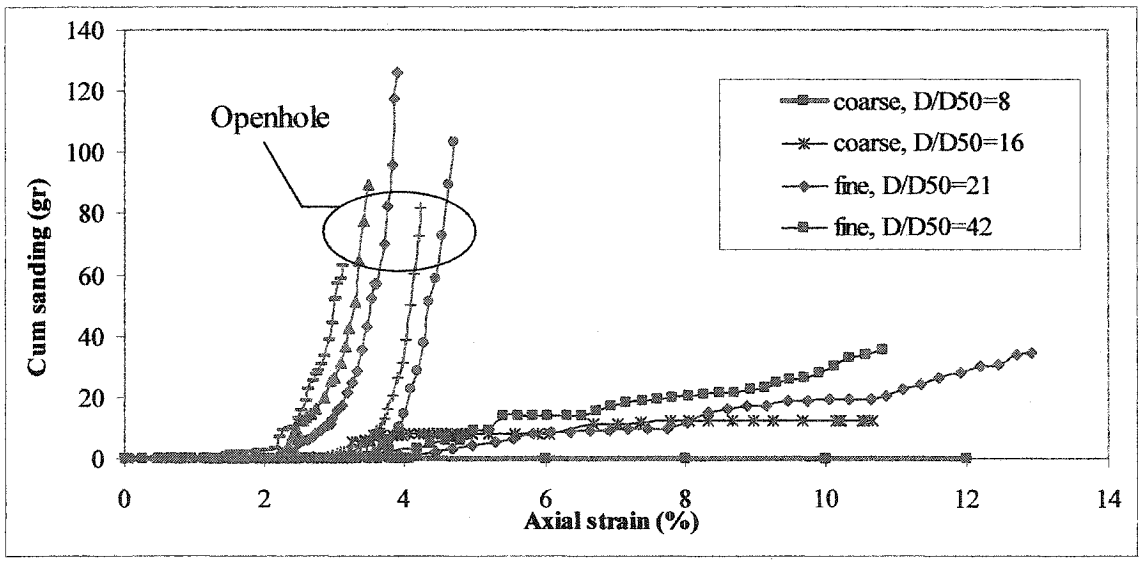

Figure 7.1. A comparison of sanding from the different sand production tests on samples with an open hole or a hole supported with a stiffener

Effect of Aperture Size on Sanding from Weakly Consolidated Samples

Figure 7.2 indicates an increased level of sanding as aperture size increases. For the samples with an open hole, a fictitious D/D50=100 has been used in this figure. The graph of cumulative sanding indicates that an aperture size of 20D50 can be used as an initial guiding design of the stiffener which is meant to support a wellbore created in

weakly consolidated sandstone. To suggest an all compassing design advice, more testing needs to be done on samples with more variety of consolidation level.

Additionally, the same figure gives an indication of the axial stress which is associated with the onset of sanding. According to the testing results, axial stress at the onset of sanding highly decreased with the increase of aperture size.

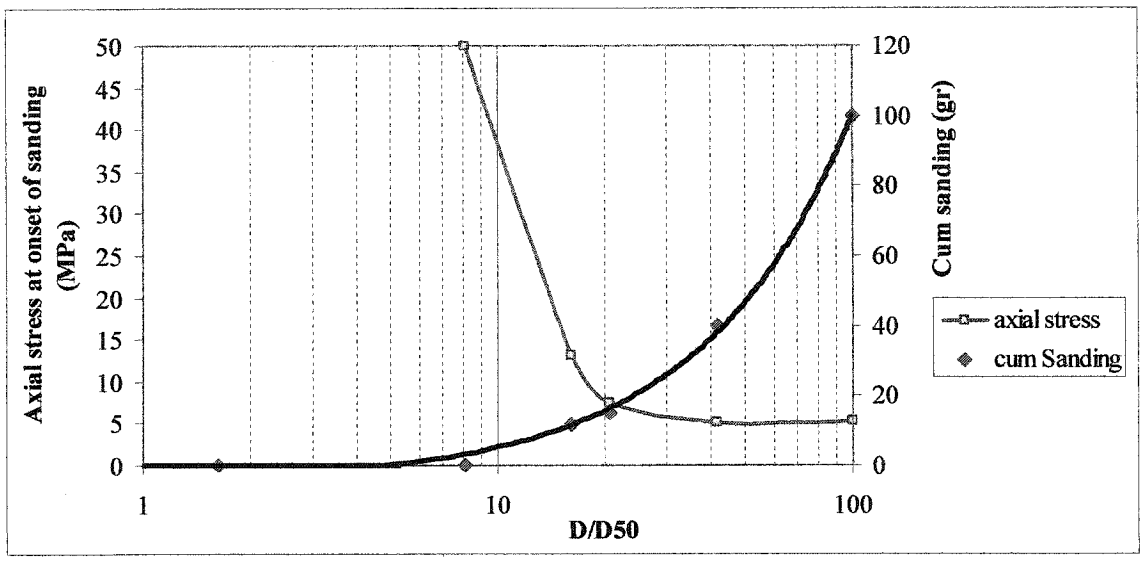

Figure 7.2. Results of different sand production experiments on weakly consolidated samples

Examining the Function of the Proposed Completion Technique in Unconsolidated Media

The worst possible case scenario was defined as a highly porous unconsolidated medium. Sand-pack samples were used to resemble such media. The experiments were conducted on both single- and two-phase flow conditions. The sand-pack samples were of about 50% porosity and two different grain sizes were used.

All of the experiments on fine and coarse grained sand-packs with single-phase flow indicated an instantaneous sand production under small flow rates. This was attributed to the lack of any cementation between the grains and small interlocks between the grains, as well as the absence of capillary cohesion in single-phase flow conditions. Therefore, no stable arches could develop. However, experiments that were conducted under two-phase flow conditions showed that capillary cohesion, albeit low, was sufficient to develop stable arches in fine grained sand-packs up to a certain limit of fluid flow rate.

The experiments in two-phase flow conditions showed a step-like sanding. Each small sand production developed the cavities which formed behind the apertures of the stiffener. An arching effect in the presence of the capillary cohesion stabilized the cavities until/unless more flow rates were applied. Development of the cavities continued until a critical flow rate collapsed them. Massive sanding followed the collapse of the cavities.

Coarse grained sand-pack samples produced sand at a smaller flow rate than the fine grained sand-pack samples. This is associated with the smaller capillary cohesion in coarser sand.

Figure 7.3 shows the pattern of the decrease in flow rate associated with the onset of sanding, the collapse of arching, and the onset of massive sanding as aperture size increases. Additionally, this figure indicates that an aperture size as drastic as 20D50 still developed stable arches and only induced a small amount of sanding in two-phase condition.

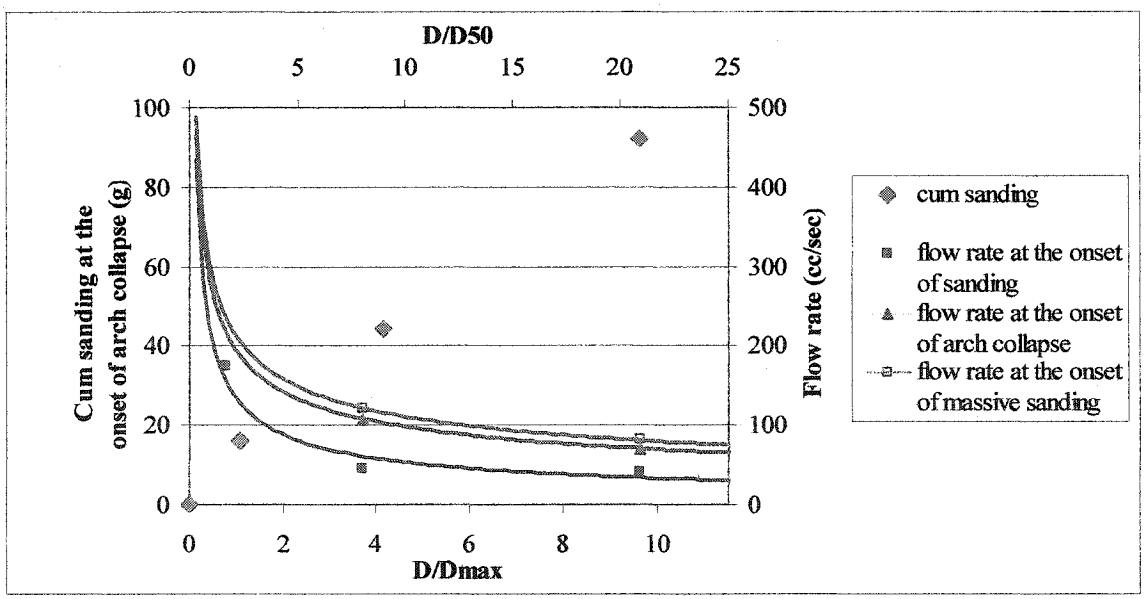

Figure 7.3. Results of various sand production experiments on unconsolidated samples

Prediction of Onset of Sanding in Single-and Two-Phase Flow

A very straightforward formula was presented in this paper, which could estimate the onset of sanding from the media around a wellbore under single- and two-phase flow. A

remarkably close prediction of the drawdown associated with sanding proved the usefulness of the formula in providing a quick and reliable estimate of the safe operational conditions.

The proposed formulation was also used to better describe the role of capillary cohesion in arch stability. According to the formula, no cohesion yields little tolerance to any pressure gradient. The importance of friction comes next to the cohesion. With little mobilized friction, there is still a chance of arch stability in low pressure gradients; although, increasing friction enhances the stability. Capillary cohesion helps in developing some tangential effective stresses, which in return mobilizes some friction which, boosts the stability of the arch.

Effect of the Proposed Completion Technique on Well Productivity

Another effect of the stiffener whose magnitude was an issue of concern was the level of possible effects from the expandable completion technique on the productivity of the wellbore. In agreement with initial expectations, as the sample compacted, the porosity and permeability of the medium decreased. However, the decline level of the permeability was less than initially thought. Therefore, if the opening sizes are designed properly, there will be high enough operational limits in terms of drawdown in place. These limits are usually set by the safe production schemes to minimize the level of sand production. Therefore, the gradual decrease in permeability can be compensated for by a proportional increase in the level of drawdown.

Chapter 8: Further Research and Studies

Introduction

As in most of studies of this order, the constraints of time presented opportunities for other researchers to advance this work to more sophisticated stages. The nature of some of the developments required a multidisciplinary team to conduct an all-encompassing research and development to make it ready for practical use.

In this chapter, the recommendations are presented for further developments of the completion technique and the sand production prediction tool separately.

For the completion technique, the specific tasks to be carried out are elaborated. The challenges that the completion design faces are specified and the required experimental and numerical analysis for advancing the technique are discussed.

At the end of the chapter, further opportunities to advance the sand production prediction tool are recommended.

Further Research on the Novel Completion Technique

Extended reach horizontal wells and multilateral horizontal wells put screens under extensive loads during the production. A large portion of the loading on the completion attributes to differential settlements in the course of depletion. This may apply significant shear loads on the completion, especially in the joint segment between the vertical and horizontal parts. Therefore, the likelihood of the damage to the screen increases, which requires high mechanical resilience to damage. Furthermore, long-term loads develop upon completion, as the reservoir depletes and effective stresses in the formation increase. This increase in effective stresses is transferred to the completion structure.

Moreover, the installation of completions in horizontal wells are often accompanied by acidizing/washing operations to remove the filter cake from the wellbore walls. Therefore, any proposed completion must be resistant to these operations and processes.

Further, operators are looking for completions that will last the lifetime of the well with minimum workovers. This ensures the economic health of the project.

Another very important requirement is zonal isolation, which is essential for future well management, or problem remediation. Many horizontal wells that have been producing for several years are now experiencing production problems that can be attributed to the lack of completion control (Goode and Wilkinson, 1991). Therefore, any completion design must consider any needed future intervention to exclude problematic sections with minimum cost.

As a result, developing a screen with these requirements presents a number of challenges:

1- It must provide effective sand filtration.

2- It must tolerate mechanical loads developing during installation and over the long life of the well. It must be noticed that long term loads develop as reservoir pressure depletes. Reservoir compaction induced by depletion may cause excessive deformations and collapse to the completion structure.

3- It must be corrosion resistant. This requires careful selection of the materials used to build the completion and a thorough review of its compatibility with the produced fluids and workover/completion/stimulation fluids.

4- It must be able to be cleaned. Any possible plugging that may occur should be physically easy to remove. The completion material must be compatible with the stimulating fluids that are used to remove scale and dissolve damage in the screen or in the near wellbore formation.

Experimental Procedures or Research Methods to be Employed

A series of experimental investigations should be conducted to ensure the integrity of the proposed systems. In summary, they are:

- Material preparation and testing
- Resin selection
    - The polymerization time must be short enough to ensure validity.
    - The resin must remain soft before the expansion phase.
    - The polymerization temperature must be as compatible to the reservoir temperature as possible to ensure that no heating element would be required for curing.

- The cured resin must be compatible to harsh downhole conditions (pressure, temperature, salinity, chemicals, etc.).

- Fibre selection
  - The fibre must supply the required strength and stiffness to the fabric so that it can sustain downhole conditions.
  - The fibre must be cost effective to ensure economic viability of the proposed technology.
- Experimental investigation of the integrity of the system by testing a laboratory scale system.
  - Establishing the global integrity of the system (by evaluating its compressive strength and stiffness, overall expansion coefficient of the system, buckling strength, etc).
  - Establishing the local integrity by evaluating the local buckling strength, de-lamination (de-lamination is defined as separation into constituent thin layers). Strength and quality of lay up at various locations, as well as their comparison to the specified design values).
  - Experimental investigation into the dynamic properties of the systems.
  - Vibration characteristics of the system must be evaluated to ensure that the installation induced impact loads do not coincide with the resonant frequencies.
- Experimental evaluation of the system with respect to the environmental factors.
  - The system will be subjected not only to relatively high operating temperatures, but also to harsh environmental associations and created with the chemical composition of the materials traveling through the system, as well as their harsh abrasion and the Glass Transition Temperature (GTT).

    GTT is the temperature at which resins of a partially crystalline polymer change from a hard and relatively brittle state to a viscous rubbery state. GTT is the upper bound working temperature of the composite structure. GTT of most traditionally used FRP are usually lower than the operating temperatures commonly experienced in those wells. The higher the

temperature generally shortens the curing time, but the cure temperature can be above the glass transition temperature. Nevertheless the working temperature of the composite structure must be below the glass transition temperature. The glass transition temperature of most of the epoxies varies with the curing temperature. To attain a high degree of cure, it must occur at a temperature close to glass transition temperature.

There are two types of epoxies, those cured at low temperature (120° C, 250° F) and used in components exposed to low or moderate temperatures, and those cured at higher temperatures (175° C, 350° F) and used in high temperatures. Polymide matrices are used for high temperature applications up to 375° C, 700° F. Table 8.1 gives an indication of the GTT of three types of Polymide.

Table 8.1. Glass transition temperature of three types of Polymide

	PMR-Flex[a]	PMR-15[a]	PETI-RTM[b]
Glass transition temperature °C	260	339	246

In the design process for each reservoir, a resin must be selected whose GTT is below the reservoir temperature. The advantage to this application is that there is no possibility that reservoir temperature increased at all at in the lifetime of the wellbore. This guarantees the proper functioning of the structure as designed. The addition of the appropriate additives have been proven to increase the glass transition temperature, but at the same time compromising the mechanical integrity of the FRP materials. Experimental investigation will be therefore tailored to evaluate the integrity of the system subject to these factors.

- Testing the selected cured materials with different fibre ratios, thickness of material, and diameter of the liner in order to verify the numerical model and capture the mechanical properties.
- Experimental evaluation of the effect of potential transportation/installation induced damages into the prep-reg system used to construct the horizontal stabilizer.

- Final lab experimentation: the final test will be to experiment the proposed system by having it installed in the ground but over a short interval so that the complexities of large-scale operations are avoided. For this test, we can consider patching a section of an eroded pipe where we can install the system inside a liner and let it comply and close the eroded section.
- Pilot testing: upon completion of lab testing a candidate well is to be selected for real application and ultimate performance evaluation.

Numerical Modeling

Numerical analyses are to be carried out in order to determine the main parameters controlling the design and downhole implementation.

Optimization of Screen Stiffness

Liner stiffness must be high enough to prevent its excessive deformation to ensure preserved casing string shape, mainly diameter for later application of wire line run operations and production optimization. At the same time it must be designed to be flexible enough to prevent excessive build up of normal stresses in the formation which in return are applied on the liner and make it structurally more demanding.

Strength Requirements

For each specific application, the liner must be numerically analyzed and designed to prevent any damage and failure of the structure under the most critical lifetime loading condition.

Further Research Related to Sand Production Prediction

Even though the proposed model in its current form has an enormous capacity to be implemented in real sand production prediction tasks, additional developments may further enhance the predictions.

It is proposed to further develop the numerical tool from its current 3D axisymmetric to a real 3D. The inclusion of the effects of slanted wells, circular perforations, and stress anisotropy necessitates three dimensional analyses.

The model, as presented in this thesis, conducts the analysis on a single phase medium, while in real case, it is usually double or multiphase. It is assumed that the gas is in the

occluded form in the fluid phase and the effect of different phases has been combined in one. Nevertheless, further developments can be carried out when considering more phases in the analysis or when making the density of the fluid pressure dependent.

References

Goode, P.A., and D.J. Wilkinson, "Inflow Performance of Partially Open Horizontal Wells", *JPT*, pp. 983-987, August 1991.

Appendix A: An Initial Design of the Experiments on the Proposed Hollow Cylinder Samples

Introduction

This Appendix covers the design of sand production experiments on open hole, as well as completed hollow cylinder samples. Designing an experiment before executing it is indispensable not only for deciding upon the best procedure, but also to provide insight into what to watch for, or anticipate from the experiment.

In the design process, the results of an elementary analysis on hollow cylinder samples with various internal and external diameters are discussed first. The objective is to investigate the effects of sample geometry and scale effects on the configuration of the stress profiles, as well as the failure status of the sample. The end result is the selection of the internal and external diameters of the sample. On the basis of the results of a series of numerical analyses, the loading strategies of various experiments are suggested.

Two different set-ups were used in the experimental program. Initially, a set-up based on a triaxial apparatus was designed and used, but performing an ideal experiment with this set-up was very difficult, therefore, after conducting a number of experiments, the design of the device changed to a "consolidation chamber"-based device.

Both perforated-liner and open-hole arrangements were studied. Cylindrical samples of weak synthetic sandstone were used. Single phase saturated, as well as two-phase tests with connate water content were investigated.

This chapter continues with the selection of an adequate sample size. Next, an initial design of various series of sand production experiments are presented. Finally, the stiffener is preliminarily analysed and designed for the completed experiments.

Selection of a Proper Sample Size

The effects of variation of the diameter of the central hole and the external diameter of the sample on profiles of stresses were studied. Elastic analytical solutions were deployed and an arbitrary external pressure of 100 was applied and the profiles of stresses were prepared.

Effect of External Diameter on Stresses Profile

The experimental set-up limits the sample to a maximum diameter of 125 mm. In order to study the size effect, a rudimentary analysis was conducted on the influence of external and internal diameters on the sample's behaviour.

Figure A.1 depicts an elastic profile of radial and tangential stresses on a series of hollow cylinder samples. The internal diameter was fixed at 2.54 cm, while the external diameter was varied between 7 cm to 20 cm. A full development of the profile was considered to be the criterion for the adequacy of the external diameter for the assumed central hole diameter. If the sizes are selected in such a way that the profile of tangential and radial stresses levels off at the boundaries, experiments will produce more realistic results. According to Figure A.1, an external diameter of 20 cm is ample enough to give such good results for the abovementioned internal diameter. A diameter of 7 cm, on the other hand, does not develop a full profile and, therefore, is not good enough unless a reduction in the internal diameter is considered. A diameter of 12.5 cm is acceptable, as it shows that the profiles levelled off at the outer boundary of the sample.

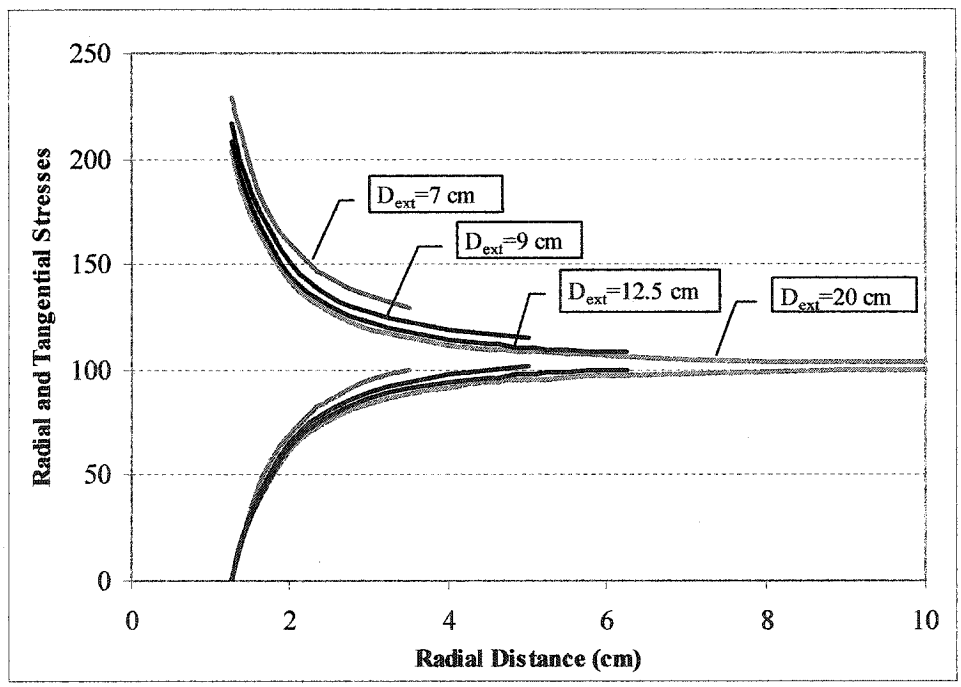

Figure A.1. Effect of external diameter on the stress profile, internal diameter of 25.4 mm, elastic analytical solution for an arbitrary external pressure of 100

Generally, the higher the internal diameter, the more the external diameter is needed to produce a well developed profile of stress. Figure A.2 depicts the profile of stresses in a hollow cylinder with an internal diameter of 10 cm. To develop a full profile of stresses, an external diameter of at least 50 cm is needed.

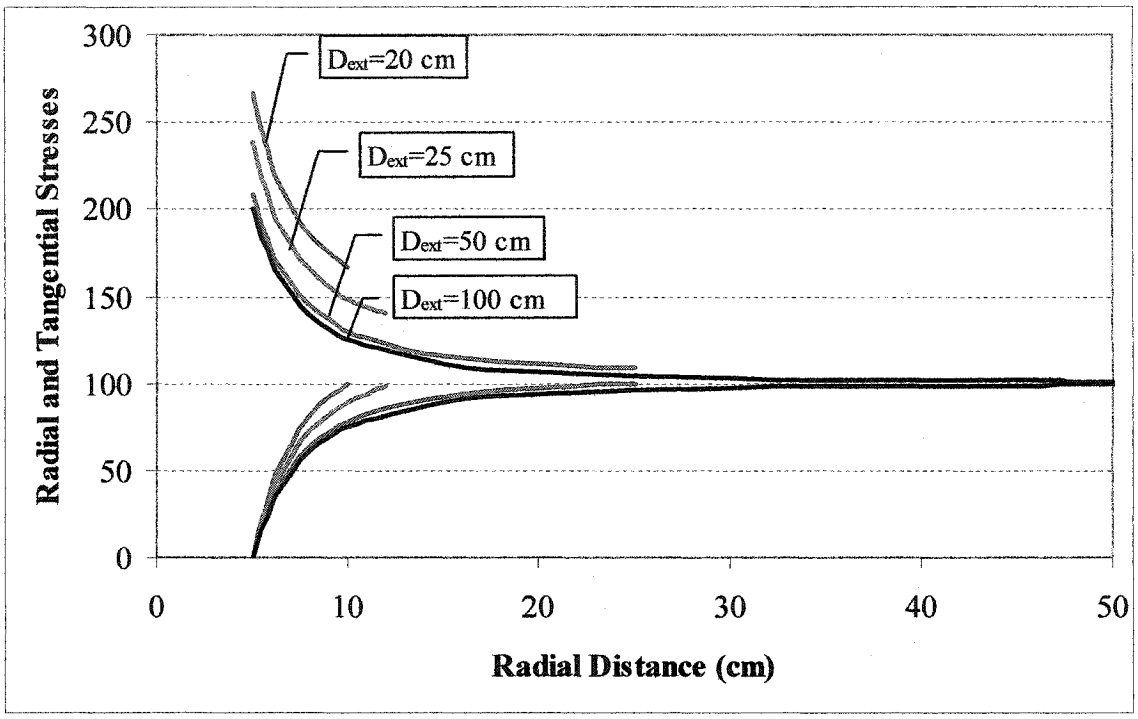

Figure A.2. Effect of external diameter on the stress profile, internal diameter of 10 cm, elastic analytical solution for an arbitrary external pressure of 100

Selection of the Internal Diameter

Having fixed the external diameter at 125 mm, the selection of the proper internal diameter size is the next focus of sample design. Figure A.3 illustrates a series of profiles of tangential stresses for different central hole diameters. In this graph, the internal diameter was varied between 10 mm to 70 mm. Again, elasticity was assumed in the analytical solution.

Figure A.3 shows that an internal diameter of 70 mm produces an immature profile of the tangential stress. Moreover, the value of tangential stress on the well face is abnormally high. High values of tangential stress at the well face cause the development of high shear stresses, which may lead to an early shear failure. A diameter of 4 cm is still large. At less than 4 cm, maximum tangential stress tends to 200. An internal diameter of 2.5

cm develops a good profile of tangential stresses whose value is very close to the limit value of 200 and therefore is selected for the sample preparation.

The above analysis neglected the grain size distribution of the sample. This preliminary analysis indicated that for a large external diameter, the size of internal diameter does not affect the stresses profiles. On the other hand, if grain size distribution is considered in the analysis, hollow cylinder strength decreases with the increasing inner hole diameter (Papamichos and van den Hoek, 1995). Tronvoll et al. (1993) suggested that the observed size effect is linked to the ability of the grains to move relative to each other. Smaller cavities would thus appear less prone to warping because of the reduced freedom of the smaller number of grains involved. Stronger size effects are realized for smaller levels of consolidation (van den Hoek et al., 1992).

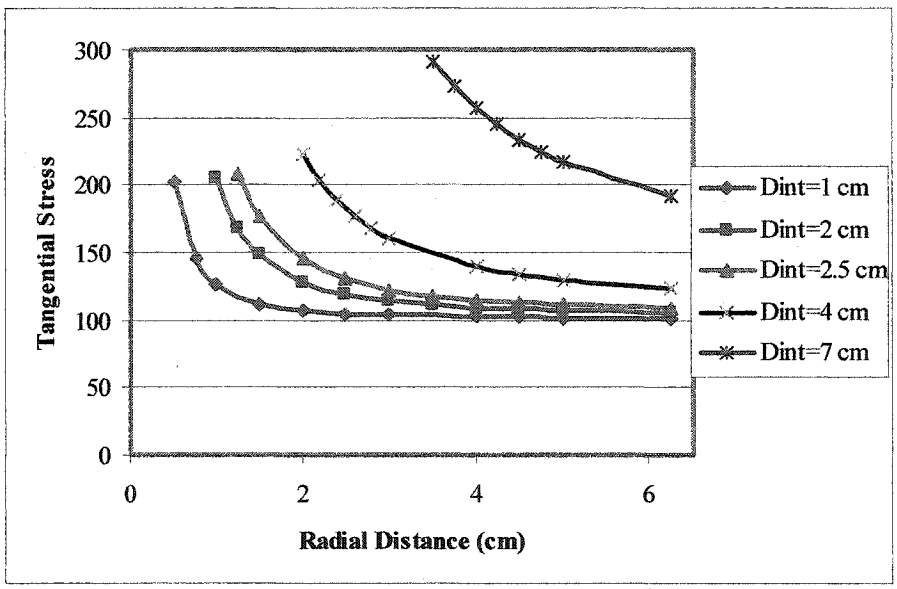

Figure A.3. Effect of internal diameter on the stress profile, external diameter of 12.5 cm, elastic analytical solution for an arbitrary external pressure of 100

According to the above analysis results, a sample with a 125 mm external diameter, 25.4 mm internal diameter, and a height of 250 mm is acceptable.

Scale Up of the Results

After selecting the sample size, the problem of establishing representative field sizes was analyzed. For this, a numerical analysis was conducted on media of two sizes. The first was the sample of the size used in the experiments, with an internal diameter of 25.4 mm

and an external diameter of 125 mm. The other was considered to be a large size sample with an internal diameter of 100 mm and an external diameter of 500 mm. The same loading sequence was used in the two where axial and radial external stresses were increased hydrostatically until the failure occurred. Figures A.4 and A.5 depict the profile of stresses at the failure initiation state for the large and small samples respectively. Comparative observation discloses that pressure associated with the failure of small and large scale samples is the same. The stress profiles of the small scale sample can be mapped to the profiles of the large scale sample.

Since the stress gradient in a small scale sample is higher than a full scale one, it is preferable to use small grain sizes for the small scale sample.

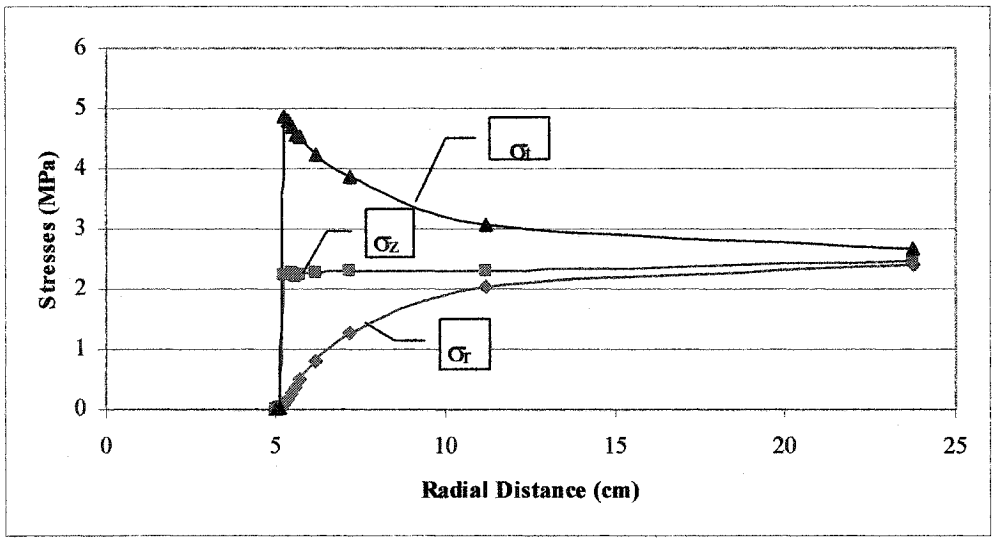

Figure A.4. Stresses profile of full scale sample

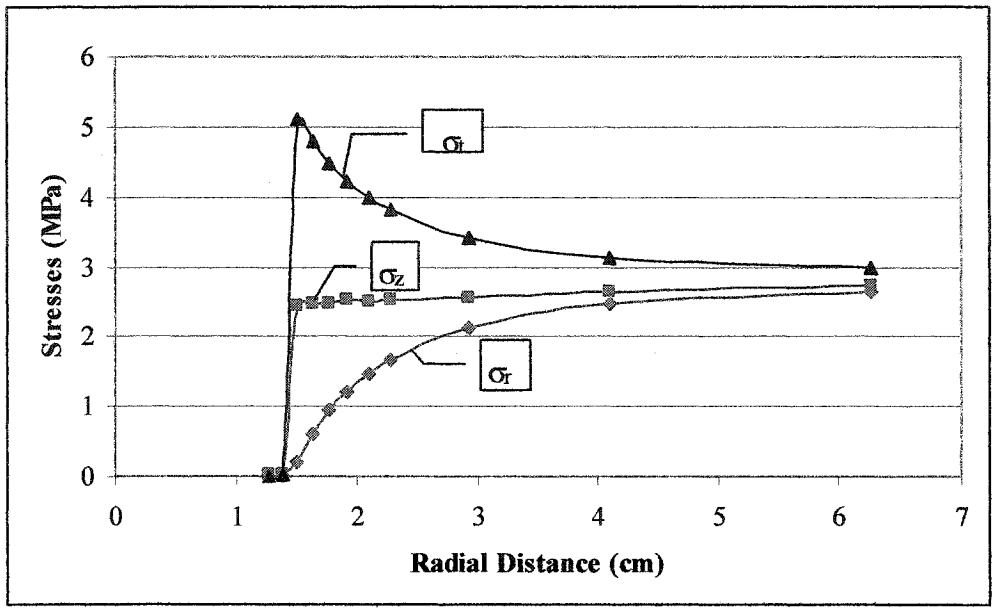

Figure A.5. Stresses profile of small scale sample

Loading Sequence in the Sand Production Experiments

The loading strategy of different experiments is suggested according to an initial numerical analysis of sand production. A Mohr-Coulomb arrangement with strain hardening/softening of the failure envelope was used. Stresses corresponding to initiation and development of failure were evaluated for suggesting an initial design of the experiments. Material parameters as suggested by material characterization were used in these analyses.

Experiments on open hole as well as completed wellbores were conducted. Moreover, both single-and two-phase pore fluid saturations were considered.

Two different set-ups were used in the experiments: triaxial, and consolidation-based. In the first, radial stress was applied by pressurizing the oil inside the triaxial chamber. In the second, radial stress was increased according to the axial stress as the lateral deformation of the sample was restrained at the outer boundary. The following initial design assumed a triaxial based set-up.

Open Hole, Single-Phase Fluid Flow

The following sequence is followed in these experiments:

- Sample is dried in an oven at 50°C. The dry weight is measured.
- Sample is saturated by OMS (or water) in a container under vacuum. The saturated weight is measured.
- Initial porosity is estimated.
- Sample is placed in the cell.
- *In situ* effective vertical and radial stresses are applied.
- A drawdown is applied whose magnitude is selected based on adequacy to produce disaggregated material to the central hole. It is estimated that an outer pressure of 70 kPa (10 psi) will flow 60 cc/sec of fluid.
- Vertical stress gradually increases. Confining pressure, however, is only increased to a portion of the axial stress (ideally 40% which is an average of 30%, 33%, 44%, 36% according to Uniaxial Strain experiments on small synthetic sandstones). In the consolidation based chamber, radial stress increases automatically accordingly to the axial stress.
- The increase of pressures continues until sand grains are produced.

These stages are reflected in Table A.1.

Table A.1. Planning of stage loading for open-hole single-phase

Phase	Description	σ_r (MPa)	σ_y (MPa)	Exterior pressure (kPa)
Drying stage	In oven, 50^{0c}, in a few days, after the sample is cured			
Saturation	Saturated under vacuum with OMS			
Placing in cell	Sample is placed in the cell			
Initial loading	Membrane/piston sit on the sample	0.70	0.7	0
Drawdown	Applying drawdwon , permeability testing	0.7	0.7	69 (10 psi)
Proportional	Proportional increase of vertical and radial stresses Ratio(horizontal/vertical)=0.4	3.34	7.3	69 (10 psi)

Open Hole, Two-Phase Fluid Flow

The same procedure is used as in the single-phase. The only difference is that the sample which is initially saturated by water is then back-flooded by oil. The process continues until, observationally, no more water is displaced. When no more visible water is

displaced, it is assumed that the sample has reached connate water content. The amount of water displaced is collected and measured, and therefore, the degree of oil and water saturation can be estimated.

Loading Procedure of Experiments on Samples with Completed Hole

The same experiments were conducted on samples with completed central holes. Stages of this experiment were initially considered to be the same as previously stated for open holes.

Stiffener Design of the Completed Hollow Cylinder Experiments

Stresses in the stiffener are estimated by conducting numerical analysis. The ANSYS package is used in the numerical analysis.

Input Data and Assumptions

Geometry

Figure A.6 illustrates the geometry of the model. A cylindrical sample of 12.5 cm and 2.54 cm for exterior and interior diameters was modeled. The height of the sample was 25 cm. An initial thickness of 5 mm for the stiffener was considered.

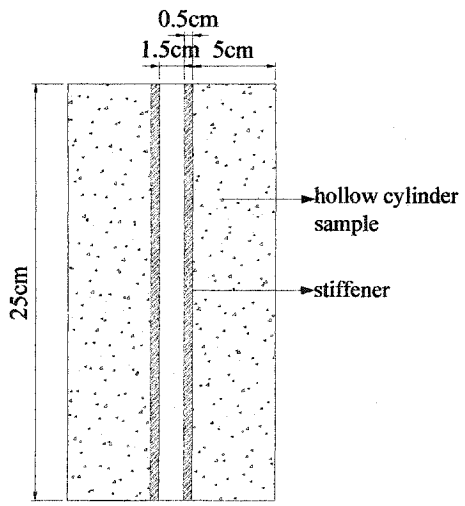

Figure A.6. Geometry of the hollow cylinder sample

Material Parameters

An elastic model was applied for modeling the steel-made stiffener. A Young's Modulus of 2.1e8 kPa and Poisson's ratio of 0.25 was used for the stiffener.

For the sample, a Drucker-Prager model was considered. Its Young's Modulus was considered 1.093e6 kPa and a Poisson's ratio of 0.44 was used. As for the Drucker-Prager model, cohesion of 460 kPa and friction and dilation angles of 37 and 13.8 were used respectively. These values are based on the experimental results of material characterization.

Loading Conditions

In the modeling, a lateral pressure of 3.34 MPa and an axial stress of 7.3 MPa were applied. The bottom of the sample was restrained in the axial direction. The top pressure had been applied only on the sample, considering the arrangement in the set-up which prevented transfer of load to the stiffener.

Analysis Assumptions

Axial symmetry was assumed in the modeling. Moreover, continuity in the mesh of stiffener and the sample was assumed for simplicity. The latter assumption was expected to disclose excessive vertical stresses in the stiffener as compared to the modelling in which contact elements are used.

Results and Discussions

Figure A.7 depicts the vertical stresses in the medium as well as the stiffener. The vertical stresses in the stiffener ranged between 0 to 134 MPa. This was well below the yield stress of steel, which is approximately 240 MPa. Therefore, it can be safely estimated that to reach the yield stress of the stiffener, an almost 13 MPa of axial pressure and 6 MPa of lateral pressure would be required.

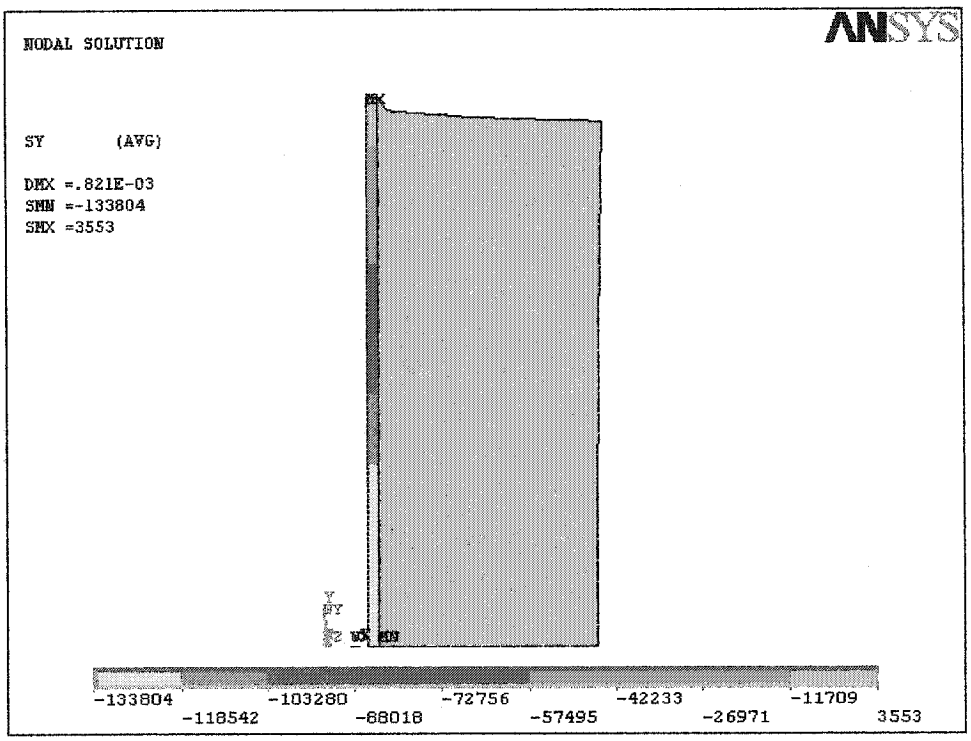

Figure A.7. Axial stress contours in the sample and stiffener

Figure A.8 shows the contours of tangential stresses in the medium as well as the stiffener. This figure is expected to provide a good estimate of the tangential stresses, since the modelling assumption of continuity between the sample and the stiffener does not affect tangential stresses as dramatically as it affects vertical stresses. As indicated in this figure, tangential stresses range between 0 to 22 MPa. This is far below the yield stress of steel, which is almost 240 MPa.

Figure A.9 illustrates the lateral displacement of the sample as well as the stiffener. The deformation of the stiffener is very small, which indicates that the stiffener of this material and thickness can be considered rigid. This ensures the ability to judge the interaction on the completion and the medium in one extreme case where the stiffener's deformation is extremely small. In that extreme, the maximum of volumetric stresses builds up in the sample. Figure A.9 also shows the tendency of the upper part of the sample to deform outward under the considered loading pattern.

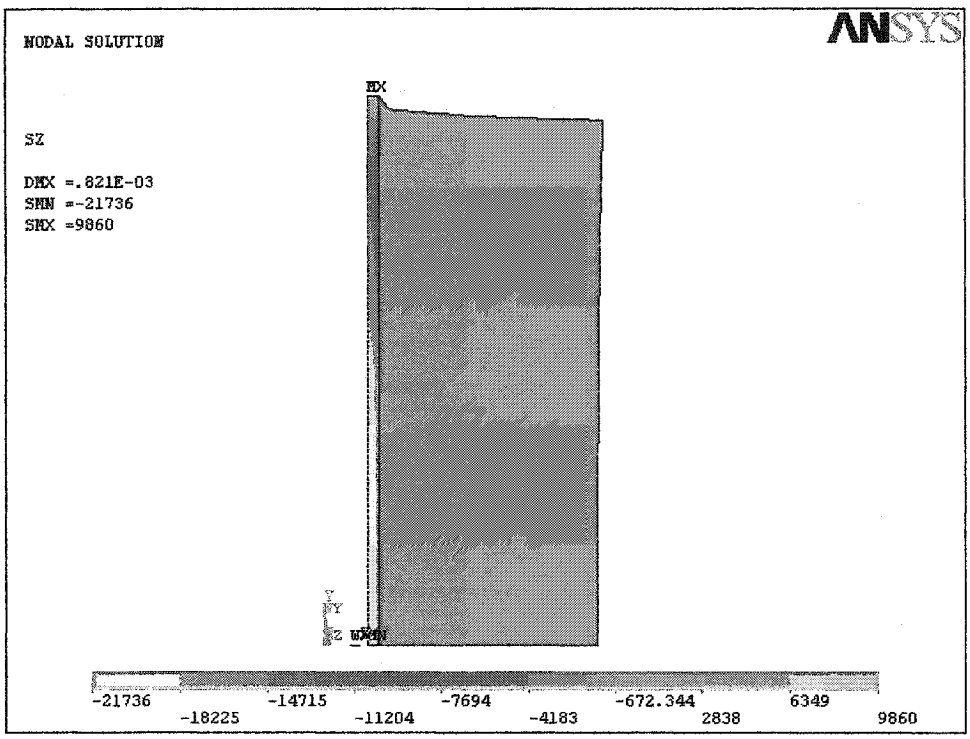

Figure A.8. Tangential stress contours in the sample and stiffener

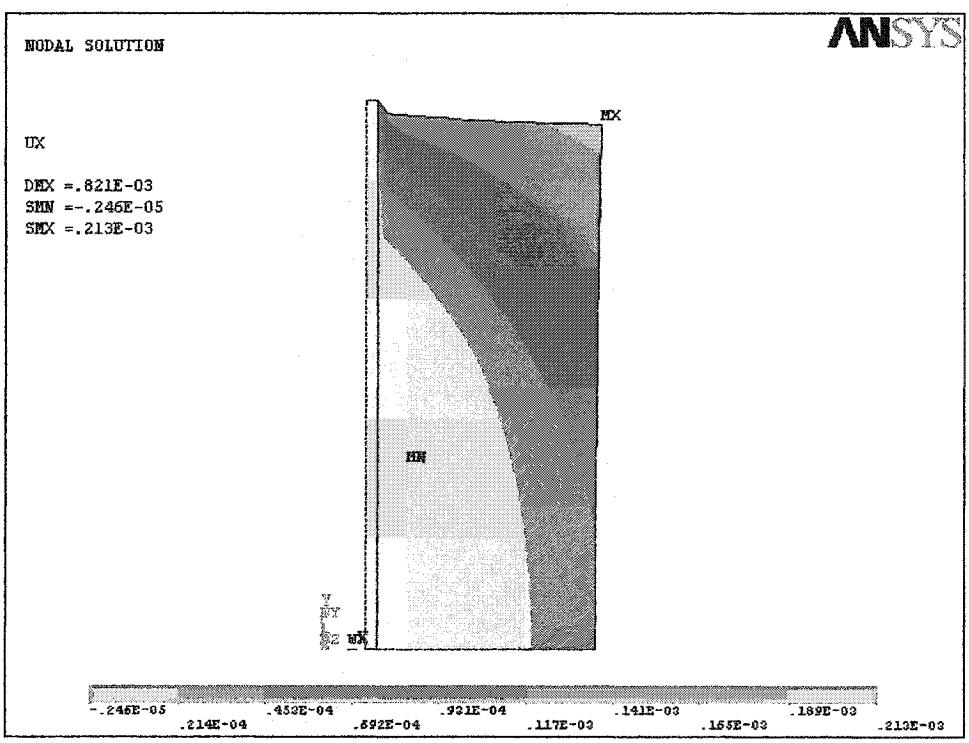

Figure A.9. Contours of radial displacement

References:

Papamichos, E., and P.J. van den Hoek, "Size dependency of Castlegate and Berea sandstone hollow cylinder strength", *Proc. 35th U.S. Symp. Rock Mech.*, Lake Tahoe, Nevada, pp. 301-306, Rotterdam, Balkema, 1995.

Van den Hoek, P.J., A.P. Kooijman, C.J. Kenter, M. Khodaverdian, C.R. Hyland, and J.D. McLennan, "Size Dependency of Hollow Cylinder Collapse Strength", *SPE 24800, 67th Annual Technical Conference and Exhibition of the Society of Petroleum Engineers*, Washington, DC, 1992.

Tronvol, J., E. Papamichos, and N. Kessler, "Perforation Cavity Stability: Investigation of Failure Mechanisms", *Geotech. Eng. of Hard Soils-Soft Rocks,* Balkema, Rotterdam, pp. 1687-1693, 1993.

Appendix B: Formulation of the Interaction of Fluid Flow and Solid Particles in Porous Media

Introduction

The objective of this appendix is to provide the mathematical formulation used in the analyses. Pore fluid interaction with the solid particles was considered which involves three mechanical effects. First, changes in pore pressure alter effective stresses. Second, the fluid in the void acts on the grain particles, therefore, inducing volume changes. Third, fluid flow may cause material removal from the cavity faces, which in turn induces stresses redistribution.

In the rest of this chapter, first the methodology and assumptions are introduced. Next, a set of partial differential governing equations are presented. Subsequently, a formulation of the Mohr-Coulomb constitutive law which was used in the modeling is discussed. Later, a finite difference alteration of the partial differential equations to algebraic form is treated. This appendix concludes with a discussion of how the formulation might be implemented.

Methodology

Partial differential equations (P.D.E.) of the governing laws, equilibrium and fluid flow, with a changing boundary condition and elastic-plastic model have no closed form solutions. The practical approach to solving such problems entails using numerical methods such as finite difference. In the finite difference method, a domain is divided into a number of zones (spatial discretization) in order to convert the P.D.E.'s into a system of algebraic equations.

The governing equations of equilibrium and fluid flow in the reservoir have been employed in an incremental form in a finite difference program, FLAC. Primary unknowns are solid velocities in three perpendicular directions and pore fluid pressure. Flow modeling may be performed by itself, independent of the usual mechanical calculations, or it may be conducted in parallel with the mechanical modeling, so as to capture the effects of fluid/solid interaction. In our analyses, the governing equations are solved simultaneously in a fully coupled manner. The objective is to incorporate all of the essential physics of the problem into the model while making simplifying assumptions.

FLAC uses explicit time-marching Lagrangian analysis in contrast to an Eulerian formulation. The incremental displacements can be added to the coordinates so that the grid moves and deforms with the material it represents. The constitutive formulation at each step is a small-strain one, but is equivalent to a large-strain formulation over many steps.

Even though FLAC finds a static solution to a problem, dynamic equations are included in the formulation. This ensures stability of the numerical schema where the physical system being modeled is unstable. With non-linear materials, there is always the possibility of such physical instability. FLAC models this process directly because the inertial terms are included in the formulation, in contrast to the schemes that must include some numerical procedures to treat physical instability. Even if the procedure is successful at preventing numerical instability, the path taken may not be a realistic one.

Different failure mechanisms have been considered in the model. To date, there has been no comprehensive mathematical model that considers all the mechanisms associated with sand production. The mechanisms include shear, tensile, and pore collapse.

The model presented in this thesis not only forecasts the initiation of sanding and the start of the failure, but provides the sanding volume and rate throughout the whole production process. The model is capable of giving an indication of the severity of sanding in real time during production. This knowledge is crucial for completion designers to make an on-time sand control plan that keeps production disruptions to a minimum. The important point, however, is the simplicity of the constitutive model employed: the Mohr-Coulomb model is one of the most recognized models for engineers whose parameters are physically sensed. By combining this model with a strain hardening/softening scheme, a powerful tool was provided which could simulate the complex behaviour of the medium and the disaggregation process.

Assumptions

In this study, the mixture of water and oil with occluded gas bubbles is considered as one fluid which flows through porous medium. As long as the gas remains in occluded form, the medium can be considered fully saturated and the effective stress principle whereby the pore pressure is represented by the pressure of the "equivalent compressible fluid" is

considered successful. The effect with respect to sanding of fluid compressibility was not a subject of this research.

Geomaterial behavior is considered elastoplastic. The Mohr-Coulomb and dilation characteristics of oilsand, as well as the leak-off phenomenon, will be investigated in detail. Strain hardening/softening concept is used in the modeling.

Even though the volume of solid grains changes as a result of the variations of the pore pressure, this phenomenon has little effect on the results, and has therefore been neglected.

Darcy's Law is assumed to be valid in the medium.

Degrees of Freedom

In the formulation, pore pressure and velocities in radial and vertical directions are taken as degrees of freedom.

Calculation Method

FLAC uses an explicit, time-marching solution scheme: the right hand side of all equations consist of known values, because the time step is chosen to be small. Therefore, information cannot physically transmit from one element to the other within that small time step.

The calculations consist of the following operations (Cundal and Board, 1988):

For all zones:

- Strain increments are derived from known nodal velocities.
- New stresses are derived from strain increments by using the constitutive model.

For all nodes:

- Nodal forces are derived from known stresses in surrounding zones.
- Updated velocities are calculated from forces using the law of motion.

Each FLAC quadrilateral is modeled as two overlaid pairs of constant stress triangles.

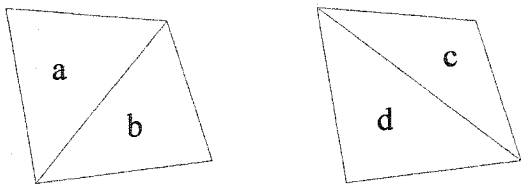

Figure B.1. Overlaid pairs of constant stress triangles

Each triangle maintains its stress component independently of the other triangles. Therefore, twelve stress components are stored for each quadrilateral in plane strain mode. The forces exerted on each node are taken to be the mean of those exerted by the quadrilaterals.

Generalized Gauss' Divergence Theorem

The difference equations for a generic triangle are derived from the generalized form of Gauss' divergence theorem (Malvern, 1969):

$$\oint_s n_i f ds = \int_A \frac{\partial f}{\partial x_i} dA \qquad [B.1]$$

where

$\oint_s$ = integral around the boundary of a closed area,

$\int_A$ = integral within the area,

n_i = the unit vector normal to the surface,

x_i = position vector,

f = a scalar, vector or tensor.

If the closed area is triangle, and f varies linearly along each side, we obtain the finite difference formula (Wilkins, 1969):

$$\left\langle \frac{\partial f}{\partial x_i} \right\rangle = \frac{1}{A} \sum_l \langle f \rangle n_i \Delta s \qquad [B.2]$$

where

$\sum_l$ = the summation over the three sides,

$\langle f \rangle$ = the average value of f over the side.

Strain Increments

[B.2] can be used to calculate the strain increments in terms of nodal velocities, $\dot{u}_i$, for a zone by substituting the velocity vector for f :

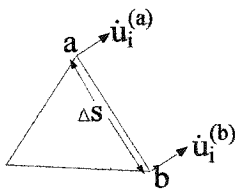

Figure B.2. Nodal velocities

$$\frac{\partial \dot{u}_i}{\partial x_j} = \frac{1}{2A} \sum_s (\dot{u}_i^{(a)} + \dot{u}_i^{(b)}) n_j \Delta s \qquad [B.3]$$

where

$\dot{u}_i^{(a)}$ = the velocity in "i" direction at node a (L/T).

From the definition of the strain (compatibility equation), the relation between strain rate and solid velocity gradient is:

$$\dot{\varepsilon}_{ij} = \frac{1}{2}\left[\frac{\partial \dot{u}_i}{\partial x_j} + \frac{\partial \dot{u}_j}{\partial x_i}\right] \qquad [B.4]$$

and so:

$$\Delta e_{ij} = \frac{1}{2}\left[\frac{\partial \dot{u}_i}{\partial x_j} + \frac{\partial \dot{u}_j}{\partial x_i}\right] \Delta t \qquad [B.5]$$

where

Δt = the time step (T).

The volumetric strain is then averaged over each pair of triangles, according to the mixed discretization scheme of Marti and Cundall (1982):

$$\Delta e_m = \frac{\Delta e_{11}^{(a)} + \Delta e_{22}^{(a)} + \Delta e_{11}^{(b)} + \Delta e_{22}^{(b)}}{2} \qquad [B.6]$$

$$\Delta e_d^{(a)} = \Delta e_{11}^{(a)} - \Delta e_{22}^{(a)} \qquad [B.7]$$

$$\Delta e_{11}^{(a)} := \frac{\Delta e_m + \Delta e_d^{(a)}}{2} \qquad [B.8]$$

$$\Delta e_{22}^{a} := \frac{\Delta e_m - \Delta e_d^{(a)}}{2} \qquad [B.9]$$

and similarly for the strains in (b) and for the triangle pair (c)-(d).

Stress Calculation

New zone effective stresses are computed by means of a specified constitutive law. According to Terzaghi, effective stress tensor, $\sigma_{ij}^{'}$, is defined as the subtract of the tensor of total stresses and pore pressure (Das, 1993):

$$\sigma_{ij}^{'} = \sigma_{ij} + P \qquad [B.10]$$

By convention, stresses and pore pressure are defined as negative and positive in compression, respectively.

Strain-Hardening/Softening Mohr-Coulomb Model

Stresses are computed from deformations by using constitutive laws. This constitutive law can have a general form as follows:

$$\sigma_{ij}^{'} = H\left(\sigma_{ij}^{'}, \varepsilon_{ij}, ...\right) \qquad [B.11]$$

where

H( )= constitutive model,

ε_{ij} = strain tensor.

The selected constitutive model may be elastic, which usually does not give realistic results for unconsolidated geomaterials, or elasto-plastic. An elaboration of

elastoplasticity can be found in the related textbooks and papers such as Desai and Siriwardane, (1984); and Vermeer and Borst, (1984).

Simulations conducted for this work used a Mohr-Coulomb model with a consideration of cohesion, friction, dilation, and tensile strength hardening or softening after the onset of plastic yield. These parameters can be defined as piecewise-linear functions of hardening parameters, measuring the plastic shear and tensile strain.

Incremental Elastic Law

The principal effective stresses and principal directions are evaluated from the effective stress tensor components and ordered so that compressive effective stresses are negative:

$$\sigma_1' \le \sigma_2' \le \sigma_3' \qquad \text{[B.12]}$$

The corresponding principal strain increments $\Delta e_1, \Delta e_2, \Delta e_3$ are decomposed as follows:

$$\Delta e_i = \Delta e_i^e + \Delta e_i^p \qquad \text{[B.13]}$$

where the subscripts "e" and "p" refer to elastic and plastic parts, respectively. The plastic components are zero during the elastic behaviour. The incremental expression of Hooke's law in terms of principal effective stress and strain has the form:

$$\Delta\sigma_i' = \alpha_1 \Delta e_i^e + \alpha_2 (\Delta e_j^e + \Delta e_k^e) \qquad \text{[B.14]}$$

where

$$\alpha_1 = K + 4G/3 \quad (\mathrm{F/L^2})$$

$$\alpha_2 = K - 2G/3 \quad (\mathrm{F/L^2})$$

Yield and Potential Functions

The shear failure envelope is defined by the Mohr-Coulomb yield function:

$$f^s = \sigma_1' - \sigma_3' N_\varphi + 2C\sqrt{N_\varphi} \qquad \text{[B.15]}$$

and the tension cut-off is defined as:

$$f^t = \sigma^{t} - \sigma_3' \qquad \text{[B.16]}$$

where

φ = friction angle,

C = cohesion (F/L^2),

σ^t = tensile strength (F/L^2),

$$N_\varphi = \frac{1+\sin\varphi}{1-\sin\varphi} \qquad \text{[B.17]}$$

The shear potential function g^s corresponds to a non-associated flow rule and has the form:

$$g^s = \sigma_1^{'} - \sigma_3^{'} N_\psi \qquad \text{[B.18]}$$

where

ψ = dilation angle,

$$N_\psi = \frac{1+\sin\psi}{1-\sin\psi} \qquad \text{[B.19]}$$

The associated flow rule for tensile failure is derived from the potential function g^t with

$$g^t = -\sigma_3^{'} \qquad \text{[B.20]}$$

Plastic Corrections

The flow rule has the form:

$$\Delta e_i^p = \lambda^s \frac{\partial g^s}{\partial \sigma_i} \qquad i = 1,3 \qquad \text{[B.21]}$$

where

λ^s = a positive number.

Using equation [B.18A] for g^s, these equations become:

$$\Delta e_1^p = \lambda^s \qquad \text{[B.22]}$$

$$\Delta e_2^p = 0$$

$$\Delta e_3^p = -\lambda^s N_\psi$$

Shear hardening parameter is defined as (Vermeer and deBorst, 1984)

$$\Delta e^{ps} = \left(\frac{1}{2}(\Delta e_1^{ps} - \Delta e_m^{ps})^2 + \frac{1}{2}(\Delta e_m^{ps})^2 + \frac{1}{2}(\Delta e_3^{ps} - \Delta e_m^{ps})^2 \right)^{\frac{1}{2}} \quad [B.23]$$

where

$$\Delta e_m^{ps} = \frac{1}{3}(\Delta e_1^{ps} + \Delta e_3^{ps}) \quad [B.24]$$

$\Delta e_j^{ps}, j = 1,3$ = the principal plastic shear strain increments.

The tensile hardening parameter e^{pt} measures the accumulated tensile plastic strain; its increment is defined as:

$$\Delta e^{pt} = \Delta e_3^{pt} \quad [B.25]$$

The tensile hardening parameter e_3^{pt} is the increment of tensile plastic strain in the direction of the minor principal effective stress.

Now friction angle, cohesion, dilation, and tensile strength are modified according to the new values of the shear and tensile strain hardening parameter.

The elastic strain increments may be expressed as the total strain increments minus the plastic strain increments.

$$\Delta e_i^e = \Delta e_i - \Delta e_i^p \quad [B.26]$$

therefore:

$$\Delta \sigma_1' = \alpha_1 \Delta e_1 + \alpha_2(\Delta e_2 + \Delta e_3) - \lambda^s(\alpha_1 - \alpha_2 N_\psi) \quad [B.27]$$

$$\Delta \sigma_2' = \alpha_1 \Delta e_2 + \alpha_2(\Delta e_1 + \Delta e_3) - \lambda^s \alpha_2(1 - N_\psi) \quad [B.28]$$

$$\Delta \sigma_3' = \alpha_1 \Delta e_3 + \alpha_2(\Delta e_1 + \Delta e_2) - \lambda^s(-\alpha_1 N_\psi + \alpha_2) \quad [B.29]$$

If the new and old effective stress states can be referred to by subscript N and O, respectively, then by definition:

$$\sigma_i'^N = \sigma_i'^o + \Delta \sigma_i' \quad [B.30]$$

Substituting in these equations the effective stress increments:

$$\sigma_1^{'N} = \sigma_1^{'I} - \lambda^s(\alpha_1 - \alpha_2 N_\psi) \quad [B.31]$$

$$\sigma_2^{'N} = \sigma_2^{'I} - \lambda^s \alpha_2 (1 - N_\psi) \quad [B.32]$$

$$\sigma_3^{'N} = \sigma_3^{'I} - \lambda^s(-\alpha_1 N_\psi + \alpha_2) \quad [B.33]$$

where subscript I is used to represent the elastic guess obtained by adding the old effective stresses and elastic increments computed by using the total strain increments.

$$\sigma_1^{'I} = \sigma_1^{'o} + \alpha_1 \Delta e_1 + \alpha_2(\Delta e_2 + \Delta e_3) \quad [B.34]$$

$$\sigma_2^{'I} = \sigma_2^{'o} + \alpha_1 \Delta e_2 + \alpha_2(\Delta e_1 + \Delta e_3) \quad [B.35]$$

$$\sigma_3^{'I} = \sigma_3^{'o} + \alpha_1 \Delta e_3 + \alpha_2(\Delta e_1 + \Delta e_2) \quad [B.36]$$

The parameter λ^s may now be defined by requiring that the new set of effective stresses be located on the shear yield surface. Substitution of σ_1^N and σ_3^N for σ_1 and σ_3 in $f^s = 0$ gives:

$$\lambda^s = \frac{f^s(\sigma_1^{'I}, \sigma_3^{'I})}{(\alpha_1 - \alpha_2 N_\psi) - (\alpha_2 - \alpha_1 N_\psi) N_\varphi} \quad [B.37]$$

In the case of tensile failure, the flow rule has the form:

$$\Delta e_i^p = \lambda^t \frac{\partial g^t}{\partial \sigma_i^{'}} \qquad i = 1,3 \quad [B.38]$$

Using the tensile potential function, plastic tensile strain increment is obtained:

$$\Delta e_1^p = 0 \quad [B.39]$$

$$\Delta e_2^p = 0 \quad [B.40]$$

$$\Delta e_3^p = -\lambda^t \quad [B.41]$$

By using these equations and substituting in equations of elastic effective stress increments, the new set of effective stresses are achieved:

$$\sigma_1^{'N} = \sigma_1^{'I} + \lambda^t \alpha_2 \qquad \text{[B.42]}$$

$$\sigma_2^{'N} = \sigma_2^{'I} + \lambda^t \alpha_2 \qquad \text{[B.43]}$$

$$\sigma_3^{'N} = \sigma_3^{'I} + \lambda^t \alpha_1 \qquad \text{[B.44]}$$

$$\text{and } \lambda^t = \frac{f^t(\sigma_3^I)}{\alpha_1} \qquad \text{[B.45]}$$

Mixed discretization is again used to equalize the isotropic effective stress between the two triangles in a pair:

$$\sigma_o^{'(a)} = \sigma_o^{'(b)} := \left[\frac{\sigma_o^{'(a)} A^{(a)} + \sigma_o^{'(b)} A^{(b)}}{A^{(a)} + A^{(b)}} \right] \qquad \text{[B.46]}$$

Mechanical Parameters in Hardening and Softening

In a Mohr-Coulomb hardening/softening model, rather than a constant friction angle, cohesion, dilation, and tensile strength; a plastic strain dependent quantity of these parameters are used.

Experience shows that the experimental curves from sand testing can usually be expressed in a simple form, e.g. the relationship:

$$\sin \overset{*}{\varphi} = 2 \frac{\sqrt{(\overset{-p}{\varepsilon}\ \varepsilon^f)}}{\overset{-p}{\varepsilon} + \varepsilon^f} \sin \phi \qquad \text{for } \overset{-p}{\varepsilon} < \varepsilon^f \qquad \text{[B.47]}$$

$$\sin \overset{*}{\varphi} = \sin \varphi \qquad \text{for } \overset{-p}{\varepsilon} > \varepsilon^f \qquad \text{[B.48]}$$

The mobilized friction angle gradually increases with strain to reach the limit friction angle when $\overset{-p}{\varepsilon}$ has reached the constant ε^f.

Test results have also indicated that concurrent to friction hardening, applying softening to the cohesion best models the behaviour of the material. A possible choice of this relationship is:

$$\overset{*}{C} = C \exp\left[-\left(\frac{\overset{-p}{\varepsilon}}{\varepsilon^{c}} \right)^{2} \right] \qquad [B.49]$$

where

ε^{c} = a constant similar to ε^{f} in the hardening relation for the mobilised friction angle.

The hardening and softening relations for friction angle and cohesion are schematically plotted in the following figure.

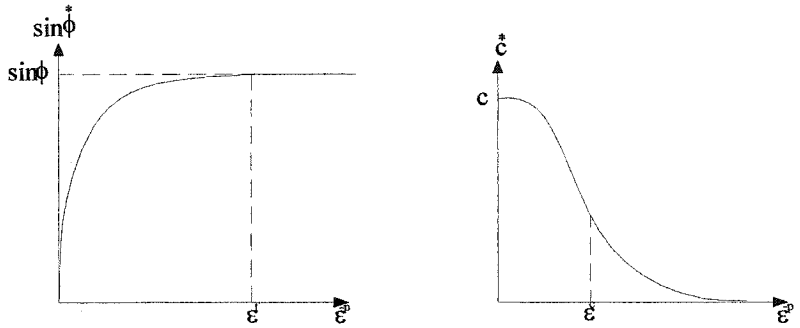

Figure B.3. Schematic variation of cohesion and friction angle with plastic strain intensity

A relationship between the mobilized dilatancy angle and the effective strain has been proposed (Vermeer and de Borst, 1984).

$$\sin \overset{*}{\psi} = \frac{\sin \overset{*}{\varphi} - \sin \varphi_{cv}}{1 - \sin \overset{*}{\varphi} \sin \varphi_{cv}} \qquad [B.50]$$

The constant φ_{cv} is readily calculated from the limit dilatancy angle ψ and limit friction angle φ.

$$\sin \varphi_{cv} = \frac{\sin \varphi - \sin \psi}{1 - \sin \varphi \sin \psi} \qquad [B.51]$$

Equation of Motion

The net force on a node is calculated from the summation of forces imposed by the zones surrounding the node. The force that one triangle contributes to the node is found from the stress vector acting on the edges of the triangle:

$$F_i = \frac{\sigma_{ij}\left[n_j^{(1)} s^{(1)} + n_j^{(2)} s^{(2)}\right]}{2} \qquad [B.52]$$

At equilibrium, or steady-state flow, the net force $\sum F_i$ on a node is zero. The acceleration is integrated numerically to obtain velocities:

$$\dot{u}_i := \dot{u}_i + \left[\sum F_i - \alpha \left|\sum F_i\right| \mathrm{sgn}\left(\dot{u}_i\right)\right]\frac{\Delta t}{m} + g_i \Delta t \qquad [B.53]$$

where

m= inertial mass of a node (M),

g_i = gravitational acceleration (L/T^2),

α damping factor.

Mass Balance Equation

A continuity equation is derived for a single-phase (equivalent) flow. Consider an arbitrary volume V_v (void volume) fixed in space, bounded by surface S, as shown in Figure B.1. If a continuous medium of density ρ_f fills the volume at time t, the total mass in V is:

$$M = \int_{V_V} \rho_f dV_v \qquad [B.54]$$

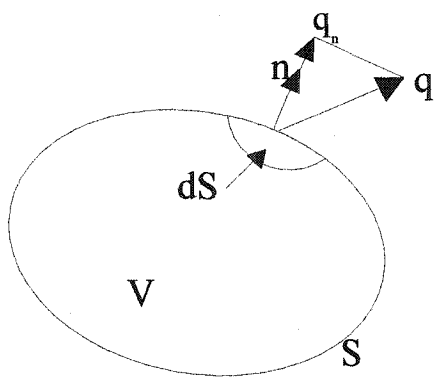

Figure B.4. Reference Volume in Space

The density of ρ_f depends on position and time. The existence of a piecewise continuous density function giving the total mass by [B.5] is postulated as part of the definition of a continuous medium. The rate of change of the total mass in the void volume is:

$$\frac{dM}{dt} = \frac{d}{dt}\int_{V_t} \rho_f dV \qquad [B.55]$$

The above integration in a system can be transformed into an integration within a control volume.

$$= \frac{d}{dt}\int_{V_0} \rho_f J dV_0 \qquad [B.56]$$

Where

J is Jacobian of transformation.

$$= \int_{V_0}\left\{\frac{d\rho_f}{dt}J + \rho_f \frac{dJ}{dt}\right\}dV_0 \qquad [B.57]$$

$$= \int_{V0}\left[\frac{d\rho_f}{dt} + \rho_f\left(\bar{\nabla}.\bar{v}\right)\right]JdV_0 \qquad [B.58]$$

A reverse transformation converts [B.58] to:

$$= \int_{V_t}\left[\frac{\partial\rho_f}{\partial t} + \bar{\nabla}.\left(\rho_f \bar{v}\right)\right]dV \qquad [B.59]$$

$$= \int_{V_t}\frac{\partial\rho_f}{\partial t}dV + \int_{V_t}\left[\nabla.\left(\rho_f \bar{v}\right)\right]dV \qquad [B.60]$$

Ultimately:

$$\frac{dM}{dt} = \frac{\partial}{\partial t}\int_{V_t}\rho_f dV + \int_{S_t}\rho_f \bar{v}.\bar{n}\, dS \qquad [B.61]$$

In porous medium with a porosity ϕ and the fluid system in the voids [B.61] is reshaped to:

$$\frac{dM}{dt} = \frac{\partial}{\partial t}\int_{V_{vt}} \rho_f dV_v + \int_{S_i} \rho_f \upsilon_i n_i \phi dS \qquad [B.55]$$

where

υ_i = the real velocity (L/T),

V_{vt} .= void volume (L^3)

Using the divergence theorem (Malvern, 1969), we get:

$$\int_V \frac{\partial(\rho_f \phi)}{\partial t} dV = -\int_V \frac{\partial}{\partial x_i}(\rho_f v_i) dV \qquad [B.56]$$

where

v_i is the vector of Darcy velocity.

$$\rho_f \frac{\partial \phi}{\partial t} + \phi \frac{\partial \rho_f}{\partial t} = -\frac{\partial}{\partial x_i}(\rho_f v_i) \qquad [B.57]$$

Therefore:

$$\rho_f \frac{\partial}{\partial t}(\frac{\phi V}{V}) + \phi \frac{\partial \rho_f}{\partial t} = \rho_f \frac{\partial}{\partial t}(\frac{V_v}{V}) + \phi \frac{\partial \rho_f}{\partial t} = -\frac{\partial}{\partial x_i}(q_i) \qquad [B.58]$$

where

q_i = the mass discharge ((M/T)/L^2).

For 100% saturation:

$$\rho_f \frac{\partial}{\partial t}(\frac{V_f}{V}) + \phi \frac{\partial \rho_f}{\partial t} = -\frac{\partial}{\partial x_i}(q_i) \qquad [B.59]$$

If ξ is defined as the change of volume of fluid in unit volume of porous material:

$$\rho_f \frac{\partial \xi}{\partial t} + \phi \frac{\partial \rho_f}{\partial t} = -\frac{\partial}{\partial x_i}(q_i) \qquad [B.60]$$

In case of presence of fluid flow source of q_v:

$$\rho_f \frac{\partial \xi}{\partial t} + \phi \frac{\partial \rho_f}{\partial t} = -\frac{\partial}{\partial x_i}(q_i) + q_v \qquad [B.61]$$

where

q_v = the input fluid mass per unit volume ((M/T)/ L^3).

Transport Law

The fluid transport can be described by Darcy's Law. In tensor notation it is formulated as:

$$v_i = -K_{ij} \frac{\partial}{\partial x_j}(P - \rho_f g_k x_k) \qquad [B.62]$$

where

K_{ij} = the mobility tensor (L^3T/M).

Neglecting gravity for the moment (it will be incorporated later), Darcy's Law for an anisotropic porous medium is:

$$v_i = -K_{ij} \frac{\partial P}{\partial xj} \qquad [B.63]$$

Each quadrilateral is divided into triangles in two different ways. The vector v can be derived for a generic triangle, and using [B.2]:

$$v_i = \frac{K_{ij}}{A} \sum P n_j s \qquad [B.64]$$

where

$\sum$ = the summation over the three sides of the triangle.

The two components of v are:

$$v_1 = \frac{1}{A}\left[K_{11} \sum P n_1 s + K_{12} \sum P n_2 s\right] \qquad [B.65]$$

$$v_2 = \frac{1}{A}\left[K_{21} \sum P n_1 s + K_{22} \sum P n_2 s\right] \qquad [B.66]$$

Considering, for example, the contribution of side "ab" of the triangle to the summation,

$$v_1^{(ab)} = \frac{1}{2A}\left[-K_{11}(P^{(b)} + P^{(a)})(x_2^{(b)} - x_2^{(a)}) + K_{12}(P^{(b)} + P^{(a)})(x_1^{(b)} - x_1^{(a)})\right] \quad \text{[B.67]}$$

$$v_2^{(ab)} = \frac{1}{2A}\left[-K_{21}(P^{(b)} + P^{(a)})(x_2^{(b)} - x_2^{(a)}) + K_{22}(P^{(b)} + P^{(a)})(x_1^{(b)} - x_1^{(a)})\right] \quad \text{[B.68]}$$

The other two sides, "bc" and "ca", provide a similar contribution to v_i. This specific discharge vector contribution is then converted to scalar volumetric flow rates at the nodes by making dot products with the normal to the three sides of the triangle. The general expression is:

$$Q = v_i n_i s \quad \text{[B.69]}$$

For example the flow rate into node (a) is

$$Q^{(a)} = \left(-v_1\left(x_2^{(b)} - x_2^{(c)}\right) + v_2\left(x_1^{(b)} - x_1^{(c)}\right)\right)/2 \quad \text{[B.70]}$$

The factor 2 accounts for the fact that the node only captures half the flow crossing a neighbouring edge (since the other half goes to the other node of the edge). Similar expressions apply for nodes (b) and (c). Nodal flow rates are added from the three triangles meeting at the node and divided by two, since the flow sum comes from two overlaid grids. The stiffness matrix, M, of the whole quadrilateral element is defined in terms of the relation between the pressures at the four nodes and the four nodal flow rates:

$$\{Q\} = \{M\}\{P\} \quad \text{[B.71]}$$

The effect of gravity is incorporated by noting that if the gridpoint pressures around a zone conform to the gradient $\frac{\partial P}{\partial x_i} = g_i \rho_w$, where g_i is the vector of gravitational acceleration, then the nodal flow rates $\{Q\}$ should be zero. Hence the equation is modified to:

$$\{Q\} = \{M\}\left\{P - \left(x_i - x_i^{(1)}\right)g_i \rho_w\right\} \quad \text{[B.72]}$$

The flow imbalance, $\sum Q$, at a node causes a change in pore pressure at a saturated node as follows:

$$\frac{\partial P}{\partial t} = -\frac{K_w}{\phi V}\left(-\sum Q + \frac{\partial V}{\partial t}\right) \qquad \text{[B.73]}$$

where

ϕV = the pore volume associated with the node (L^3),

ϕ = porosity,

V = the total volume (L^3).

The term $\sum Q$ includes contributions from the four surrounding zones.

In finite difference this equation becomes:

$$P := P - \frac{K_w(\sum -Q\Delta t + \Delta V_{mech})}{\phi V} \qquad \text{[B.74]}$$

where

ΔV_{mech} = the equivalent nodal volume increase arising from mechanical deformation of the grid (L^3).

The term ϕV is computed as the sum of the contributions from all triangular sub-zones connected to the node. Each triangle contributes a third of its volume-porosity product; the resulting sum is divided by two to account for the double overlay of the zones.

Constitutive Law of Fluid

The response equation for the pore fluid can be written as:

$$\frac{\partial P}{\partial t} = \frac{K_f}{\phi}\left(\frac{\partial \xi}{\partial t} - \frac{\partial \varepsilon_v}{\partial t}\right) \qquad \text{[B.75]}$$

where

K_f = the bulk modulus of the fluid (F/L^2),

ε_v = volumetric strain of solid.

Variation of Permeability with Porosity

In a material devolution process, permeability changes occur as a result of material dilation, fine movements, porosity changes, and so on. In the numerical analysis, whenever the live data of permeability during the test was not available, it was estimated by applying the Kozeny-Carman equation. This equation estimates the variation of permeability with the change of porosity during the loading process.

$$K = C\frac{\phi^3}{1-\phi} \qquad [B.76]$$

where

ϕ = porosity,

C= a constant which is calculated based on the initial porosity and permeability.

Implementation process

In the implementation process, discharge velocity is computed from [B.67] and [B.68] by using the existing nodal pressures. Discharge velocities are computed for each triangle. Volumetric flow rates at nodes are obtained from the zonal discharge velocity by using [B.72]. Iteration is conducted in which nodal pressures are modified from the flow imbalance at nodes, and again the computation of discharge velocities was reached by using the modified pressures. After the balance is achieved, the variation of fluid volume is computed from [B.61] and substituted at [B.75] to obtain the changes in pore pressure. The achieved pore pressures are used in the next step of mechanical calculations to obtain effective stresses.

In the implementation of the mechanical portion, strains are computed from the velocities. New effective stresses for this step are computed assuming elasticity. Plastic strains are then computed and effective stresses are modified for the plasticity effect. Hardening parameters, and effective strain are updated, and mechanical parameters are modified. New stresses are used to evaluate unbalanced forces at the nodes and the equation of motion is used to calculate the nodal velocity. Strains are incremented for the effect of the computed velocity and computation goes on.

References

Cundall, P.A., and M. Board, "A Microcomputer Program for Modelling Large-Strain Plasticity Problems", in *Numerical Methods in Geomechanics. & Proc. 6th Int. Conf. on Numerical Methods in Geomechanics*, Innsbruck, Austria, April 11-15, Swododa C.(ed), Rotterdam, Balkema, pp. 2101-2108, 1988.

Das, B.M., *Principles of Geotechnical Engineering*, PWS Publishing Co., Boston, 1993.

Desai, C.S. and H.J. Siriwardane, *Constitutive Laws for Engineering Materials with Emphasis on Geologic Material*, Prentice-Hall Publishing Co., 1984.

Malvern, L.E., *Introduction to the Mechanics of a Continuous Medium*, Prentice-Hall Publishing Co., 1969.

Vermeer, P.A., and R. de Borst, "Non-Associated Plasticity for Soils", *Concrete and Rock*, **29**, no. 3, pp. 1-64, 1984.

Wilkins, M.L., "Calculation of Elastic-Plastic Flow", *Report UCRL-7322*, Lawrence Radiation Laboratory, Livermore, 1969.

Appendix C: Material Properties

Introduction

The objective of this appendix is to provide the material parameters of the synthetic sandstone samples that were used in the experimental program. These parameters are required for conducting the numerical analysis as well as the design of the sand production experiments.

Experimental Procedure

Three types of experiments were considered. They included Uniaxial Compressive Strength (UCS), Uniaxial Strain Test (UST), and Conventional Triaxial Compression (CTC).

In UST experiments, samples were first taken under conditions of *in situ* stress. Subsequently, the depletion process was simulated by dropping the pore pressure where no lateral deformation was allowed in the sample. These tests were mainly designed to determine the stress state at pore collapse. The depletion process takes place in the reservoir during production as well as in the medium around the wellbore supported by gravel packing or expandable techniques.

CTC experiments were performed to determine the shear envelope of the samples. CTC and UCS experiments were conducted on samples of both coarse and fine grained. UST experiments were conducted on coarse grained samples.

The Set-Up Used for Mechanical Characterization

The triaxial set up that was used for specifying shear and cap envelopes is shown in Figure C.1. Test equipments include a loading unit, a back pressure supplier, and instrumentation.

Loading Unit

The individual components are:

- A 250 KN axial loading system with feedback control and continuous displays of axial load and platen displacement.
- A high pressure triaxial cell which allows confining pressure of up to 64 MPa (10000 psi).

- A 128 MPa (20000 psi) Digital Pressure/Volume Controllers for supplying the confining pressure.
- Two 64 MPa (10000 psi) Digital Pressure/Volume Controllers for supplying back pressure and base pressure (base pressure is different from back pressure if permeability is to be measured).

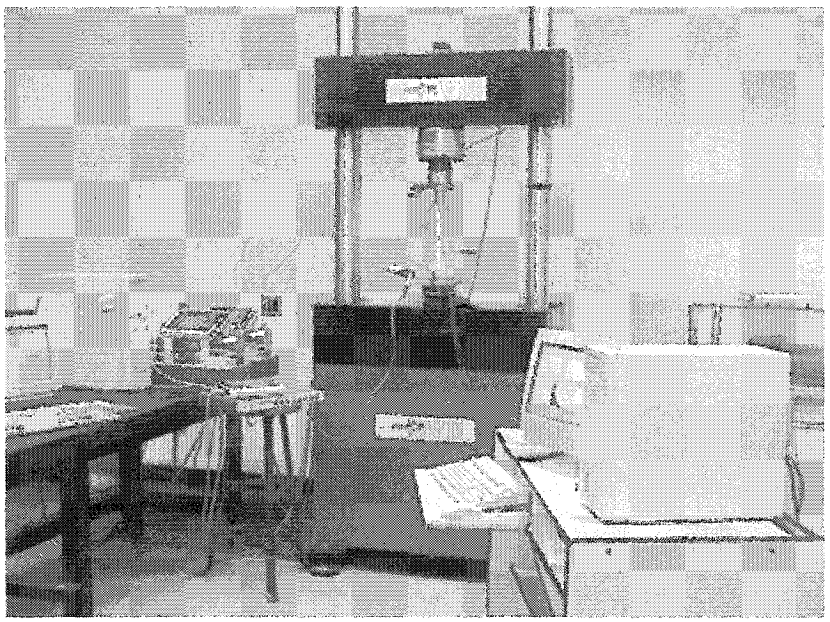

Figure C.1. An image of the experimental set-up for material mechanical description

Instrumentation

Both axial load and displacements were measured by built-in load and displacement transducers on the loading frame. Confining and back pressures were measured and displayed by the built-in pressure transducer of the confining and back pressure Digital Pressure/Volume Controllers.

Constitutive Model Identification

In order to capture the physics of the failure and consider the possible contribution of all possible failure mechanisms, the use of a bilinear Mohr-Coulomb mixed hardening/softening model is helpful. A schematic of the model is depicted in Figure C.2.

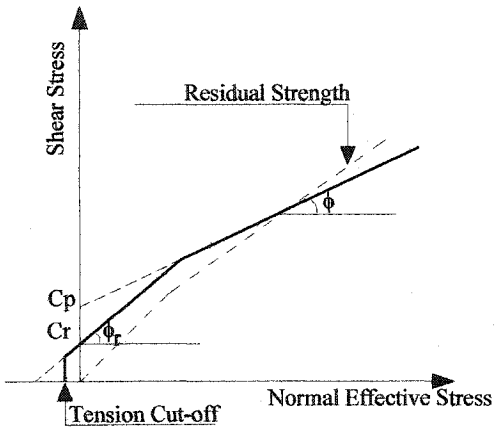

Figure C.2. Bilinear strain hardening/softening Mohr-Coulomb model

According to the model, tensile failure takes place when the stress tensor meets the tension cut-off. Shear failure occurs when the stress tensor touches the shear envelope.

Results of UCS Experiments on Synthetic Samples

A number of UCS experiments on samples with coarse grain distribution of various ages were conducted. The results of these experiments are reflected in Figure C.3. This graph shows that in the first five days more than 80% of the strength is gained.

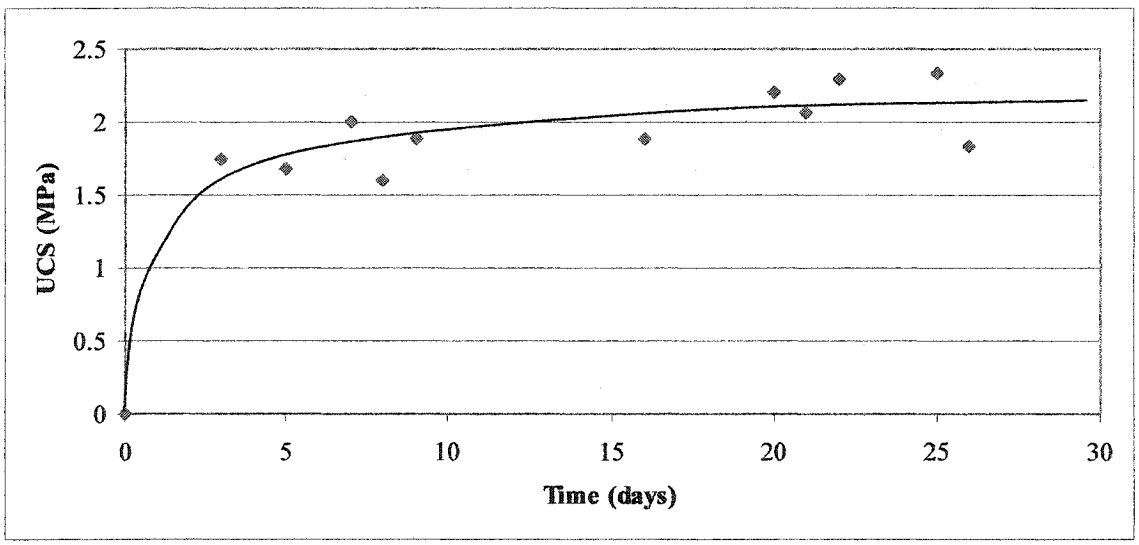

Figure C.3. UCS of artificial coarse grained samples with time

In addition, two UCS experiments on fine grain samples of 125 mm in diameter and 250 mm in height were conducted. The samples were saturated with water. The experiments concluded a UCS of 1030 kPa for both of the samples.

Results of CTC Experiments on Synthetic Samples

CTC experiments were conducted on both coarse and fine grained samples.

CTC Experiments on Coarse Grained Samples

CTC experiments were conducted on several samples under different confining pressures from 200 to 4000 kPa. Figure C.4 depicts the results of such experiments. The response of the samples under confining pressures of 200, and 750 kPa are typical, as an initial elastic response is followed by a flat peak in the curve. Moreover, the peak strength increases with radial stress. Compaction of the sample in confining pressures above 2 MPa results in a hardening phase past the yield stress.

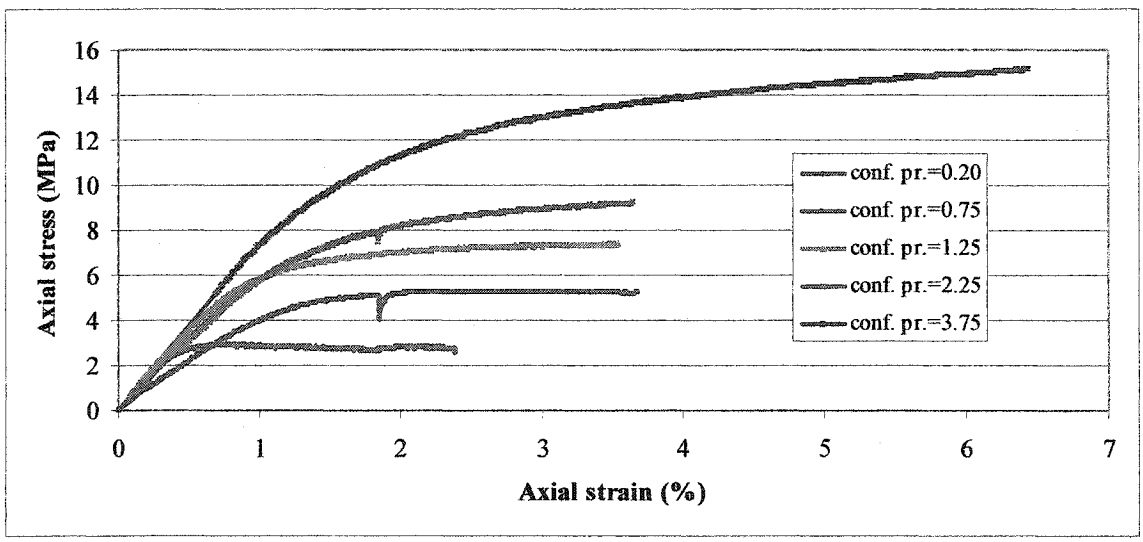

Figure C.4. CTC strength of coarse grained synthetic samples under different confining pressures

CTC Experiments on Fine Grained Sandstone

The response of fine grained samples in CTC experiments is depicted in Figure C.5. The experiments were conducted under confining pressures of 300, 500, 1000, and 4000 kPa.

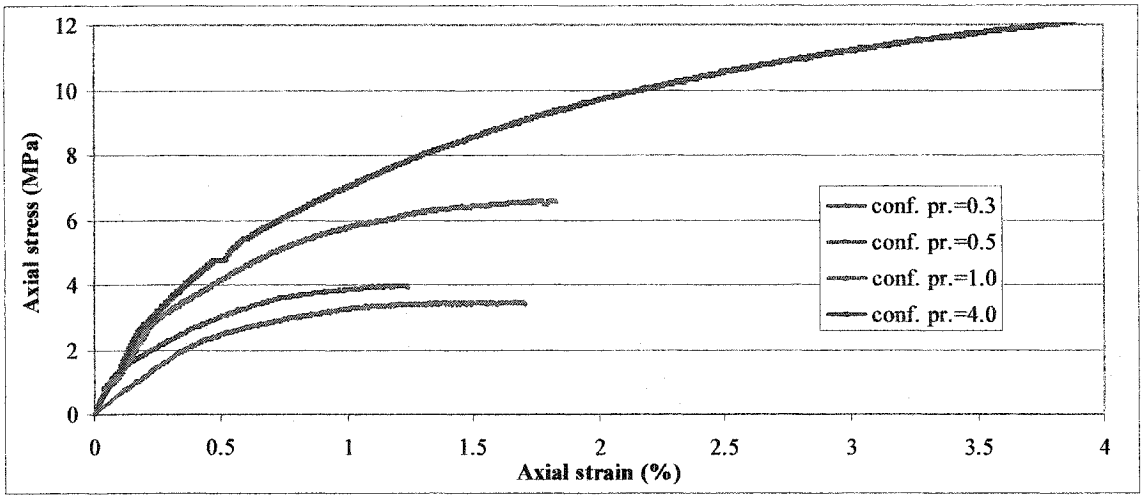

Figure C.5. CTC strength of coarse grained synthetic samples under different confining pressures

Mohr-Coulomb Envelope of Synthetic Samples

Table C.1 summarizes the mechanical properties of the artificial sandstones. Mohr-Coulomb circles and shear envelopes of coarse and fine grained samples are shown in Figures C.6 and C.7.

Table C.1. Mechanical properties of the artificial sandstone

	UCS (MPa)	Young's modulus E (MPa)	ν	C_p (kPa)	C_r (kPa)	φ (degrees)	φ_r (degrees)
Coarse grained	2.1	400	0.05	810	480	34	39
Fine grained	1.03	-	-	1230	425	26	38

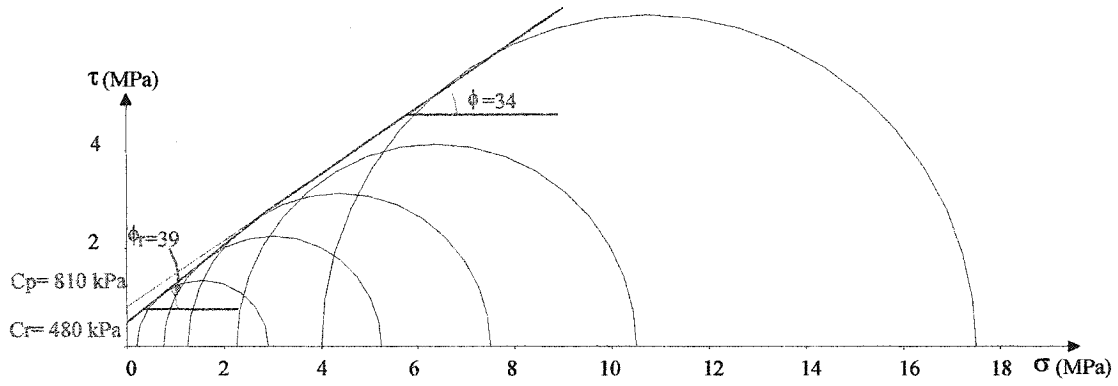

Figure C.6. Mohr-Coulomb envelope of the coarse grained synthetic sandstone

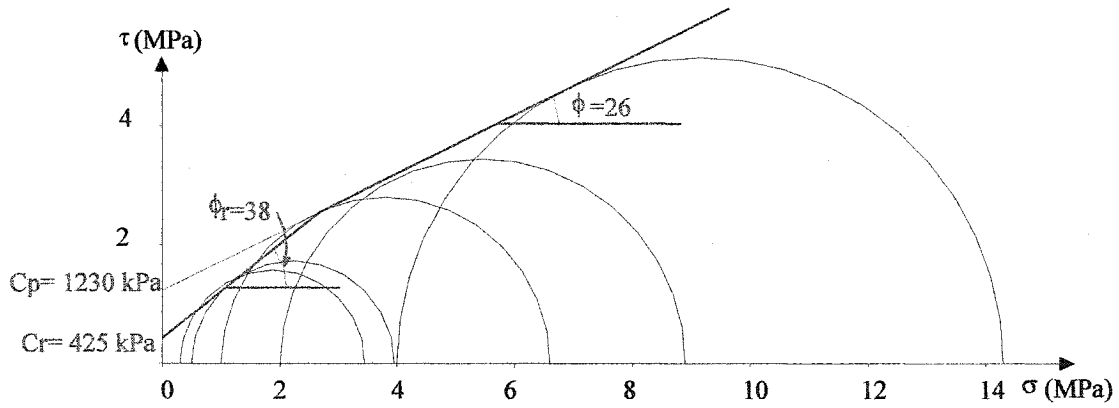

Figure C.7. Mohr-Coulomb envelope of the fine grained synthetic sandstone

Shear envelopes of the fine and coarse grained samples are also illustrated in Figure C.8. The symbol data (without a trend line) in Figure C.8 represent the pore collapse state in uniaxial strain experiments whose detail is presented in Appendix D. At first glance, the data of pore collapse may appear to have dispersed. However, keeping in mind the weak consolidation of the samples, the first invariant of effective stresses of all the data points range less than 4 MPa. Small changes in cementation between the grains would cause differences in pore collapse status.

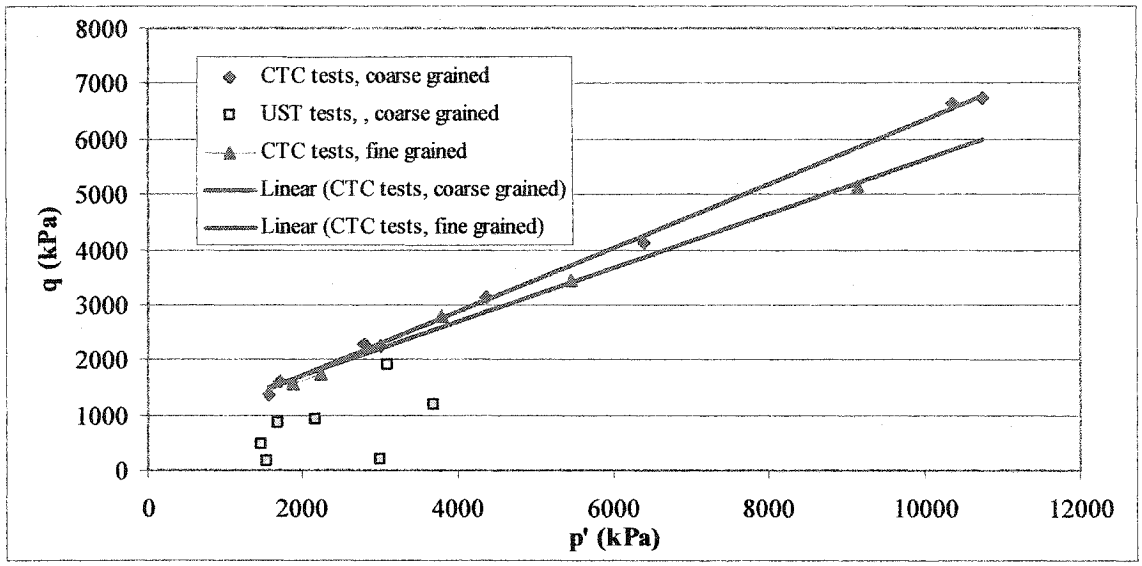

Figure C.8. Shear envelope and pore collapse data of the synthetic sandstone

Appendix D: Experimental Studies of Pore Collapse

Introduction

Experimental studies of pore collapse is important, since an expandable completion is expected to develop high volumetric stresses in the medium around the wellbore. This importance is two-fold: how high is the mean stress state associated with pore collapse, and if it occurs, how extensive is the damage that it causes to the rock? This appendix studies the first concern. (The second concern is addressed in Chapter 5.)

Substantial research has been conducted on the subject of pore collapse and its possible product - land subsidence. Extensive pore collapse of depleted reservoirs have been reported for a number of reservoirs, e.g. the Ekofisk field (Lawrence et al., 1991). Hamilton and Shafer (1991) studied pore collapse characteristics of a high porosity diatomite and carbonate rock.

The pore collapse pressure corresponding to cap pressure depends highly on porosity and UCS (or any another strength representative) of a sample. As an example, Soares and Ferreira (2002) reported test results of pore collapse experiments on limestone samples taken from the Campos basin with a porosity in the range of 20 to 35%. Cap pressure of these samples ranged from almost 40 MPa for samples with 31% porosity to almost 90 MPa for those with 20% porosity.

At the other extreme, Hamilton and Shafer (1991) experimented with fine grained diatomite with a porosity over 50% and concluded a cap pressure of almost 3 MPa. They also performed the same test on carbonate samples with over 20% porosity, and the cap pressure was 24 MPa. For the Ekofisk field the pore collapse of the chalk medium resulted in over four meters of sea floor subsidence. A cap pressure of almost 22 MPa was concluded (Lawrence et al., 1991).

Similar tests were performed by Ditzhuijzen et al. (1984) on samples from offshore Sarawak. Mouldic limestone and dolomite samples ranged from 26.8 to 40.7% in porosity. Mouldic limestone samples resulted in 15 to 36 MPa vertical failure stress. Dolomitic samples ranged from 33 to 47 MPa. Smits et al. (1986) reported a pore collapse vertical effective stress of 20 MPa to 50 MPa for Mouldic limestone with porosity in the range of 27 to 39%. They also concluded a failure stress of 18 MPa to 60

MPa for Danian and Maastrichtian chalk samples that were in range of 35 to 50% porosity.

Experimental Studies of Pore Collapse

Experimental studies of pore collapse pressure used both synthetic samples and samples taken from outcrops. The experiments on synthetic samples were elaborated upon in Appendix C. In the following paragraphs, the experiments on two consolidated sandstone samples that were conducted under uniaxial strain condition are discussed.

Table D.1 shows some of the properties of these two samples, namely, Glass Sandstone Fine-grained (GSF) and the Middle member of the Horton Bluff formation (MHB). Both of the samples were retrieved from an outcrop in Windsor, Nova Scotia (Canada). The GSF samples were taken from the uppermost portion of the Horton Bluff Formation. The unit is dominated (90% or more) by quartzarenites. MHB samples are predominantly of black to grey shale, coaly shale, siltstone, and nodular carbonate beds.

Table D.1. Characteristics of the samples used in the experiments

Sample	Initial porosity	γ_d (gr/cm^3)	γ_{sat} (gr/cm^3)	UCS (MPa)
MHB	23	2.00	2.23	45
GSF	13	2.24	2.37	57

Results of Uniaxial Strain Tests (UST)

Experiment on Synthetic Coarse Grained Samples

At relatively high mean effective stresses and low shear stresses, pore collapse is a possible mechanism of failure. At this point, inter-particle bonds between the grains begin to collapse. In brittle material, pore collapse can be very quick, while in less compressible material it can be more gradual. In the case of a quick pore collapse, pore pressure may increase in the failed zone because of the tendency for material compression. In this case, effective stress decreases. Following pore collapse, compacting behaviour takes place at a lower stress level. With increasing strain, the average inter-granular stress increases, and very high strains may be achieved in higher stresses. The strain hardening behaviour after pore collapse occurs in a completely

different microstructure than the original one, and is therefore different from the original strain hardening behaviour. High porosity, low strength, and high mean effective stresses at relatively low differential stresses increase the chance of pore collapse. A cap model is needed to capture this behaviour in a mathematical modeling.

Results of UST experiments are shown in Figure D.1. This figure consists of three pairs of curves each containing a curve of effective radial and axial stresses. The pairs of curves are illustrated in the same color. These three pairs are representative of many more experiments of the same type. In these curves, the point of pore collapse can be recognized by a sudden change of the slope of stress-strain curve. Figure D.1 shows that a very drastic pore collapse and volumetric deformation takes place in low strength samples. It is only after a dramatic compaction and grain rearrangement that the hardening phase resumes, which follows more compaction accompanying strength gain. Stronger materials show higher failure stress and a less significant stress-strain slope change. In these samples, the hardening phase started immediately following the failure.

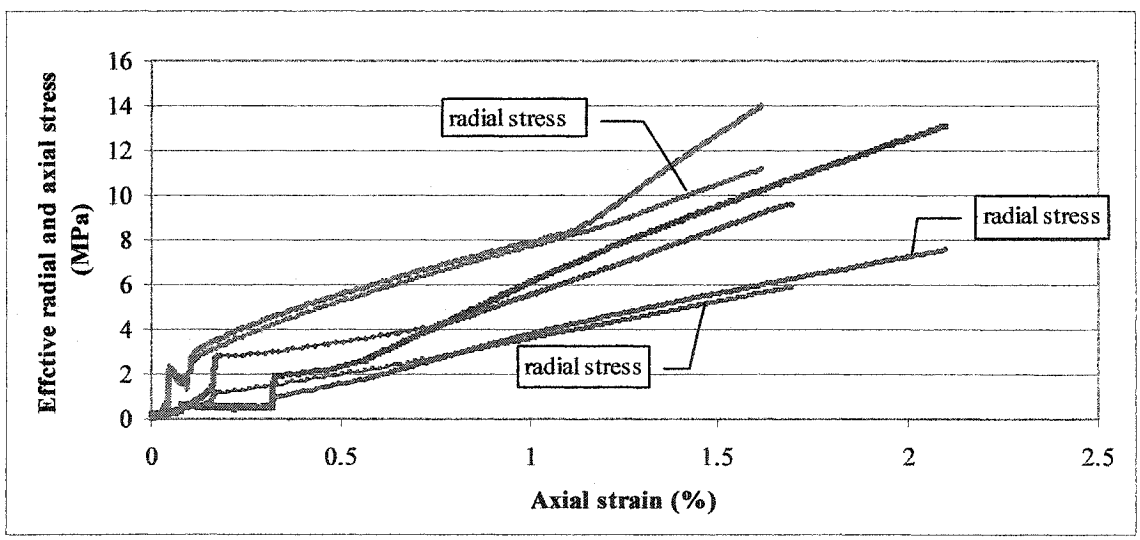

Figure D.1. Three couples of radial and axial effective stresses from uniaxial strain experiments

Experiment on the MHB Sample

For the MHB sample, first axial stress was increased, when radial pressure and backpressure were constant at 3445 kPa and 2000 kPa, respectively. Subsequently, the

sample was unloaded as depicted in Figure D.2. This figure shows a predominantly elastic behaviour in this cycle.

In the next stage, confining pressure was increased from 3445 to 67445 kPa, axial stress was increased from 5167 to 69167 kPa, and back pressure was increased from 2500 to 64000 kPa. Depletion of the sample under the uniaxial strain condition is the next stage of the experiment with a gradual decrease of back pressure to an ultimate level of 6000 kPa. The uniaxial strain condition was enforced by keeping the confining volume constant. Figure D.3 shows the effective axial increase as pore pressure depleted. Radial effective stress increased almost as much as axial stress did. This was attributed to the extreme stiffness of the sample causing little lateral deformation of the sample. Consequently, few changes in the level of confining pressure were induced in the course of depletion.

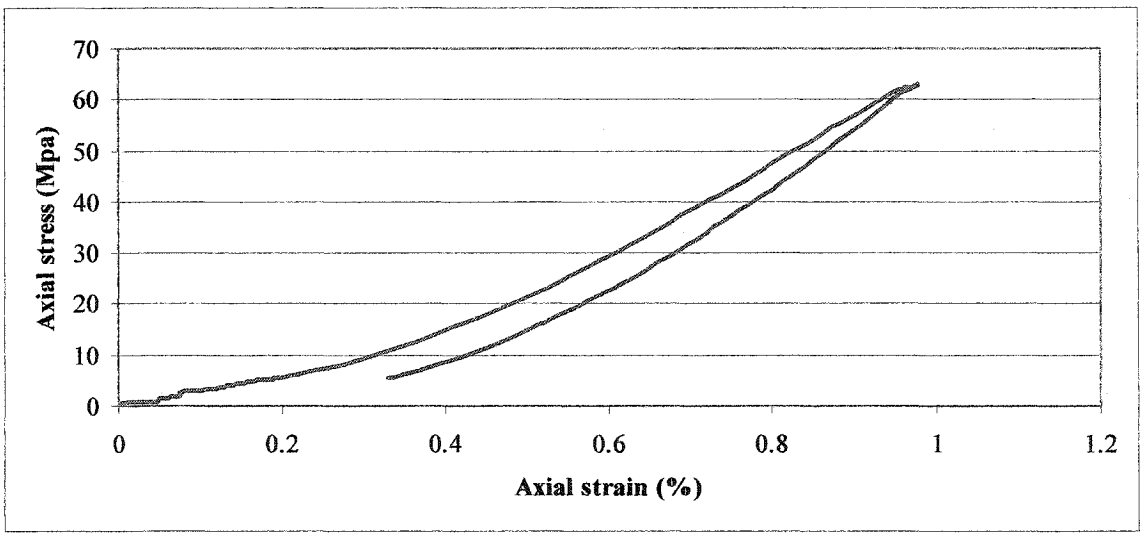

Figure D.2. Axial loading of the MHB sample under a confining pressure of 3445 kPa and a back pressure of 2000 kPa

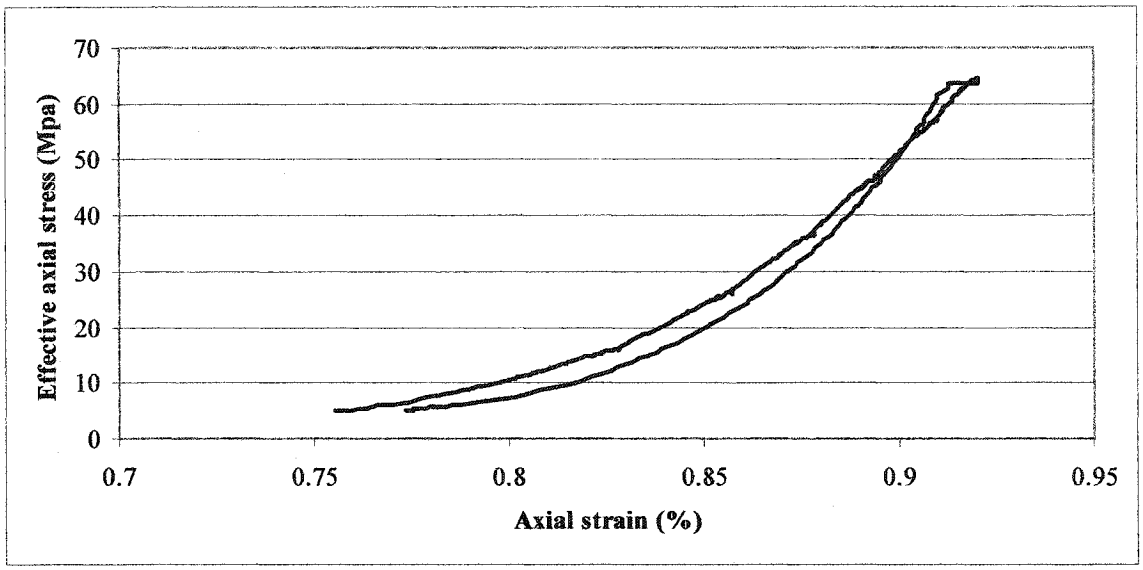

Figure D.3. Depletion of the MHB sample under uniaxial strain condition

Experiment on the GSF Sample

The GSF sample is initially brought to a confining pressure of 8, an axial stress of 15, and a back pressure of 3 MPa. Axial stress continued to increase under a constant confining volume. As illustrated in Figures D.4 and D.5, the whole deformation of the sample is in a predominantly elastic domain. In addition, Figure D.5 shows that confining pressure has only marginally changed with axial loading. This suggests that the sample has deformed only slightly in a radial direction. This is attributed to the compressibility of the oil. This small deformation would be enough to increase lateral stresses in a stiff rock, but not in the rather compressible oil that was controlling the confining pressure.

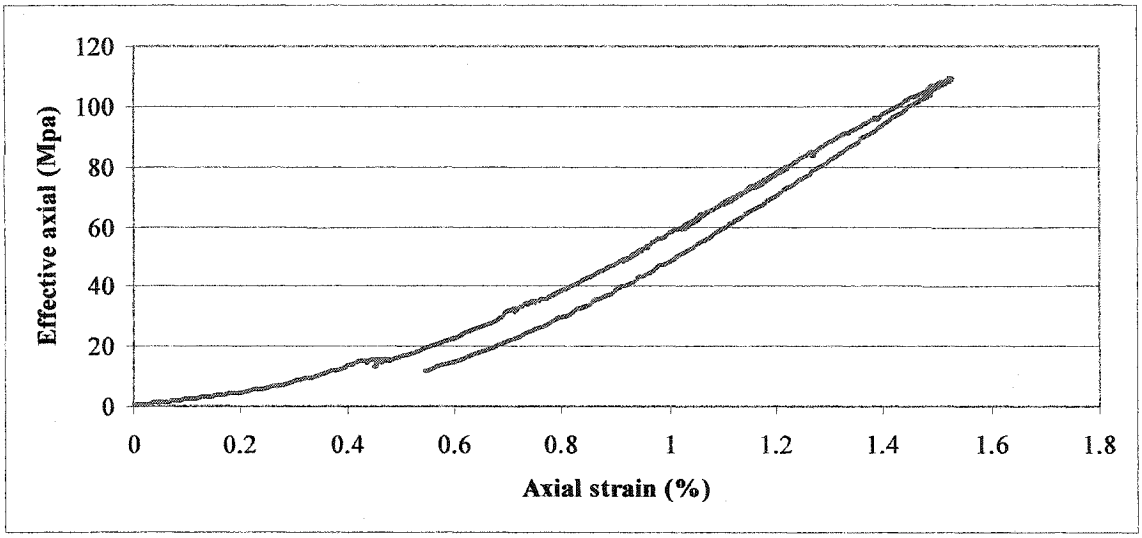

Figure D.4. Axial stress increase under uniaxial strain condition

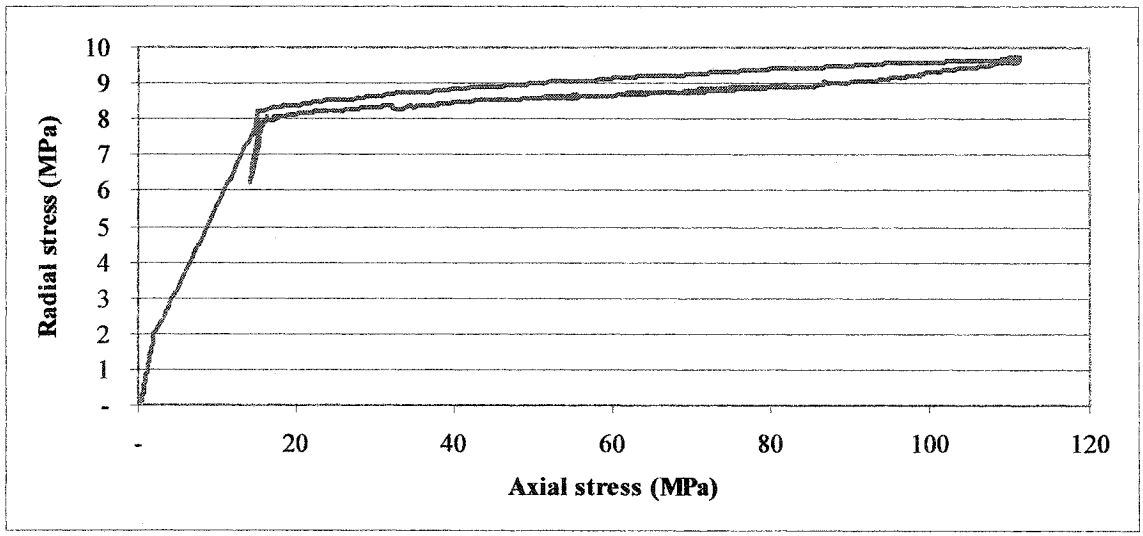

Figure D.5. Radial stress increase under uniaxial strain condition while axial stress increased

Concluding Remarks

Generally speaking, the volumetric yield pressure of most of the rock material has been reported to be high. This result was abstracted from literature and was confirmed by the two experiments on GSF and MHB samples. These two samples, remained in an elastic domain even under excessive loading conditions, and showed no sign of pore collapse.

Subsequently, if pore collapse does not take place, the prospective effective stresses of a reservoir do not meet the cap.

Higher strength of samples and lower porosity decreases the likelihood of the incidence of pore collapse.

References

Ditzhuijzen P.J.D., and J.A. Waal, "Reservoir Compaction and Surface Subsidence in the Central Luconia Gas bearing Carbonates, Offshore Sarwak, East Malaysia", *SPE 12400, SPE 5th Offshore South East Asia Conference*, Singapore, 1984.

Hamilton, J.M., and J.L. Shafer, "Measurement of Pore Compressibility Characteristics in Rock Exhibiting Pore Collapse and Volumetric Creep", *SCA Conference*, Paper Number 9124, 1991.

Lawrence W.T., D.W. Rhett, and H.E. Farrell, "Effect of Reservoir Depletion and Pore Pressure Drawdown on In Situ Stress and Deformation in the Ekofisk Field, North Sea", *Rock Mechanics and Multidisiplinary Science*, Balkema, Rotterdom, 1991.

Smits R.M.M., A. Waal, and J.F.C. Kooten, "Prediction of Abrupt Reservoir Compaction and Surface Subsidence Due to Pore Collapse in Carbonates", *SPE 15642, 61st Annual SPE Conference*, New Orleans, LA, 1986.

Soares A.C., and F.H. Ferreira, "An Experimental Study for Mechanical Formation Damage", *SPE 73734, SPE International Symposium and Exhibition on Formation Damage Control*, Lafayette, Louisiana, 2002.

Appendix E: An Introduction to a Novel Expandable FRC Casing Liner for Completion of Oil and Gas Wells

Introduction

Sanding related costs directly and indirectly constitute an immense portion of the wellbore and operational costs. Nevertheless, no completion technique has been deployed by the oil industry which can eliminate sanding without any impairment in well production. A completion technique is hereby proposed which accomplishes sand free and high rate oil production.

In the following sections several completion techniques are briefly explained. Subsequently the shortcomings of the current completion techniques are discussed, followed by a proposed solution, which aims to eliminate the weaknesses of the current completion technologies.

A Review of Currently Practiced Completion Techniques

The oldest and the most commonly used completion technique for oil wells is open hole completion. It is still used today, although several other completion techniques are available (Retnanto and Yamin, 1999). The competence of the formation rock is a first consideration in deciding how to complete a well. Borehole instability and collapse as a result of shear failure is a common consequence of using this technique especially in heterogeneous and unconsolidated formations.

In general, the active sand control techniques can be divided into two main categories, namely filtering techniques and borehole reinforcement techniques. Filtering consists of removing particles larger than a given size through a mechanical means such as a pre-packed screen. Most gravel packs are designed as filters, although gravel packing in principle is supposed to reinforce the borehole wall. Reinforcement works through the radial stress counter acting on the radial deformation due to drawdown/depletion induced stresses.

Filtering Completion Techniques

Included in this category, the stand-alone technique, gravel packing, and open hole completions using Expandable Casing Packers (ECP) are briefly described.

One of the popular filtering techniques is the stand-alone screen. It is considered an open hole completion technique since a gap is left between the stand-alone screen and the wellbore. Therefore, the main disadvantage of this technique is the possible borehole collapse as well as screen corrosion during production.

Gravel pack technology is normally used for completion of weak formations. However, permeability damage during gravel placement is often significant especially in highly permeable formations. Another problem of this completion is the gradual plug of pore throats of the gravel pack with fines migrated from the medium by seepage force. Gravel pack operations can increase logistical requirements in horizontal and extended reach wellbores.

Open hole horizontal completion using External Casing Packers (ECP) for zonal isolation is another filtering technology that was developed in the 1990s. This completion is installed with a slotted pipe, or a screen across production intervals that are separated by ECPs (Jesse, 1999). Jesse (1999) also proposed an alternative isolation method wherein non-elastomeric sliding sleeves replaced the slotted pipe between the ECPs. To reduce rig time during the installation phase, Coronado and Knebel (1998) proposed a one-trip ECP cement inflation and stage cementing system.

For permanent applications, cement as used for inflation of ECPs proved to be problematic. This is because of concerns such as free water, particle segregation, and bulk volume loss. Moreover, some operators have concerns about cement leak and possible sealing of productive sections of formation. As a result, a non-inflatable alternative to ECP's was developed by Coronado et al. (2002). This is a rather complex open hole completion technique which includes a screen assembly, packer (including a sealing element and seal containment system), packer shifting tool, setting system (including a hydrostatic chamber and a coiling tube), gravel pack for controlling sand production, and a wash pipe and fluid diverter valve for creation of void in gravel pack, wherever the packer is located. To complete this technique, Corbett et al. (2002) presented three methods to install one-trip multiple zone isolation. Zonal isolation is achieved with either inflation set or mechanically set open-hole packers.

A setback of ECP and non-inflatable completions is their complexity in structure as well as in installation. Moreover, in the absence of the combination of ECP and gravel packing, wellbore instability and sand production are real dangers to the wellbore. On the other hand, the use of gravel packing not only complicates the installation process, but also brings about all of the disadvantages that associate with it when is used alone.

All of the completion techniques that do not support the wellbore allow failure and collapse of the wellbore and intense sand production may follow.

Reinforcing Completion Techniques

The casing/cementing/perforating, which is one of the most popular completions techniques, fits into this category. Furthermore, the main concept of the expandable completion technique is based on reinforcing the wellbore.

Casing/Cementing/Perforating Technique

One of the most popular reinforcing techniques is the casing/cementing/perforating technique (Venkitaraman et al., 2001). Perforations may be gravel-packed or frac-packed, in some circumstances frac-packing without a screen may also be used (Morita et al., 1998).

This completion technique has also been used in many horizontal wells (Stagg and Relley, 1991). There are two main obstacles in obtaining proper mud displacement in a horizontal wellbore. The first is the difficulty in obtaining sufficient pipe centralization. De-centralized pipe creates small areas where it is difficult, if not impossible, for the spacer/cement to displace mud during the cementing process. Gravity also adds to the problem in achieving successful cementing job. The displaced cement is generally heavier than the mud and, therefore, gravitates to the bottom of the hole, leaving a potential flow path along the top of the lateral wellbore. Cementing practices have changed in an attempt to overcome these problems, however, most operators agree that to successfully isolate a horizontal well with a standard cement job is highly unlikely and very expensive (Coronado and Knebel, 1998).

A major set-back of the casing/cementing/perforating technique is that intense shear stresses can potentially develop around the perforation tunnels and may lead to their

collapse. The cavities may grow and get interconnected which may induce even more sanding as well as buckling of casing.

Expandable Completion Techniques

Expandable techniques are supposed to eliminate all deficiencies associated with other completion techniques. They increase the sand screen surface area, thus increasing production rates (SPE 73750). Secondly, they support the wellbore and stabilize the borehole and minimize the potential for sand production.

It has been only a little over a decade since expandable metal technology was adapted to oilfield tubular products. Since then, expandable metal technology has been used in more than a thousand downhole applications. Most of the early wells that successfully employed this technology are in the former Soviet Union and Vietnam (Sumrow, 2002). Today, the technology is being used throughout the world to repair or seal worn and damaged pipe and to help operators construct deeper, slimmer wells that are more productive, while using fewer casing sizes. True mono-bore wells will allow successive use of a single, slim casing size without any loss in internal diameter throughout the wellbore. The willingness of companies beyond the super-majors to apply the technology and a string of recent operational accomplishments indicate that oil industry is just beginning to derive a potentially high value from expandable downhole assemblies (Emerson, 2003).

Expandable completions are operationally simple and save rig time. They have a high PI, which can give higher production; and they can improve the reservoir recovery factor.

Current Expandable Technologies and A Few Application Examples

Expandable metal products use base metals that are annealed in their pre-formed or "initial" condition and become hardened after the expansion process. The tubular products are expanded by forcing the walls of the pipe to expand in various percentages while retaining sufficient mechanical properties. Two basic types of expandable tubular products are available for downhole use: those made of solid pipe and those with slots or perforations cut through the wall. Expandable solids are used for wellbore construction and remediation, while expandable perforated pipe is used for sand control.

In January 2002, Baker Oil Tools ran an expandable liner hanger in a well in Prudhoe Bay, Alaska (Hay et al., 2003; Santoso et al., 2003). The hanger was set at a measured depth of 3150 m (10,335 ft) with a liner length of 335 m (1,100 ft). This was the first expandable liner top completion, with the completion string stabbed into the liner top. The EXPress TM screen is an example of a downhole sand control device that can be expanded outward to greatly reduce or eliminate the annular space between the wellbore and the screen. A well completed in Indonesia in November 2001, using the EXPress screen with expandable solid pipe and expandable openhole isolation packers and a conventional liner hanger, achieved outstanding results with no sand production and a reported productivity index about five times greater than that of offset wells.

Methods of Expansion

Methods of expansion vary with applications and products. Baker Oil Tools' preferred methodology is a top-down expansion process that uses hydraulic pressure fed into a piston. Hydraulic pressure anchors the system in place and opens the piston, which progressively pushes an expansion cone through the completion assembly, setting the liner hanger, expanding the blank pipe, setting the isolation packer and expanding the screen. After the expansion process is complete, the expansion tool is retrieved from the well. Using this system, thousands of feet of tubulars can be expanded in a single trip. Because the system does not rely on pushing or pulling energy from the drill-string, it can be activated easily in highly deviated wells.

Expandable Technology for Rehabilitation Purposes

Expandable tubular products can be used to provide cost-effective solutions for remediation operations. Rehabilitative expandable cladding is used to repair damaged casing and shut off perforations in cased hole, open hole, and sand control completions. In cased-hole applications, expandable cladding can be used to blank off perforations to minimize water inflow. To repair worn or damaged casing, a protective lining made of expandable solid pipe is lowered into place and expanded inside corroded or damaged pipe. The expansion "clads" the two pipes into one, giving the well a new liner with minimal reduction in the internal diameter of the original, damaged pipe.

The first expandable metal casing patch to repair a damaged casing section was installed in June, 2003 to a well, drilled in the early 1050s in south central Oklahoma (Jabs et al., 2004). The solution was a new expandable cladding technique perfected by Baker Oil Tools. It enables extended length casing repair and would allow max ID after placed in the wellbore. As well, it creates a definitive pressure integrity seal of the annulus area. The system is deployed and expanded utilizing an innovative hydraulic piston/anchor system that allows flexibility in the length of the deployed clad from short sections to unlimited length. The cladding was secured to the host casing via a top and bottom seal section which incorporated rubber elements and profile grooves to anchor the clad material when expanded to the host casing ID.

Expandable Technology for Selective Wellbore Completion

In open hole environments, the cladding can be used with expandable open hole packers to reduce or shut off water inflow. Used together with an expandable screen system in sand control completions, it can create a definitive mechanical fluid flow barrier that allows selective wellbore sections to shut-off. Baker Oil Tools' expandable wellbore liner is placed below a casing string and expanded to maintain the same through-put ID as the liner string located above it. The system can be used to block off unexpected problematic drill sections or as part of the initial well design (Gilmer and Emerson, 2004).

In July 2002, Baker Oil Tools installed the world's first single selective completion inside an expandable sand screen completion. The 6 1/8-in. open hole wellbore penetrated both oil and gas producing zones (Gilmer and Emerson, 2004). The objective was to achieve the ability to produce the oil zone first, and later, open the system to flow from the gas zone.

Expandable Technology for Zonal Isolation

An important issue in designing horizontal well completions is the zonal isolation. Zonal isolation for production and fluid placement during stimulation may suggest the segmentation of a horizontal well. This is to detect the origin of the problems, such as water or gas influx. Faults or fractures close to, or crossing the horizontal wellbore,

accelerate gas and water influx. After the location of the problematic section is detected, expandable techniques can be applied to effectively seal the section.

What is Wrong with the Current Expandable Solutions?

The current expandable techniques are based on a plastic expansion of a metal liner to the well face. As the expansion tool unloads, the elastic portion of the liner's deformation is recovered. This, in return, supplies a gap between the well face and the completion, which may reduce the efficiency of the expandable technique to something similar to stand-alone completion.

How to Rectify the Problem?

An expandable technology must be developed which avoids depending on mechanical deformation of a liner by using an expansion force. What is suggested in this thesis is a technology that is based on a Fiber Reinforced Composite (FRC).

Background on a Fiber Reinforced Composite (FRC) Material and Some Applications

As a consequence of their extraordinary attributes and properties, the use of FRC materials for fabrication of various structural components has increased in an exponential rate in the past few decades. Attributes such as light weight, high specific strength and stiffness, excellent fatigue properties, better corrosion resistance, thermal insulation, and vibration damping are some of the noteworthy properties associated with FRC. These materials, once primarily used for aerospace applications, are now used in several marine and civil applications, as well as in consumer products. FRC are generally more expensive than traditional materials such as steel and concrete; however, as their use increases, their cost will decrease, as it has been the case in the past decade. For instance, the cost of some carbon fibers has halved during the past ten yeas.

One of the most interesting applications of FRC, in relation to the oil and gas industry, has been the recent certification of a FRC drilling riser for use in aggressive, high-risk applications that will enable oil production in water depths approaching 3,000m. This follows the continuation of the efforts that have been devoted in the past twenty years to using FRC components to replace traditional materials in topside piping, gratings, ladders, handrails, wellhead enclosures, and buoyancy elements.

The riser, which is the pipeline that connects the drilling platform or drill ship on the water surface to the wellbore at the seabed, is made up of individual 15- 25 m long FRC pipes and connected together by metallic joints. The challenges for such pipelines are that they must have adequate strength and must be durable enough to withstand abrasion and corrosive chemicals while assuring flow.

In a design study presented at the Third International Conference on Composite Materials for Offshore Operations (CM003, sponsored by the Composites Engineering & Applications Center at the University of Houston), Chevron and CSO Aker Maritime (Houston, Texas), demonstrated that a FRC riser system (with composite air cans for buoyancy) could decrease the baseline cost of a truss spar hull design by more than 50%.

In the area of composite application for downhole applications, Leighton et al. (1998) and Saltel et al. (1999) suggested an inflatable composite sleeve to repair damaged tubing as well as to shut off undesired perforations. The sleeve is run-in on an electric wireline, inflated to push the composite against the inside of the casing, then heated to polymerize the resins.

Proposed Technological Solutions

Two different techniques are proposed for implementation in horizontal and vertical/slanted wellbores. Even though the technique that is suggested for horizontal wellbore is deployable in all other wellbores, to reduce the cost and ease the installation process, another technique is suggested for vertical and slanted wellbores as described in the following paragraphs.

The Proposed Technique for Horizontal Wellbores

The expandable stabilizer liner is based on using prepreg FRC tapes to weave a long wicker cylinder, surrounding a durable plastic liner. Prepreg is fiber-glass fabric impregnated with partially hardened resin and FRC tape is a fabric of already manufactured fibers and resin. The wicker construction will allow the fluid to seep into the horizontal well, after of course, the plastic liner has been removed (the removal stage will be discussed in below). The system, originally flexible (while the prepreg is uncured), will become stiff and strong upon the cure of the tapes.

Prepreg tapes (fibers) will be placed strategically, to produce appropriately thick rings, to provide the liner with the adequate hoop strength to endure the potential collapse of the well. The longitudinal tapes (fibers) will be placed so as to offer the resilience required, in the event that a portion of the well settles differentially from another, the horizontal ligament will simply displace, while the hoop rings will remain solid and stiff to endure the circumferential stress. In a sense, the liner will produce the maximum required hoop strength, while it would be compliant to move vertically from one station to another. This assembly, while flexible to start with, can be lowered through the vertical segment of the wellbore to the location of entry into the horizontal part. At that point, the liner, which still has its inner plastic balloon, can be pushed inward into the well by applying overbalance pressure.

The advantage of the proposed system is that the existing temperature inside the well will induce the curing process of the FRC basket, thus making the process much less costly. If the system was to be cured conventionally, that is by applying the required heat by an oven, the required energy cost would obviously have been considerable. The prepreg FRC can cure to attain their specified strength within a few hours (6-8 hrs) in temperatures as low as 150 ^{o}F. If higher temperatures are available (as some wells have temperatures as high as 350 ^{o}F), then the curing process is achieved within 2-3 hours. Once the FRC wicker is fully cured, the inside plastic balloon will be deflated and removed.

As can be seen, the proposed system is a resilient and cost-effective one, with strength and stiffness provided as needed. The fabrication process is also novel, in that it will use the existing energy available in the well, thus significantly reducing costs.

The Proposed Technique for Vertical/Slanted Wellbores

For vertical/slanted wellbores, a simpler technique is proposed. Even though it is expected that the above technology can be adopted for both horizontal and vertical wells, in order to decrease the overall cost of the proposed system, another technology is suggested for vertical/slanted wells.

In this solution, the vertical liner will be fabricated based on coupled pultrusion/filament winding fabrication technologies. Therefore, no ballooning is needed; and this feature

decreases the cost of installation. In the beginning, the diameter of the liner before curing is slightly less than the diameter of the hole. It will expand to the diameter of the wellbore upon curing by reservoir heat.

No limitations are expected for the deviation of the wellbore, as long as it is straight. The thickness of the completion depends on the strength for mechanical stability of the liner and the stiffness for its deformation. It is expected that the thickness would not exceed the currently used casing thicknesses. Factors that determine stiffness and strength are the type of the fiber that is used (like carbon, glass, boron...), and its volume ratio as well as orientation. For each field condition, e.g. temperature, pressure, *in situ* stresses, and medium strength, the completion has to be custom designed. The liner has a solid wall up to a certain length, and then will have perforated portion, much like a wicker basket. The perforation would allow the fluid to flow through the liner.

The vertical liner will be fabricated based on coupled pultrusion/filament winding fabrication technologies. Pultrusion is a continuous, semi automated process for manufacturing composite materials. As schematically shown in Figure E.1, continuous fibers or fabrics made of glass or carbon fibers are impregnated with a resin in the impregnation bath. The material is then drawn through a heated die, by a pulling system located near the end of the pultruder. The composite is then cut into lengths with a cut-off saw.

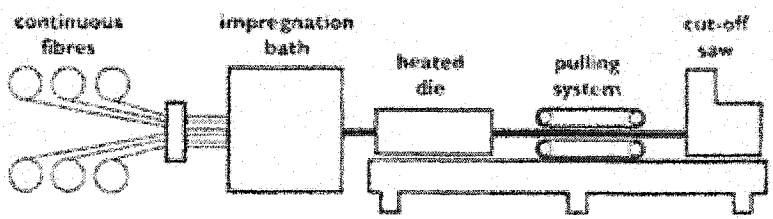

Figure E.1. A schematic of pultrusion process for manufacturing composite materials

Filament winding is the process of winding resin-impregnated fiber or tape on a mandrel surface in a precise geometric pattern. This is accomplished by rotating the mandrel while a delivery head precisely positions fibers on the mandrel surface. By winding

continuous strands of carbon fiber, fiberglass, or other material in very precise patterns, structures can be built with properties stronger than steel at much lighter weights.

Filament winding machines, as schematically shown in Figure E.2, operate on the principles of controlling machine motion through various axes of motion. These filament winding machines are computer numerically controlled (CNC) machines, highly automated and may be set-up and operating in a matter of minutes. The most basic motions are the spindle or mandrel rotational axis, the horizontal carriage motion axis, and the cross or radial carriage motion axis. Additional axes may be added, typically a rotating eye axis or a yaw motion axis, and when the pattern calls for more precise fiber placement, further additional axes may be added. The last step in the filament winding process requires pulling or "stripping" the mandrel out of the cured composite structure. While supporting the composite structure, the mandrel is attached to an extractor carriage and slowly removed from the center of the part, leaving behind the composite structure that is ready for assembly.

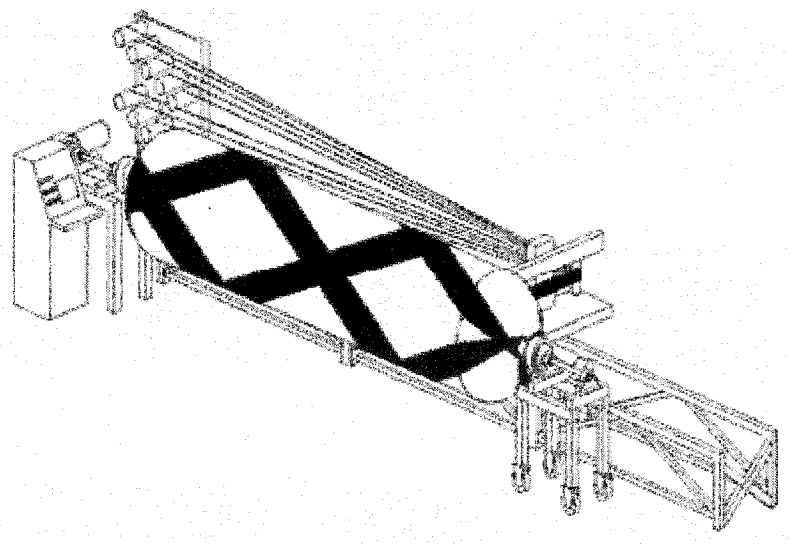

Figure E.2. A schematic of filament winding machines

The axial strength of the casing is ensured by longitudinal fibers laid by the pultrusion process. The longitudinally laid casing pipe will then be used as a mandrel. In filament winding, resin impregnated fibers or rovings of glass or carbon fiber are wound on a rotating mandrel in predetermined patterns. The filament winding thereby eliminates the cost of a mandrel and reduces the time consumed for demandreling

The filament winding process places fibers in various specified angles to provide the casing with the required shear (and bending) strength. Since filament winding is a computer controlled process, the fibers can be laid very closely together, as they are done in conventional filament winding to complete the solid portion of the riser. The benefit of this is its easy assembly without any need of inflation. The fiber placement then will be strategically placed, within appropriate increments, to produce the perforated (wicker) effect at the desired length of the pipe.

In order to make the component more economical, if the need arises, a high endurance metallic alloy can be used to constitute its tip ring portion (thus to resist the non-uniform forces and stress concentration experienced by these casing during their placement. This metallic ring can be easily included on the mandrel, and wrapped with fibers to make it an integral part of the riser. The entire system, with the ring, can then be cured to achieve the optimum strength.

Another advantage of the proposed system is that one can optimize the thermal expansion coefficient of the FRC used in forming the casing by altering the fiber orientation. Indeed one can obtain positive, negative, or zero thermal expansion coefficients by laying fibers at certain orientations. Therefore the coefficient of thermal expansion of the casing is optimized, so that when it experiences the elevated operation temperature, it would attain maximum expansion, thus providing the optimum stability by applying pressure to the hosting well bore.

References:

Corbet, T.G. and E.H. Vickery, "Multiple Zone Open Hole Gravel Packing Techniques with Zonal Isolation", *SPE 77214, IADC/SPE Asia Pacific Drilling Technology,* Jakarta, Indonesia, 2002.

Coronado, M.P., H. Bjorkesett, D.G. Jiral, and H. Fordedal, "Advanced Open hole Completions Utilizing a Simplified Zone Isolation System", *SPE 77438, SPE Annual Technical Conference and Exhibition,* San Antonio, Texas 2002.

Coronado, M.P., and M.J. Knebel, "Development Of One-Trip ECP Cement Inflation and Stage Cementing System for Open hole Completions," *SPE 39345, IADC/SPE Drilling Conference,* Dallas, Texas, 1998.

Demong, K., M. Rivenbark, and D. Mason, "Breakthroughs Using Solid Expandable Tubulars to Construct Extended Reach Wells", *SPE 87209, IADC/SPE Drilling Conference,* Dallas, Texas, 2004.

Emerson, A.B., "Expanding the Value of Expandable Metals", *Journal of Petroleum Technology*, pp. 24-25, January 2003.

Gilmer, M., and B. Emerson, "World's First Completion Set Inside Expandable Screen" *SPE 87201, IADC/SPE Drilling Conference,* Dallas, Texas, 2004.

Goode, P.A. and D.J. Wilkinson, "Inflow Performance of Partially Open Horizontal Wells," *JPT,* pp. 983-987, August 1991.

Hay, B., M. Jabs, and M. Nicol, "Utilizing Re-formable Technology to Enhance Production in North Sea Application", *High Tech Wells Conference*, Galveston, Texas, February 2003.

Jabs, M., C.E. Harmon, S.E. Harmon, and R.E. Harmon, "New Expandable Cladding Technique Enables Extended Length Casing Repair", *SPE 87212, IADC/SPE Drilling Conference,* Dallas, Texas, 2004.

Jesse, J.C., "Selective Production of Horizontal Open hole Completions Using ECP Sand Sliding Sleeve Technology", *SPE 55618, SPE Rocky Mountain Regional Meeting,* Gillette, Wyoming, 1999.

Leighton, J., J.L. Saltel, J. Morrison, R. Welch, and J. Pilla, "Water Shut-Off Using an Inflatable Composite Sleeve Polymerised In-Situ. A Case History on Forties Delta", *SPE 50620, SPE European Petroleum Conference,* the Hague, the Netherlands, 1998.

Morita N., R.C. Burton, and E. Davis, "Fracturing, and Formation Failure Control: Can Screenless Completions Prevent Sand Production?", *SPE 51187, SPE Annual Technical Conference and Exhibition,* Denver, 1998.

Retnanto, A., and M. Yamin, "Impact of Completion Technique on Horizontal Well Productivity", *SPE 54302, SPE Asia Pacific Oil and Gas Conference and Exhibition*, Jakarta, Indonesia, 1999.

Saltel, J.L., J.R.N. Leighton, A.M. Faure, and T. Baaijens, "In-Situ Polymerisation of an Inflatable Composite Sleeve to Reline Damaged Tubing and Shut Off Perforations", *SPE 56867 Offshore Technology Conference,* Houston, 1996.

Santoso, B.T., M. Sofyan, A. Liew, and B. White, "Convergence of Technologies: Intelligent Completions, Expandables & Multilaterals", *Petromin*, January/February 2003.

Stagg, T.O., and R.H. Relley, "Horizontal Well Completions in Alaska", *SPE Print Series, Horizontal Drilling,* no. 33, pp. 123-128, 1991.

Sumrow, M., "Expandable Tubulars Gaining Industry Confidence", *Oil & Gas Journal*, pp. 33-37, January 2002.

Venkitaraman A., J.F. Manrique, and B.D. Poe Jr., "A Comprehensive Approach to Completion Optimization", *SPE 72386, SPE Eastern Regional Meeting,* Canton, Ohio, 2001.

References:

Antheunis, D., J. Geertsma, and P.B. Vriezen, "Mechanical Stability of Perforation Tunnels In Friable Sandstones", *Proc. 31th Annual Petr. Mech. Engr. Conf. of the ASME*, Mexico City, 1976a.

Antheunis, D., P.B. Vriezen, B.A. Schipper, and A.C. van der Vlis, "Perforation Collapse: Failure of Perforated Friable Sandstones", *SPE 5750, European Spring Meeting*, Amsterdam, 1976b.

Barril, R.J., and L.G. Gay, "Controlling Sand Production in High Rate Gas Wells", *World oil*, pp. 52-56, 1983.

Bathe, K.J., *Finite element procedures in Engineering Analysis*, Prentice-Hall, Inc., Englewood Cliffs, N. J., 1982.

Belhaj, H.A., A. Nouri, H.H. Vaziri, S.D. Butt, and M.R. Islam: "Experimental Determination of the Effect of Pore Collapse on Permeability and Porosity of Sandstone Reservoirs," *proc., PAPG-SPE Annual Technical Conference*, Karachi, Pakistan, 2-4 November 2002.

Berg, R.R., "Capillary Pressures in Stratigraphic Traps", *Bull. Amer. Assoc. Petrol. Geol.*, **59**, no. 6, pp. 939-956, 1975.

Bianco, L.C.B., and P.M. Halleck, "Mechanisms of Arch Instability and Sand Production in Two-Phase Saturated Poorly Consolidated Sandstones", *SPE 68932, SPE European Formation Damage Conference*, the Netherlands, 2001.

Bratly, R.K., and R. Risnes, "Stability and Failure of Sand Arches", *SPEJ*, pp. 236-248, 1981.

Charlez, P.A., *Rock Mechanics-Vol 2: Petroleum Applications*, Editions Technip, 1st Edition, 1997.

Coates, D.R., and S.A. Denoo, "Mechanical Properties Program Using Borehole Analysis, and Mohr's Circle", *Proceedings SPW/La 22nd Annual Logging Symposium*, pp. 23-26, 1981.

Corbet, T.G. and E.H. Vickery, "Multiple Zone Open Hole Gravel Packing Techniques with Zonal Isolation", *SPE 77214, IADC/SPE Asia Pacific Drilling Technology,* Jakarta, Indonesia, 2002.

Coronado, M.P., H. Bjorkesett, D.G. Jiral, and H. Fordedal, "Advanced Openhole Completions Utilizing a Simplified Zone Isolation System", *SPE 77438, SPE Annual Technical Conference and Exhibition,* San Antonio, Texas 2002.

Coronado, M.P. and M.J. Knebel, "Development Of One-Trip ECP Cement Inflation and Stage Cementing System for Openhole Completions," *SPE 39345, IADC/SPE Drilling Conference,* Dallas, Texas, 1998.

Cundall P.A., and M. Board, "A Microcomputer Program for Modelling Large-Strain Plasticity Problems", *Numerical Methods in Geomechanics. Proc. 6th Int. Conf. on Numerical Methods in Geomechanics*, Innsbruck, Austria, April 11-15, Swododa C.(ed), Rotterdam, Balkema, pp. 2101-2108, 1988.

Cuthbertson, R.L., A. Green, J.A. Dewar, and B.D. Truelove, "Completion of an Underbalanced Well Using Expandable Sand Screen for Sand Control", *SPE/IADC 79792, SPE/IADC Drilling Conference*, Amsterdam, the Netherlands, 2003.

Das, B.M., *Principles of Geotechnical Engineering,* Fourth Edition, PWS-KENT Publishing Company, 1998.

Demong, K., M. Rivenbark, and D. Mason, "Breakthroughs Using Solid Expandable Tubulars to Construct Extended Reach Wells", *SPE 87209, IADC/SPE Drilling Conference,* Dallas, Texas, 2004.

Desai, C.S. and H.J. Siriwardane, *Constitutive Laws for Engineering Materials with Emphasis on Geologic Material*, Prentice-Hall Publishing Co., 1984.

Ditzhuijzen P.J.D., and J.A. Waal, "Reservoir Compaction and Surface Subsidence in the Central Luconia Gas bearing Carbonates, Offshore Sarwak, East Malaysia", *SPE 12400, SPE 5th Offshore South East Asia Conference*, Singapore, 1984.

Durrett, J.L., W.T. Golbin, J.W. Murray, and R.E. Tighe, "Seeking a Solution to Sand Control", *JPT*, pp. 1664-1672, 1977.

Dusseault, M.B. and S. El-Sayed, "Heavy-Oil Production Enhancement by Encouraging Sand Production", *SPE 59276, SPE International Symposium on Formation Damage*, Lafayette, Louisiana, 2000.

Echols, R., J. Gano, P. Shy, C. Tuckness, H. Zhang, and D. Campo, "Development and Testing of an Expandable Sand Screen and Expansion Tool", *SPE 73750, SPE International Symposium and Exhibition on Formation Damage Control*, Lafayette, Louisiana, 2002.

Edwards, D., H. Joranson, and J. Spurlin, "Field Normalization of Formation Mechanical Properties", *SPWLA, 29th Annual Logging Symposium*, 1988.

Edwards, D.P., Y. Sharma, and A. Charron, "Zones of Sand Production Identified by Log-Derived Mechanical Properties: A Case Study", *Proceeding SPWLA 8th European Formation Evaluation Symposium*, London, 1983.

Emerson, A.B., "Expanding the Value of Expandable Metals", *Journal of Petroleum Technology*, pp. 24-25, January 2003.

Geilikman, M.B., F.A.L. Dullien, and M.B. Dusseault, "Erosional Creep of Fluid-Saturated Granular Medium", *J. of Eng. Mechanics of ASCE*, no. 123, pp. 653-659, 1997.

Gilmer, M., B. Emerson, "World's First Completion Set Inside Expandable Screen", *IADC/SPE 87201, IADC/SPE Drilling Conference*, Dallas, TX, 2004.

Goode, P.A. and D.J. Wilkinson, "Inflow Performance of Partially Open Horizontal Wells", *JPT*, pp. 983-987, August 1991.

Hackworth, M., C. Johnson, J. Heiland, J. McClukin, D. Eubank, M. Kemp. L.M. Schetky, and P.S. Smith, "Development and First Aplicaion of Bistable Expandable Sand Screen", *SPE 84265, SPE Annual Conference and Exhibition*, Denver, Colorado, 2003.

Hall, C.D., and W.H. Harrisburger, "Stability of Sand Arches: A Key to Sand Control", *J. Pet Technology*, pp. 821-829, 1970.

Hamilton, J.M., and J.L. Shafer, "Measurement of Pore Compressibility Charachteristics in Rock Exhibiting Pore Collapse and Volumetric Creep", *SCA Conference*, Paper Number 9124, 1991.

Han, G., and M.B. Dusseault, "Quantitative Analysis of Mechanisms for Water-Related Sand Production", SPE 73737, *SPE Symposium and Exhibition on Formation Damage*, Lafayette, Louisiana, 2002.

Hay, B., M. Jabs, and M. Nicol, "Utilizing Re-formable Technology to Enhance Production in North Sea Application", *High Tech Wells Conference*, Galveston, Texas, February 2003.

Itasca Consulting Group, FLAC- Fast Lagrangian Analysis of Continua- User's Guide 3.4, Minneapolis, Minnesota, 1998.

Jabs, M., C.E. Harmon, S.E. Harmon, and R.E. Harmon, "New Expandable Cladding Technique Enables Extended Length Casing Repair", *SPE 87212, IADC/SPE Drilling Conference,* Dallas, Texas, 2004.

Jesse, J.C., "Selective Production of Horizontal Openhole Completions Using ECP Sand Sliding Sleeve Technology", *SPE 55618, SPE Rocky Mountain Regional Meeting,* Gillette, Wyoming, 1999.

Kessler, N., Y. Wang, and F.J. Santarelli, "A Simplified Pseudo-3D Model to Evaluate Sand Production Risk in Deviated Cased Holes", *SPE 26541, Proc. 68th SPE Annual Tech. Mtg.*, **2**, 1993.

Kooijman, A.P., P.J. van den Hoek, Ph. De Bree, C. J. Kenter, B.V Z. Zheng, and M. Khodaverdian, "Horizontal Wellbore Stability and Sand Production in Weakly Consolidated Sandstones", *SPE 36419, SPE Annual Technical Conference and Exhibition,* Denver, Colorado, 1996.

Lawrence W.T., D.W. Rhett, and H.E. Farrell, "Effect of Reservoir Depletion and Pore Pressure Drawdown on In Situ Stress and Deformation in the Ekofisk Field, North Sea", *Rock Mechanics and Multidisiplinary Science*, Balkema, Rotterdom, 1991.

Leighton, J., J.L. Saltel, J. Morrison, R. Welch, and J. Pilla, "Water Shut-Off Using an Inflatable Composite Sleeve Polymerised In-Situ. A Case History on Forties Delta", *SPE 50620, SPE European Petroleum Conference,* the Hague, the Netherlands, 1998.

Malvern, L.E., *Introduction to the Mechanics of a Continuous Medium*, Prentice-Hall Publishing Co., 1969.

Metcalfe, P., and C. Whitelaw, "The Development of the First Expandable Sand Screen", *SPE 11032, Offshore Technology Conference*, Houston, TX, 1999.

Morita N., R.C. Burton, and E. Davis, "Fracturing, and Formation Failure Control: Can Screenless Completions Prevent Sand Production?", *SPE 51187, SPE Annual Technical Conference and Exhibition,* Denver, 1998.

Morita, N., D.L. Whitfill, I. Massie, and T.W. Knudsen, "Realistic Sand Production Prediction: Numerical Approach", *SPE 16989, SPE Prod. Eng.*, 15-24, 1989a.

Morita, N., D.L. Whitfill, O.P. Fedde, and T.H. Lovik, "Parametric Study of Sand Production Prediction: Analytical Approach", *SPE 16990, SPE Prod. Eng.*, pp. 25-33, 1989b.

Morita, N., and G.F. Fuh, "Prediction of Sand Problems of a Horizontal Well From Sand Production Histories of Perforated Cased Wells", *SPE 48975, SPE Annual Technical Conference and Exhibition*, New Orleans, Louisiana, 1998.

Morita, N., and P.A. Boyd, "Typical Sand Production Problems: Case Studies and Strategies for Sand Control", SPE *22739, 66th Annual Conference*, Dallas, TX, 1991.

Nordgren, R.P., "Strength of Well Completions", *Proceeding 18th US Symposium on Rock Mechanics*, Keystones, Co, 4A3-1, 4A3-9, 1977.

Nouri, A., H. Vaziri, H. Belhaj, and R. Islam, "Effect of Volumetric Failure on Sand Production in Oil-Wellbores", *SPE 80448, SPE Asia Pacific Oil and Gas Conference and Exhibition,* Jakarta, Indonesia, 2003.

Papamichos, E., and E.M. Malmanger, "A Sand Erosion Model for Volumetric Sand Productions in a North Sea Reservoir", *SPE 54007, SPE Latin American and Caribbean Petroleum Engineering Conference*, Caracas, Venezuela, 1999.

Papamichos, E., and P.J. van den Hoek, "Size dependency of Castlegate and Berea sandstone hollow cylinder strength", *Proc. 35th U.S. Symp. Rock Mech.*, Lake Tahoe, Nevada, pp. 301-306, Rotterdam, Balkema, 1995.

Papanastasiou, P., and I. Vardoulakis, "Numerical Treatment of Progressive Localisation in Relation to Borehole Stability", *Int. journal Numer. Anal. Meth. Geomech.*, no.16, pp. 389-424, 1992.

Perkins, T.K., and J.S. Weingarten, "Stability and Failure of Spherical Cavities in Unconsolidated Sand and Weakly Consolidated Rock", *SPE 18244, 63rd Annual Technical Conference*, Houston, Texas, 1988.

Philips, F.L., and S.R. Whitt, "Success of Openhole Completions in the Northeast Butterfly Field, Southern Oklahoma", *SPE 11555, Production Operation Symposium*, Oklahoma City, 1983.

Retnanto, A., and M. Yamin, "Impact of Completion Technique on Horizontal Well Productivity", *SPE 54302, SPE Asia Pacific Oil and Gas Conference and Exhibition*, Jakarta, Indonesia, 1999.

Risnes, R., R.K. Bratli, and P. Harsrud, "Sand Stresses around a Wellbore", *SPEJ*, pp. 883-898, 1982.

Ruistuen, H., L.W. Teufel, and D. Rhett, "Influence Of Reservoir Stress Path on Deformation and Permeability of Weakly Cemented Sandstone Reservoir", *SPE 36535, SPE Annual Technical Conference and Exhibition*, Denver, Colorado,1996.

Saltel, J.L., J.R.N. Leighton, A.M. Faure, and T. Baaijens, "In-Situ Polymerisation of an Inflatable Composite Sleeve to Reline Damaged Tubing and Shut Off Perforations", *SPE 56867 Offshore Technology Conference,* Houston, 1996.

Sanfilippo F., G. Ripa, M. Brignoli, and F.J. Santarelli, "Economical Management of Sand Production by a Methodology Validated on an Extensive Database of Field Data", *SPE 30472, Annual Technical Conference*, Dallas, 1995.

Sanfilippo F., M. Brignoli, D. Giacca, and F.J. Santarelli, "Sand Production: From Prediction to Management", *SPE 38185, SPE European Formation Damage Conference*, the Netherlands, 1997.

Santoso, B.T., M. Sofyan, A. Liew, and B. White, "Convergence of Technologies: Intelligent Completions, Expandables & Multilaterals", *Petromin*, January/February 2003.

Schutjens, P.M.T.M., T.H. Hanssen, M.H.H. Hettema, J. Merour, J.Ph. de Bree, J.W.A. Coremans, and G. Helliesen, "Completion-Induced Porosity/Permeability Reduction in Sandstone Reservoirs. Data and Model for Elasticity-Dominated Deformation", *SPE 71337, SPE Annual Technical Conference and Exhibition,* New Orleans, Louisiana, 2001.

Skjarstein, A., J. Tronvoll, F.J. Santarelli, and H. Joranson, "Effect of Water Breakthrough on Sand Production: Experimental and Field Evidences", *SPE 38806, SPE Annual Conference and Exhibition*, San Antonio, Texas, 1997.

Smith, G.E., "Fluid Flow and Sand Production in Heavy Oil Reservoirs under Solution Gas Drive", SPE 15094, SPE California regional meeting, Oakland, California, 1986.

Smits R.M.M., A. Waal, and J.F.C. Kooten, "Prediction of Abrupt Reservoir Compaction and Surface Subsidence Due to Pore Collapse in Carbonates", *SPE 15642, 61st Annual SPE Conference*, New Orleans, LA, 1986.

Soares A.C., and F.H. Ferreira, "An Experimental Study for Mechanical Formation Damage", *SPE 73734, SPE International Symposium and Exhibition on Formation Damage Control*, Lafayette, Louisiana, 2002.

Stagg, T.O. and R.H. Relley, "Horizontal Well Completions in Alaska", *SPE Print Series, Horizontal Drilling,* no. 33, pp. 123-128, 1991.

Stavropoulou, M., P. Papanastasiou, and I. Vardoulakis, "Coupled Wellbore Erosion and Stability Analysis", *Int. J. Num. Anal. Methods Geomech.*, no. 22, pp. 749-769, 1998.

Stein, N., "Calculate Drawdown That Will Cause Sand Production", *World oil*, pp. 48-49, 1988.

Sumrow, M., "Expandable Tubulars Gaining Industry Confidence", *Oil & Gas Journal*, pp. 33-37, January 2002.

Tronvol, J., M.B. Dusseault, F. Sanfilippo, and F.J. Santarelli, "The Tools Of Sand Management", *SPE 71673, SPE Annual Technical Conference and Exhibition*, New Orleans, Louisiana, 2001.

Tonvol, J., A. Skjarstein, and E. Papamichos, "Sand Production: Mechanical Failure or Hydromechanic Erosion?", *Int. J. Rock Mech & Min. Sci.*, **34**, no. 3-4, 1997a.

Tronvol, J., E. Papamichos, A. Skjarstein, and F. Sanfilippo, "Sand Production in Ultra-Weak Sandstones: Is Sand Control Absolutely Necessary?", *SPE 39042, fifth Latin American and Caribbean conf. and Exhibition*, Rio de Janeiro, Brazil, 1997b.

Tronvol, J., E. Papamichos, and N. Kessler, "Perforation Cavity Stability: Investigation of Failure Mechanisms", *Geotech. Eng. of Hard Soils-Soft Rocks*, Balkema, Rotterdam, pp. 1687-1693, 1993.

Tronvol, J., M.B. Dusseault, F. Sanfilippo, and F.J. Santarelli, "The Tools of Sand Management", *SPE 71673, SPE Annual Technical Conference and Exhibition*, New Orleans, Louisiana, 2001.

Tronvol, J., N. Morita, and F.J. Santareli, "Perforation Cavity Stability: Comprehensive Laboratory Experiments and Numerical Analysis", *SPE 24799, 67th SPE ATM*, Washington DC, 1992.

Tronvoll J., and P.M. Halleck, "Observations of Sand Production and Perforation Cleanup in A Weak Sandstone", *Proc. EUROCK' 94*, Balkema, Rotterdam, pp. 355-360, 1994.

Van Buren, M., L. van den Broek, and C. Whitelaw, "Trial of an Expandable Sand Screen to Replace Internal Gravel Packing", *SPE/IADC 57565, SPE/IADC Middle East Drilling Technology Conference*, Abu Dhabi, UAE, 1999.

Van den Hoek, P.J., A.P. Kooijman, C.J. Kenter, M. Khodaverdian, C.R. Hyland, and J.D. McLennan, "Size Dependency of Hollow Cylinder Collapse Strength", *SPE 24800, 67th Annual Technical Conference and Exhibition of the Society of Petroleum Engineers*, Washington, DC, 1992.

Van den Hoek, P.J., Hertogh, G.M.M, Koijman, A.P., De Bree, Ph., Kenter, and E. Papamichos, "A New Concept of Sand Production Prediction: Theory And Laboratory Experiments", *SPE 36418, 71th SPE annual Tech. Conf.*, Denver Colorado, 1996.

Vardoulakis, I., M. Stavropoulou, and P. Papanastasiou, "Hydromechanical Aspects of the Sand Production Problem", *Transport in Porous Media*, no. 22, pp. 225-244, 1996.

Vaziri, H., B. Barree, Y. Xiao, I. Palmer, and M. Kutas: "What Is the Magic of Water in Producing Sand?", *SPE 77683, SPE Annual Technical Conference and Exhibition*, San Antonio, Texas, 2002.

Vaziri, H., and I. Palmer, "Evaluation of Openhole Cavity Completion Technique in Coalbed Methane Reservoirs", *3rd North American Rock Mechanics Symposium*, Cancun, Mexico, 1998.

Vaziri, H., X. Wang, and I. Palmer, "Wellbore Completion Technique and Geotechnical Parameters Influencing Gas Production", *the Canadian Geotechnical Journal*, no. 34, pp. 87-101, 1997.

Veeken C.A.M., Davies, D.R., Kenter, C.J., and Kooijman, A.P., "Sand Production Prediction Review: Developing an Integrated Approach", *SPE 22792, 66th Annual Tech. Conf.*, Dallas, Texas, 1991.

Venkitaraman A., J.F. Manrique, and B.D. Poe Jr., "A Comprehensive Approach to Completion Optimization", *SPE 72386, SPE Eastern Regional Meeting,* Canton, Ohio, 2001.

Vermeer, P.A., and R. de Borst, "Non-Associated Plasticity for Soils, Concrete and Rock", *Heron*, **29**, no. 3, pp. 1-64, 1984.

Wang, Y., and C.C. Chen, "Improved Production and Sand(Cold) Production in Conventional and Heavy Oil Reservoirs- A Field Case and Simulation", *SPE 57290, SPE Asia Pecific improved oil recovery Conference*, Kuala Lampur, Malaysia, 1999.

Wang, Y., C.C. Chen, and M.B. Dusseault, "An Integrated Reservoir Model for Sand Production and Foamy Oil Flow during Cold Heavy Oil Production", *SPE 69714, SPE International Thermal Operations and Heavy Oil Symposium,* Margarita, Venezuela, 2001.

Wang, Y., and M.B. Dusseault, "Sand Production Potential Near Inclined, Perforated Wellbores", *Paper 96-27, Proc. CIM 47th Annual Tech. Mtg*, Calgary, AB, 1996.

Weingarten, J.S., and T.K. Perkins, "Prediction of Sand Production in Gas Wells: Methods and Gulf of Mexico Case Studies", *SPE 24797, SPE 67th Annual Technical Conference and Exhibition*, Washington D.C., 1992.

Wilkins, M.L., "Calculation of Elastic-Plastic Flow", *Report UCRL-7322*, Lawrence Radiation Laboratory, Livermore, 1969.